Supporting Information
Abiotic Origin of the Citric Acid Cycle Intermediates

Mason McAnally[1,2], Jana Bocková[3], Andrew M. Turner[1,2], Nana Hara[1,2], Daria Mikhnova[1,2], Cornelia Meinert[3*], Ralf I. Kaiser[1,2*]

[1] Department of Chemistry, University of Hawaii at Mānoa, Honolulu, HI 96822

[2] W.M. Keck Laboratory in Astrochemistry, University of Hawaii at Mānoa, Honolulu, HI 96822

[3] Université Côte d'Azur, Institut de Chimie de Nice, UMR 7272 CNRS, 06108 Nice, France

*Corresponding authors:

*Cornelia.MEINERT@univ-cotedazur.fr, *ralfk@hawaii.edu

Supporting Text

Degradation of α-ketoglutaric acid

In the sample injections of derivatized α-ketoglutaric acid (Figure S13–S14), three different peaks are observed in the chromatograms which have the same mass spectra. Previous work derivatizing α-ketoglutaric acid have noted this process (and similar derivatization techniques) results in different isomeric forms of α-ketoglutaric acid (1, 2). In the case of MTBSTFA derivatization of α-ketoglutaric acid, three peaks are detected associated with bis-, tris-, and tetrakis-*t*BDMS derivatives (3). The reference standard injections here show the same mass spectra for the three different eluting peaks in the chromatograms. In the reference standard injections the highest peak intensity follows for α-ketoglutaric acid-1, α-ketoglutaric acid-2, and α-ketoglutaric acid-3 (Figure S14), this was not the case for the sample injections (Figure 3b). The mismatch in peak intensity profiles for the three peaks associated with α-ketoglutaric acid may suggest additional ketoacids are present in the sample matrix.

Retrosynthesis

Three comprehensive retrosynthetic pathways are illustrated in Figures S16–S52, and a list of the deconstructed molecules can be found in Table S31. In condensed-phase chemical reactions on icy mantles, thermochemical reactions are limited; however, ionizing irradiation can provide the energy necessary to facilitate bond ruptures. These bond breakings primarily result in suprathermal hydrogen molecules that overcome the entrance barriers for addition reactions to double and triple bonds (4-6).

The process begins by breaking single bonds in the product molecules (molecules **1–9**) to form two radical intermediates. These intermediates can undergo hydrogen addition or hydrogen elimination or any combination of the two. Typically, the addition or elimination of hydrogen atoms leads to stable closed-shell molecules. In some cases, these reactions can also produce diradicals. For the purposes of this retrosynthesis, diradicals were not considered due to their instability. As an example, acetic acid (Figure S32A–S32B) can undergo two different bond-breaking processes: one producing the methyl radical and hydroxycarbonyl radical (Figure 32A) and the other producing the hydroxyl radical and acetyl radical (Figure 32B). Subsequently, hydrogens are added or eliminated. The methyl radical has two possibilities: hydrogen addition to methane (CH_4) or hydrogen elimination to produce methylene (CH_2); both components are known

to occur during irradiation of hydrocarbons (7, 8). Similarly, the acetyl radical once reacted with a hydrogen atom can produce acetaldehyde (CH_3CHO) or hydrogen elimination to form ethenone (H_2CCO). This process can be repeated for larger molecules until we reach known components of interstellar ices.

Table S1. Experimental conditions used in interstellar analog ice simulations. Included is the molecular ratio, ice thickness and irradiation dose. Errors in ratios are on the order of ± 0.3.

Experiment	Ice Composition	Ratio	Thickness (nm)
1	CH_4:CO_2:CO:H_2O	1.1:1.2:1:3	1200 ± 80
2	CH_4:CO_2	2.2:1	1200 ± 80
3	CH_4:CO_2	1.7:1	1200 ± 80
4	CH_4:CO_2:CO	1:1.1:2.1	1380 ± 100
5	CH_4:CO_2:CH_3OH	1.4:1.4:1	1070 ± 70
6	CH_4:CO_2:H_2O	1.1:1:1.4	1220 ± 60
7	CH_3CH_2OH:CO_2	1:1.8	1290 ± 70
8	CH_3CH_2OH:CO_2:CH_4	1:2.1:1.7	1290 ± 70
9	CH_3CH_2OH:CO_2:CH_4	1:2.8:1.8	1300 ± 80
10	C_2H_6:CO_2	2:1	1320 ± 80
11	C_2H_6:CO_2:CO	1.2:1.1:1	1600 ± 100
12	CO_2:CH_3CHO	2:1	1550 ± 100

Table S2. Band Strengths used to identify molecular ratio of ice components.

Molecule	Vibrational Mode	Band Position (cm^{-1})	Band Strength (molecule cm^{-2})	Refractive Index (n)	References
H_2O				1.29	(9)
	ν_2	1660	1.2×10^{-17}		(10)
	ν_1/ν_3	3280	2.0×10^{-16}		(10)
$^{13}CO_2$				1.21	(11)
	ν_3	2283	6.8×10^{-17}		(10)
	$2\nu_2 + \nu_3$	3596	1.25×10^{-18}		(12)
^{13}CO				1.28	(13)
	ν_1	2092	1.32×10^{-17}		(10)
$^{13}CH_4$				1.28	(14)
	ν_3	3010	1.40×10^{-17}		(14)
$^{13}CH_3OH^{\dagger}$				1.296	(15)
	ν_8	1026	1.8×10^{-17}		(16)
$^{13}CH_3{}^{13}CH_2OH^{\dagger}$				1.26	(17)
	ν_4	1090	7.35×10^{-18}		(17)
		1050	1.41×10^{-17}		(17)
		886, 879	3.24×10^{-18}		(17)
$^{13}C_2H_6^{\dagger}$				1.27	(18)
	ν_{11}	1462	3.76×10^{-18}		(19)
	ν_{12}	817	1.99×10^{-18}		(19)
$^{13}CH_3{}^{13}CHO^{\dagger}$				1.303	(20)
	ν_{12}	1428	1.09×10^{-17}		(21)
	$2\nu_9$	1721	2.98×10^{-17}		(21)

†Band strengths are of non-isotopically labelled species.

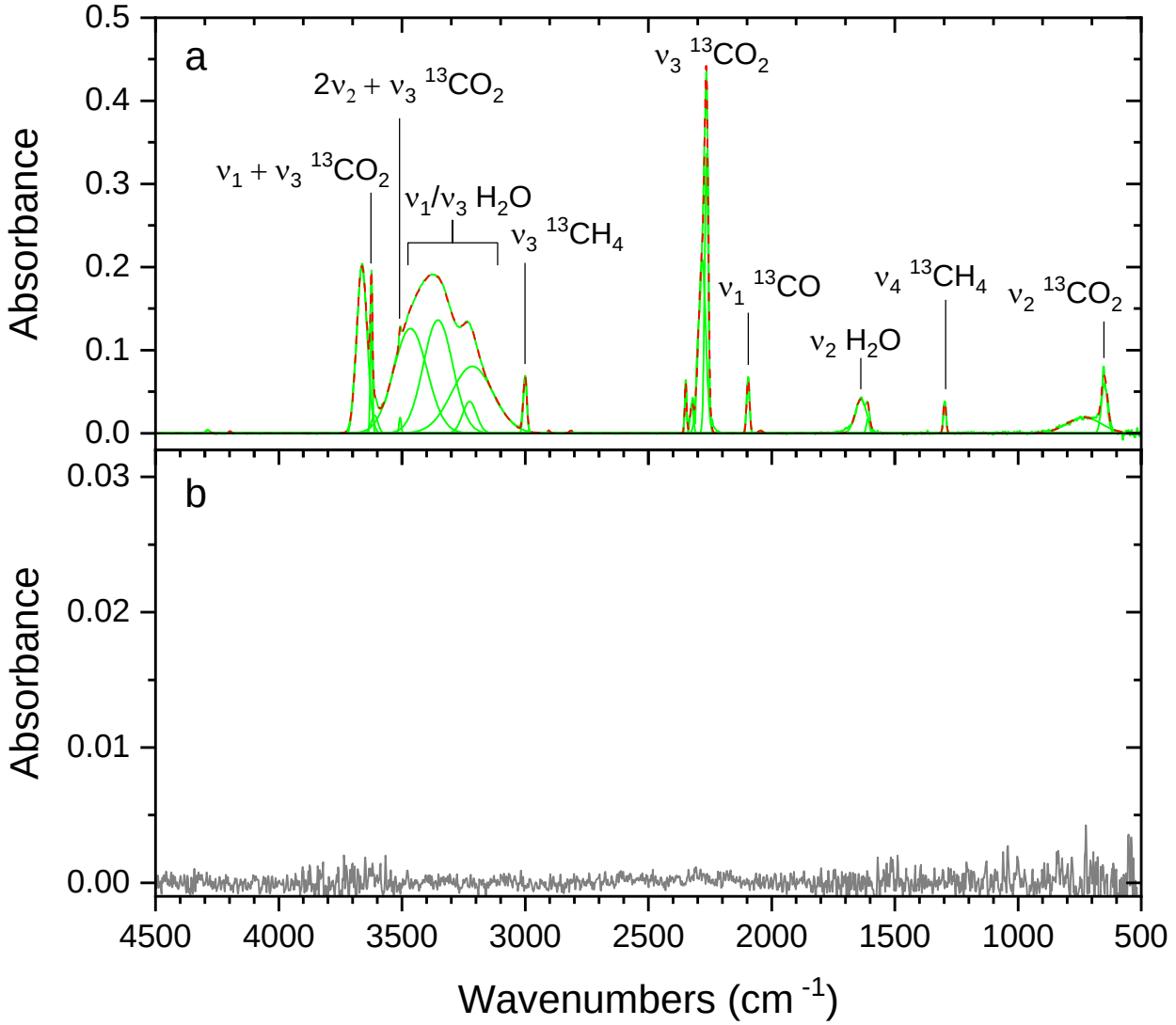

Figure S1. FTIR spectra of methane ($^{13}CH_4$)/carbon dioxide ($^{13}CO_2$)/carbon monoxide (^{13}CO)/water (H_2O) blank experiment after deposition and the resulting residue after warm-up to 320 K. The spectra (a) after deposition and (b) at 320 K are deconvoluted from the original spectra (gray) to reveal functional groups related to the reagents (green).

Table S3. Infrared absorption assignments for $^{13}CH_4/^{13}CO_2/^{13}CO/H_2O$ ice (blank).

Peaks after deposition (10 K)		
Position (cm^{-1})	Identity	References
4288	$\nu_2 + \nu_3$ $^{13}CH_4$	(7)
4198	$\nu_3 + \nu_4$ $^{13}CH_4$	(7)
3662	dangling OH	(22)
3624	$\nu_1 + \nu_3$ $^{13}CO_2$	(23)
3611	$\nu_1 + \nu_3$ $^{13}C^{18}O_2$	(23)
3507	$2\nu_2 + \nu_3$ $^{13}CO_2$	(23)
3466, 3353, 3225, 3214	ν_1/ν_3 H_2O	(23)
3000	ν_3 $^{13}CH_4$	(7)
2904	ν_1 $^{13}CH_4$	(7)
2814	$\nu_2 + \nu_4$ $^{13}CH_4$	(7)
2348	ν_3 $^{12}CO_2$	(23)
2322	ν_3 $^{12}C^{16}O^{18}O$	(23)
2282, 2264	ν_3 $^{13}CO_2$	(23)
2045	ν_1 ^{13}CO	(23)
1638, 1609	ν_2 H_2O	(22)
1297	ν_4 $^{13}CH_4$	(7)
732	ν_L H_2O	(22)
644	ν_2 $^{13}CO_2$	(23)

Note. L indicates the lattice vibrational mode.

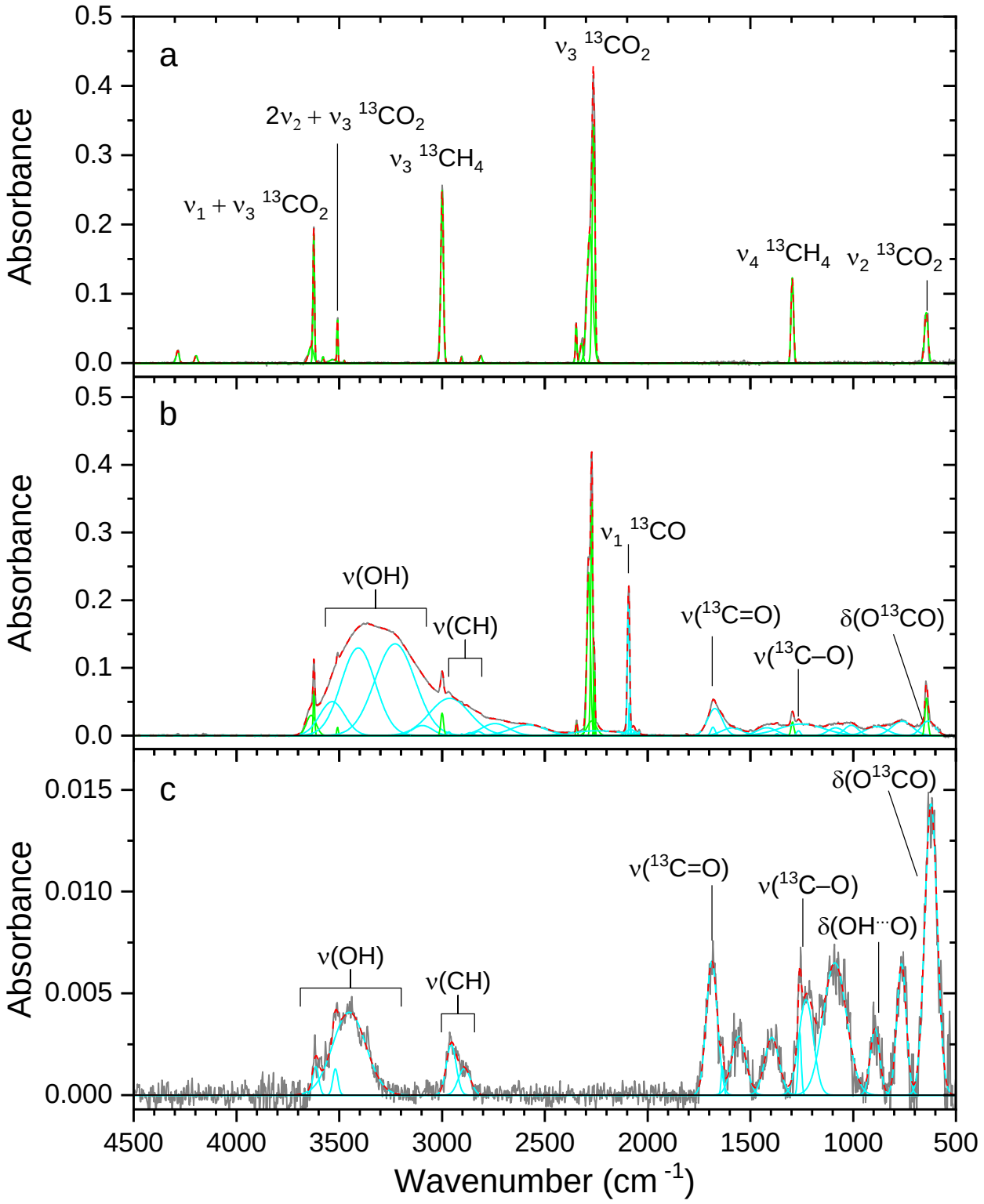

Figure S2. FTIR spectra of methane (CH_4)/carbon dioxide (CO_2) ices before irradiation, after irradiation by energetic electrons at 2000 nA for 1 hrs, and the resulting residue after warm-up to 320 K. The spectra (a) before irradiation, (b) after irradiation, and (c) the residue are deconvoluted from the original spectra (gray) to reveal functional groups related to the reagents (green) and irradiation products (cyan).

Table S4. Infrared absorption assignments for $^{13}CO_2/^{13}CH_4$ ice (2000 nA, 1 hrs).

Peaks before irradiation (10 K)		
Position (cm^{-1})	Identity	References
4285	$\nu_2 + \nu_3$ $^{13}CH_4$	(7)
4195	$\nu_3 + \nu_4$ $^{13}CH_4$	(7)
3639, 3624	$\nu_1 + \nu_3$ $^{13}CO_2$	(23)
3578	$\nu_1 + \nu_3$ $^{13}C^{18}O_2$	(23)
3531, 3509	$2\nu_2 + \nu_3$ $^{13}CO_2$	(23)
3475	$2\nu_2 + \nu_3$ $^{13}C^{18}O_2$	(23)
2999	ν_3 $^{13}CH_4$	(7)
2905	ν_1 $^{13}CH_4$	(7)
2810	$\nu_2 + \nu_4$ $^{13}CH_4$	(7)
2347, 2340	ν_3 $^{12}CO_2$	(23)
2285, 2265	ν_3 $^{13}CO_2$	(23)
1296	ν_4 $^{13}CH_4$	(7)
644	ν_2 $^{13}CO_2$	(23)

Table S5. Infrared absorption assignments for $^{13}CO_2/^{13}CH_4$ ice (2000 nA, 1 hrs)

Peaks after irradiation (10 K)		
Position (cm^{-1})	Identity	References
4284	$\nu_2 + \nu_3$ $^{13}CH_4$	(7)
4194	$\nu_3 + \nu_4$ $^{13}CH_4$	(7)
3643	dangling OH	(24)
3622, 3525	ν(OH)	(24)
3507	$2\nu_2 + \nu_3$ $^{13}CO_2$	(23)
3384, 3209, 3106	ν(OH)	(24)
3000	ν_3 $^{13}CH_4$	(7)
2986	ν(OH)	(24)
2967	ν_{10} C_2H_6	(25)
2953, 2940	$\nu(^{13}CH)$	(24)
2905	ν_1 $^{13}CH_4$	(7)
2879, 2875	$\nu(^{13}CH)$	(24)
2809	$\nu_2 + \nu_4$ $^{13}CH_4$	(7)
2732, 2565, 2434	ν(OH) acid	(24)
2345	ν_3 $^{12}CO_2$	(23)
2334	ν(OH) acid	(24)
2276	ν_3 $^{13}CO_2$	(23)
2225, 2196, 2134	$\nu(^{13}C\equiv{}^{13}C)$	(24)
2092	ν_1 ^{13}CO	(24)
2067	ν_1 $^{12}C^{18}O$	(23)
2041	ν_1 $^{13}C^{18}O$	(23)
2004	$\nu(^{13}C\equiv{}^{13}C)$?	(24)
1810	$\nu(^{13}C{=}O)$ HOCO	(24)
1682	$\nu(^{13}C{=}O)$ acid	(24)
1663	ν_2 H_2O, $\nu(^{13}C{=}O)$	(24, 26)
1498	$\nu(^{13}C{=}{}^{13}C)$	(24)
1462, 1439	$^{13}CH_2/^{13}CH_3$ asym. deformation	(24)
1370, 1366, 1313	$^{13}CH_2/^{13}CH_3$ sym. deformation	(24)
1294	ν_4 $^{13}CH_4$	(7)
1267	$\nu(^{13}C{-}O)$ acid, δ(OH)	(24)
1006	$\nu(^{13}C{-}O)$	(24)
644	ν_2 $^{13}CO_2$	(23)

Note. δ defines a bending mode.

Table S6. Infrared absorption assignments for $^{13}CO_2/^{13}CH_4$ ice (2000 nA, 1 hrs).

Residue (320 K)		
Position (cm^{-1})	Identity	References
3382, 3223	ν(OH)	(24)
2941, 2876	$\nu(^{13}CH)$	(24)
1688	$\nu(^{13}C{=}O)$ acid	(24)
1602	$\nu(^{13}C{=}O)$	(24)
919	$\nu(^{13}C{-}O)$	(24)

Table S7. Infrared absorption assignments for $^{13}CO_2/^{13}CH_4$ ice (5000 nA, 5 hrs).

Peaks before irradiation (10 K)		
Position (cm^{-1})	Identity	References
4286	$\nu_2 + \nu_3$ $^{13}CH_4$	(7)
4196	$\nu_3 + \nu_4$ $^{13}CH_4$	(7)
3637, 3624	$\nu_1 + \nu_3$ $^{13}CO_2$	(23)
3579	$\nu_1 + \nu_3$ $^{13}C^{18}O_2$	(23)
3530, 3509	$2\nu_2 + \nu_3$ $^{13}CO_2$	(23)
3476	$2\nu_2 + \nu_3$ $^{13}C^{18}O_2$	(23)
3000	ν_3 $^{13}CH_4$	(7)
2905	ν_1 $^{13}CH_4$	(7)
2812	$\nu_2 + \nu_4$ $^{13}CH_4$	(7)
2347	ν_3 $^{12}CO_2$	(23)
2322	ν_3 $^{12}C^{16}O^{18}O$	(23)
2281, 2263	ν_3 $^{13}CO_2$	(23)
1296	ν_4 $^{13}CH_4$	(7)
644	ν_2 $^{13}CO_2$	(23)

Table S8. Infrared absorption assignments for $^{13}CO_2/^{13}CH_4$ ice (5000 nA, 5 hrs)

Peaks after irradiation (10 K)		
Position (cm^{-1})	Identity	References
3636, 3623	$\nu_1 + \nu_3$ $^{13}CO_2$	(23)
3534	ν(OH)	(24)
3508	$2\nu_2 + \nu_3$ $^{13}CO_2$	(23)
3408, 3228, 3095	ν(OH)	(24)
3000	ν_3 $^{13}CH_4$	(7)
2967	ν(^{13}CH)	(24)
2962	ν(OH)	(24)
2904	ν_1 $^{13}CH_4$	(7)
2880, 2864, 2824	ν(CH)	(24)
2742	ν(OH)	(24)
2582	ν(OH) acid	(24)
2345	ν_3 $^{12}CO_2$	(23)
2287, 2272, 2271, 2259	ν_3 $^{13}CO_2$	(23)
2242	ν(OH) acid	(24)
2093, 2089, 2083	ν_1 ^{13}CO	(23)
2067	ν_1 $^{12}C^{18}O$	(23)
2041	ν_1 $^{13}C^{18}O$	(23)
1809	ν(^{13}C=O) HOCO	(24)
1682	ν(^{13}C=O) acid	(24)
1673	ν_2 H_2O, ν(^{13}C=O)	(24, 26)
1589	ν(^{13}C=O)	(24)
1500	ν(^{13}C=^{13}C)	(24)
1420, 1370	$^{13}CH_2/^{13}CH_3$ deformation	(24)
1295	ν_4 $^{13}CH_4$	(7)
1266, 1252	ν(^{13}C–O) acid, δ(OH)	(24)
1085, 1009	ν(^{13}C–O)	(24)
887, 762	δ(OH···O)	(24)
643	ν_2 $^{13}CO_2$	(23)
635	δ(OCO) acid	(24)

Note. δ defines a bending mode.

Table S9. Infrared absorption assignments for $^{13}CO_2/^{13}CH_4$ ice (5000 nA, 5 hrs).

Residue (320 K)		
Position (cm^{-1})	Identity	References
3614, 3519, 3451	ν(OH)	(24)
2955, 2891	$\nu(^{13}CH)$	(24)
1688	$\nu(^{13}C{=}O)$ acid	(24)
1636	$\nu(^{13}C{=}O)$	(24)
1557	$\nu(^{13}C{=}^{13}C)$	(24)
1396	$^{13}CH_2/^{13}CH_3$ deformation	(24)
1260, 1229	$\nu(^{13}C{-}O)$ acid, δ(OH)	(24)
1089	$\nu(^{13}C{-}O)$	(24)
894, 765	δ(OH···O)	(24)
621	δ(OCO) acid	(24)

Note. δ defines a bending mode.

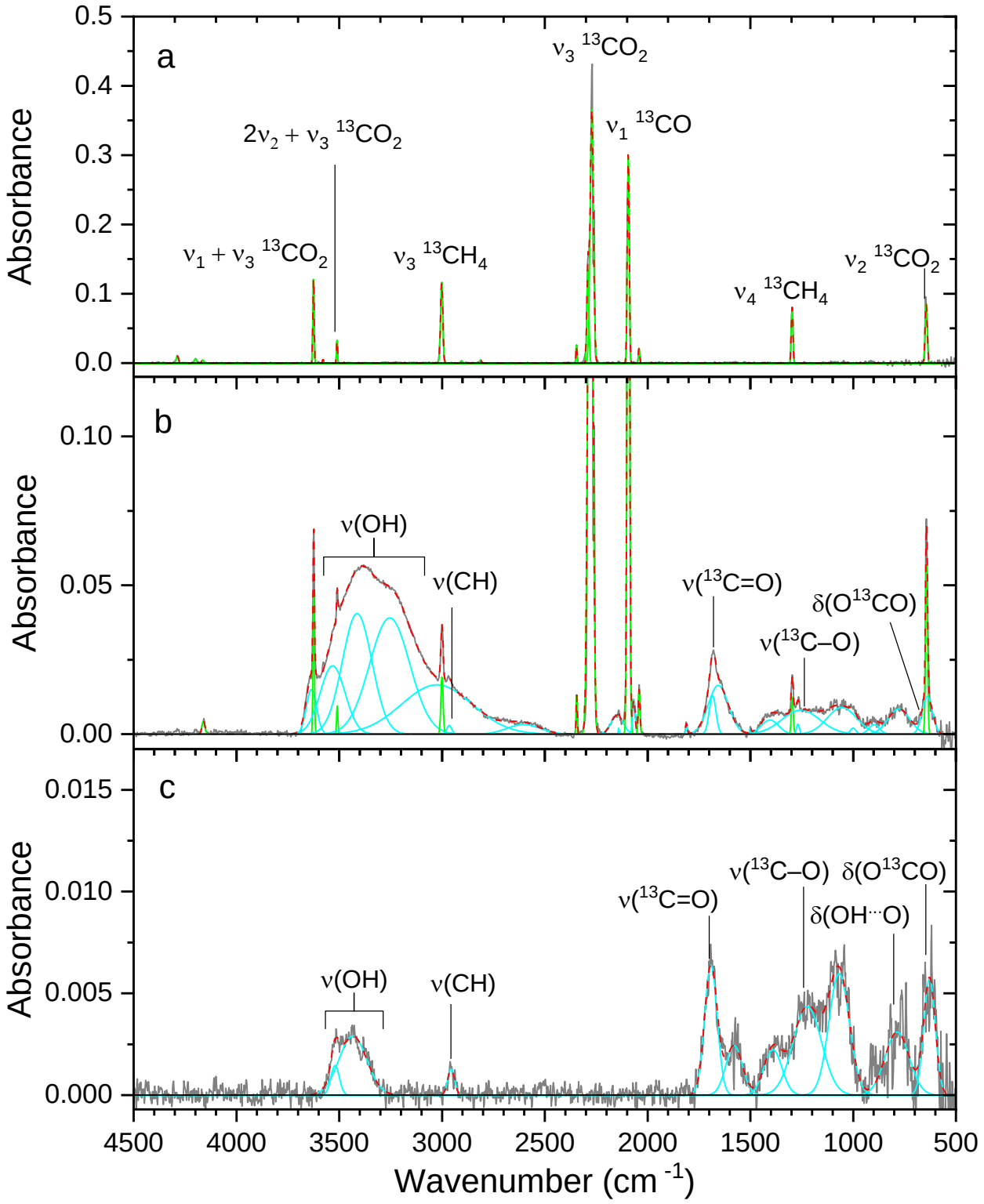

Figure S3. FTIR spectra of methane (CH_4)/carbon dioxide (CO_2)/carbon monoxide (CO) ices before irradiation, after irradiation by energetic electrons at 5000 nA for 5 hrs, and the resulting residue after warm-up to 320 K. The spectra (a) before irradiation, (b) after irradiation, and (c) the residue are deconvoluted from the original spectra (gray) to reveal functional groups related to the reagents (green) and irradiation products (cyan).

Table S10. Infrared absorption assignments for $^{13}CH_4/^{13}CO_2/^{13}CO$ ice (5000 nA, 5 hrs).

Peaks before irradiation (10 K)		
Position (cm^{-1})	Identity	References
4288	$\nu_2 + \nu_3$ $^{13}CH_4$	(7)
4199	$\nu_3 + \nu_4$ $^{13}CH_4$	(7)
4164	$\nu_1 + \nu_4$ $^{13}CH_4$	(7)
3625	$\nu_1 + \nu_3$ $^{13}CO_2$	(23)
3578	$\nu_1 + \nu_3$ $^{13}C^{18}O_2$	(23)
3511	$2\nu_2 + \nu_3$ $^{13}CO_2$	(23)
3001	ν_3 $^{13}CH_4$	(7)
2905	ν_1 $^{13}CH_4$	(7)
2812	$\nu_2 + \nu_4$ $^{13}CH_4$	(7)
2346	ν_3 $^{12}CO_2$	(23)
2290, 2271	ν_3 $^{13}CO_2$	(23)
2094	ν_1 ^{13}CO	(23)
2041	ν_1 $^{13}C^{18}O$	(23)
1297	ν_4 $^{13}CH_4$	(7)
645	ν_2 $^{13}CO_2$	(23)

Table S11. Infrared absorption assignments for $^{13}CH_4/^{13}CO_2/^{13}CO$ ice (5000 nA, 5 hrs).

Peaks after irradiation (10 K)		
Position (cm^{-1})	Identity	References
4160	$\nu_1 + \nu_4$ $^{13}CH_4$	(7)
3635	dangling ν(OH)	(24)
3624	$\nu_1 + \nu_3$ $^{13}CO_2$	(23)
3532	ν(OH)	(24)
3510	$2\nu_2 + \nu_3$ $^{13}CO_2$	(23)
3413, 3254, 3025	ν(OH)	(24)
3000	ν_3 $^{13}CH_4$	(7)
2965	$\nu(^{13}CH)$	(24)
2604	ν(OH) acid	(24)
2345	ν_3 $^{12}CO_2$	(23)
2279	ν_3 $^{13}CO_2$	(23)
2148	$\nu(^{13}C\equiv{}^{13}C)$	(24)
2140	$\nu(^{13}C\equiv{}^{13}C)$	(24)
2097	ν_1 ^{13}CO	(23)
2067	$\nu(^{13}C\equiv{}^{13}C)$	(24)
2041	ν_1 $^{13}C^{18}O$	(23)
1811	$\nu(^{13}C{=}O)$ HOCO	(24)
1684	$\nu(^{13}C{=}O)$ acid	(24)
1656	ν_2 H_2O, $\nu(^{13}C{=}O)$	(24, 26)
1499	$\nu(^{13}C{=}{}^{13}C)$	(24)
1405	$^{13}CH_2/^{13}CH_3$ deformation	(24)
1296	ν_4 $^{13}CH_4$	(7)
1268, 1255	$\nu(^{13}C{-}O)$ acid, δ(OH)	(24)
1054, 1001	$\nu(^{13}C{-}O)$	(24)
898, 777	$\delta(OH\cdots O)$	(24)
643	ν_2 $^{13}CO_2$	(23)
639	δ(OCO) acid	(24)

Note. δ defines a bending mode.

Table S12. Infrared absorption assignments for $^{13}CO_2/^{13}CH_4$ ice (5000 nA, 5 hrs).

Residue (320 K)		
Position (cm^{-1})	Identity	References
3520, 3434	ν(OH)	(24)
2955	$\nu(^{13}CH)$	(24)
1692	$\nu(^{13}C{=}O)$ acid	(24)
1579	$\nu(^{13}C{=}^{13}C)$	(24)
1390	$^{13}CH_2/^{13}CH_3$ deformation	(24)
1223	$\nu(^{13}C{-}O)$ acid, δ(OH)	(24)
1068	$\nu(^{13}C{-}O)$	(24)
786	δ(OH···O)	(24)
628	δ(OCO) acid	(24)

Note. δ defines a bending mode.

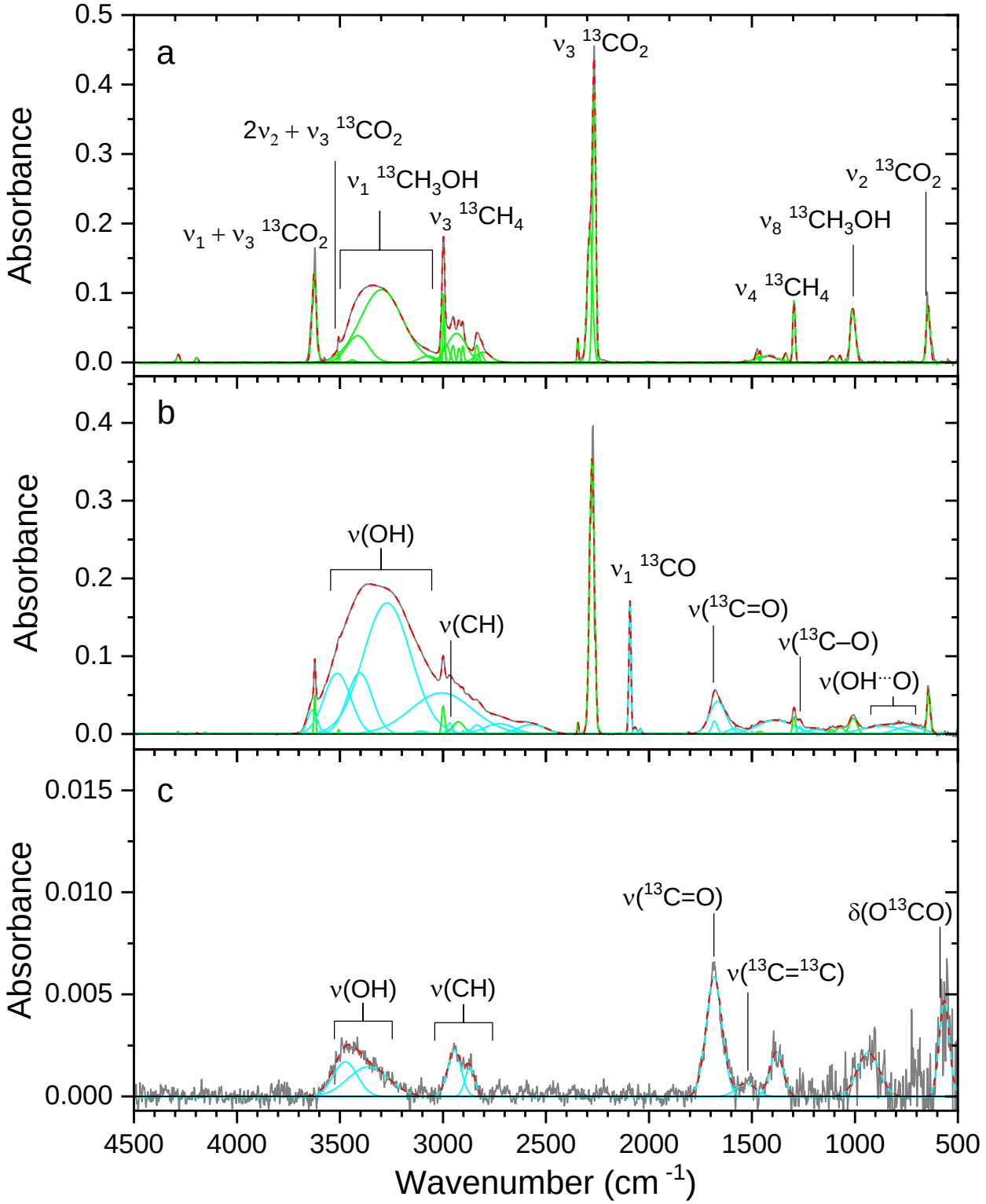

Figure S4. **FTIR spectra of methane (CH_4)/carbon dioxide (CO_2)/methanol (CH_3OH) ices before irradiation, after irradiation by energetic electrons at 5000 nA for 5 hrs, and the resulting residue after warm-up to 320 K.** The spectra (a) before irradiation, (b) after irradiation, and (c) the residue are deconvoluted from the original spectra (gray) to reveal functional groups related to the reagents (green) and irradiation products (cyan).

Table S13. Infrared absorption assignments for $^{13}CH_4/^{13}CO_2/^{13}CH_3OH$ ice (5000 nA, 5 hrs).

Peaks before irradiation (10 K)		
Position (cm^{-1})	Identity	References
4284	$\nu_2 + \nu_3$ $^{13}CH_4$	(7)
4195	$\nu_3 + \nu_4$ $^{13}CH_4$	(7)
3625	$\nu_1 + \nu_3$ $^{13}CO_2$	(23)
3507	$2\nu_2 + \nu_3$ $^{13}CO_2$	(23)
3440, 3414, 3299, 3073	ν_1 $^{13}CH_3OH$	(27, 28)
3001, 2995	ν_3 $^{13}CH_4$	(7)
2986	Combination $^{13}CH_3OH$	(27, 28)
2951	ν_2 $^{13}CH_3OH$	(27, 28)
2934	Combination $^{13}CH_3OH$	(27, 28)
2922	ν_9 $^{13}CH_3OH$	(27, 28)
2903	ν_1 $^{13}CH_4$	(7)
2836	ν_3 $^{13}CH_3OH$	(27, 28)
2816	$\nu_2 + \nu_4$ $^{13}CH_4$	(7)
2805	$2\nu_2$ $^{13}CH_3OH$	(27, 28)
2345	ν_3 $^{12}CO_2$	(23)
2287, 2266	ν_3 $^{13}CO_2$	(23)
1475	ν_4 $^{13}CH_3OH$	(27, 28)
1460	ν_{10} $^{13}CH_3OH$	(27, 28)
1425	ν_6 $^{13}CH_3OH$	(27, 28)
1336	?	(27, 28)
1297	ν_4 $^{13}CH_4$	(7)
1111	ν_{11} $^{13}CH_3OH$	(27, 28)
1073	ν_7 $^{13}CH_3OH$	(27, 28)
1010	ν_8 $^{13}CH_3OH$	(27, 28)
645	ν_2 $^{13}CO_2$	(23)

Table S14. Infrared absorption assignments for $^{13}CH_4/^{13}CO_2/^{13}CH_3OH$ ice (5000 nA, 5 hrs).

Peaks after irradiation (10 K)		
Position (cm^{-1})	Identity	References
4286	$\nu_2 + \nu_3$ $^{13}CH_4$	(7)
4195	$\nu_1 + \nu_4$ $^{13}CH_4$	(7)
3634	dangling ν(OH)	(24)
3622	$\nu_1 + \nu_3$ $^{13}CO_2$	(23)
3580, 3513	ν(OH)	(24)
3506	$2\nu_2 + \nu_3$ $^{13}CO_2$	(23)
3404, 3271, 3104, 3006	ν(OH)	(24)
2999	ν_3 $^{13}CH_4$	(7)
2967	$\nu(^{13}CH)$	(24)
2925	ν_9 $^{13}CH_3OH$	(27, 28)
2903, 2876	$\nu(^{13}CH)$	(24)
2834, 2570, 2344	ν(OH) acid	(24)
2344	ν_3 $^{12}CO_2$	(23)
2276	ν_3 $^{13}CO_2$	(23)
2092	ν_1 ^{13}CO	(23)
2067	$\nu(^{13}C\equiv{}^{13}C)$	(24)
2042	ν_1 $^{13}C^{18}O$	(23)
1808	$\nu(^{13}C{=}O)$ HOCO	(24)
1682	$\nu(^{13}C{=}O)$ acid	(24)
1667	ν_2 H_2O, $\nu(^{13}C{=}O)$	(24, 26)
1582, 1500	$\nu(^{13}C{=}{}^{13}C)$	(24)
1462	ν_{10} $^{13}CH_3OH$	(23)
1462, 1384	$^{13}CH_2/^{13}CH_3$ deformation	(24)
1295	ν_4 $^{13}CH_4$	(7)
1269, 1186	$\nu(^{13}C{-}O)$ acid, δ(OH)	(24)
1113	ν_{11} $^{13}CH_3OH$	(27, 28)
1073	ν_7 $^{13}CH_3OH$	(27, 28)
1008	ν_8 $^{13}CH_3OH$	(27, 28)
871, 733	δ(OH···O)	(24)
643	ν_2 $^{13}CO_2$	(23)

Note. δ defines a bending mode.

Table S15. Infrared absorption assignments for $^{13}CH_4/^{13}CO_2/^{13}CH_3OH$ ice (5000 nA, 5 hrs).

Residue (320 K)		
Position (cm^{-1})	Identity	References
3474, 3362	ν(OH)	(24)
2945, 2869	$\nu(^{13}CH)$	(24)
1683	$\nu(^{13}C{=}O)$ acid	(24)
1530	$\nu(^{13}C{=}^{13}C)$	(24)
1381	$^{13}CH_2/^{13}CH_3$ deformation	(24)
935	$\nu(^{13}C{-}O)$	(24)
566	δ(OCO) acid	(24)

Note. δ defines a bending mode.

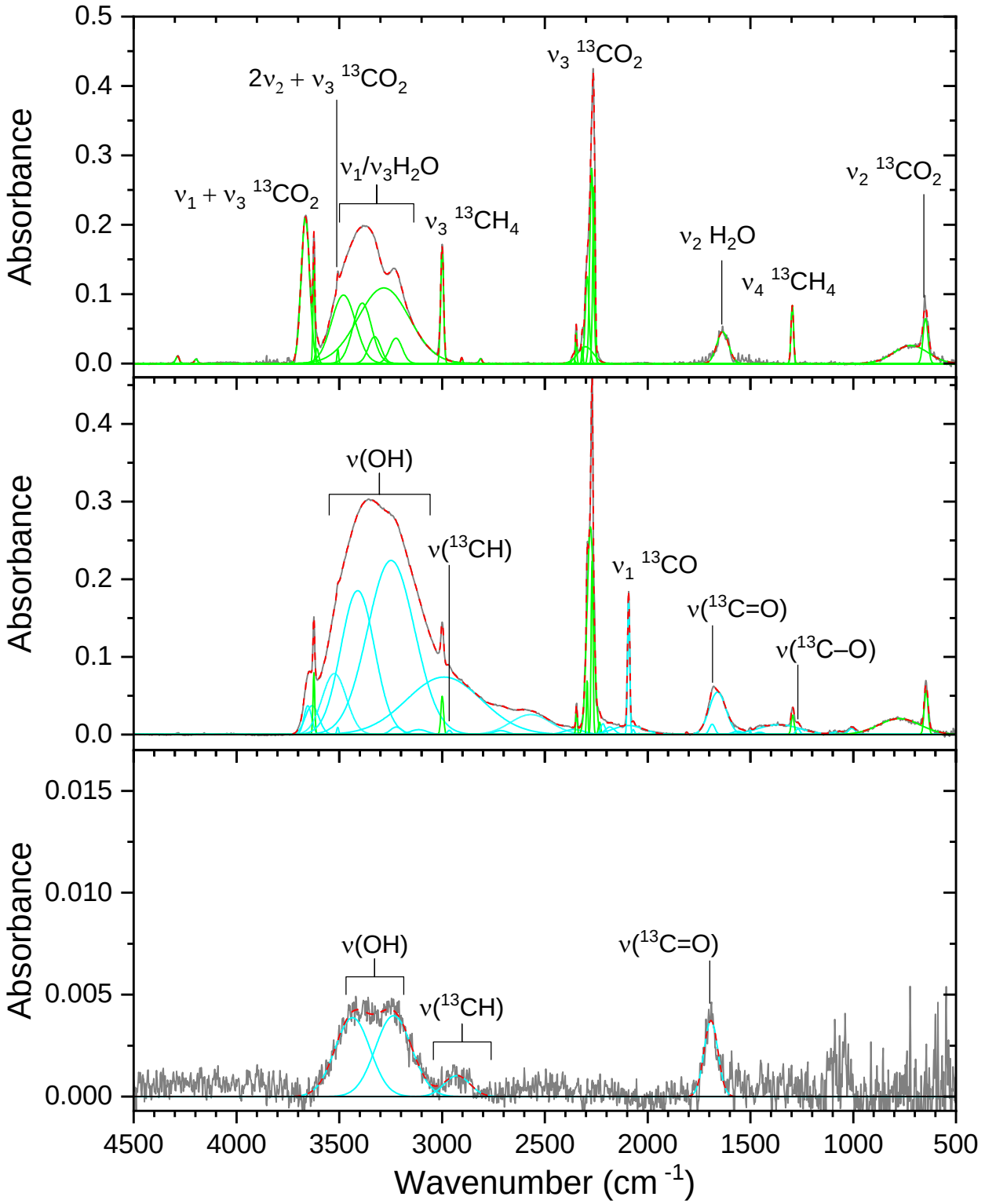

Figure S5. FTIR spectra of methane (CH_4)/carbon dioxide (CO_2)/water (H_2O) ices before irradiation, after irradiation by energetic electrons at 5000 nA for 5 hrs, and the resulting residue after warm-up to 320 K. The spectra (a) before irradiation, (b) after irradiation, and (c) the residue are deconvoluted from the original spectra (gray) to reveal functional groups related to the reagents (green) and irradiation products (cyan).

Table S16. Infrared absorption assignments for $^{13}CH_4/^{13}CO_2/H_2O$ ice (5000 nA, 5 hrs).

Peaks after deposition (10 K)		
Position (cm^{-1})	Identity	References
4287	$\nu_2 + \nu_3$ $^{13}CH_4$	(7)
4197	$\nu_3 + \nu_4$ $^{13}CH_4$	(7)
3665	dangling OH	(26)
3623	$\nu_1 + \nu_3$ $^{13}CO_2$	(23)
3609	$\nu_1 + \nu_3$ $^{13}C^{18}O_2$	(23)
3507	$2\nu_2 + \nu_3$ $^{13}CO_2$	(23)
3479, 3388, 3328, 3284, 3224	ν_1/ν_3 H_2O	(26)
2999	ν_3 $^{13}CH_4$	(7)
2904	ν_1 $^{13}CH_4$	(7)
2812	$\nu_2 + \nu_4$ $^{13}CH_4$	(7)
2348	ν_3 $^{12}CO_2$	(23)
2318	ν_3 $^{12}C^{16}O^{18}O$	(23)
2294, 2273, 2261	ν_3 $^{13}CO_2$	(23)
1635	ν_2 H_2O	(26)
1296	ν_4 $^{13}CH_4$	(7)
719	ν_L H_2O	(26)
648	ν_2 $^{13}CO_2$	(23)

Note. L indicates the lattice vibrational mode.

Table S17. Infrared absorption assignments for $^{13}CH_4/^{13}CO_2/H_2O$ ice (5000 nA, 5 hrs).

Peaks after irradiation (10 K)		
Position (cm^{-1})	Identity	References
3653, 3632	dangling ν(OH)	(24)
3623	$\nu_1 + \nu_3$ $^{13}CO_2$	(23)
3524	ν(OH)	(24)
3507	$2\nu_2 + \nu_3$ $^{13}CO_2$	(23)
3410, 3248, 3222, 3114	ν(OH), ν_1/ν_3 H_2O	(24, 26)
2999	ν_3 $^{13}CH_4$	(7)
2990	ν(OH)	(24)
2965	$\nu(^{13}CH)$	(24)
2904	$\nu(^{13}CH)$	(24)
2714, 2569, 2358	ν(OH) acid	(24)
2346	ν_3 $^{12}CO_2$	(23)
2294, 2278, 2270	ν_3 $^{13}CO_2$	(23)
2234	ν_3 $^{13}C^{16}O^{18}O$	(23)
2217, 2184	$\nu(^{13}C\equiv{}^{13}C)$	(24)
2093	ν(OH) acid	(24)
2092	ν_1 ^{13}CO	(23)
2070	$\nu(^{13}C\equiv{}^{13}C)$	(24)
2042	ν_1 $^{13}C^{18}O$	(23)
1810	$\nu(^{13}C{=}O)$ HOCO	(24)
1686	$\nu(^{13}C{=}O)$ acid	(24)
1660	ν_2 H_2O, $\nu(^{13}C{=}O)$	(24, 26)
1562, 1501	$\nu(^{13}C{=}{}^{13}C)$	(24)
1454, 1361	$^{13}CH_2/^{13}CH_3$ deformation	(24)
1294	ν_4 $^{13}CH_4$	(7)
1269	$\nu(^{13}C{-}O)$ acid, δ(OH)	(24)
1075	ν_7 $^{13}CH_3OH$	(27, 28)
1012	ν_8 $^{13}CH_3OH$	(27, 28)
775	ν_L H_2O	(26)
645	ν_2 $^{13}CO_2$	(23)

Note. δ defines a bending mode.

Table S18. Infrared absorption assignments for $^{13}CH_4/^{13}CO_2/H_2O$ ice (5000 nA, 5 hrs).

Residue (320 K)		
Position (cm^{-1})	Identity	References
3465, 3236	*v*(OH)	(24)
2927	*v*(^{13}CH)	(24)
1692	*v*(^{13}C=O) acid	(24)

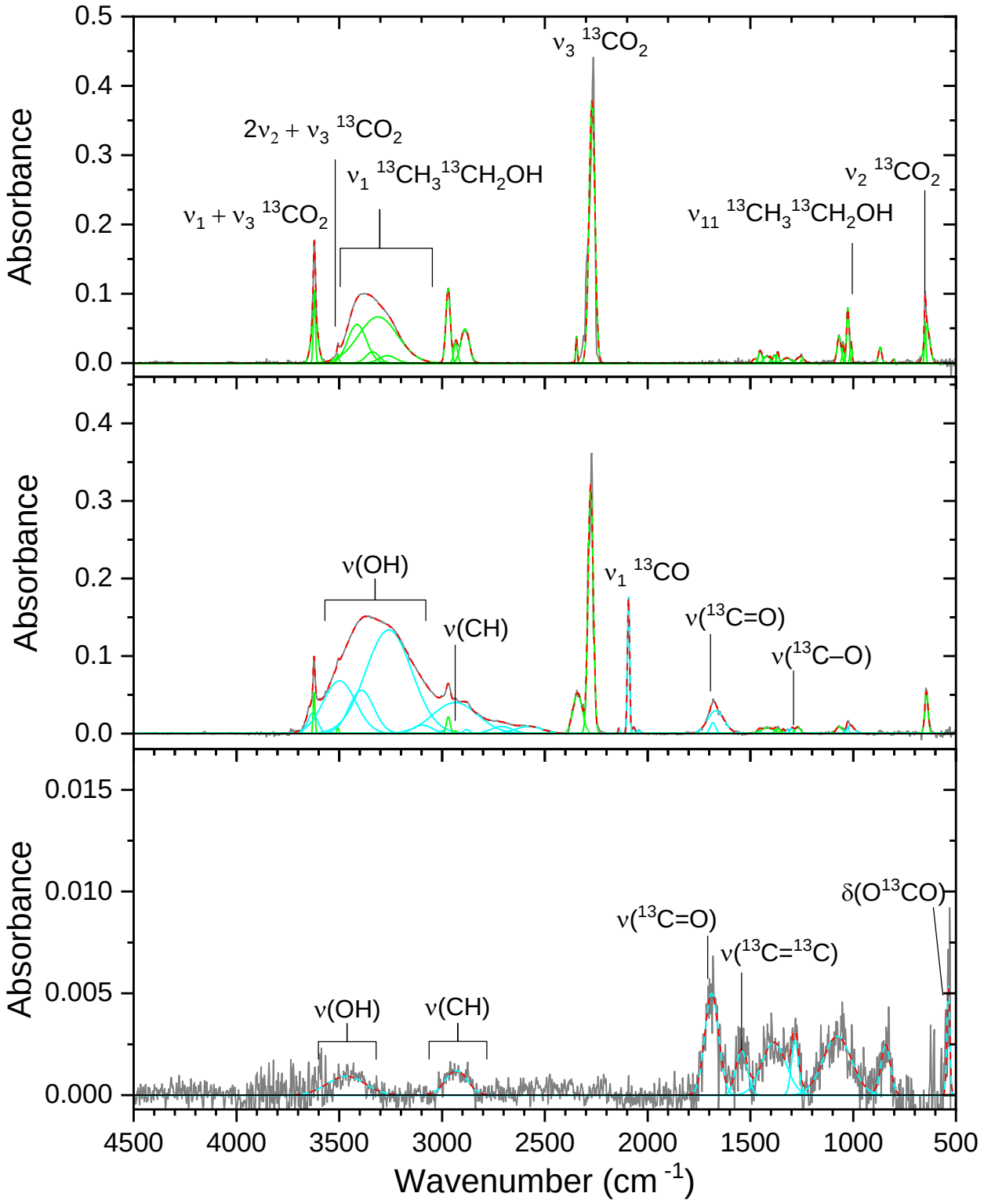

Figure S6. FTIR spectra of ethanol (CH_3CH_2OH)/carbon dioxide (CO_2) ices before irradiation, after irradiation by energetic electrons at 5000 nA for 5 hrs, and the resulting residue after warm-up to 320 K. The spectra (a) before irradiation, (b) after irradiation, and (c) the residue are deconvoluted from the original spectra (gray) to reveal functional groups related to the reagents (green) and irradiation products (cyan).

Table S19. Infrared absorption assignments for $^{13}CH_3{}^{13}CH_2OH/^{13}CO_2$ ice (5000 nA, 5 hrs).

Peaks after deposition (10 K)		
Position (cm^{-1})	Identity	References
3623	$\nu_1 + \nu_3$ $^{13}CO_2$	(23)
3620	ν_1 $^{13}CH_3{}^{13}CH_2OH$	(17, 29)
3506	$2\nu_2 + \nu_3$ $^{13}CO_2$	(23)
3413, 3338, 3311, 3265	ν_1 $^{13}CH_3{}^{13}CH_2OH$	(17, 29)
2970	ν_2 $^{13}CH_3{}^{13}CH_2OH$	(17, 29)
2934	ν_3/ν_{15} $^{13}CH_3{}^{13}CH_2OH$	(17, 29)
2888	ν_4 $^{13}CH_3{}^{13}CH_2OH$	(17, 29)
2346	ν_3 $^{12}CO_2$	(23)
2271	ν_3 $^{13}CO_2$	(23)
1479	ν_5 $^{13}CH_3{}^{13}CH_2OH$	(17, 29)
1452	ν_6 $^{13}CH_3{}^{13}CH_2OH$	(17, 29)
1419	ν_{16} $^{13}CH_3{}^{13}CH_2OH$	(17, 29)
1402	ν_7 $^{13}CH_3{}^{13}CH_2OH$	(17, 29)
1383	Combination?	(17, 29)
1367	ν_8 $^{13}CH_3{}^{13}CH_2OH$	(17, 29)
1323	Combination?	(17, 29)
1257	ν_{17} $^{13}CH_3{}^{13}CH_2OH$	(17, 29)
1251	ν_9 $^{13}CH_3{}^{13}CH_2OH$	(17, 29)
1069	ν_{10} $^{13}CH_3{}^{13}CH_2OH$	(17, 29)
1049	ν_{18} $^{13}CH_3{}^{13}CH_2OH$	(17, 29)
1026, 1010	ν_{11} $^{13}CH_3{}^{13}CH_2OH$	(17, 29)
869	ν_{12} $^{13}CH_3{}^{13}CH_2OH$	(17, 29)
803	ν_{19} $^{13}CH_3{}^{13}CH_2OH$	(17, 29)
650, 641	ν_2 $^{13}CO_2$	(23)

Table S20. Infrared absorption assignments for $^{13}CH_3{}^{13}CH_2OH/^{13}CO_2$ ice (5000 nA, 5 hrs).

Peaks after deposition (10 K)		
Position (cm^{-1})	Identity	References
3629	ν(OH)	(24)
3620	$\nu_1 + \nu_3$ $^{13}CO_2$	(23)
3506	$2\nu_2 + \nu_3$ $^{13}CO_2$	(23)
3499, 3392, 3259, 3095	ν_1 $^{13}CH_3{}^{13}CH_2OH$, ν(OH)	(17, 29)
2996	$\nu(^{13}CH)$	(24)
2970	ν_2 $^{13}CH_3{}^{13}CH_2OH$	(17, 29)
2935	ν(OH)	(24)
2934	ν_3/ν_{15} $^{13}CH_3{}^{13}CH_2OH$	(17, 29)
2880	$\nu(^{13}CH)$	(17, 29)
2710, 2578	ν(OH) acid	(24)
2340	ν_3 $^{12}CO_2$	(23)
2277	ν_3 $^{13}CO_2$	(23)
2140	ν_1 ^{12}CO	(23)
2093	ν_1 ^{13}CO	(23)
2068, 2043	$\nu(^{13}C\equiv{}^{13}C)$	(24)
1682	$\nu(^{13}C{=}O)$	(24)
1668	$\nu(^{13}C{=}O)$, $\nu(H_2O)$	(24, 26)
1456	$^{13}CH_2/^{13}CH_3$ deformation	(24)
1417	ν_{16} $^{13}CH_3{}^{13}CH_2OH$	(17, 29)
1402	ν_7 $^{13}CH_3{}^{13}CH_2OH$	(17, 29)
1367	ν_8 $^{13}CH_3{}^{13}CH_2OH$	(17, 29)
1340, 1321	$^{13}CH_2/^{13}CH_3$ deformation	(24)
1297, 1269	ν_{17} $^{13}CH_3{}^{13}CH_2OH$	(17, 29)
1067	ν_{10} $^{13}CH_3{}^{13}CH_2OH$	(17, 29)
1026, 1012	ν_{11} $^{13}CH_3{}^{13}CH_2OH$, $\nu(^{13}C–O)$	(17, 24,
643	ν_2 $^{13}CO_2$	(23)

Table S21. Infrared absorption assignments for $^{13}CH_3{}^{13}CH_2OH/^{13}CO_2$ ice (5000 nA, 5 hrs).

Residue (320 K)		
Position (cm^{-1})	Identity	References
3465	ν(OH)	(24)
2930	$\nu(^{13}CH)$	(24)
1688	$\nu(^{13}C{=}O)$ acid	(24)
1543	$\nu(^{13}C{=}{}^{13}C)$	(24)
1386	$^{13}CH_2/^{13}CH_3$ deformation	(24)
1283	$\nu(^{13}C{-}O)$ acid, δ(OH)	(24)
1077	$\nu(^{13}C{-}O)$	(24)
842	δ(OH···O)	(24)
537	δ(OCO) acid	(24)

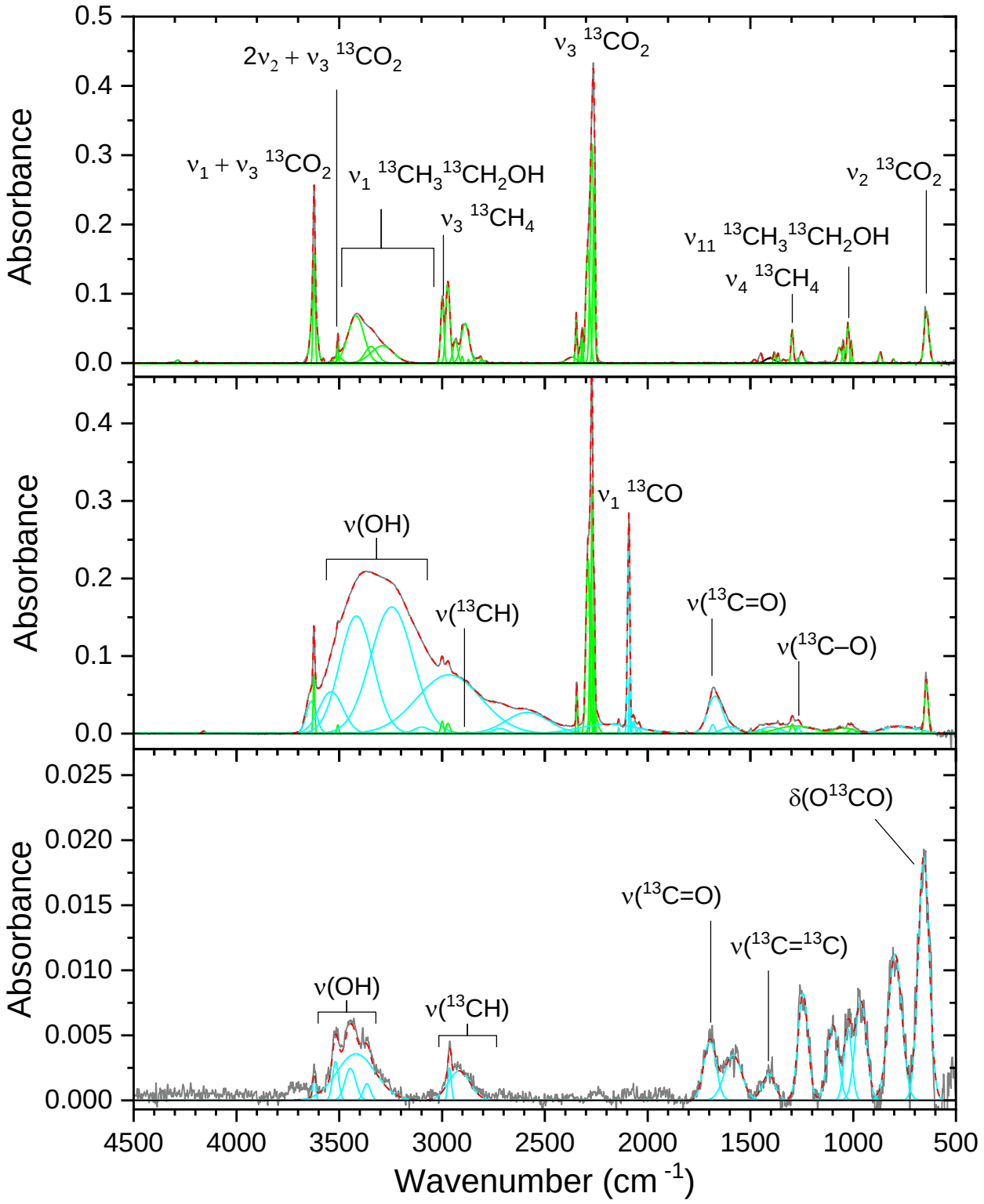

Figure S7. FTIR spectra of ethanol (CH_3CH_2OH)/carbon dioxide (CO_2)/methane (CH_4) ices before irradiation, after irradiation by energetic electrons at 5000 nA for 5 hrs, and the resulting residue after warm-up to 320 K. The spectra (a) before irradiation, (b) after irradiation, and (c) the residue are deconvoluted from the original spectra (gray) to reveal functional groups related to the reagents (green) and irradiation products (cyan).

Table S22. Infrared absorption assignments for $^{13}CH_3{}^{13}CH_2OH/^{13}CO_2/^{13}CH_4$ ice (5000 nA, 5 hrs).

Peaks after deposition (10 K)		
Position (cm^{-1})	Identity	References
4288	$\nu_2 + \nu_3$ $^{13}CH_4$	(7)
4195	$\nu_3 + \nu_4$ $^{13}CH_4$	(7)
3624	$\nu_1 + \nu_3$ $^{13}CO_2$	(23)
3622, 3577, 3533	ν_1 $^{13}CH_3{}^{13}CH_2OH$	(17, 29)
3507	$2\nu_2 + \nu_3$ $^{13}CO_2$	(23)
3506, 3419, 3345, 3291	ν_1 $^{13}CH_3{}^{13}CH_2OH$	(17, 29)
2999	ν_3 $^{13}CH_4$	(7)
2971	ν_2 $^{13}CH_3{}^{13}CH_2OH$	(17, 29)
2935	ν_3/ν_{15} $^{13}CH_3{}^{13}CH_2OH$	(17, 29)
2902	ν_1 $^{13}CH_4$	(7)
2888	ν_4 $^{13}CH_3{}^{13}CH_2OH$	(17, 29)
2871	Combination	(17, 29)
2823	Combination	(17, 29)
2812	$\nu_2 + \nu_4$ $^{13}CH_4$	(7)
2785	?	
2369	$\nu_3 + \nu_L$ $^{13}CO_2$	(23)
2347	ν_3 $^{12}CO_2$	(23)
2327, 2317	ν_3 $^{13}C^{18}O^{16}O$	(23)
2291, 2271, 2260	ν_3 $^{13}CO_2$	(23)
1480	ν_5 $^{13}CH_3{}^{13}CH_2OH$	(17, 29)
1450	ν_6 $^{13}CH_3{}^{13}CH_2OH$	(17, 29)
1406	ν_7 $^{13}CH_3{}^{13}CH_2OH$	(17, 29)
1383	Combination?	(17, 29)
1365	ν_8 $^{13}CH_3{}^{13}CH_2OH$	(17, 29)
1339	Combination?	(17, 29)
1296	ν_4 $^{13}CH_4$	(7)
1272	ν_{17} $^{13}CH_3{}^{13}CH_2OH$	(17, 29)
1251	ν_9 $^{13}CH_3{}^{13}CH_2OH$	(17, 29)
1067	ν_{10} $^{13}CH_3{}^{13}CH_2OH$	(17, 29)
1048	ν_{18} $^{13}CH_3{}^{13}CH_2OH$	(17, 29)
1025, 1009	ν_{11} $^{13}CH_3{}^{13}CH_2OH$	(17, 29)
868	ν_{12} $^{13}CH_3{}^{13}CH_2OH$	(17, 29)
804	ν_{19} $^{13}CH_3{}^{13}CH_2OH$	(17, 29)
643	ν_2 $^{13}CO_2$	(23)

Note. L indicates a lattice mode.

Table S23. Infrared absorption assignments for $^{13}CH_3{}^{13}CH_2OH/{}^{13}CO_2/{}^{13}CH_4$ ice (5000 nA, 5 hrs).

Peaks after irradiation (10 K)		
Position (cm^{-1})	Identity	References
4159	$\nu_3 + \nu_4$ $^{13}CH_4$	(7)
3635	ν(OH)	(24)
3623	$\nu_1 + \nu_3$ $^{13}CO_2$	(23)
3540	ν_1 $^{13}CH_3{}^{13}CH_2OH$, ν(OH)	(17, 29)
3507	$2\nu_2 + \nu_3$ $^{13}CO_2$	(23)
3416, 3245, 3098	ν_1 $^{13}CH_3{}^{13}CH_2OH$, ν(OH)	(17, 24, 29)
2999	ν_3 $^{13}CH_4$	(7)
2971	ν_2 $^{13}CH_3{}^{13}CH_2OH$	(17, 29)
2966	ν(OH)	(24)
2933	ν_3/ν_{15} $^{13}CH_3{}^{13}CH_2OH$	(17, 29)
2903	ν_1 $^{13}CH_4$	(7)
2888	ν_4 $^{13}CH_3{}^{13}CH_2OH$	(17, 29)
2877	$\nu(^{13}CH)$	(24)
2718, 2585	ν(OH) acid	(24)
2345	ν_3 $^{12}CO_2$	(23)
2291, 2276, 2270, 2262, 2259	ν_3 $^{13}CO_2$	(23)
2188	ν(OH) acid	(24)
2140	ν_1 ^{12}CO	(23)
2093, 2089	ν_1 ^{13}CO	(23)
2069, 2043	$\nu(^{13}C\equiv{}^{13}C)$	(24)
1810	$\nu(^{13}C{=}O)$ HOCO	(24)
1683	$\nu(^{13}C{=}O)$	(24)
1672	ν_2 H_2O, $\nu(^{13}C{=}O)$	(24, 26)
1599	$\nu(^{13}C{=}O)$	(24)
1498	$\nu(^{13}C{=}{}^{13}C)$	(24)
1453	ν_6 $^{13}CH_3{}^{13}CH_2OH$	(17, 29)
1400, 1366, 1341	$^{13}CH_2/{}^{13}CH_3$ deformation	(17, 29)
1296, 1279	ν_{17} $^{13}CH_3{}^{13}CH_2OH$	(17, 29)
1268	$\nu(^{13}C{-}O)$	(24)
1048	ν_{18} $^{13}CH_3{}^{13}CH_2OH$	(17, 29)
1025, 1006	ν_{11} $^{13}CH_3{}^{13}CH_2OH$	(17, 29)
769	$\delta(OH\cdots O)$	(24)
643	ν_2 $^{13}CO_2$	(23)

Note. L indicates a lattice mode.

Table S24. Infrared absorption assignments for $^{13}CH_3{}^{13}CH_2OH/^{13}CO_2/^{13}CH_4$ ice (5000 nA, 5 hrs).

Residue (320 K)		
Position (cm^{-1})	Identity	References
3622, 3518, 3446, 3418, 3365	ν(OH)	(24)
2963, 2917	$\nu(^{13}CH)$	(24)
1697	$\nu(^{13}C{=}O)$ acid	(24)
1585	$\nu(^{13}C{=}{}^{13}C)$	(24)
1411	$^{13}CH_2/^{13}CH_3$ deformation	(24)
1244	$\nu(^{13}C{-}O)$ acid, δ(OH)	(24)
1099, 1025, 963	$\nu(^{13}C{-}O)$	(24)
796	δ(OH···O)	(24)
657	δ(OCO) acid	(24)

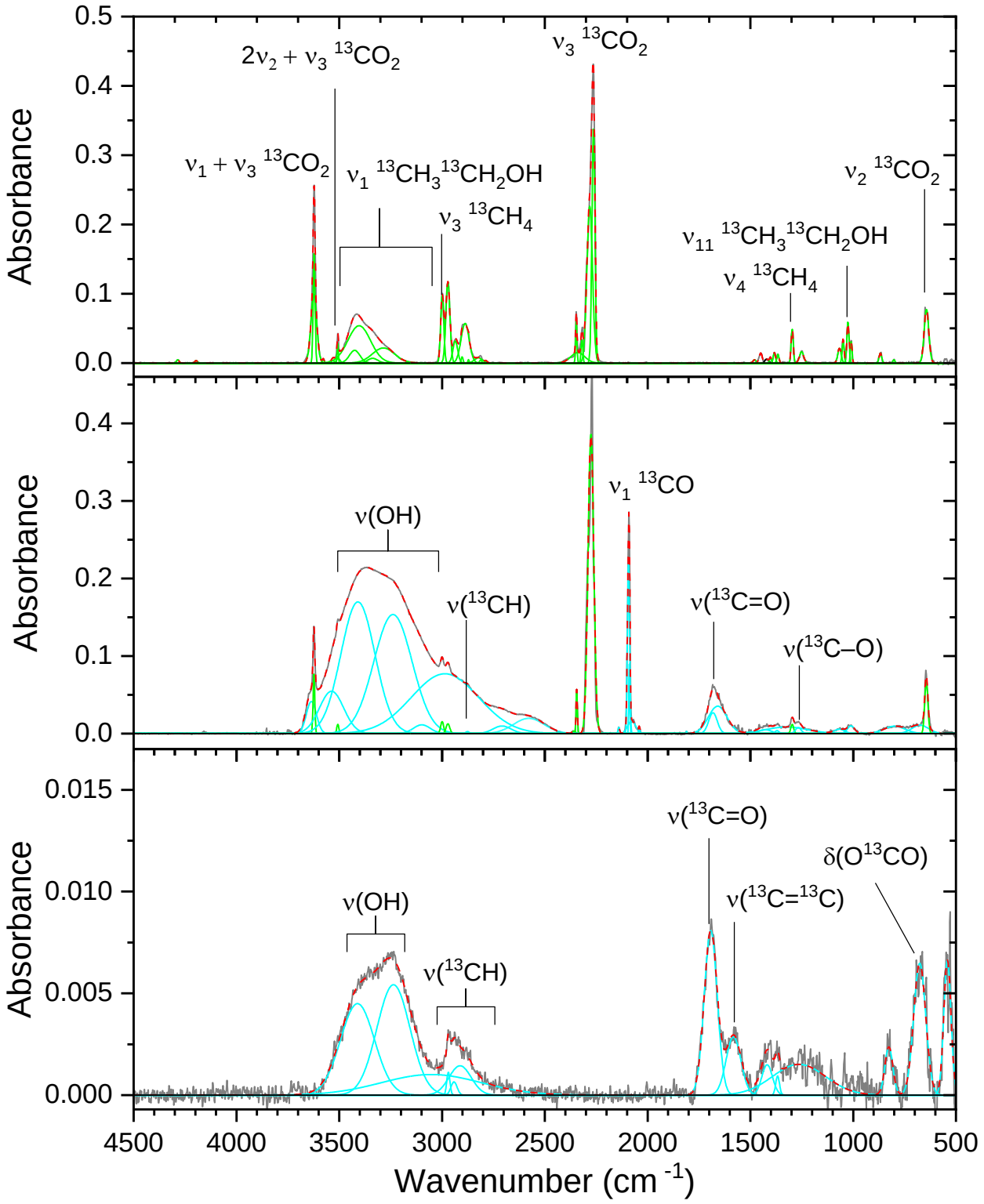

Figure S8. FTIR spectra of ethanol (CH_3CH_2OH)/carbon dioxide (CO_2)/methane (CH_4) ices before irradiation, after irradiation by energetic electrons at 5000 nA for 5 hrs, and the resulting residue after warm-up to 320 K. The spectra (a) before irradiation, (b) after irradiation, and (c) the residue are deconvoluted from the original spectra (gray) to reveal functional groups related to the reagents (green) and irradiation products (cyan).

Table S25. Infrared absorption assignments for $^{13}CH_3{}^{13}CH_2OH/^{13}CO_2/^{13}CH_4$ ice (5000 nA, 5 hrs).

Peaks after deposition (10 K)		
Position (cm^{-1})	Identity	References
4285	$\nu_2 + \nu_3$ $^{13}CH_4$	(7)
4196	$\nu_3 + \nu_4$ $^{13}CH_4$	(7)
3624	$\nu_1 + \nu_3$ $^{13}CO_2$	(23)
3622, 3578, 3531	ν_1 $^{13}CH_3{}^{13}CH_2OH$	(17, 29)
3507	$2\nu_2 + \nu_3$ $^{13}CO_2$	(23)
3505, 3425, 3403, 3337, 3285	ν_1 $^{13}CH_3{}^{13}CH_2OH$	(17, 29)
2999	ν_3 $^{13}CH_4$	(7)
2971	ν_2 $^{13}CH_3{}^{13}CH_2OH$	(17, 29)
2935	ν_3/ν_{15} $^{13}CH_3{}^{13}CH_2OH$	(17, 29)
2902	ν_1 $^{13}CH_4$	(7)
2888	ν_4 $^{13}CH_3{}^{13}CH_2OH$	(17, 29)
2871	Combination	(17, 29)
2823	Combination	(17, 29)
2812	$\nu_2 + \nu_4$ $^{13}CH_4$	(7)
2786	?	
2347	ν_3 $^{12}CO_2$	(23)
2339	$\nu_3 + \nu_L$ $^{13}CO_2$	(23)
2320	ν_3 $^{13}C^{18}O^{16}O$	(23)
2282, 2263	ν_3 $^{13}CO_2$	(23)
1480	ν_5 $^{13}CH_3{}^{13}CH_2OH$	(17, 29)
1450	ν_6 $^{13}CH_3{}^{13}CH_2OH$	(17, 29)
1420	?	
1402	ν_7 $^{13}CH_3{}^{13}CH_2OH$	(17, 29)
1383	Combination?	(17, 29)
1366	ν_8 $^{13}CH_3{}^{13}CH_2OH$	(17, 29)
1296	ν_4 $^{13}CH_4$	(7)
1251	ν_9 $^{13}CH_3{}^{13}CH_2OH$	(17, 29)
1067	ν_{10} $^{13}CH_3{}^{13}CH_2OH$	(17, 29)
1049	ν_{18} $^{13}CH_3{}^{13}CH_2OH$	(17, 29)
1025, 1009	ν_{11} $^{13}CH_3{}^{13}CH_2OH$	(17, 29)
868	ν_{12} $^{13}CH_3{}^{13}CH_2OH$	(17, 29)
802	ν_{19} $^{13}CH_3{}^{13}CH_2OH$	(17, 29)
643	ν_2 $^{13}CO_2$	(23)

Note. L indicates a lattice mode.

Table S26. Infrared absorption assignments for $^{13}CH_3{}^{13}CH_2OH/{}^{13}CO_2/{}^{13}CH_4$ ice (5000 nA, 5 hrs).

Peaks after irradiation (10 K)		
Position (cm^{-1})	Identity	References
3635	ν(OH)	(24)
3623	$\nu_1 + \nu_3$ $^{13}CO_2$	(23)
3537	ν_1 $^{13}CH_3{}^{13}CH_2OH$, ν(OH)	(17, 24, 29)
3507	$2\nu_2 + \nu_3$ $^{13}CO_2$	(23)
3409, 3239, 3098	ν_1 $^{13}CH_3{}^{13}CH_2OH$, ν(OH)	(17, 24, 29)
2999	ν_3 $^{13}CH_4$	(7)
2986	ν(OH)	(24)
2971	ν_2 $^{13}CH_3{}^{13}CH_2OH$	(17, 29)
2966	ν(OH)	(24)
2876	ν(^{13}CH)	(24)
2708, 2578	ν(OH) acid	(24)
2345	ν_3 $^{12}CO_2$	(23)
2276	ν_3 $^{13}CO_2$	(23)
2140	ν_1 ^{12}CO	(23)
2093, 2089	ν_1 ^{13}CO	(23)
2077, 2040	ν(^{13}C≡^{13}C)	(24)
1810	ν(^{13}C=O) HO^{13}CO	(24)
1682	ν(^{13}C=O)	(24)
1659	ν_2 H_2O, ν(^{13}C=O)	(24, 26)
1428, 1370, 1324	$^{13}CH_2/{}^{13}CH_3$ deformation	(24)
1296	ν_{17} $^{13}CH_3{}^{13}CH_2OH$	(17, 29)
1267	ν(^{13}C–O) acid	(24)
1066, 1011	ν(^{13}C–O)	(24)
769, 674	δ(OH···O)	(24)
644	ν_2 $^{13}CO_2$	(23)

Note. L indicates a lattice mode.

Table S27. Infrared absorption assignments for $^{13}CH_3{}^{13}CH_2OH/^{13}CO_2/^{13}CH_4$ ice (5000 nA, 5 hrs).

Residue (320 K)		
Position (cm^{-1})	Identity	References
3411 3236, 3052	ν(OH)	(24)
2969, 2942, 2912	$\nu(^{13}CH)$	(24)
1693	$\nu(^{13}C{=}O)$ acid	(24)
1582	$\nu(^{13}C{=}{}^{13}C)$	(24)
1419, 1368	$^{13}CH_2/^{13}CH_3$ deformation	(24)
1263	$\nu(^{13}C{-}O)$ acid, δ(OH)	(24)
826, 796	δ(OH···O)	(24)
676, 542	δ(OCO) acid	(24)

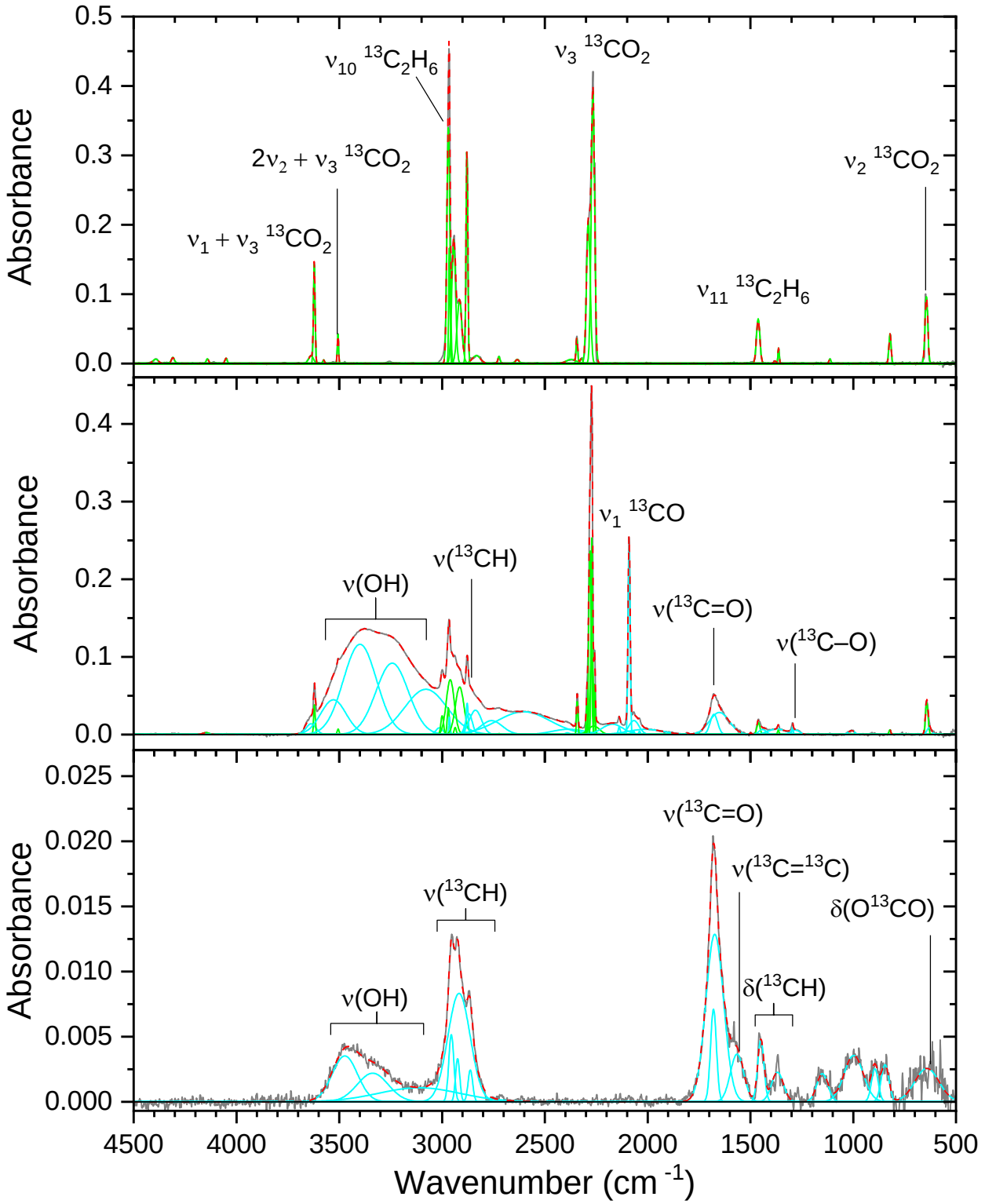

Figure S9. FTIR spectra of ethane (C_2H_6)/carbon dioxide (CO_2) ices before irradiation, after irradiation by energetic electrons at 5000 nA for 5 hrs, and the resulting residue after warm-up to 320 K. The spectra (a) before irradiation, (b) after irradiation, and (c) the residue are deconvoluted from the original spectra (gray) to reveal functional groups related to the reagents (green) and irradiation products (cyan).

Table S28. Infrared absorption assignments for $^{13}C_2H_6/^{13}CO_2$ ice (5000 nA, 5 hrs).

Peaks after deposition (10 K)		
Position (cm^{-1})	Identity	References
4393, 4309, 4141, 4050	Overtones/Combination $^{13}C_2H_6$	(25, 30)
3638, 3621, 3576	$\nu_1 + \nu_3$ $^{13}CO_2$	(23)
3506	$2\nu_2 + \nu_3$ $^{13}CO_2$	(23)
2969, 2964	ν_{10} $^{13}C_2H_6$	(25, 30)
2943, 2915	$\nu_8 + \nu_{11}$ $^{13}C_2H_6$	(25, 30)
2879	ν_5 $^{13}C_2H_6$	(25, 30)
2833	$\nu_2 + \nu_4 + \nu_{12}$ $^{13}C_2H_6$	(25, 30)
2723	$\nu_2 + \nu_6$ $^{13}C_2H_6$	(25, 30)
2634	$\nu_8 + \nu_{12}$ $^{13}C_2H_6$	(25, 30)
2371	$\nu_3 + \nu_L$ $^{13}CO_2$	(23)
2344	ν_3 $^{12}CO_2$	(23)
2322	ν_3 $^{13}C^{18}O^{16}O$	(23)
2288, 2266	ν_3 $^{13}CO_2$	(23)
1462	ν_{11} $^{13}C_2H_6$	(25, 30)
1381, 1363	ν_6 $^{13}C_2H_6$	(25, 30)
1113	?	
821	ν_{12} $^{13}C_2H_6$	(25, 30)
643	ν_2 $^{13}CO_2$	(25, 30)

Note. L indicates a lattice mode.

Table S29. Infrared absorption assignments for $^{13}C_2H_6/^{13}CO_2$ ice (5000 nA, 5 hrs).

Peaks after deposition (10 K)		
Position (cm^{-1})	Identity	References
4148	Combination $^{13}C_2H_6$	(7)
3637	ν(OH) dangling	(24)
3621	$\nu_1 + \nu_3$ $^{13}CO_2$	(23)
3529	ν(OH)	(24)
3506	$2\nu_2 + \nu_3$ $^{13}CO_2$	(23)
3399, 3242, 3078	ν(OH)	(24)
3013	$\nu(^{13}CH)$	(24)
2999	ν_3 $^{13}CH_4$	(7)
2970	$\nu(^{13}CH)$	(24)
2964, 2960	ν_{10} $^{13}C_2H_6$	(25, 30)
2936	$\nu(^{13}CH)$	(7)
2914	$\nu_8 + \nu_{11}$ $^{13}C_2H_6$	(25, 30)
2878	ν_5 $^{13}C_2H_6$	(25, 30)
2869, 2837	$\nu(^{13}CH)$	(24)
2759	ν(OH)	(24)
2721	$\nu_2 + \nu_6$ $^{13}C_2H_6$	(25, 30)
2602	ν(OH) acid	(24)
2391	?	
2384	ν(OH) acid	(24)
2342	ν_3 $^{12}CO_2$	(23)
2339	$\nu_3 + \nu_L$ $^{13}CO_2$	(23)
2320	ν_3 $^{13}C^{18}O^{16}O$	(23)
2294, 2280, 2272, 2262, 2258	ν_3 $^{13}CO_2$	(23)
2171	ν(OH) acid	(24)
2138	ν_1 ^{12}CO	(23)
2090	ν_1 ^{13}CO	(23)
2068	ν_1 $^{13}C^{18}O$	(23)
2067, 2039	$\nu(^{13}C\equiv{}^{13}C)$	(24)
2011	ν(OH) acid	(24)
1807	$\nu(^{13}C{=}O)$ $HO^{13}CO$	(24)
1678	$\nu(^{13}C{=}O)$	(24)
1651	ν_2 H_2O, $\nu(^{13}C{=}O)$	(24, 26)
1498	$^{13}CH_2/^{13}CH_3$ deformation	(24)
1461	ν_{11} $^{13}C_2H_6$	(25, 30)
1441, 1371	$^{13}CH_2/^{13}CH_3$ deformation	(24)
1364	ν_6 $^{13}C_2H_6$	(25, 30)
1296	ν_4 $^{13}CH_4$	(7)
1282	$\nu(^{13}C{-}O)$ acid, δ(OH)	(24)
1009	$\nu(^{13}C{-}O)$	(24)
821	ν_{12} $^{13}C_2H_6$	(25, 30)
643	ν_2 $^{13}CO_2$	(23)
629	δ(OCO) acid	(24)

Note. L indicates a lattice mode.

Table S30. Infrared absorption assignments for $^{13}C_2H_6/^{13}CO_2$ ice (5000 nA, 5 hrs).

Residue (320 K)		
Position (cm^{-1})	Identity	References
3473, 3337, 3112	ν(OH)	(24)
2955, 2924, 2917, 2862	$\nu(^{13}CH)$	(24)
1680, 1673	$\nu(^{13}C{=}O)$ acid	(24)
1565	$\nu(^{13}C{=}^{13}C)$	(24)
1449, 1368	$^{13}CH_2/^{13}CH_3$ deformation	(24)
1150	$\nu(^{13}C{-}O)$ acid, δ(OH)	(24)
895, 845	δ(OH···O)	(24)
642	δ(OCO) acid	(24)

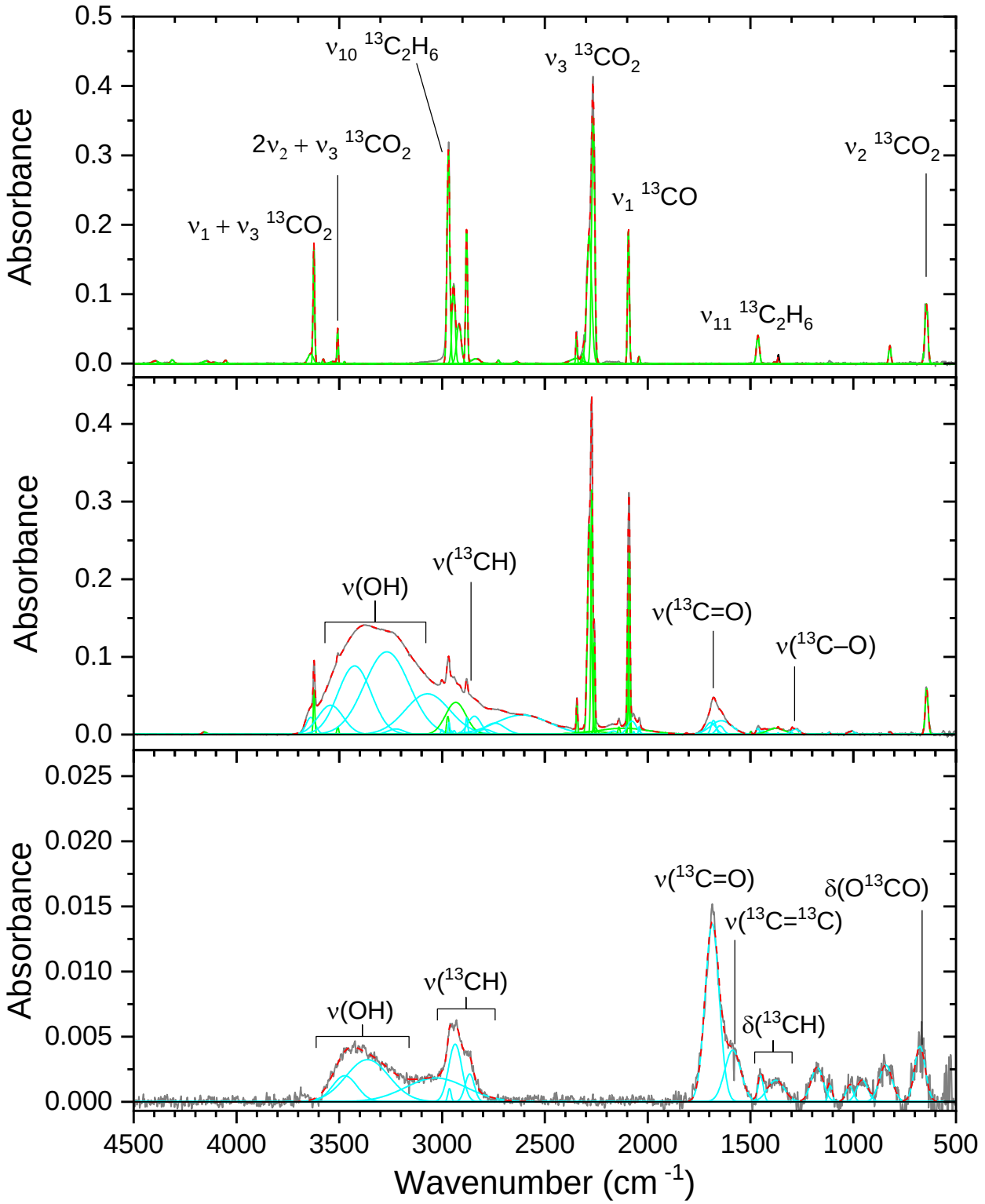

Figure S10. FTIR spectra of ethane (C_2H_6)/carbon dioxide (CO_2)/carbon monoxide (CO) ices before irradiation, after irradiation by energetic electrons at 5000 nA for 5 hrs, and the resulting residue after warm-up to 320 K. The spectra (a) before irradiation, (b) after irradiation, and (c) the residue are deconvoluted from the original spectra (gray) to reveal functional groups related to the reagents (green) and irradiation products (cyan).

Table S31. Infrared absorption assignments for $^{13}C_2H_6$/$^{13}CO_2$/^{13}CO ice (5000 nA, 5 hrs).

Peaks after deposition (10 K)		
Position (cm^{-1})	Identity	References
4395, 4312, 4149, 4106, 4054	Overtones/Combination $^{13}C_2H_6$	(25, 30)
3639, 3623, 3577, 3528	$\nu_1 + \nu_3$ $^{13}CO_2$	(23)
3508	$2\nu_2 + \nu_3$ $^{13}CO_2$	(23)
3475	$2\nu_2 + \nu_3$ $^{13}C^{18}O^{16}O$	(23)
2969	ν_{10} $^{13}C_2H_6$	(25, 30)
2944, 2918	$\nu_8 + \nu_{11}$ $^{13}C_2H_6$	(25, 30)
2881	ν_5 $^{13}C_2H_6$	(25, 30)
2837	$\nu_2 + \nu_4 + \nu_{12}$ $^{13}C_2H_6$	(25, 30)
2726	$\nu_2 + \nu_6$ $^{13}C_2H_6$	(25, 30)
2637	$\nu_8 + \nu_{12}$ $^{13}C_2H_6$	(25, 30)
2348	$\nu_3 + \nu_L$ $^{13}CO_2$	(23)
2346	ν_3 $^{12}CO_2$	(23)
2315	ν_3 $^{13}C^{18}O^{16}O$	(23)
2284, 2265	ν_3 $^{13}CO_2$	(23)
2093	ν_1 ^{13}CO	(23)
2042	ν_1 $^{13}C^{18}O$	(23)
1463	ν_{11} $^{13}C_2H_6$	(25, 30)
1381, 1364	ν_6 $^{13}C_2H_6$	(25, 30)
821	ν_{12} $^{13}C_2H_6$	(25, 30)
643	ν_2 $^{13}CO_2$	(25, 30)

Note. L indicates a lattice mode.

Table S32. Infrared absorption assignments for $^{13}C_2H_6/^{13}CO_2/^{13}CO$ ice (5000 nA, 5 hrs).

Peaks after deposition (10 K)		
Position (cm^{-1})	Identity	References
4155	Combination $^{13}C_2H_6$	(7)
3639	ν(OH) dangling	(24)
3622	$\nu_1 + \nu_3$ $^{13}CO_2$	(23)
3542	ν(OH)	(24)
3507	$2\nu_2 + \nu_3$ $^{13}CO_2$	(23)
3425, 3269, 3071	ν(OH)	(24)
3001	ν_3 $^{13}CH_4$	(7)
2972	$\nu(^{13}CH)$	(24)
2965	ν_{10} $^{13}C_2H_6$	(25, 30)
2953, 2941	$\nu(^{13}CH)$	(7)
2933	ν(OH)	(24)
2912	$\nu_8 + \nu_{11}$ $^{13}C_2H_6$	(25, 30)
2880	ν_5 $^{13}C_2H_6$	(25, 30)
2864, 2842	$\nu(^{13}CH)$	(24)
2792, 2743, 2609, 2395	ν(OH) acid	(24)
2344	ν_3 $^{12}CO_2$	(23)
2335	$\nu_3 + \nu_L$ $^{13}CO_2$	(23)
2283, 2271, 2267, 2259, 2255	ν_3 $^{13}CO_2$	(23)
2166	ν(OH) acid	(24)
2139	ν_1 ^{12}CO	(23)
2095, 2089	ν_1 ^{13}CO	(23)
2077	ν_1 $^{13}C^{18}O$	(23)
2067, 2040	$\nu(^{13}C\equiv{}^{13}C)$	(24)
1811	$\nu(^{13}C{=}O)$ $HO^{13}CO$	(24)
1693, 1680	$\nu(^{13}C{=}O)$	(24)
1648, 1642	ν_2 H_2O, $\nu(^{13}C{=}O)$	(24, 26)
1497	$^{13}CH_2/^{13}CH_3$ deformation	(24)
1463	ν_{11} $^{13}C_2H_6$	(25, 30)
1440, 1375	$^{13}CH_2/^{13}CH_3$ deformation	(24)
1365	ν_6 $^{13}C_2H_6$	(25, 30)
1297	ν_4 $^{13}CH_4$	(7)
1282	$\nu(^{13}C{-}O)$ acid, δ(OH)	(24)
1117	$\nu(^{13}C{-}O)$	(24)
1009	$\nu(^{13}C{-}O)$	(24)
821	ν_{12} $^{13}C_2H_6$	(25, 30)
643	ν_2 $^{13}CO_2$	(23)

Note. L indicates a lattice mode.

Table S33. Infrared absorption assignments for $^{13}C_2H_6/^{13}CO_2/^{13}CO$ ice (5000 nA, 5 hrs).

Residue (320 K)		
Position (cm^{-1})	Identity	References
3473, 3363, 3030	ν(OH)	(24)
2964, 2936, 2865	$\nu(^{13}CH)$	(24)
1686	$\nu(^{13}C{=}O)$ acid	(24)
1586	$\nu(^{13}C{=}^{13}C)$	(24)
1450, 1367	$^{13}CH_2/^{13}CH_3$ deformation	(24)
1176, 1112	$\nu(^{13}C{-}O)$ acid, δ(OH)	(24)
956, 842	$\nu(^{13}C{-}O)$, δ(OH···O)	(24)
642	δ(OCO) acid	(24)

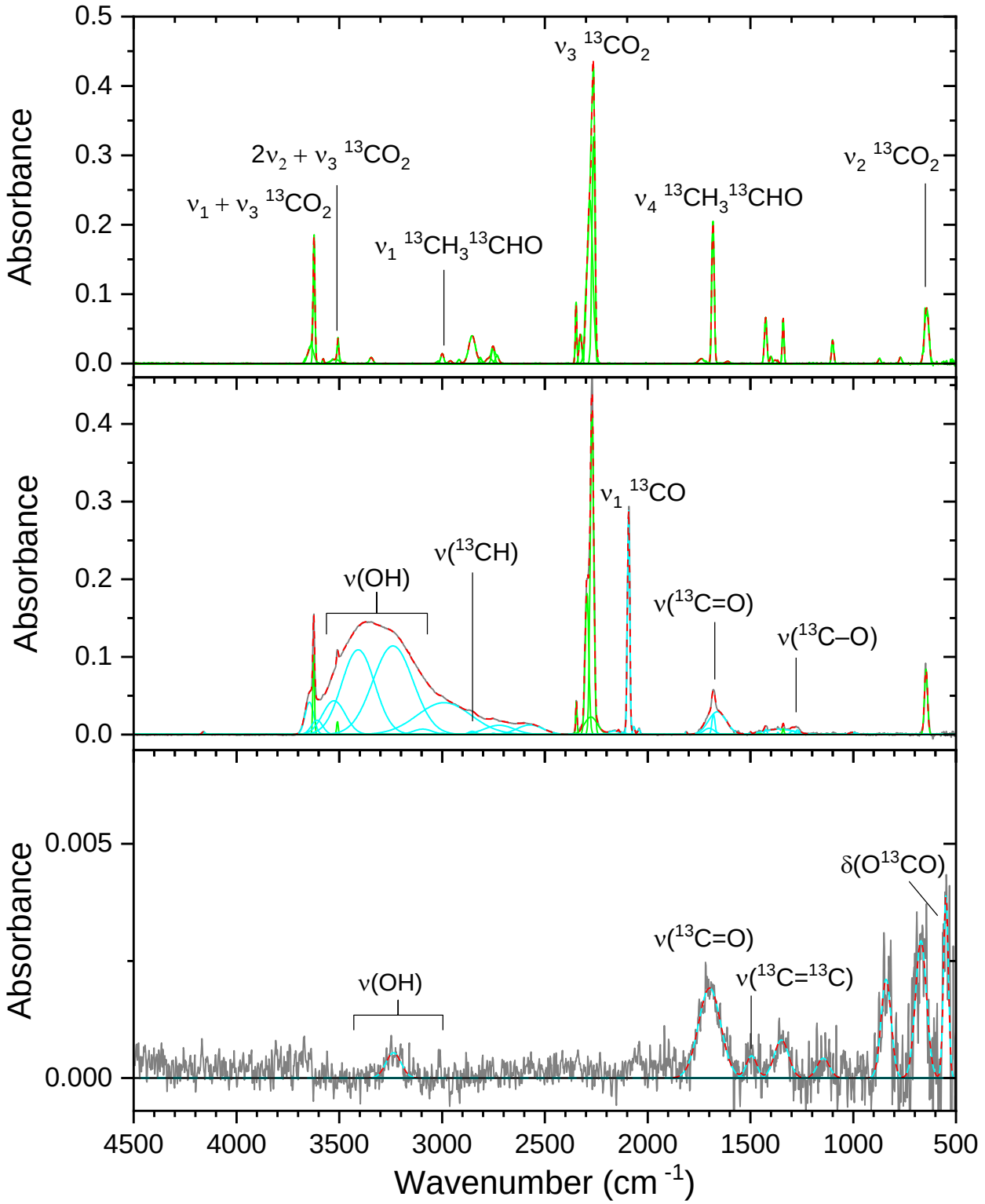

Figure S11. FTIR spectra of acetaldehyde ($^{13}CH_3{}^{13}CHO$)/carbon dioxide (CO_2) ices before irradiation, after irradiation by energetic electrons at 5000 nA for 5 hrs, and the resulting residue after warmup to 320 K. The spectra (a) before irradiation, (b) after irradiation, and (c) the residue are deconvoluted from the original spectra (gray) to reveal functional groups related to the reagents (green) and irradiation products (cyan).

Table S34. Infrared absorption assignments for $^{13}CH_3{}^{13}CHO/{}^{13}CO_2$ ice (5000 nA, 5 hrs).

Peaks after deposition (10 K)		
Position (cm^{-1})	Identity	References
3638, 3623	$\nu_1 + \nu_3$ $^{13}CO_2$	(23)
3578, 3521	$\nu_1 + \nu_3$ $^{13}C^{18}O^{16}O$	(23)
3506	$2\nu_2 + \nu_3$ $^{13}CO_2$	(23)
3345	$2\nu_2$ $^{13}CH_3{}^{13}CHO$	(21)
3020	Overtone $^{13}CH_3{}^{13}CHO$	(21)
2999	ν_1 $^{13}CH_3{}^{13}CHO$	(21)
2960	ν_{11} $^{13}CH_3{}^{13}CHO$	(21)
2917	ν_2 $^{13}CH_3{}^{13}CHO$	(21)
2854	$2\nu_6$ $^{13}CH_3{}^{13}CHO$	(21)
2813	Overtone $^{13}CH_3{}^{13}CHO$	(21)
2771	ν_1 $^{13}CH_3{}^{13}CHO$	(21)
2752	ν_3 $^{13}CH_3{}^{13}CHO$	(21)
2348	$\nu_3 + \nu_L$ $^{13}CO_2$	(23)
2327	ν_3 $^{12}CO_2$	(23)
2281, 2263	ν_3 $^{13}CO_2$	(23)
1738	$2\nu_9$ $^{13}CH_3{}^{13}CHO$	(21)
1682	ν_4 $^{13}CH_3{}^{13}CHO$	(21)
1611	ν_1 $^{13}CH_3{}^{13}CHO$	(21)
1426	ν_{12} $^{13}CH_3{}^{13}CHO$	(21)
1400	$\nu_9 + \nu_{10}$ $^{13}CH_3{}^{13}CHO$	(21)
1380	ν_6 $^{13}CH_3{}^{13}CHO$	(21)
1341	ν_7 $^{13}CH_3{}^{13}CHO$	(21)
1100	ν_8 $^{13}CH_3{}^{13}CHO$	(21)
872	ν_9 $^{13}CH_3{}^{13}CHO$	(21)
770	ν_{14} $^{13}CH_3{}^{13}CHO$	(21)
643	ν_2 $^{13}CO_2$	(23)

Note. L indicates a lattice mode.

Table S35. Infrared absorption assignments for $^{13}CH_3{}^{13}CHO/^{13}CO_2$ ice (5000 nA, 5 hrs).

Peaks after irradiation (10 K)		
Position (cm^{-1})	Identity	References
4161	Combination	(24)
3645	ν(OH)	(24)
3624	$\nu_1 + \nu_3$ $^{13}CO_2$	(23)
3608, 3526	ν(OH)	(24)
3508	$2\nu_2 + \nu_3$ $^{13}CO_2$	(23)
3407, 3239	$2\nu_2$ $^{13}CH_3{}^{13}CHO$	(21)
3160	$\nu(^{13}CH)$	(24)
3094	ν(OH)	(24)
2998	ν_1 $^{13}CH_3{}^{13}CHO$	(21)
2990	ν(OH)	(24)
2853	ν(OH) acid	(24)
2750	ν_3 $^{13}CH_3{}^{13}CHO$	(21)
2722, 2572	ν(OH) acid	(24)
2347	ν_3 $^{12}CO_2$	(23)
2295, 2276, 2271	ν_3 $^{13}CO_2$	(23)
2156	ν(OH) acid	(24)
2142	ν_1 ^{12}CO	(23)
2093	ν_1 ^{13}CO	(23)
2067, 2042	$\nu(^{13}C\equiv{}^{13}C)$	(24)
1812	$\nu(^{13}C{=}O)$ $HO^{13}CO$	(24)
1701	$\nu(^{13}C{=}O)$	(24)
1680	ν_4 $^{13}CH_3{}^{13}CHO$	(21)
1661	ν_2 H_2O, $\nu(^{13}C{=}O)$	(24, 26)
1499	$\nu(^{13}C{=}{}^{13}C)$	(24)
1458	$^{13}CH_2/^{13}CH_3$ deformation	(24)
1426	ν_{12} $^{13}CH_3{}^{13}CHO$	(21)
1366, 1361	$^{13}CH_2/^{13}CH_3$ deformation	(24)
1340	ν_7 $^{13}CH_3{}^{13}CHO$	(21)
1294, 1270	$\nu(^{13}C{-}O)$ acid, δ(OH)	(24)
1002	$\nu(^{13}C{-}O)$	(24)
646	ν_2 $^{13}CO_2$	(23)

Note. L indicates a lattice mode.

Table S36. Infrared absorption assignments for $^{13}CH_3{}^{13}CHO/^{13}CO_2$ ice (5000 nA, 5 hrs).

Residue (320 K)		
Position (cm^{-1})	Identity	References
3236	ν(OH)	(24)
1699	$\nu(^{13}C{=}O)$ acid	(24)
1495	$\nu(^{13}C{=}{}^{13}C)$	(24)
1349	$^{13}CH_2/^{13}CH_3$ deformation	(24)
1146	$\nu(^{13}C{-}O)$ acid, δ(OH)	(24)
840	$\nu(^{13}C{-}O)$, δ(OH···O)	(24)
670, 549	δ(OCO) acid	(24)

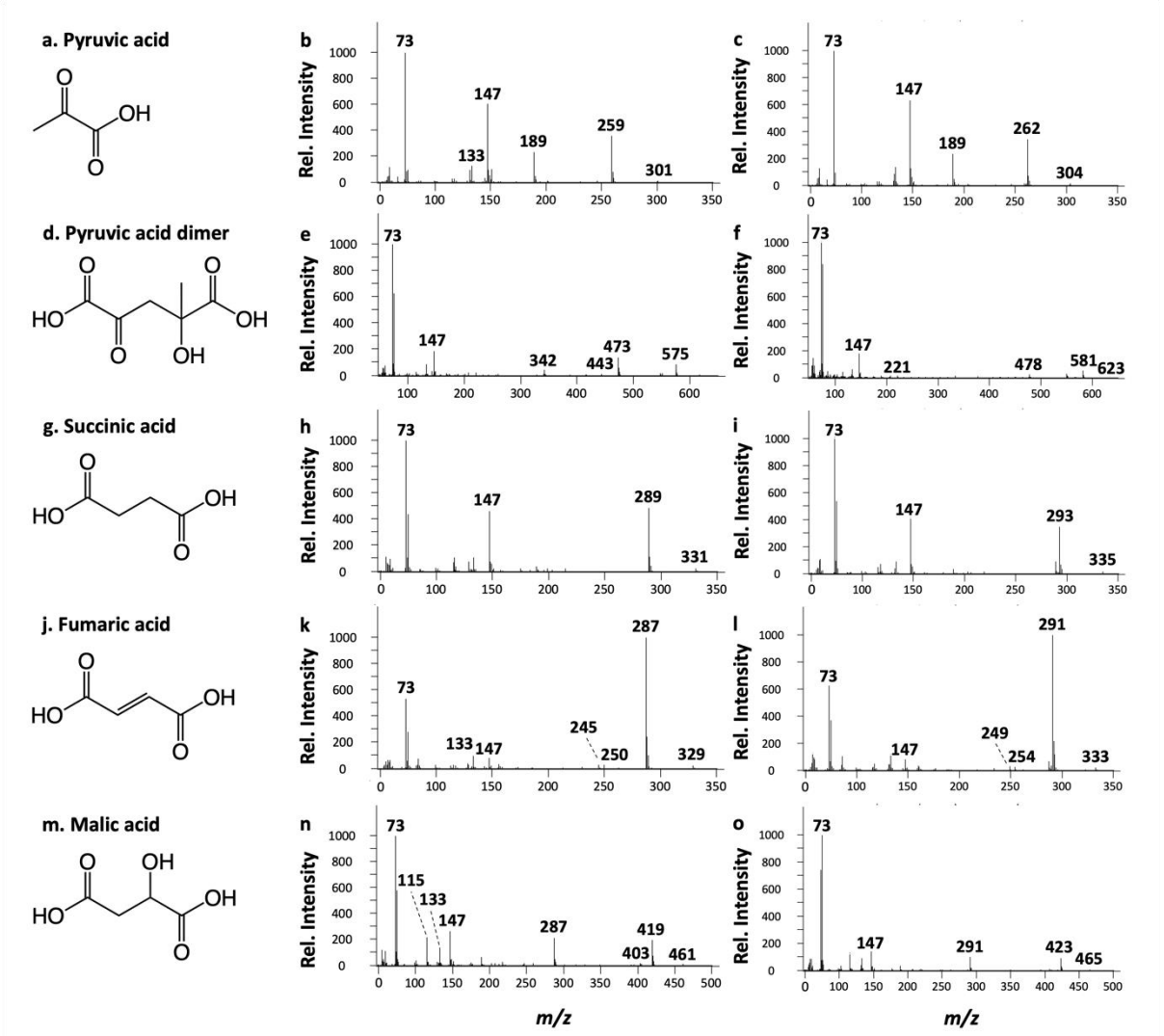

Figure S12. Structures (a, d, g, j, and m) along with the mass spectra of *t*BDMS derivatives of the citric acid cycle compounds. Note that *m/z* highlighted in **b, e, h, k,** and **n** are the ones used for the identification of compounds from a mixture of standards, while *m/z* ($M–15^+$) and *m/z* ($M–57^+$) were used for the identification of their ^{13}C labelled analogs from the electron irradiated simulated interstellar ice analog residue.

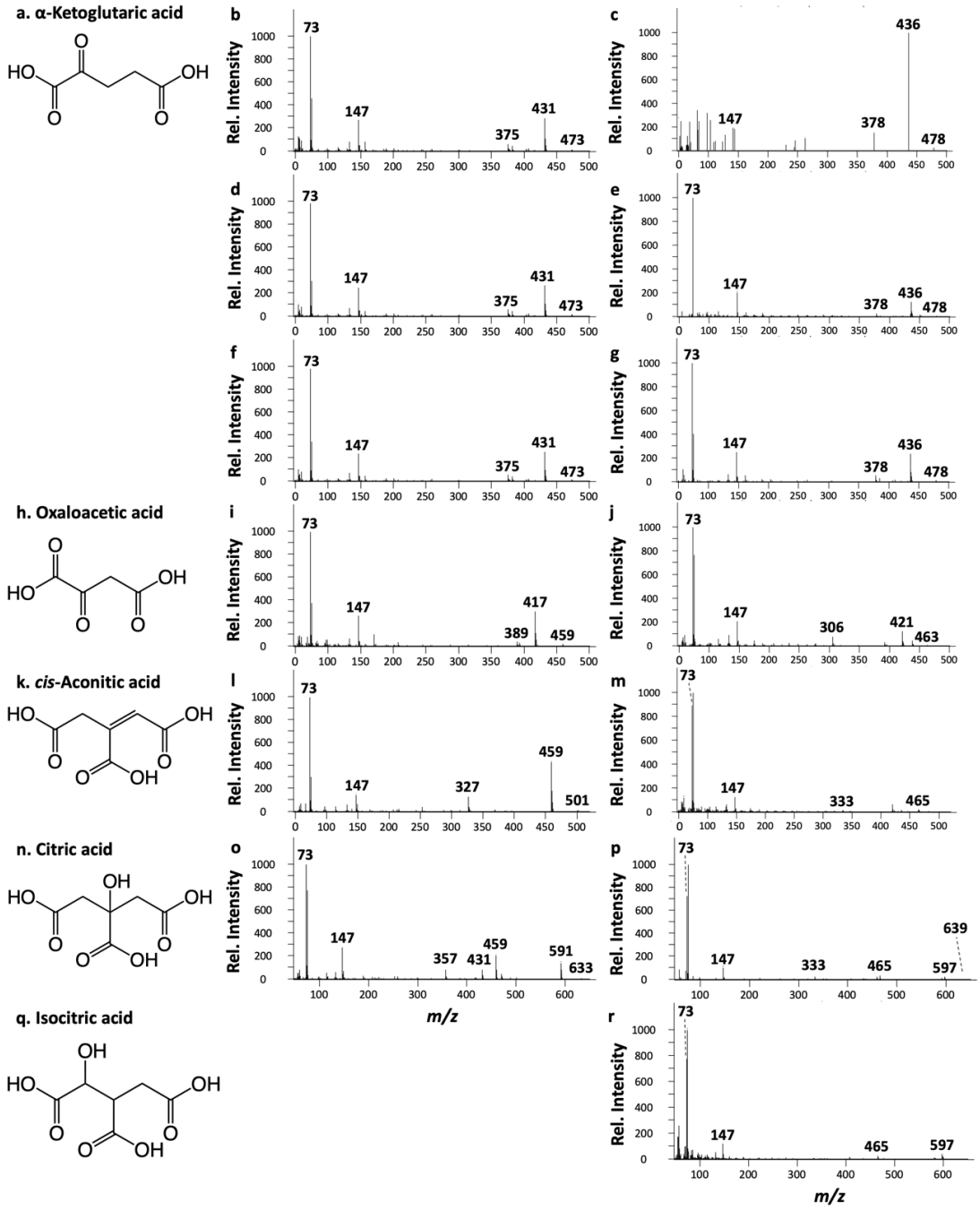

Figure S13. Structures (a, h, k, n, and q) along with the mass spectra of *t*BDMS derivatives of the citric acid cycle compounds. Note that *m/z* highlighted in **b, d, f, i, l,** and **o** are the ones used for the identification of compounds from a mixture of standards, while *m/z* highlighted in **c, e, g, j, m, p,** and **r** were used for the identification of their ^{13}C labelled analogs from the electron irradiated simulated interstellar ice analog residue. Note that for α-ketoglutaric acid three different peaks with the same mass spectra were identified in the standard (**b, d,** and **f**). Their corresponding ^{13}C labeled analogs are shown in **c, e,** and **g**. The assignment of isocitric acid in **r** is tentative due to the lack of a reference standard.

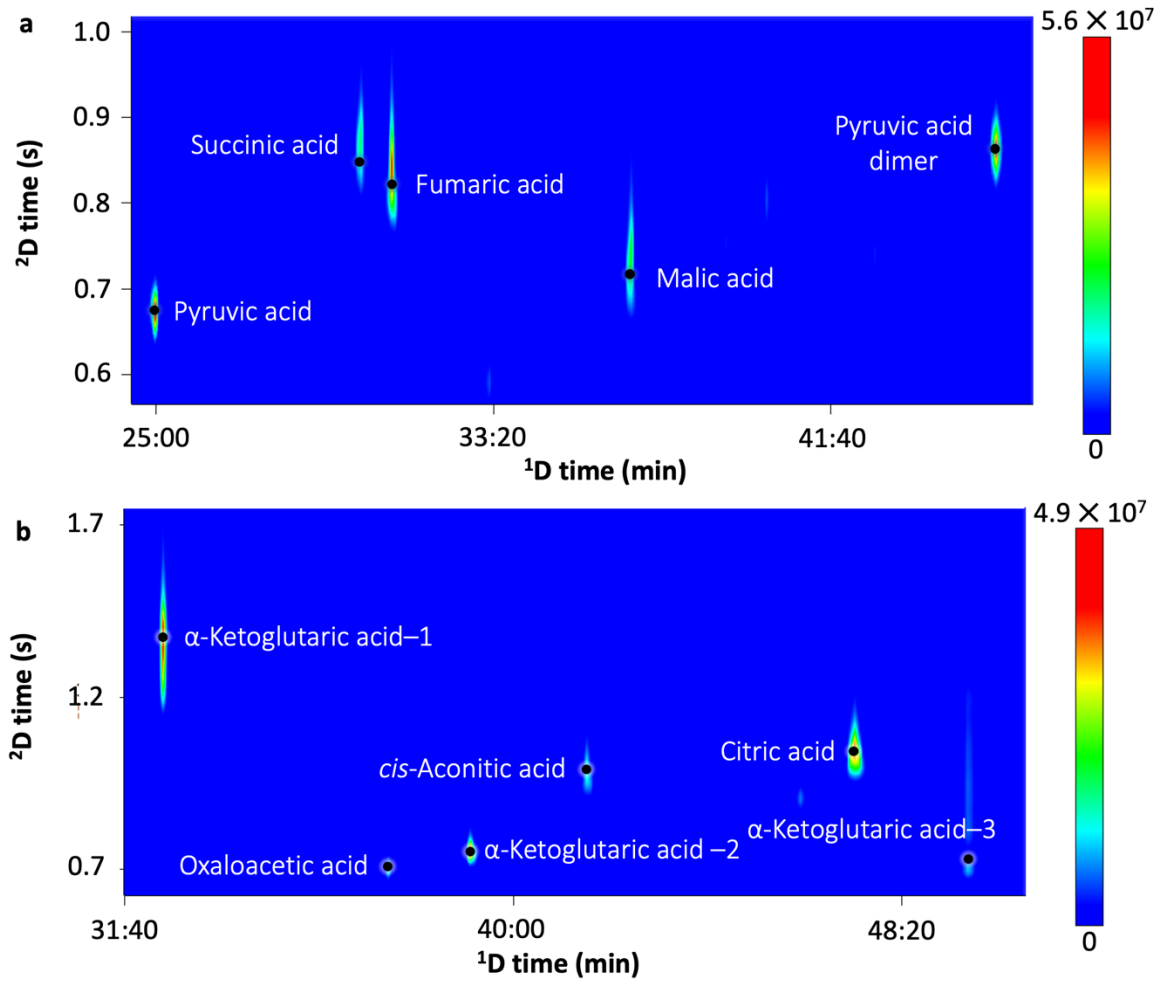

Figure S14. Pyruvic, succinic, fumaric, L-malic, oxaloacetic, *cis*-aconitic, isocitric, citric, α-ketoglutaric acid and pyruvic acid dimer detected in a standard mixture. Multidimensional gas-chromatograms of *t*BDMS derivatives of **a** pyruvic, succinic, fumaric, and L-malic acid and **b** α-ketoglutaric, oxaloacetic, *cis*-aconitic, and citric acid in a standard mixture (5×10^{-5} M). Note that for α-ketoglutaric acid three different peaks with the same mass spectra were identified in the residue and are marked as 1–3.

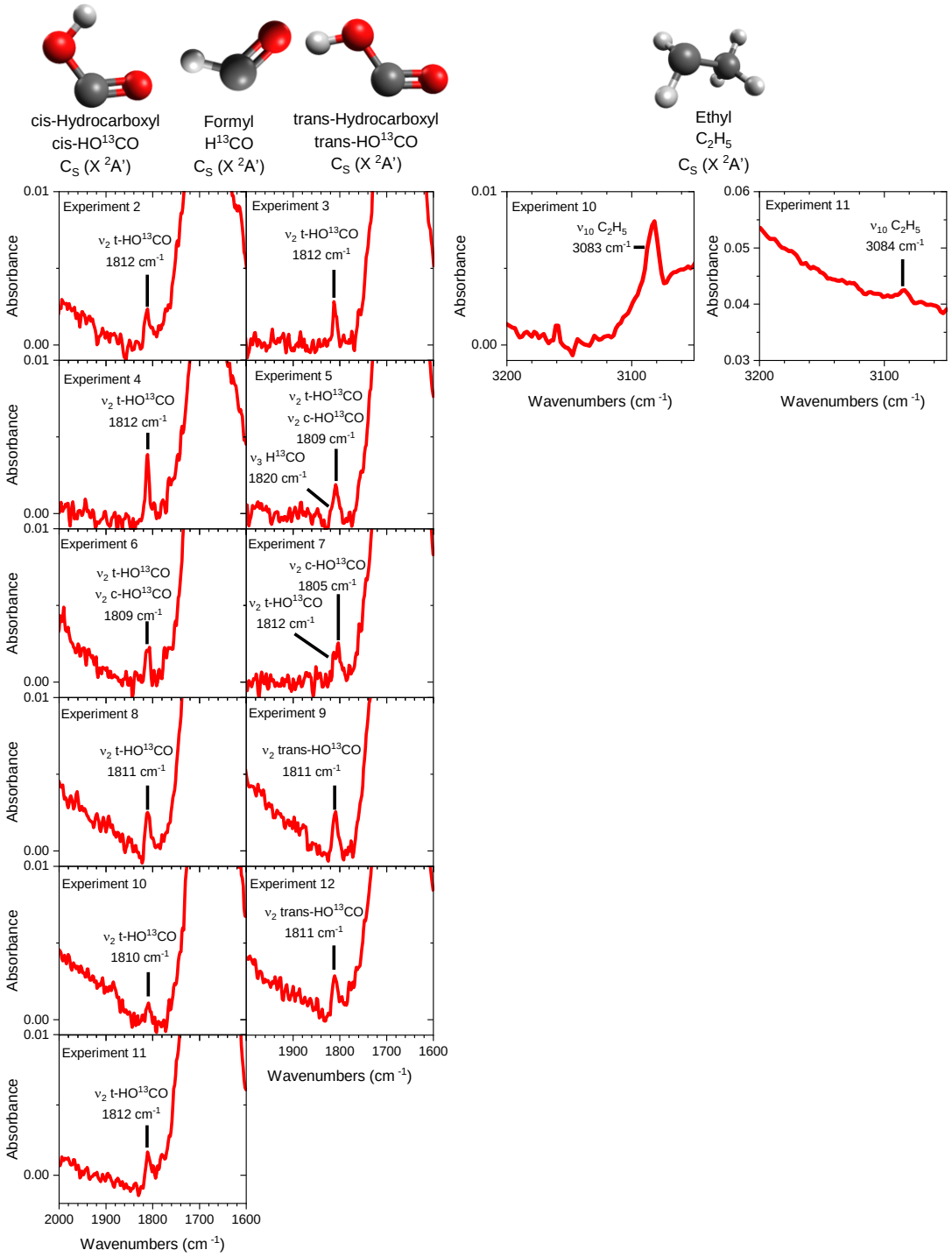

Figure S15. Infrared spectra of ice experiments during irradiation showing vibrational modes of radicals. Fourier transform infrared spectra revealing vibrational modes of the cis- and trans-hydrocarboxyl-^{13}C (c/t-HO^{13}CO), formyl-^{13}C (H^{13}CO), ethyl-$^{13}C_2$ ($^{13}C_2H_5$), and methyl-^{13}C ($^{13}CH_3$) found during irradiation of experiments **2-12**.

RETROSYNTHESIS

Table S37. Legend of all deconstructed molecules in the retrosynthesis of pyruvic acid, oxaloacetic acid, and α-ketoglutaric acid.

Molecule	Figure Number
pyruvic acid (1)	Figure S16
2-oxoacetic acid	Figure S17
2-oxopropanal	Figure S18
oxalaldehyde	Figure S19
formic acid	Figure S20
ethenone	Figure S21
formaldehyde	Figure S21
oxaloacetic acid (7)	Figure S22
3,4-dioxobutanoic acid	Figure S23
3-oxopropanoic acid	Figure S24
3-oxoacrylic acid	Figure S25
2,4-dioxobutanoic acid	Figure S26
2,4-dioxobut-3-enoic acid	Figure S27
2-oxosuccinaldehyde	Figure S28
2,4-dioxobut-3-enal	Figure S29
malonaldehyde	Figure S30
3-oxoacrylaldehyde	Figure S31
acetic acid	Figure S32
α-ketoglutaric acid (5)	Figure S33
2,5-dioxopentanoic acid	Figure S34
2,5-dioxopent-4-enoic acid	Figure S35
2-oxobutanoic acid	Figure S36
2-oxobut-3-enoic acid	Figure S37
propionic acid	Figure S38
acrylic acid	Figure S39
4-oxobutanoic acid	Figure S40
4-oxobut-3-enoic acid	Figure S41
4,5-dioxopentanoic acid	Figure S42
propionaldehyde	Figure S43
acrylaldehyde	Figure S44
succinaldehyde	Figure S45
4-oxobut-3-enal	Figure S46
2-oxopentanedial	Figure S47
prop-1-en-1-one	Figure S48
buta-1,3-diene-1,4-dione	Figure S49
2,5-dioxopent-4-enal	Figure S50
2-oxobutanal	Figure S51
2-oxobut-3-enal	Figure S52

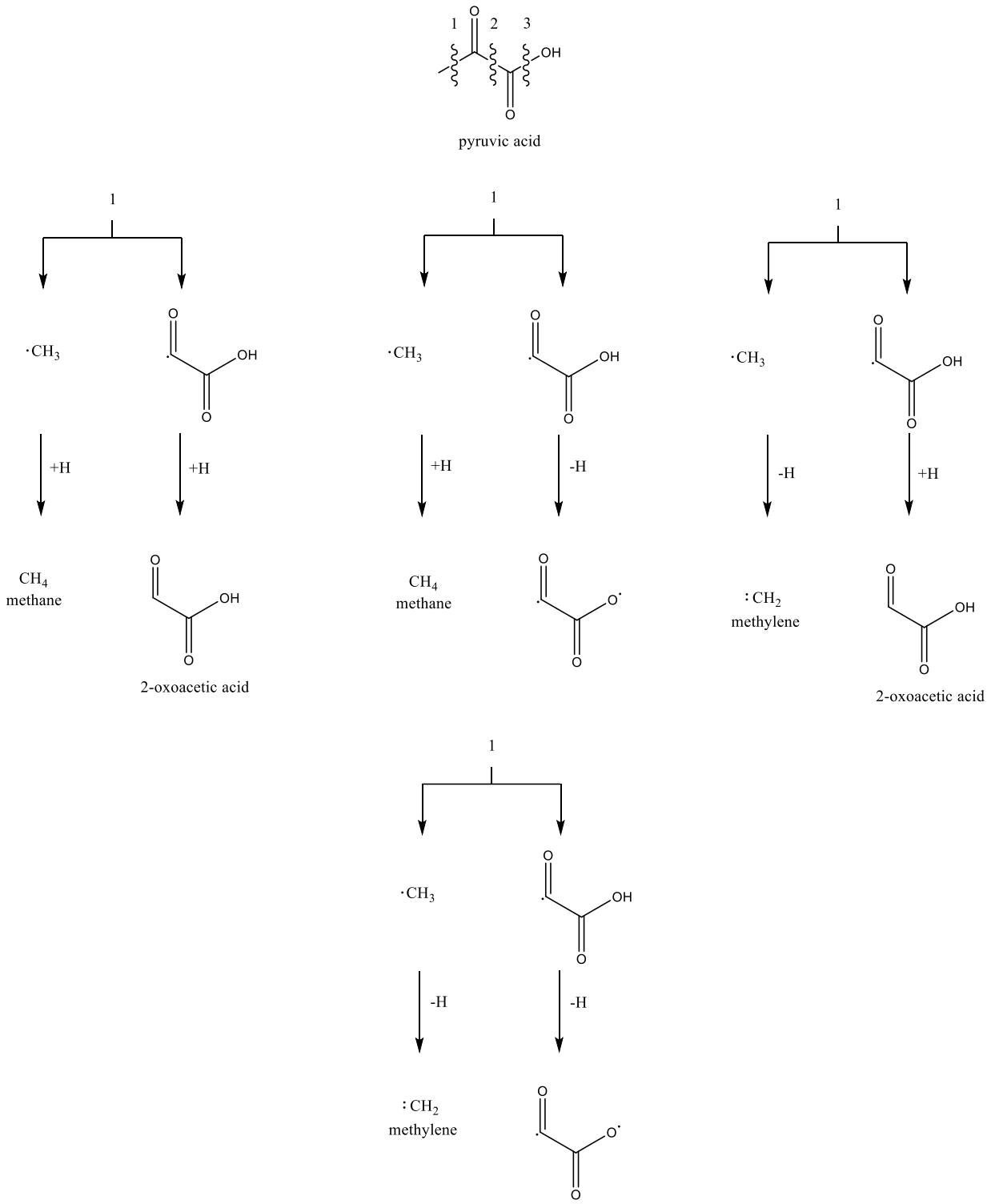

Figure S16A. Retrosynthesis of pyruvic acid (**1**) utilizing single-bond cleavage and subsequent hydrogen addition/elimination.

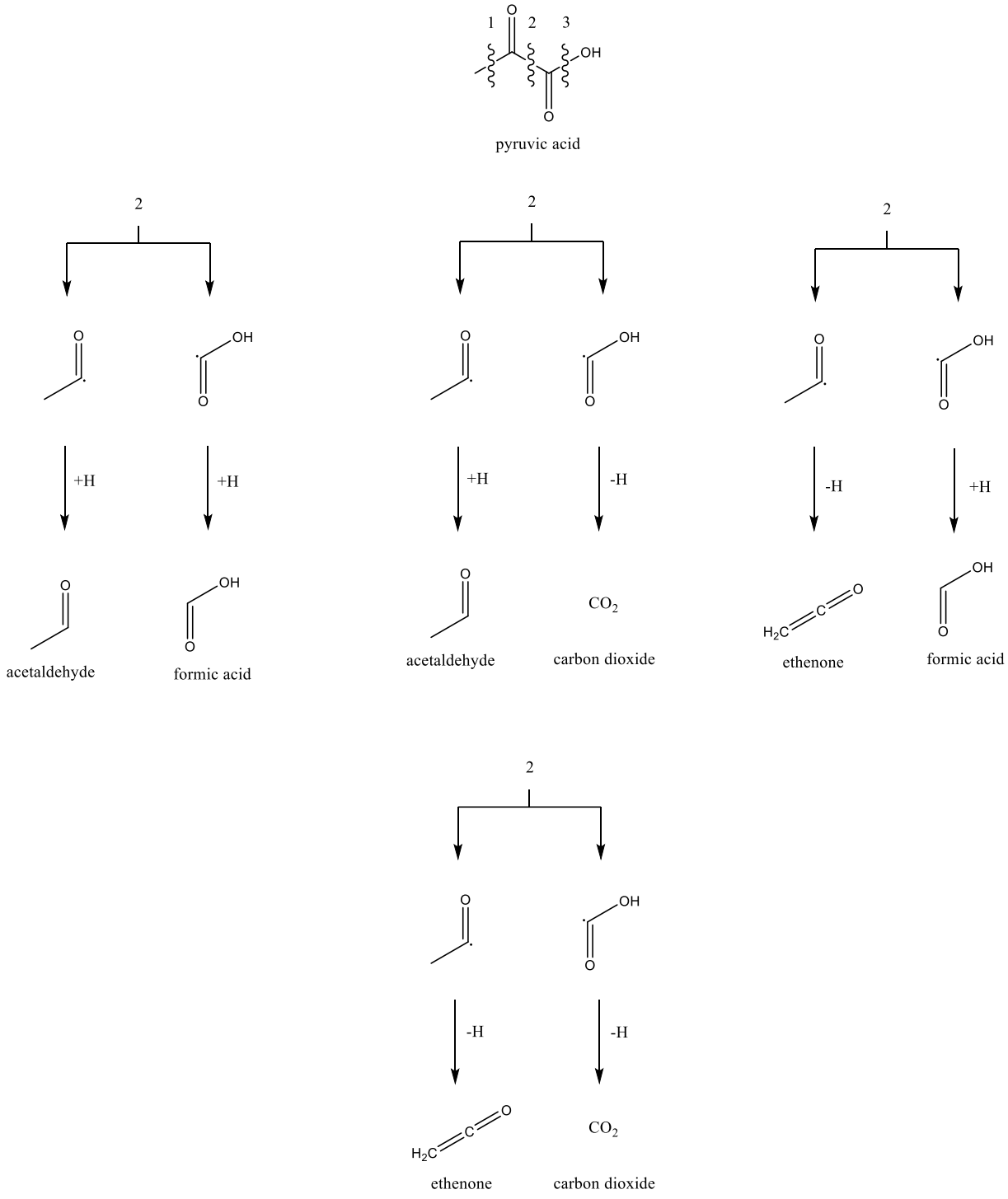

Figure S16B. Retrosynthesis of pyruvic acid (**1**) utilizing single-bond cleavage and subsequent hydrogen addition/elimination.

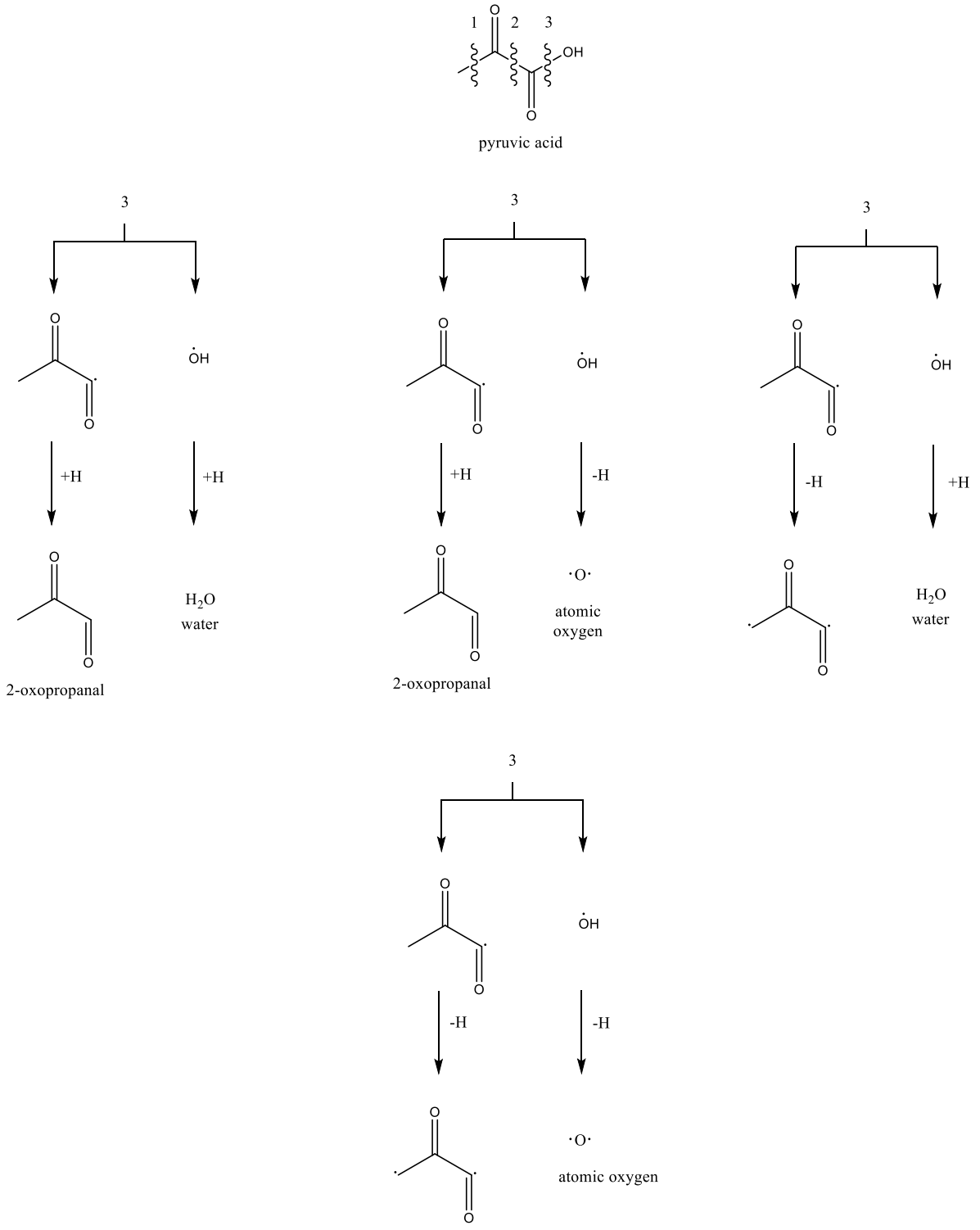

Figure S16C. Retrosynthesis of pyruvic acid (**1**) utilizing single-bond cleavage and subsequent hydrogen addition/elimination.

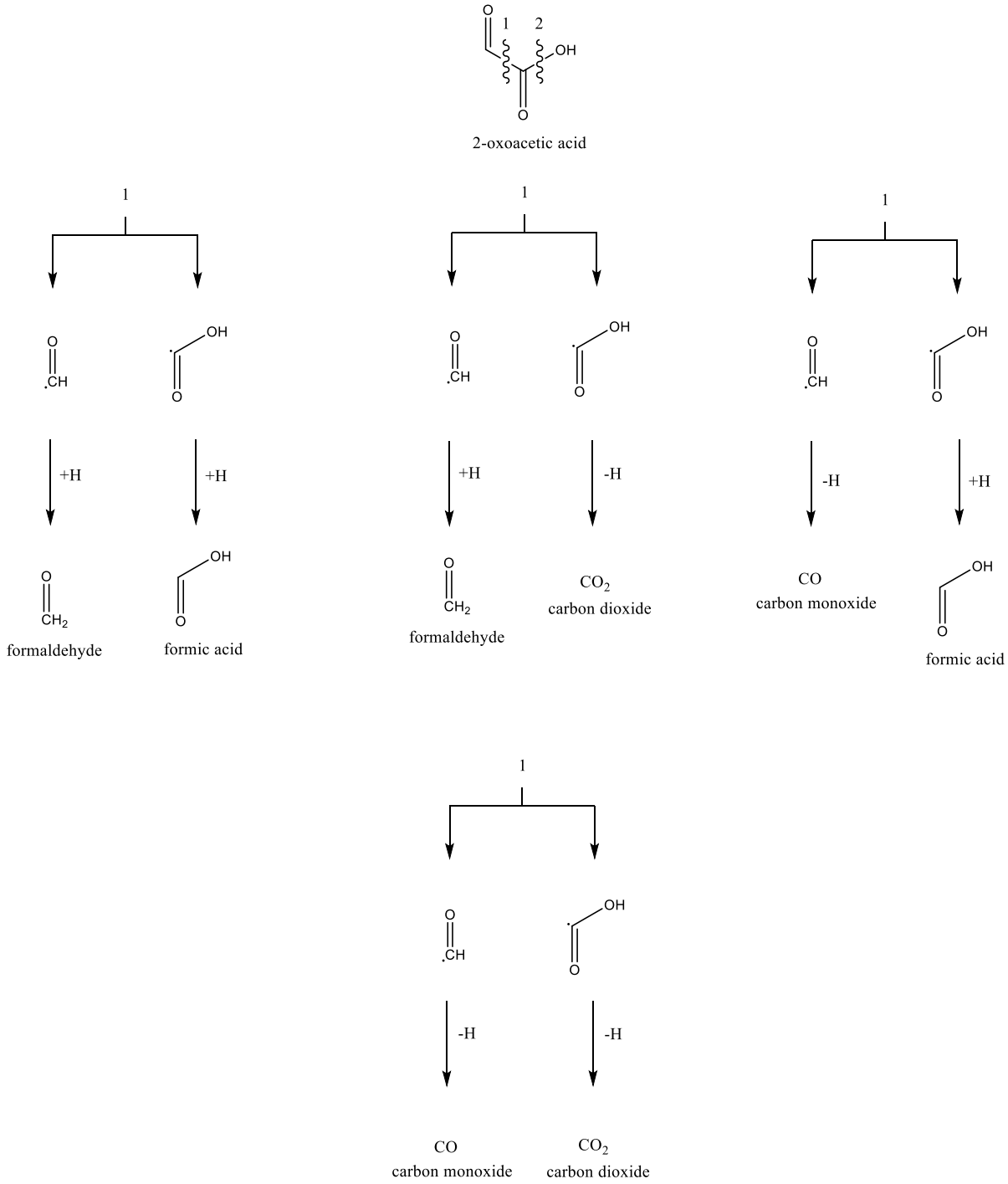

Figure S17A. Retrosynthesis of 2-oxoacetic acid utilizing single-bond cleavage and subsequent hydrogen addition/elimination.

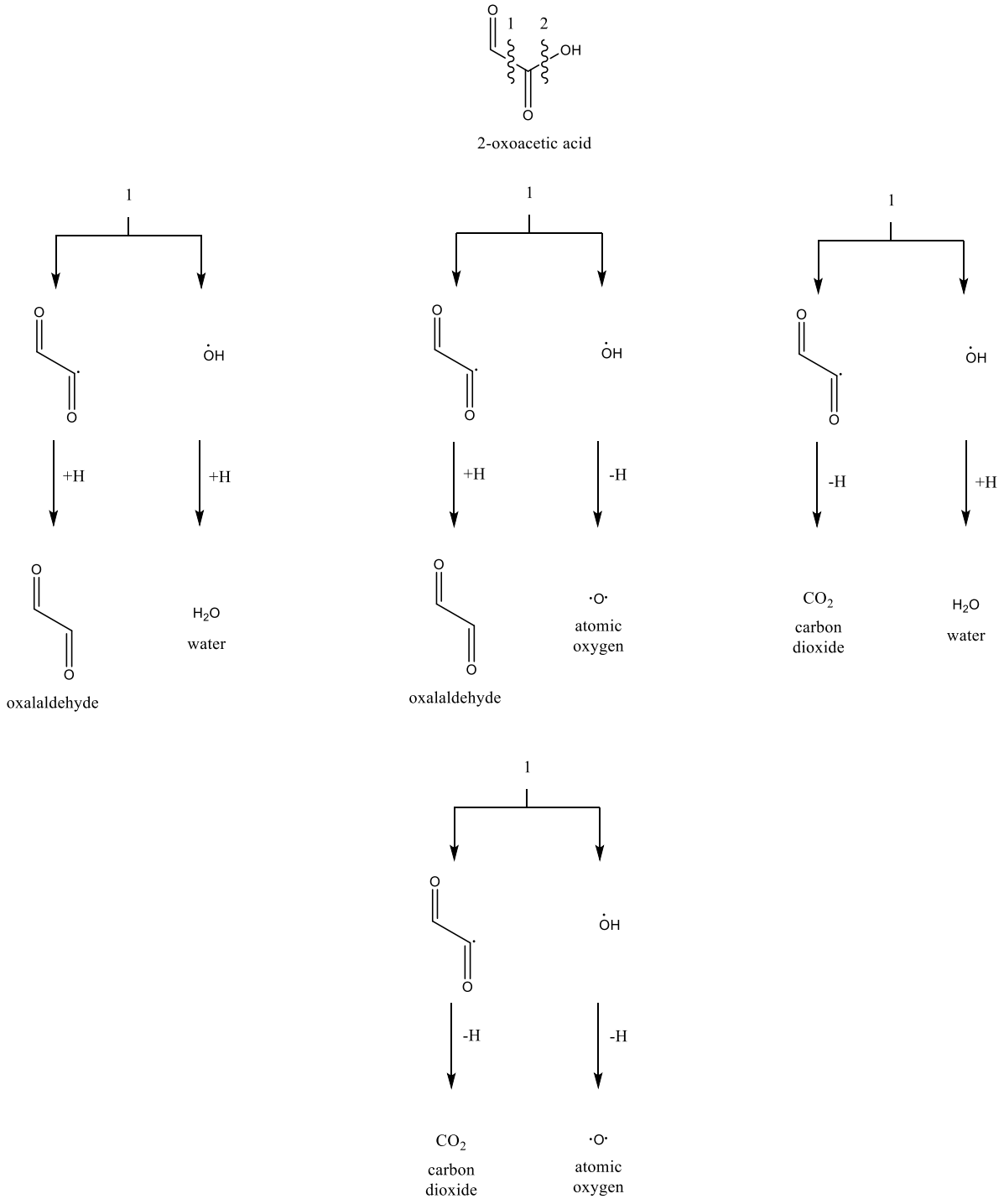

Figure S17B. Retrosynthesis of 2-oxoacetic acid utilizing single-bond cleavage and subsequent hydrogen addition/elimination.

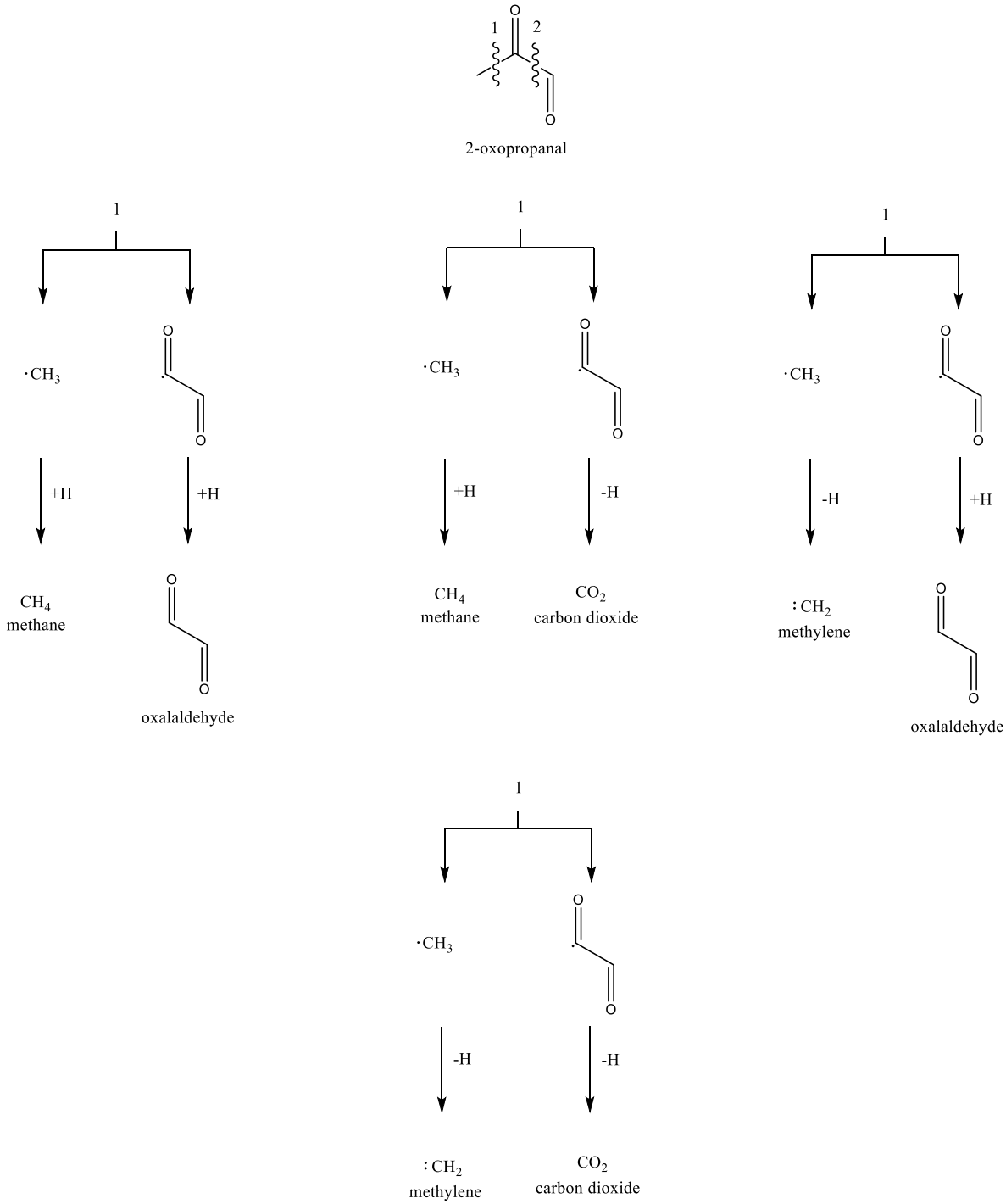

Figure S18A. Retrosynthesis of 2-oxopropanal utilizing single-bond cleavage and subsequent hydrogen addition/elimination.

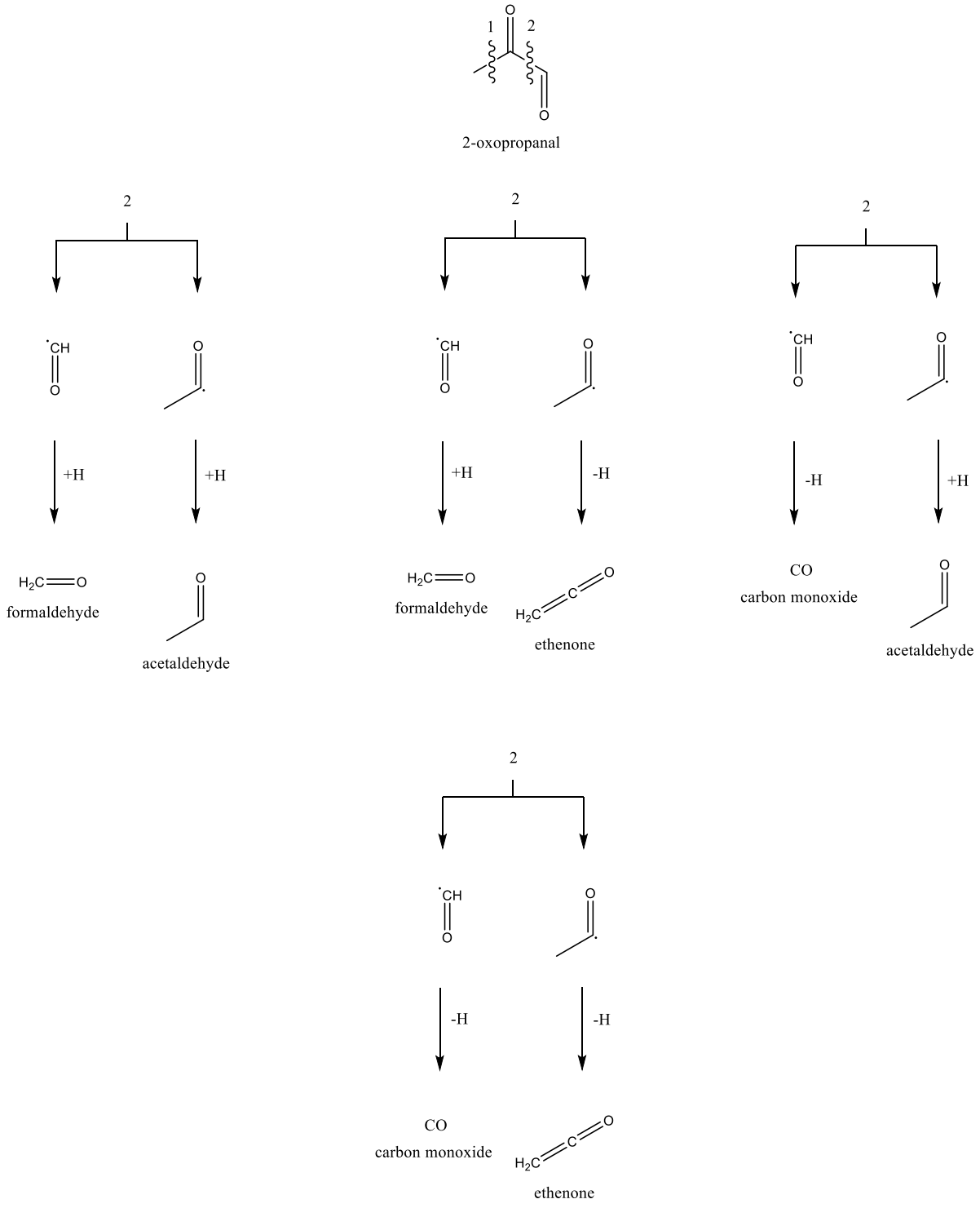

Figure S18B. Retrosynthesis of 2-oxopropanal utilizing single-bond cleavage and subsequent hydrogen addition/elimination.

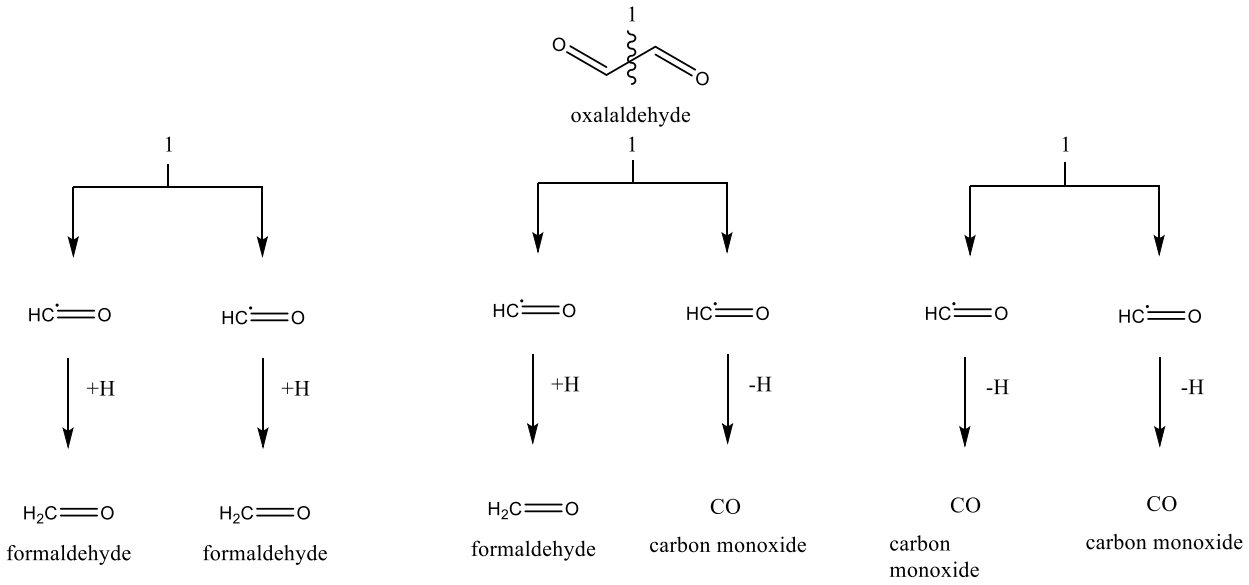

Figure S19. Retrosynthesis of oxalaldehyde utilizing single-bond cleavage and subsequent hydrogen addition/elimination.

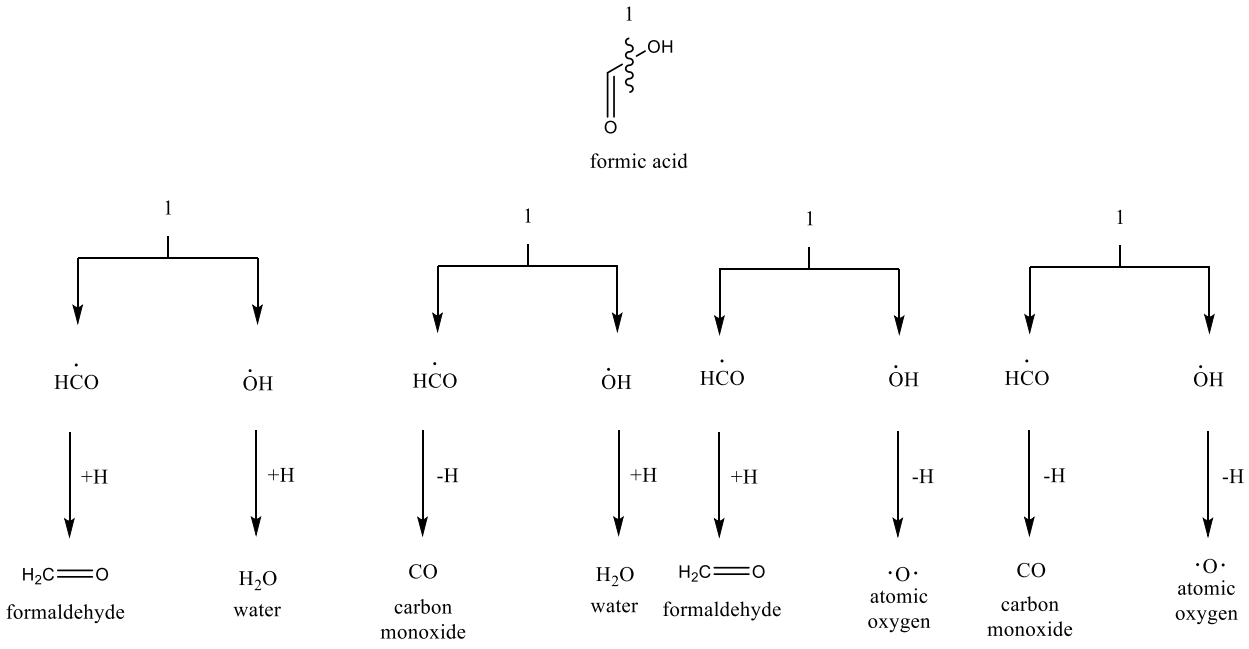

Figure S20. Retrosynthesis of oxalaldehyde utilizing single-bond cleavage and subsequent hydrogen addition/elimination.

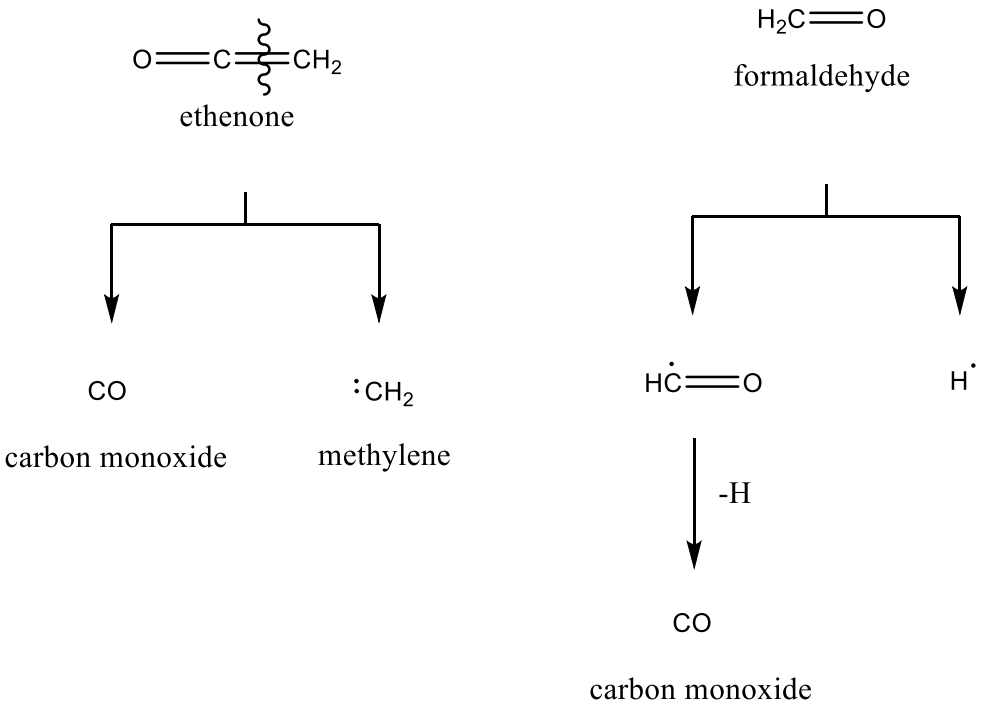

Figure S21. Retrosynthesis of ethenone and formaldehyde shown to derive from carbon monoxide following bond breaking.

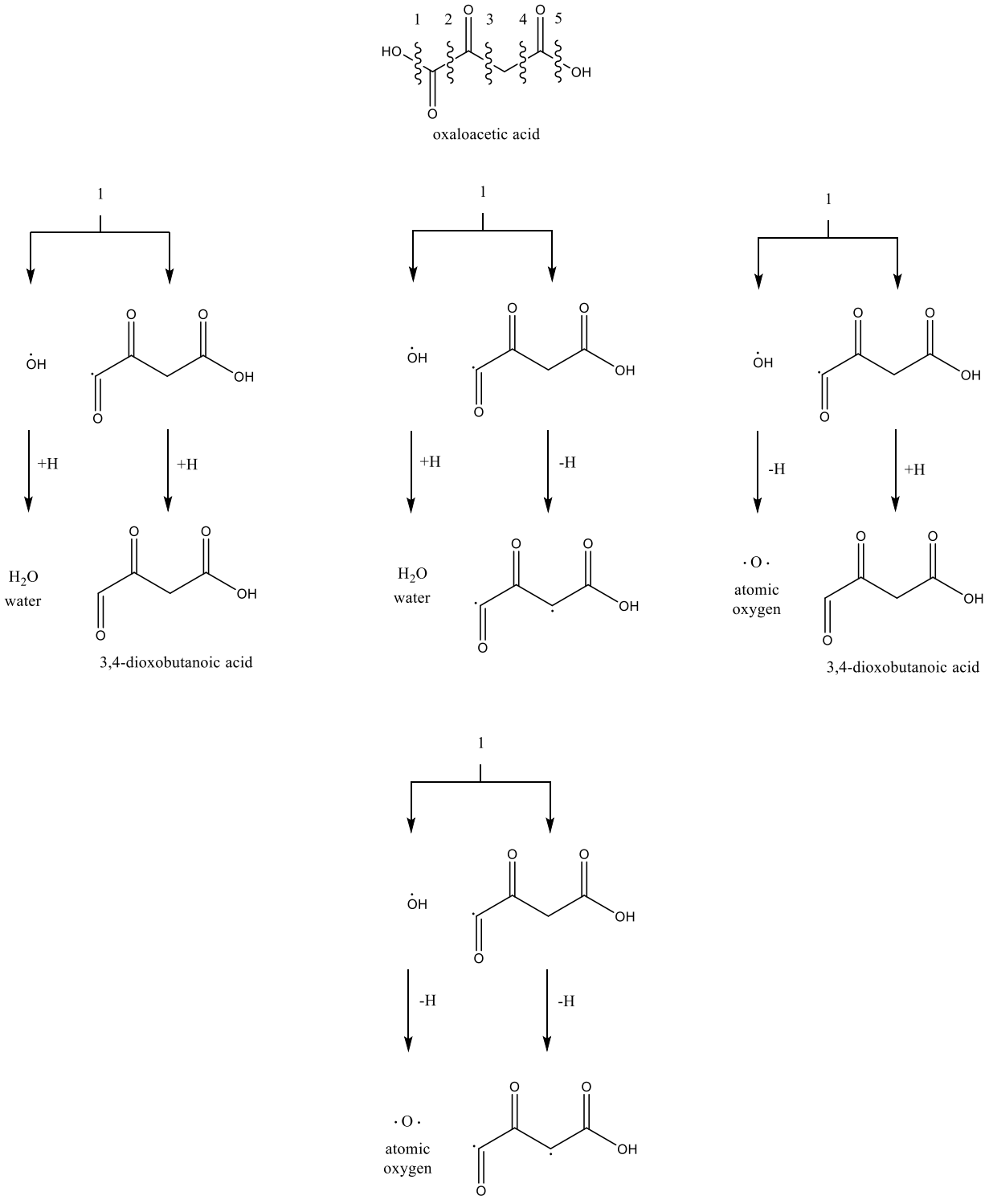

Figure S22A. Retrosynthesis of oxaloacetic acid (**9**) utilizing single-bond cleavage and subsequent hydrogen addition/elimination.

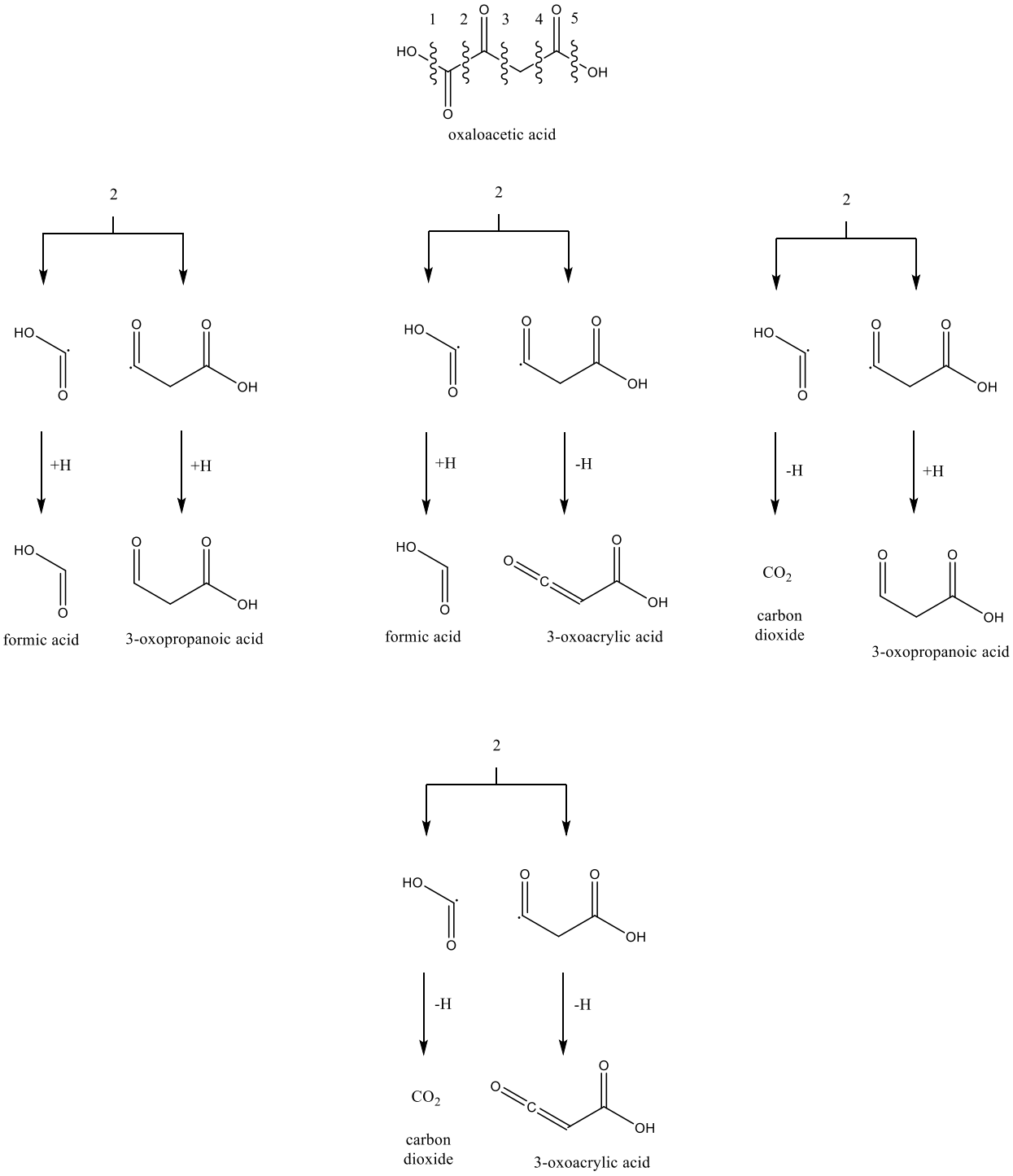

Figure S22B. Retrosynthesis of oxaloacetic acid (**9**) utilizing single-bond cleavage and subsequent hydrogen addition/elimination.

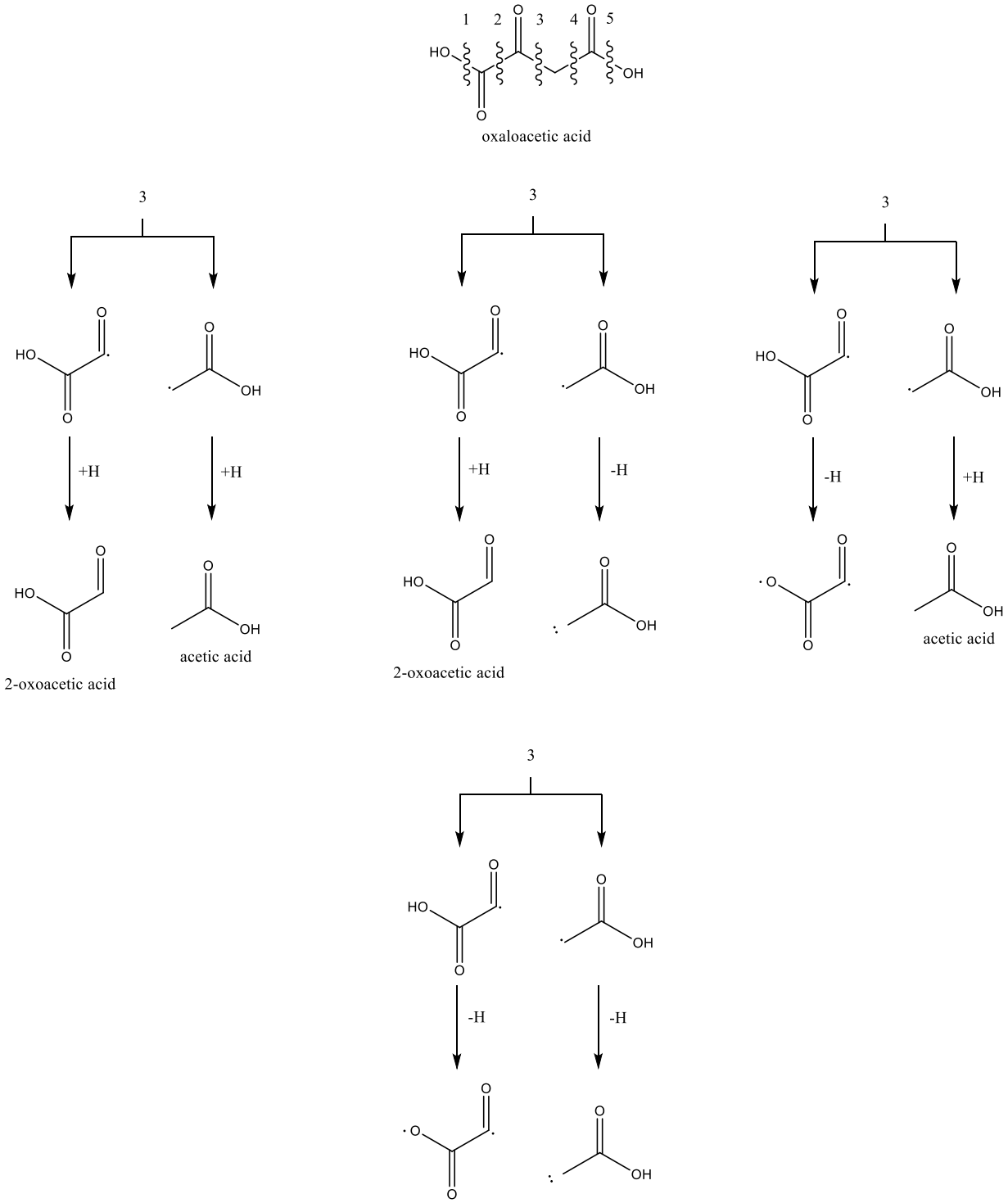

Figure S22C. Retrosynthesis of oxaloacetic acid (**9**) utilizing single-bond cleavage and subsequent hydrogen addition/elimination.

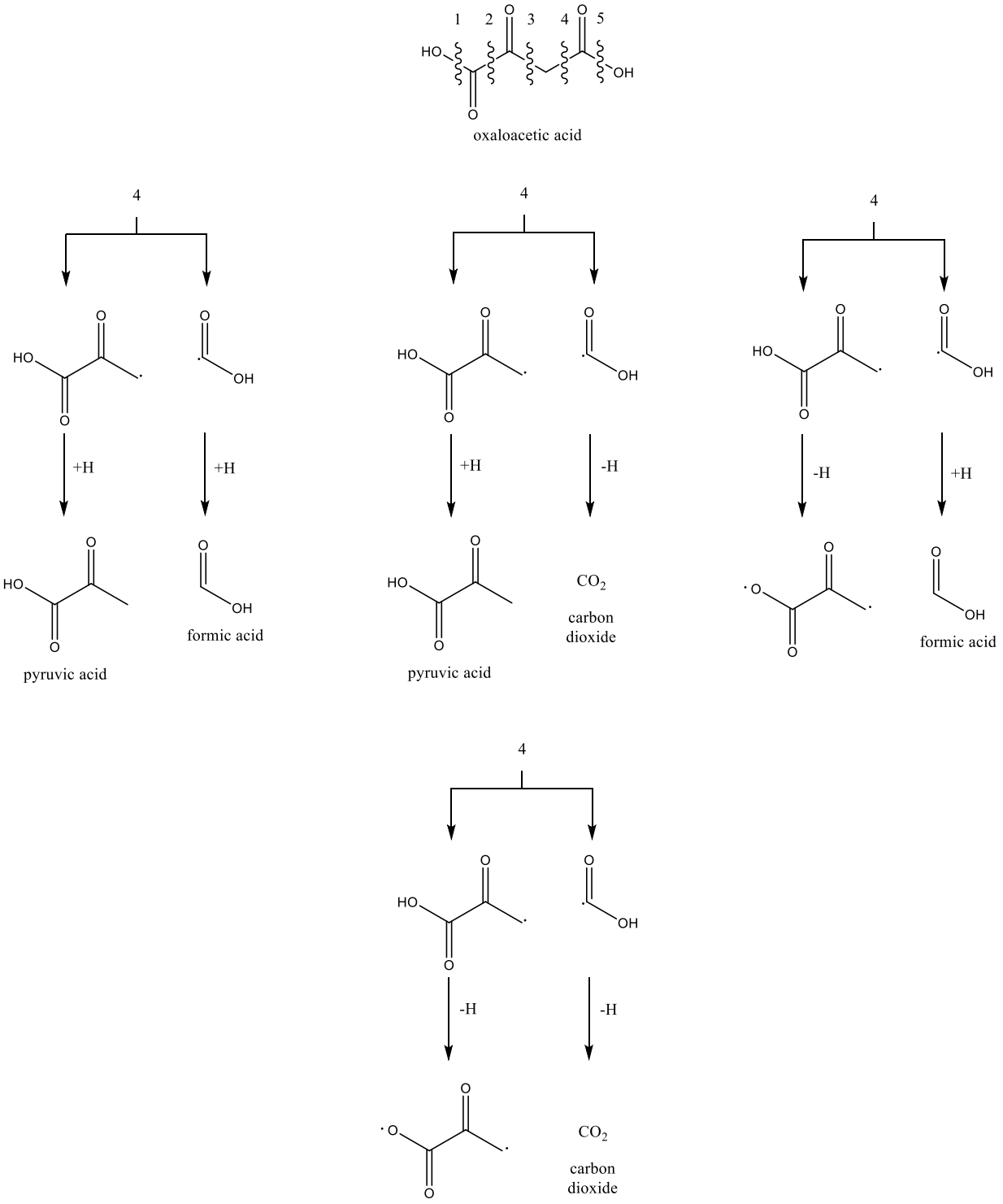

Figure S22D. Retrosynthesis of oxaloacetic acid (**9**) utilizing single-bond cleavage and subsequent hydrogen addition/elimination.

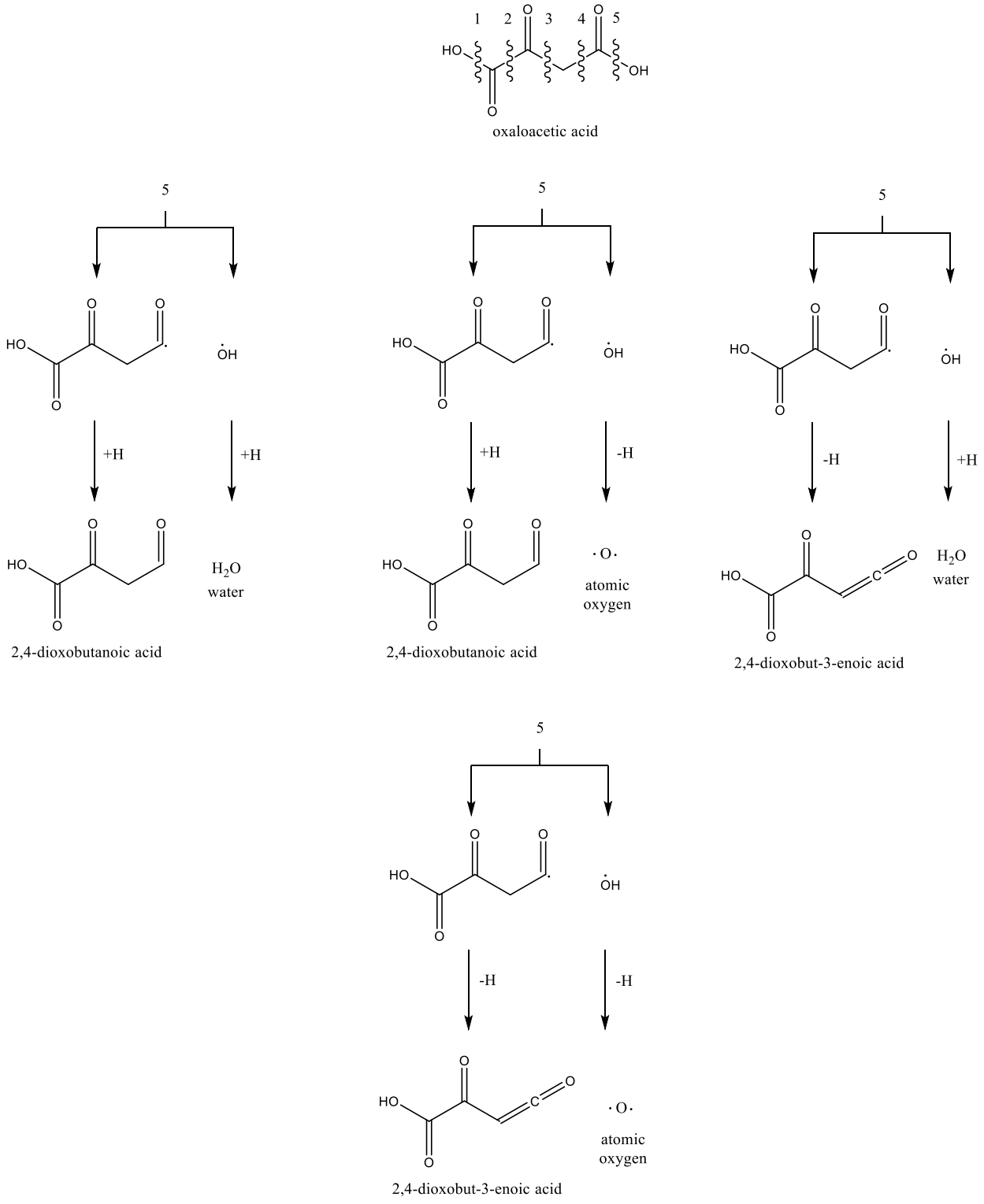

Figure S22E. Retrosynthesis of oxaloacetic acid (**9**) utilizing single-bond cleavage and subsequent hydrogen addition/elimination.

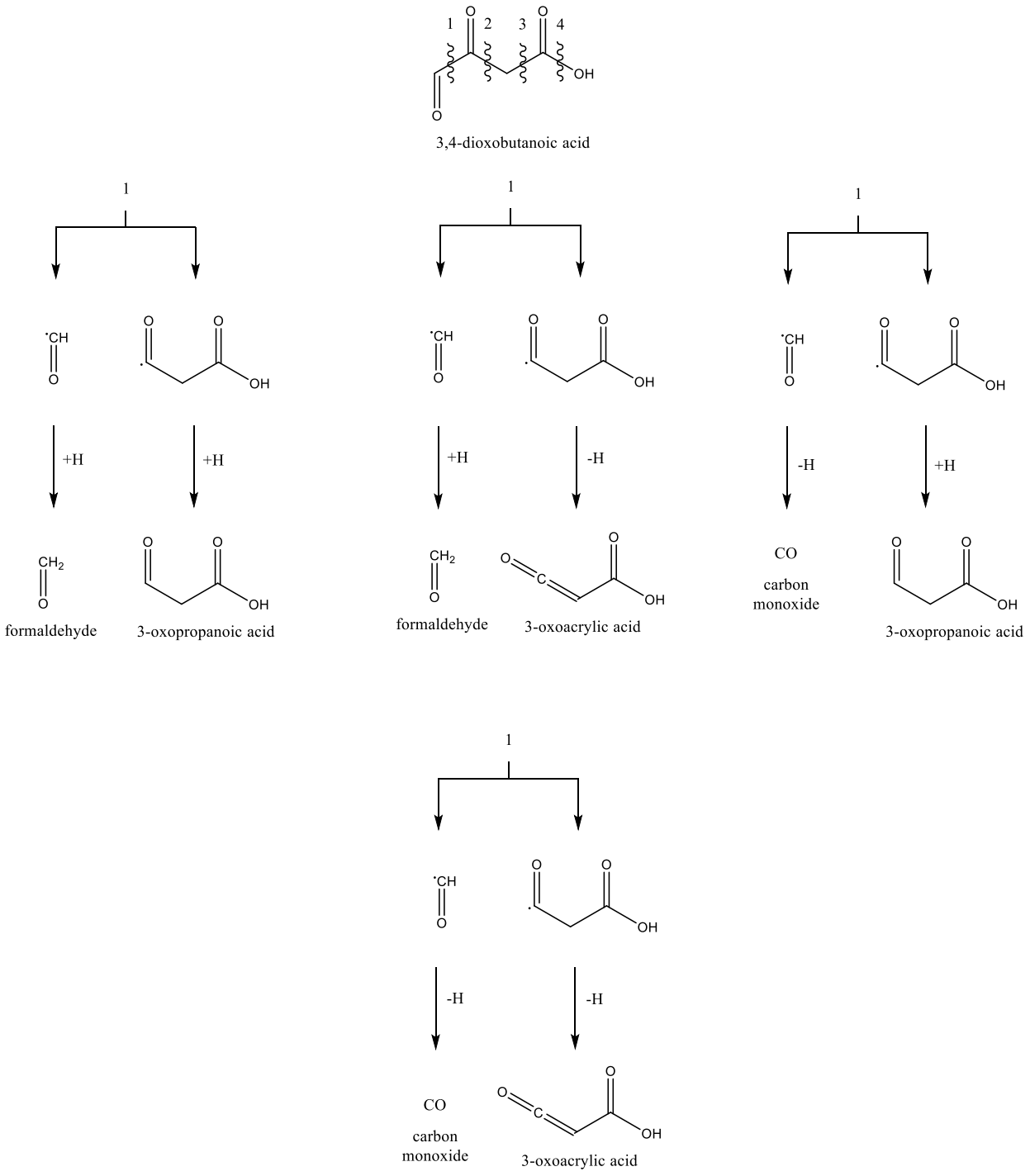

Figure S23A. Retrosynthesis of 3,4-dioxobutanoic acid utilizing single-bond cleavage and subsequent hydrogen addition/elimination.

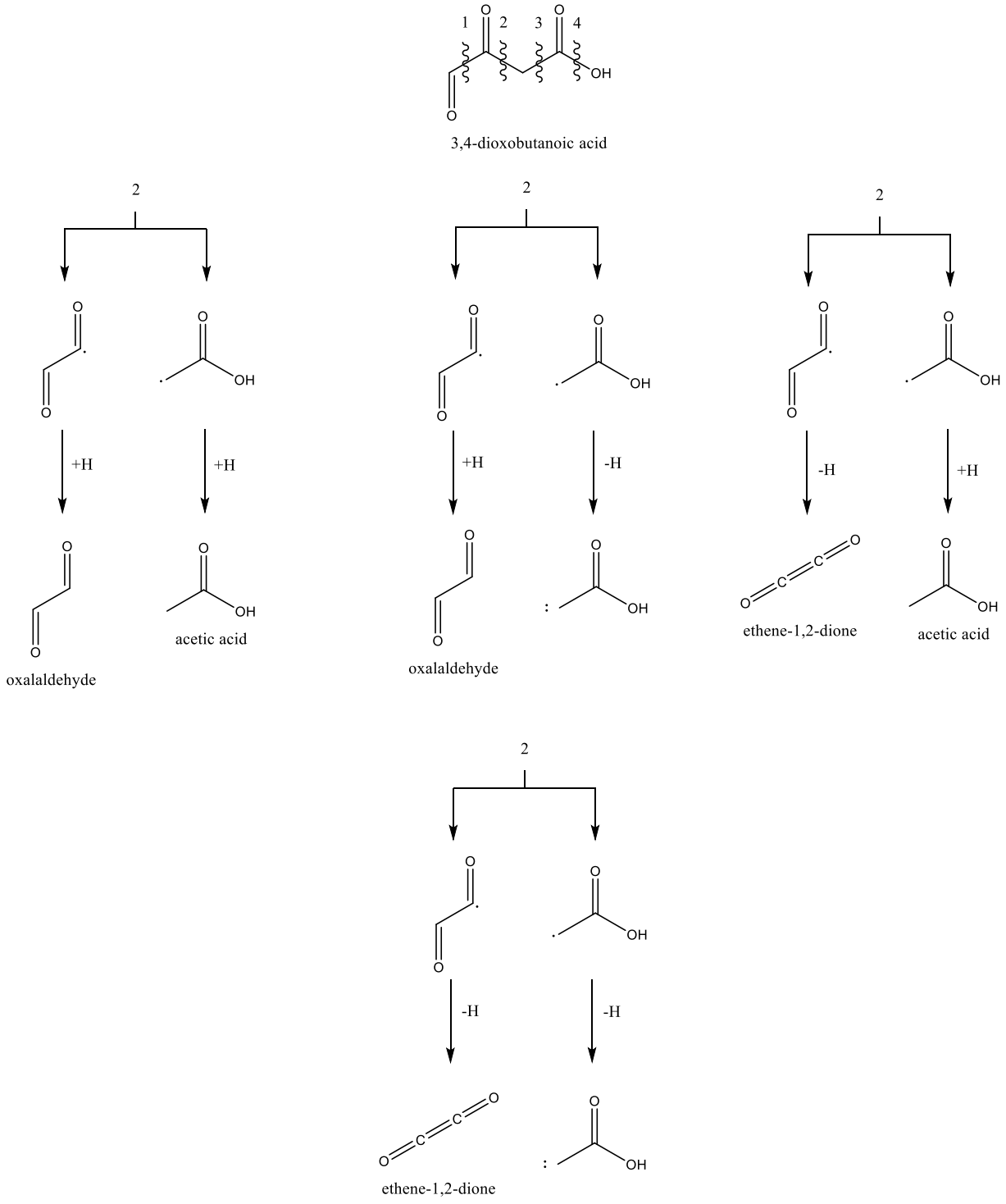

Figure S23B. Retrosynthesis of 3,4-dioxobutanoic acid utilizing single-bond cleavage and subsequent hydrogen addition/elimination.

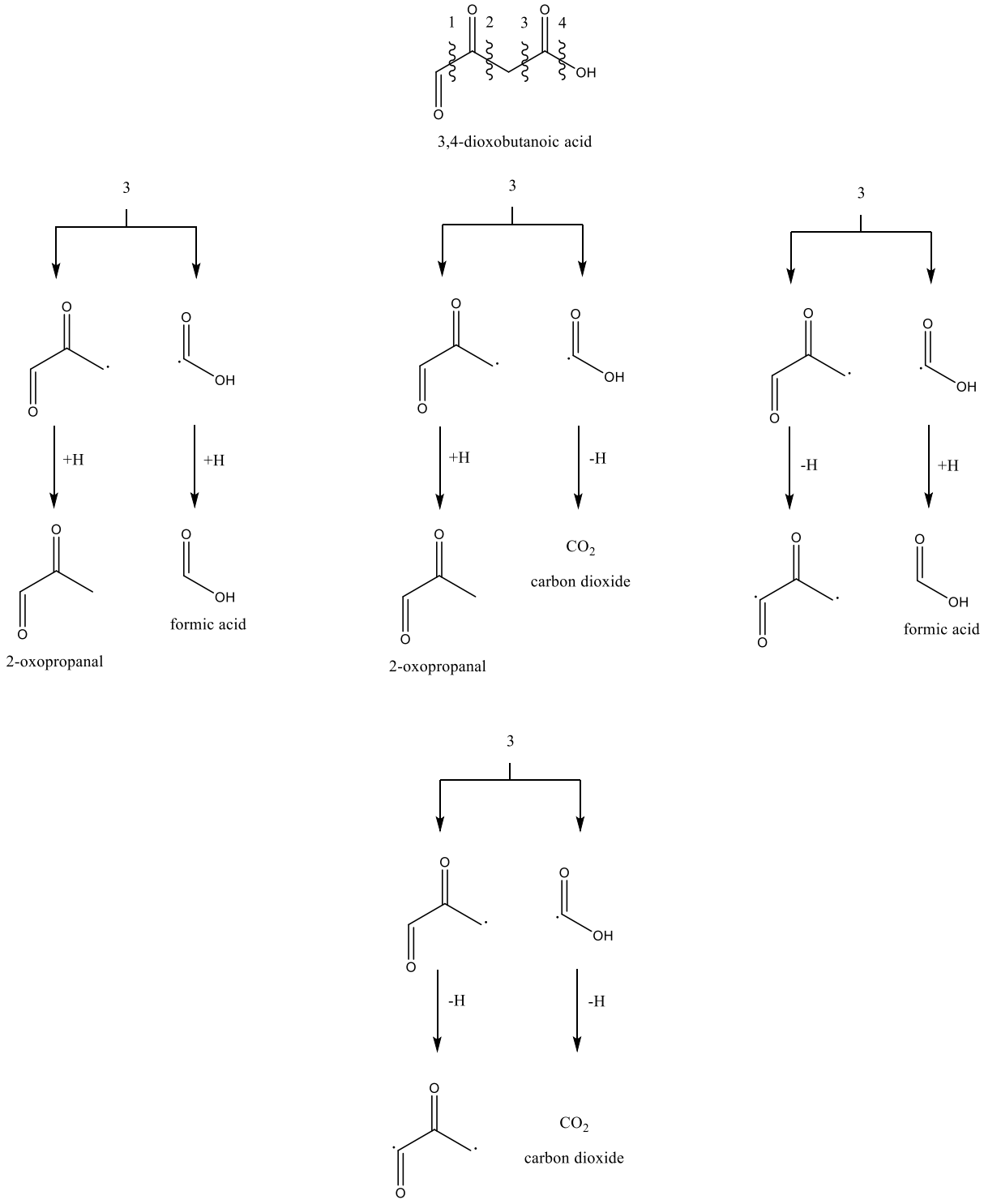

Figure S23C. Retrosynthesis of 3,4-dioxobutanoic acid utilizing single-bond cleavage and subsequent hydrogen addition/elimination.

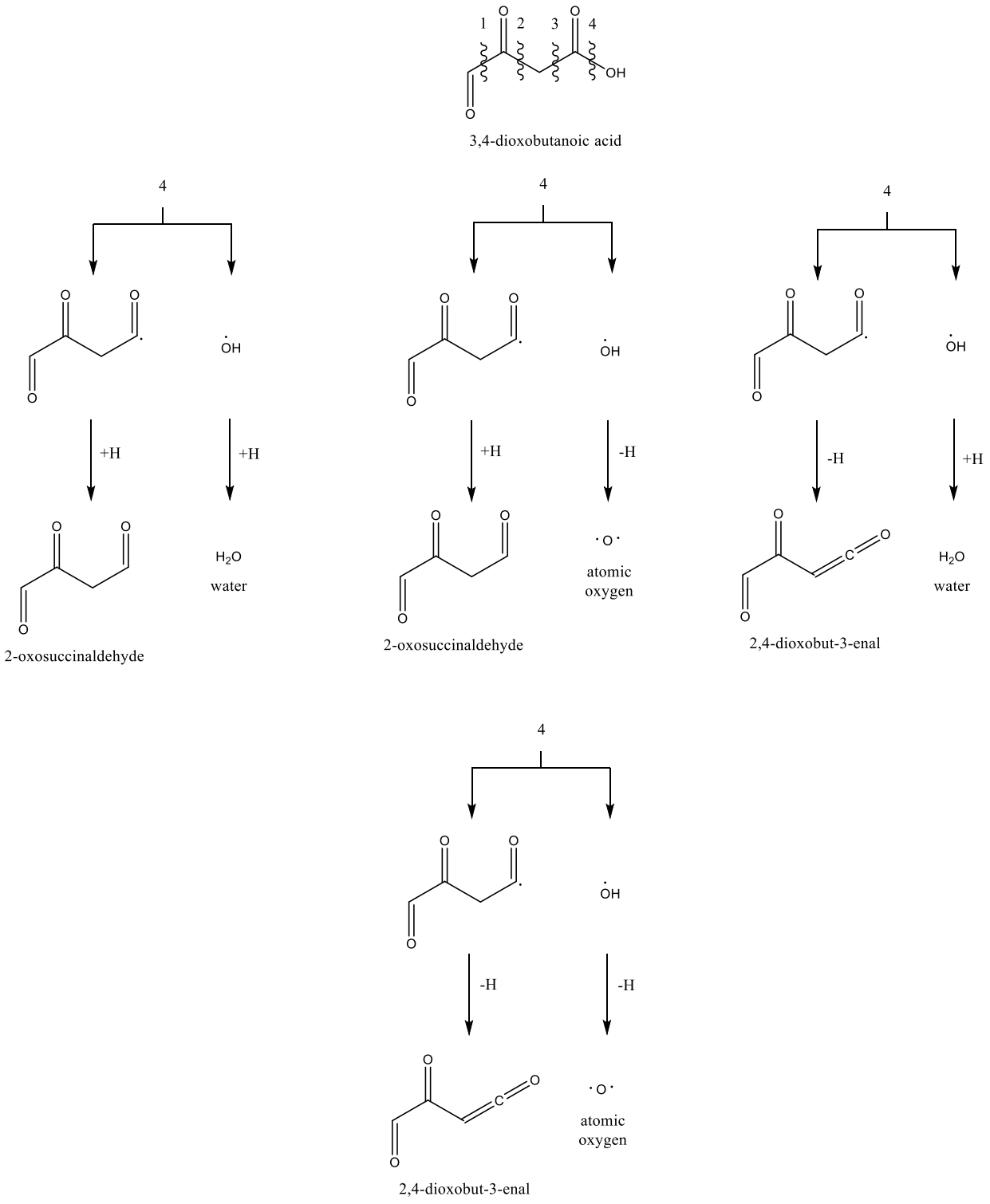

Figure S23D. Retrosynthesis of 3,4-dioxobutanoic acid utilizing single-bond cleavage and subsequent hydrogen addition/elimination.

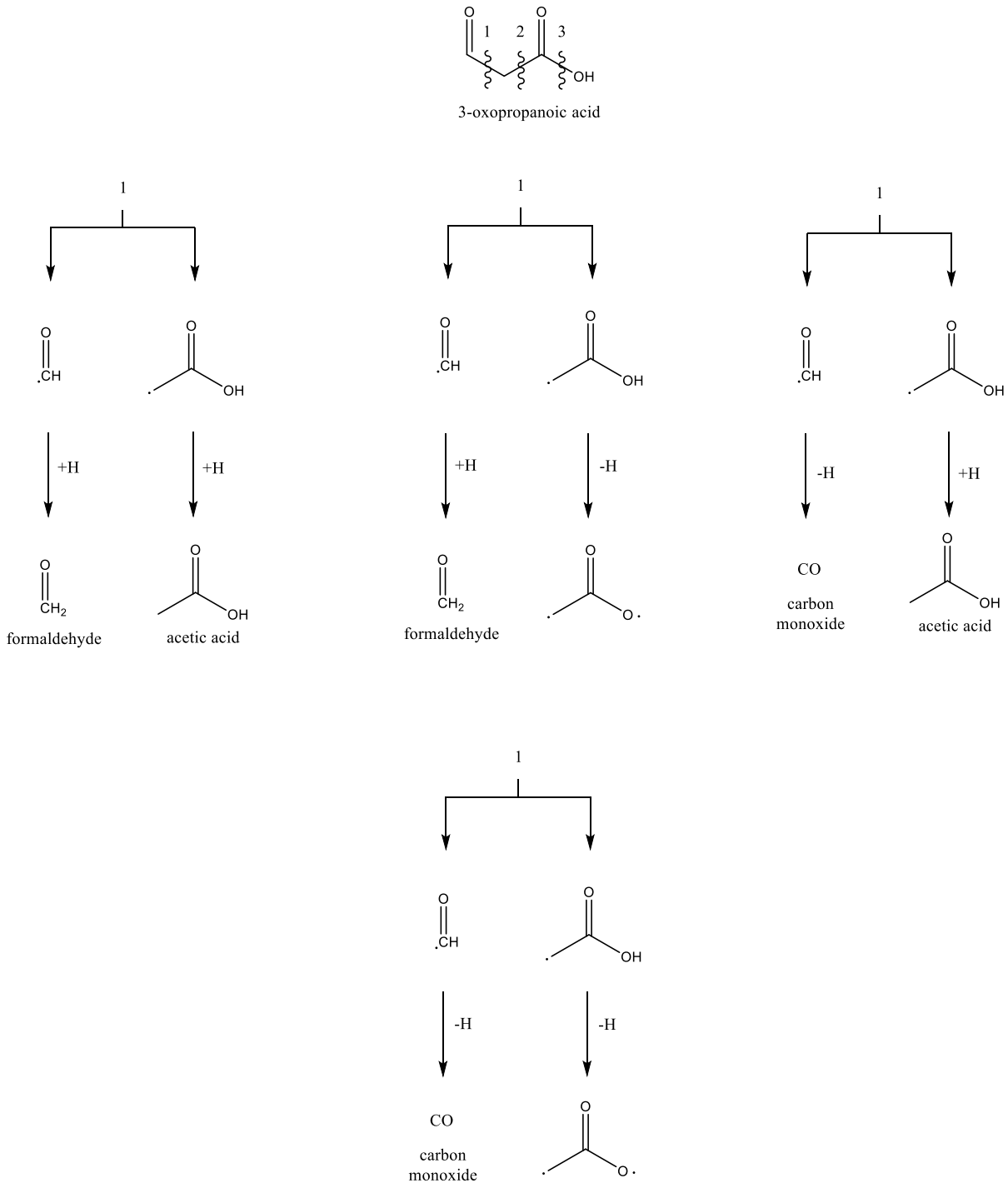

Figure S24A. Retrosynthesis of 3-oxopropanoic acid utilizing single-bond cleavage and subsequent hydrogen addition/elimination.

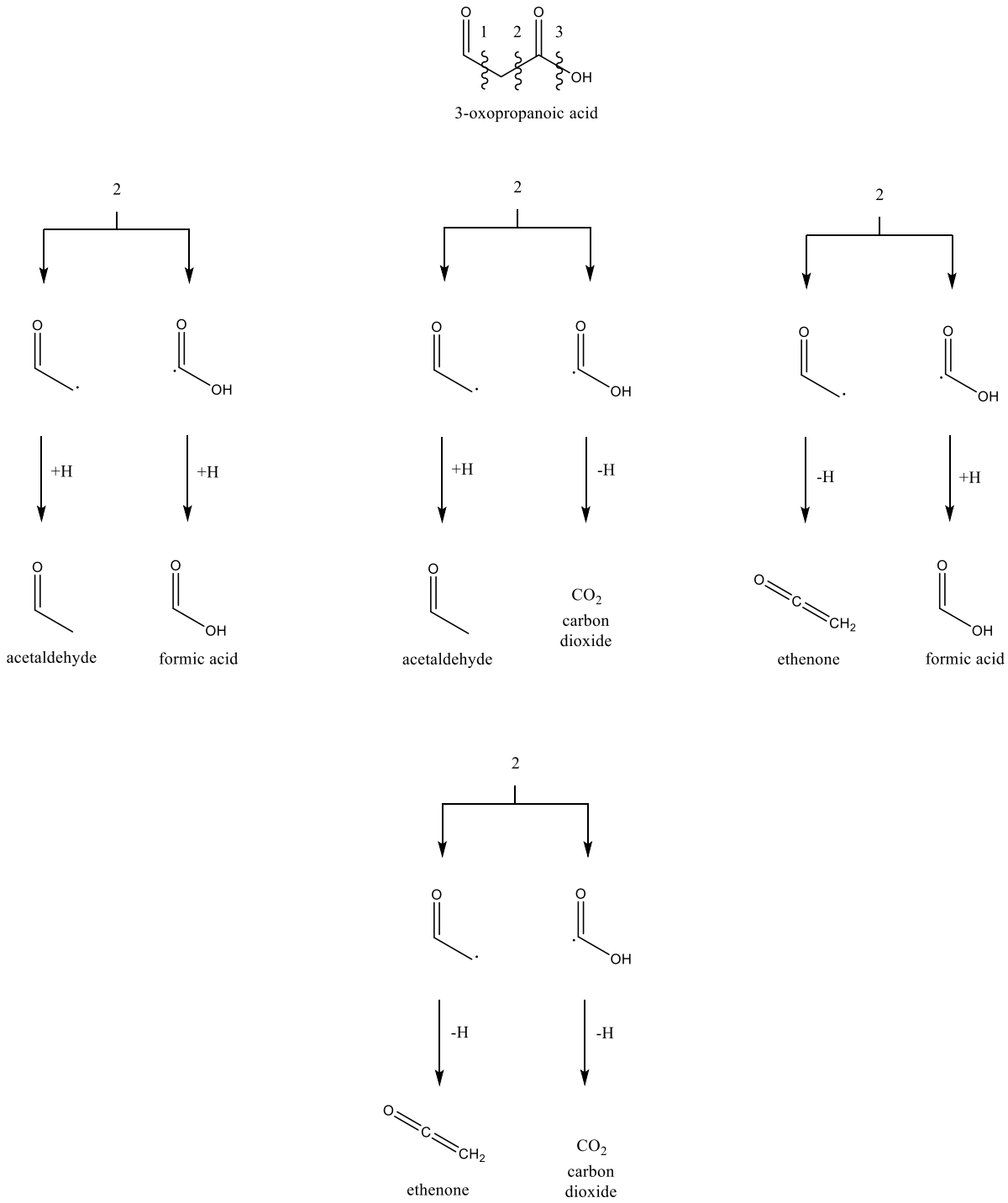

Figure S24B. Retrosynthesis of 3-oxopropanoic acid utilizing single-bond cleavage and subsequent hydrogen addition/elimination.

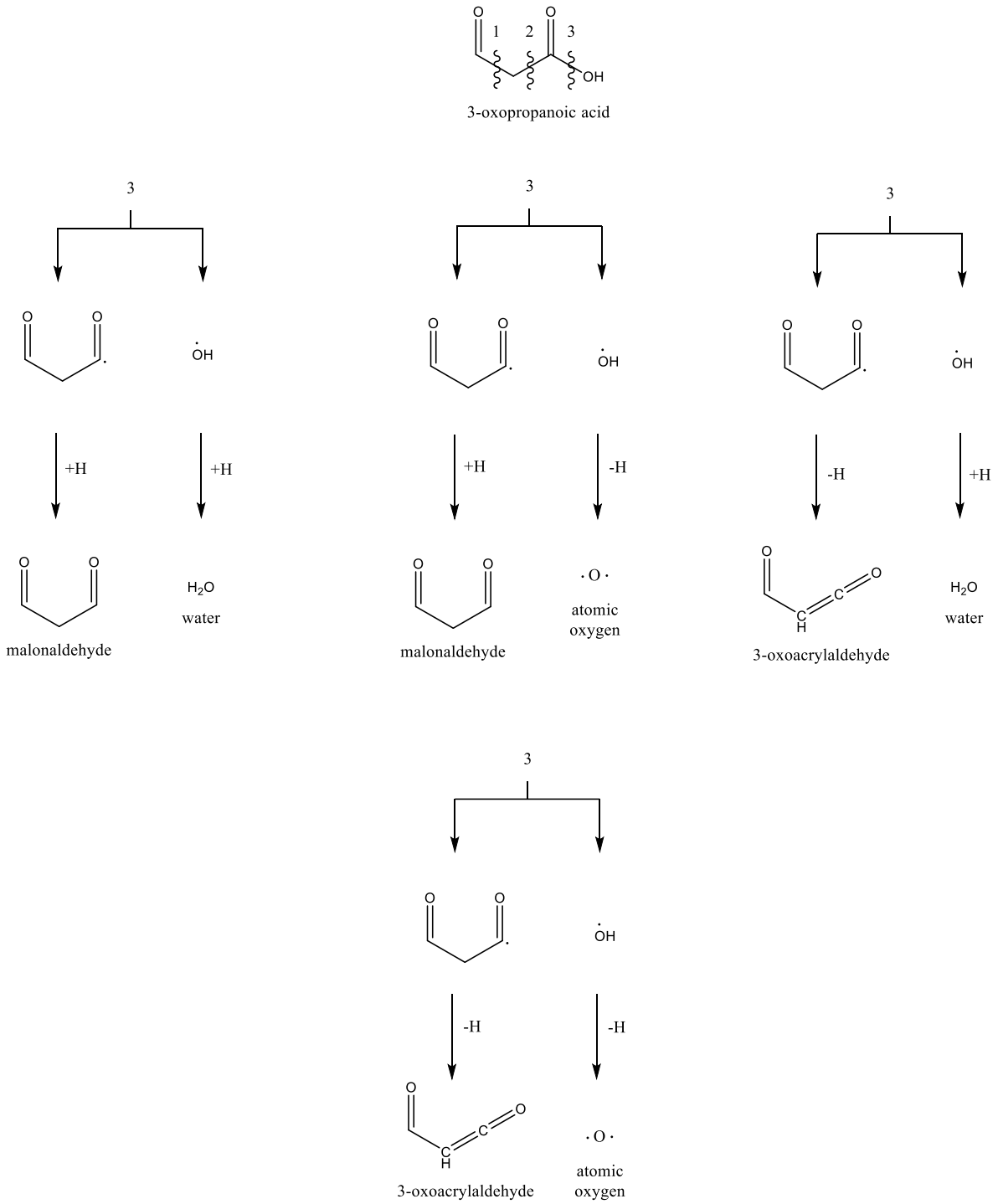

Figure S24C. Retrosynthesis of 3-oxopropanoic acid utilizing single-bond cleavage and subsequent hydrogen addition/elimination.

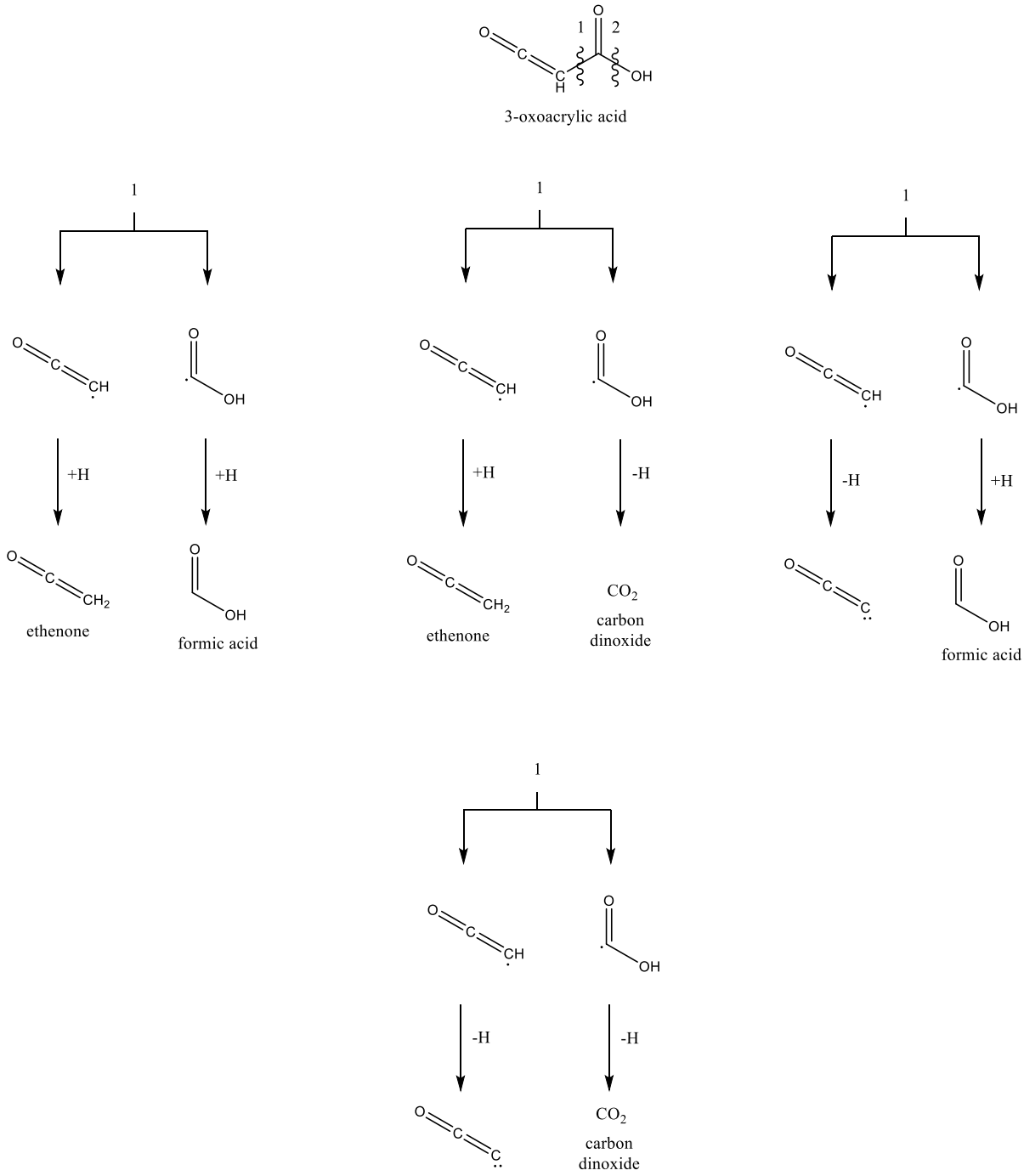

Figure S25A. Retrosynthesis of 3-oxoacrylic acid utilizing single-bond cleavage and subsequent hydrogen addition/elimination.

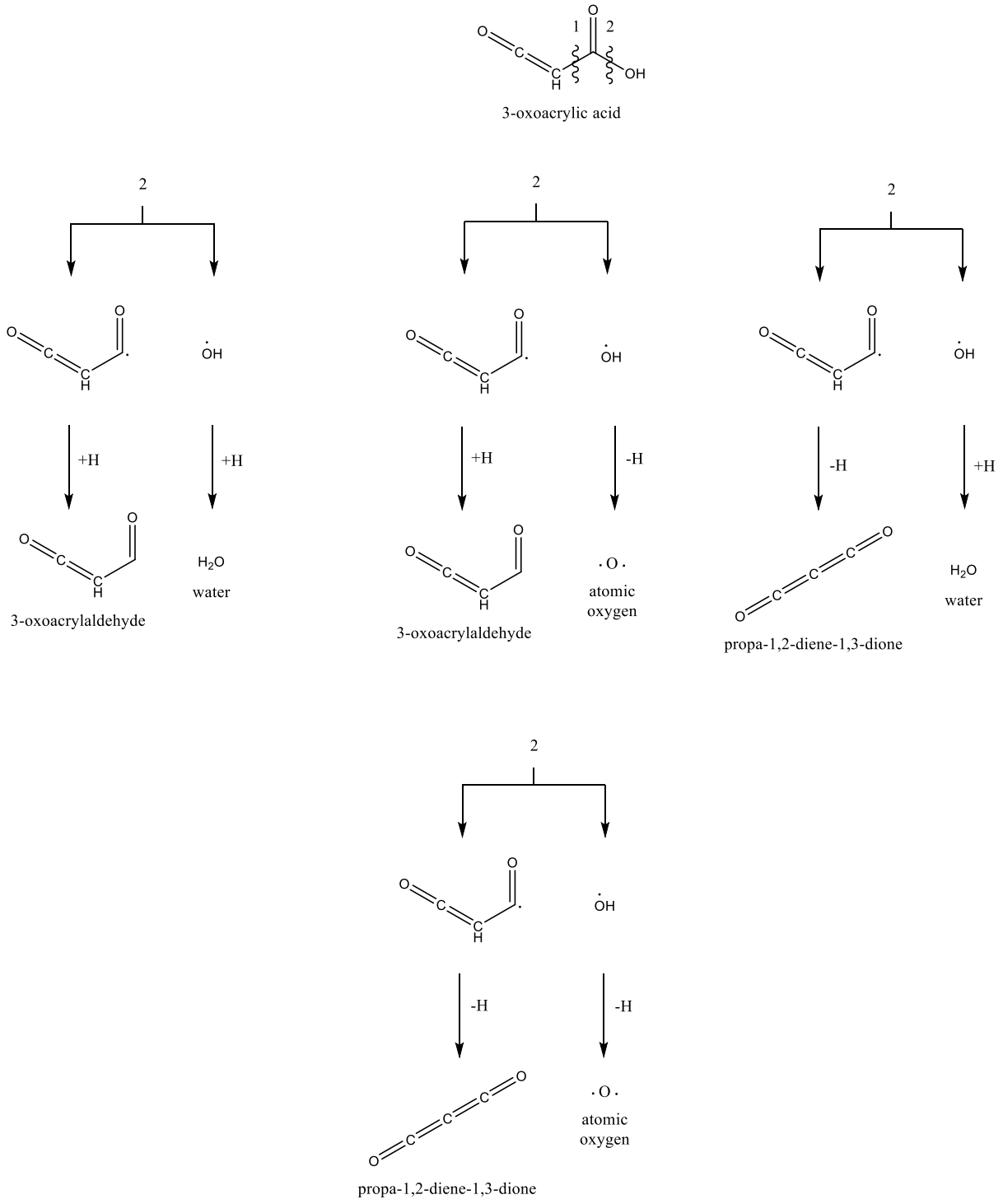

Figure S25B. Retrosynthesis of 3-oxoacrylic acid utilizing single-bond cleavage and subsequent hydrogen addition/elimination.

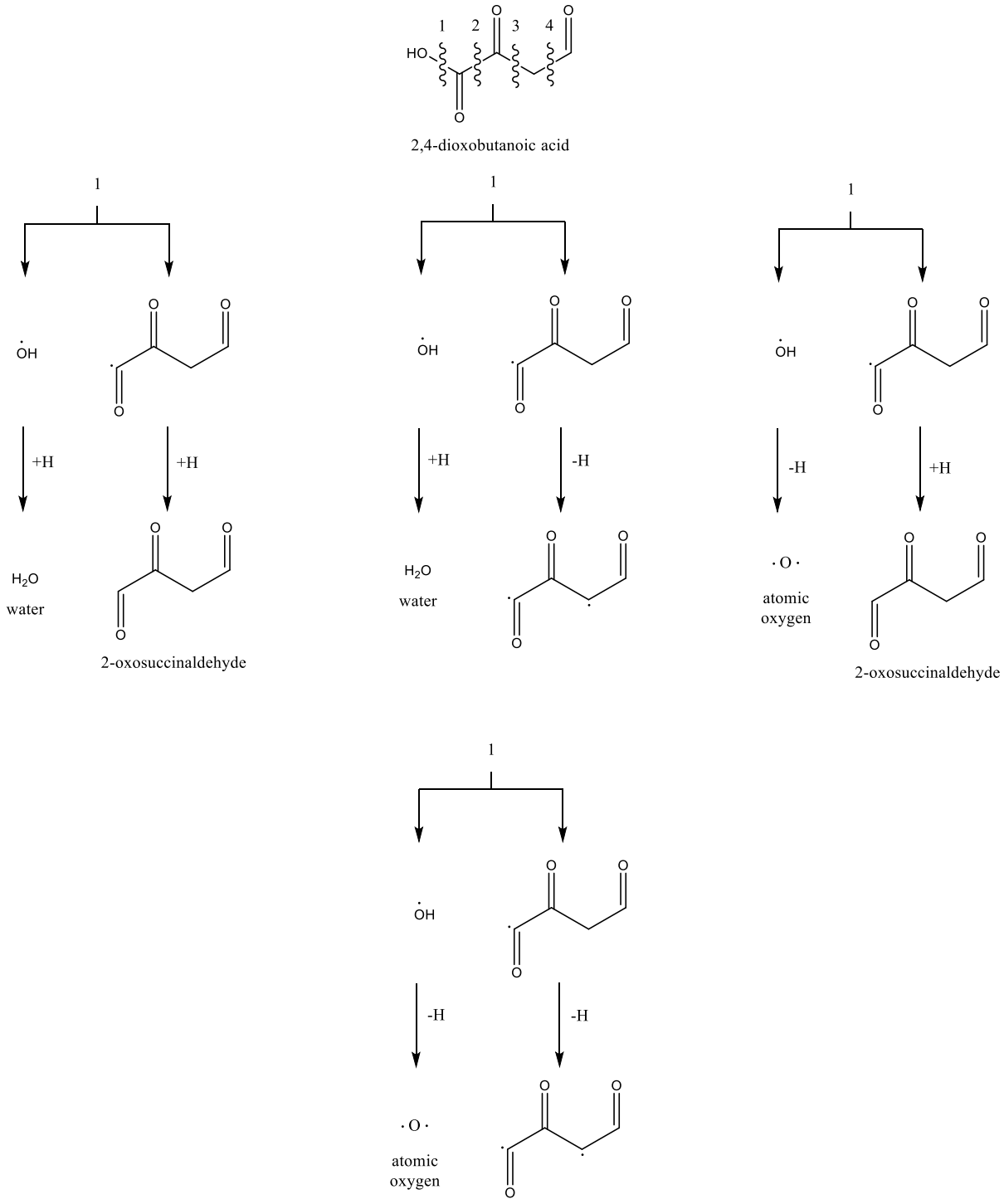

Figure S26A. Retrosynthesis of 2,4-dioxobutanoic acid utilizing single-bond cleavage and subsequent hydrogen addition/elimination.

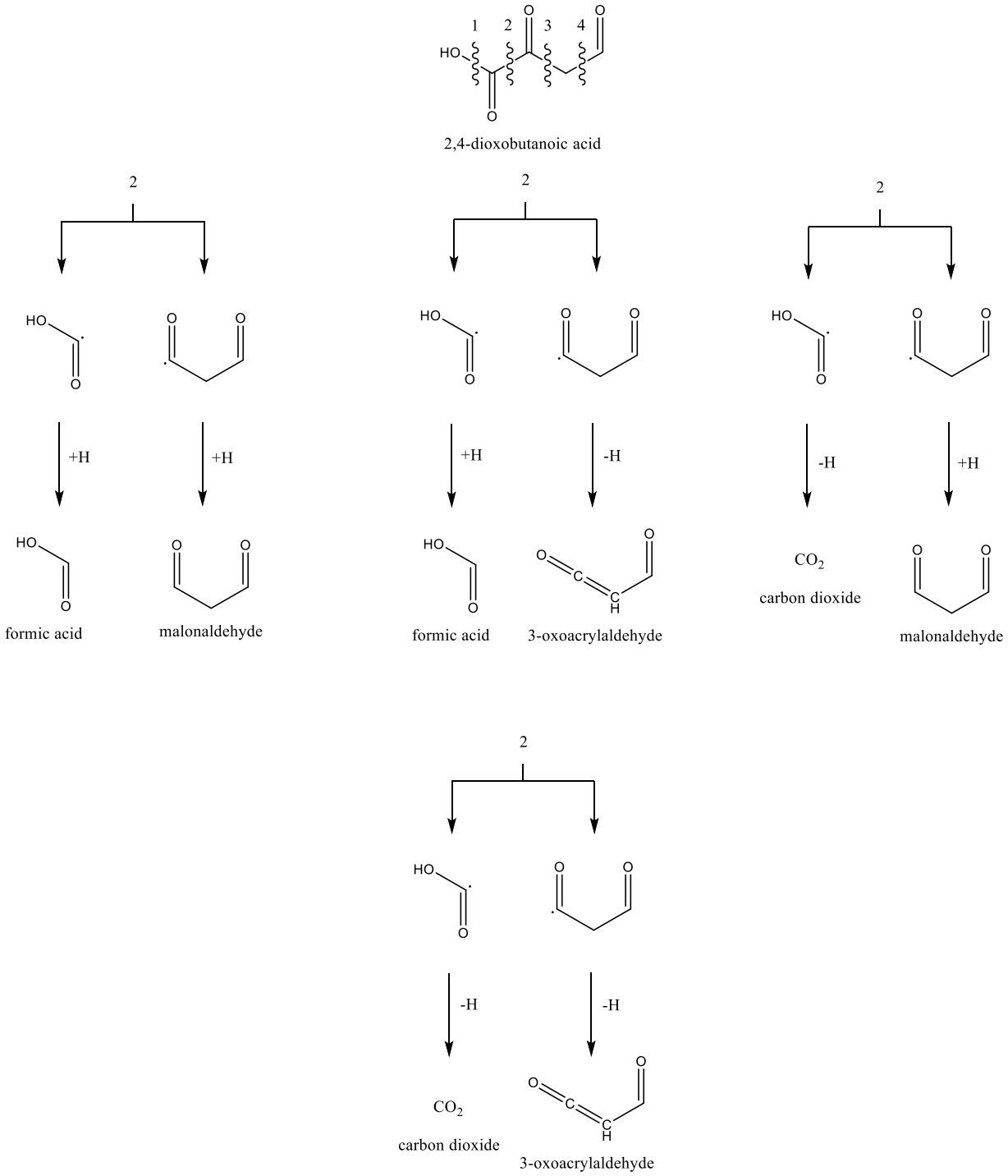

Figure S26B. Retrosynthesis of 2,4-dioxobutanoic acid utilizing single-bond cleavage and subsequent hydrogen addition/elimination.

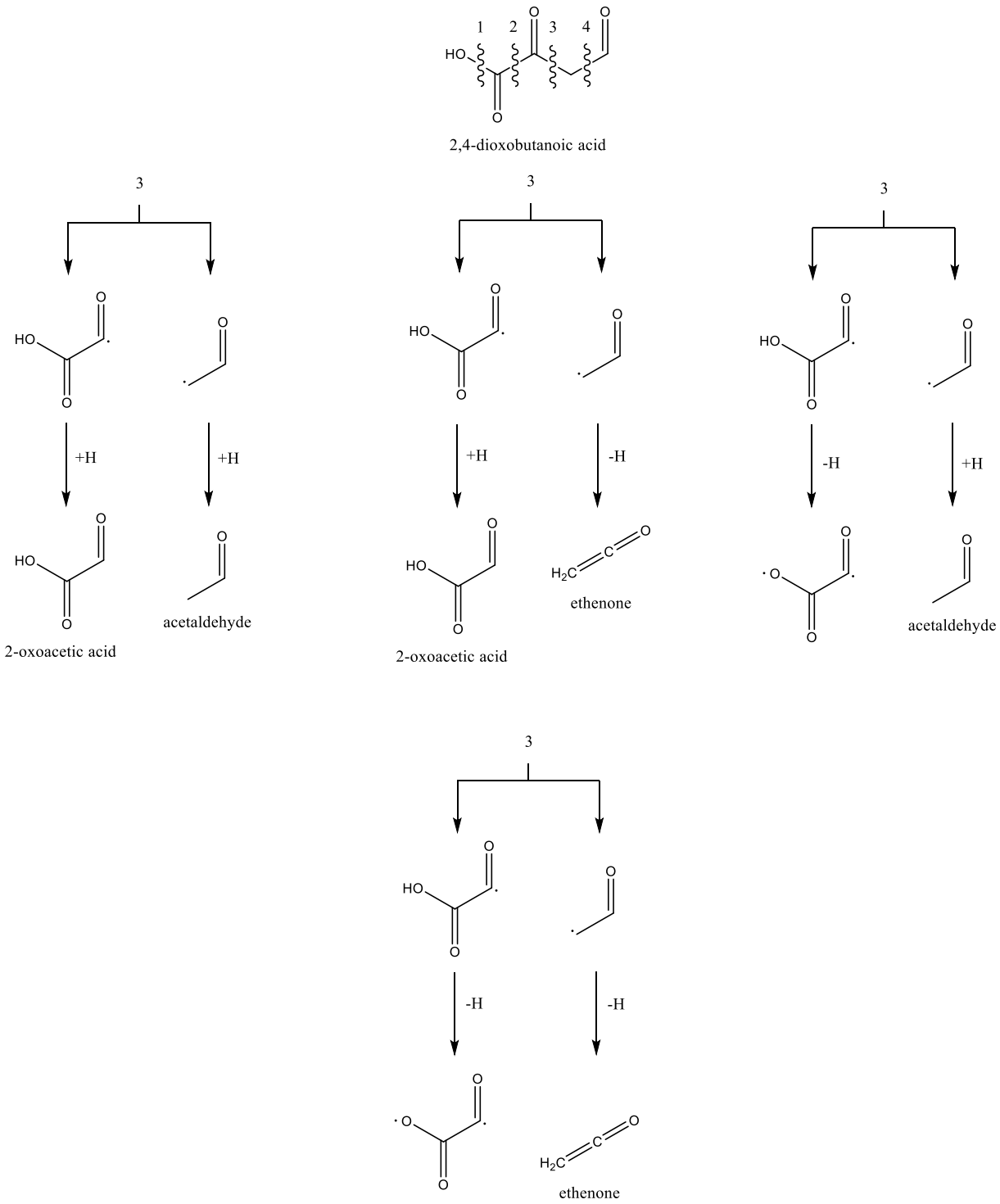

Figure S26C. Retrosynthesis of 2,4-dioxobutanoic acid utilizing single-bond cleavage and subsequent hydrogen addition/elimination.

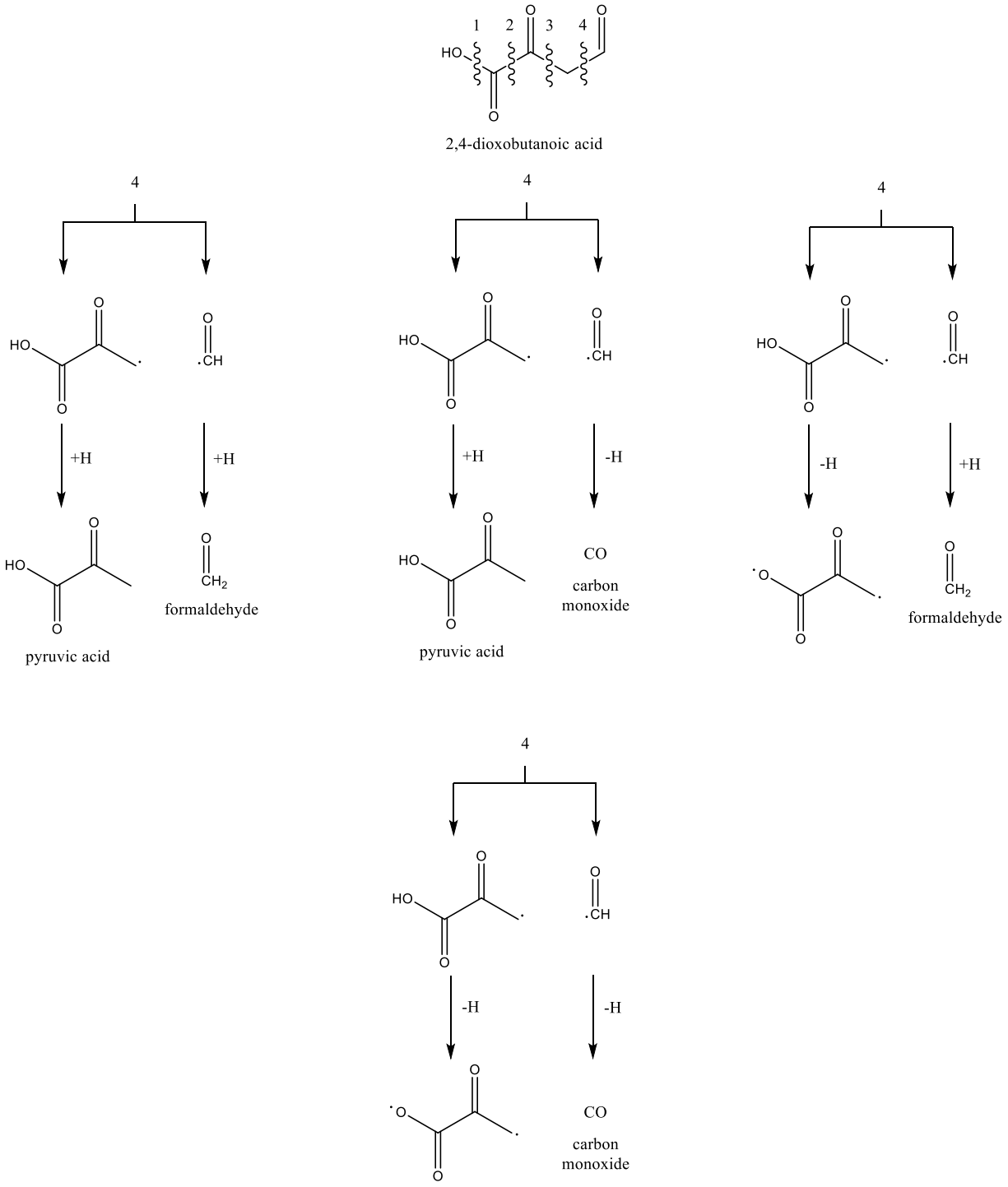

Figure S26D. Retrosynthesis of 2,4-dioxobutanoic acid utilizing single-bond cleavage and subsequent hydrogen addition/elimination.

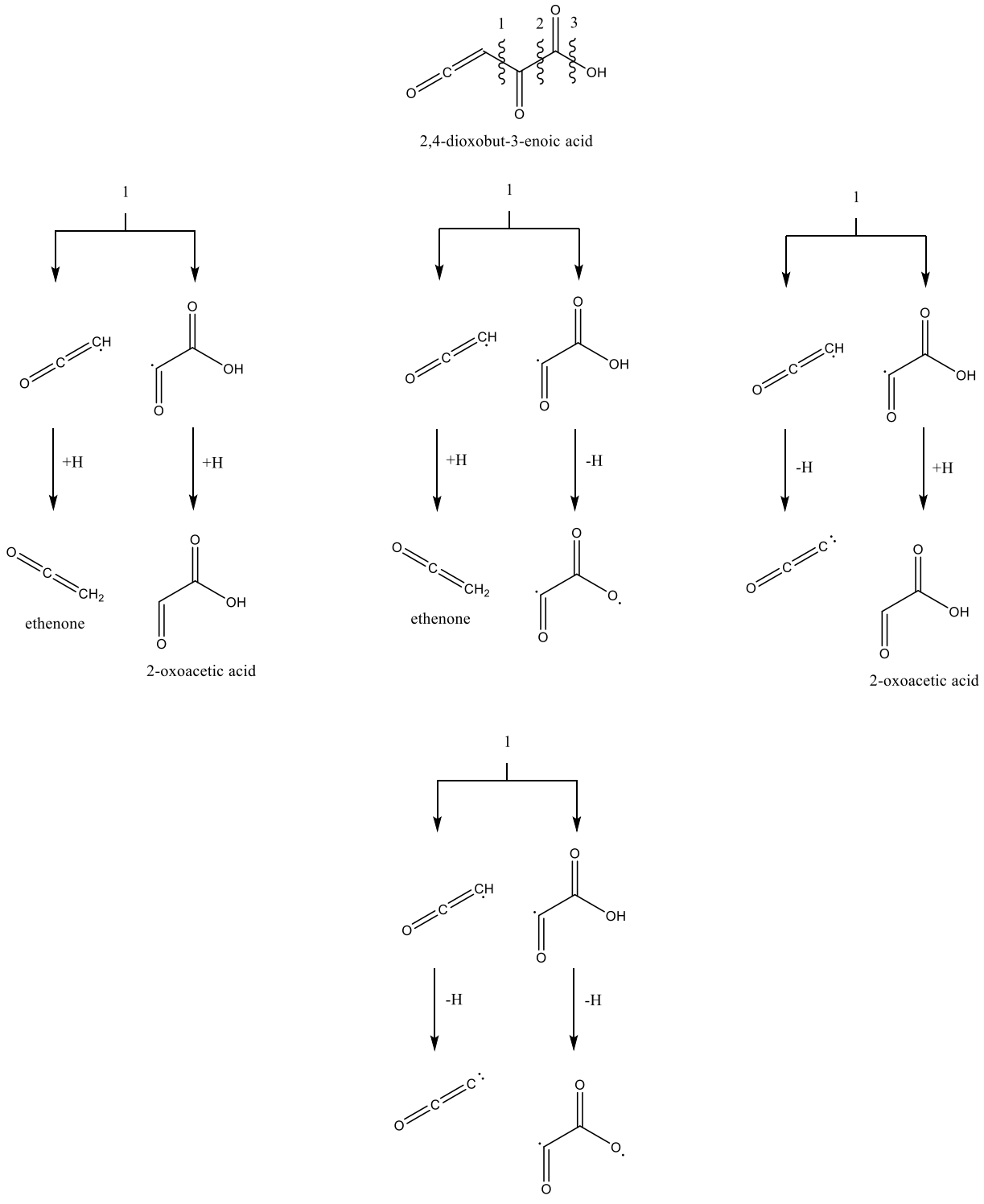

Figure S27A. Retrosynthesis of 2,4-dioxobut-3-enoic acid utilizing single-bond cleavage and subsequent hydrogen addition/elimination.

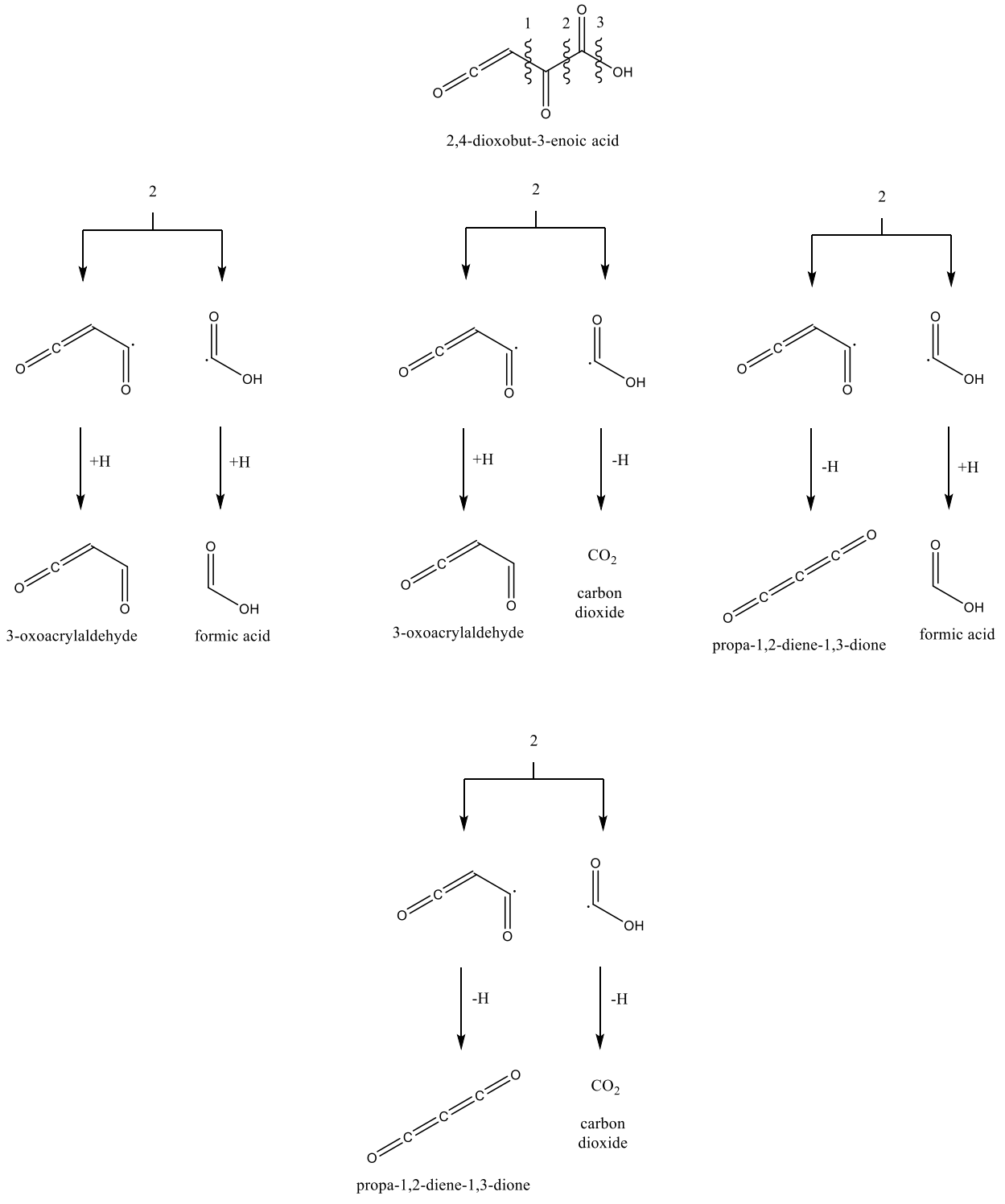

Figure S27B. Retrosynthesis of 2,4-dioxobut-3-enoic acid utilizing single-bond cleavage and subsequent hydrogen addition/elimination.

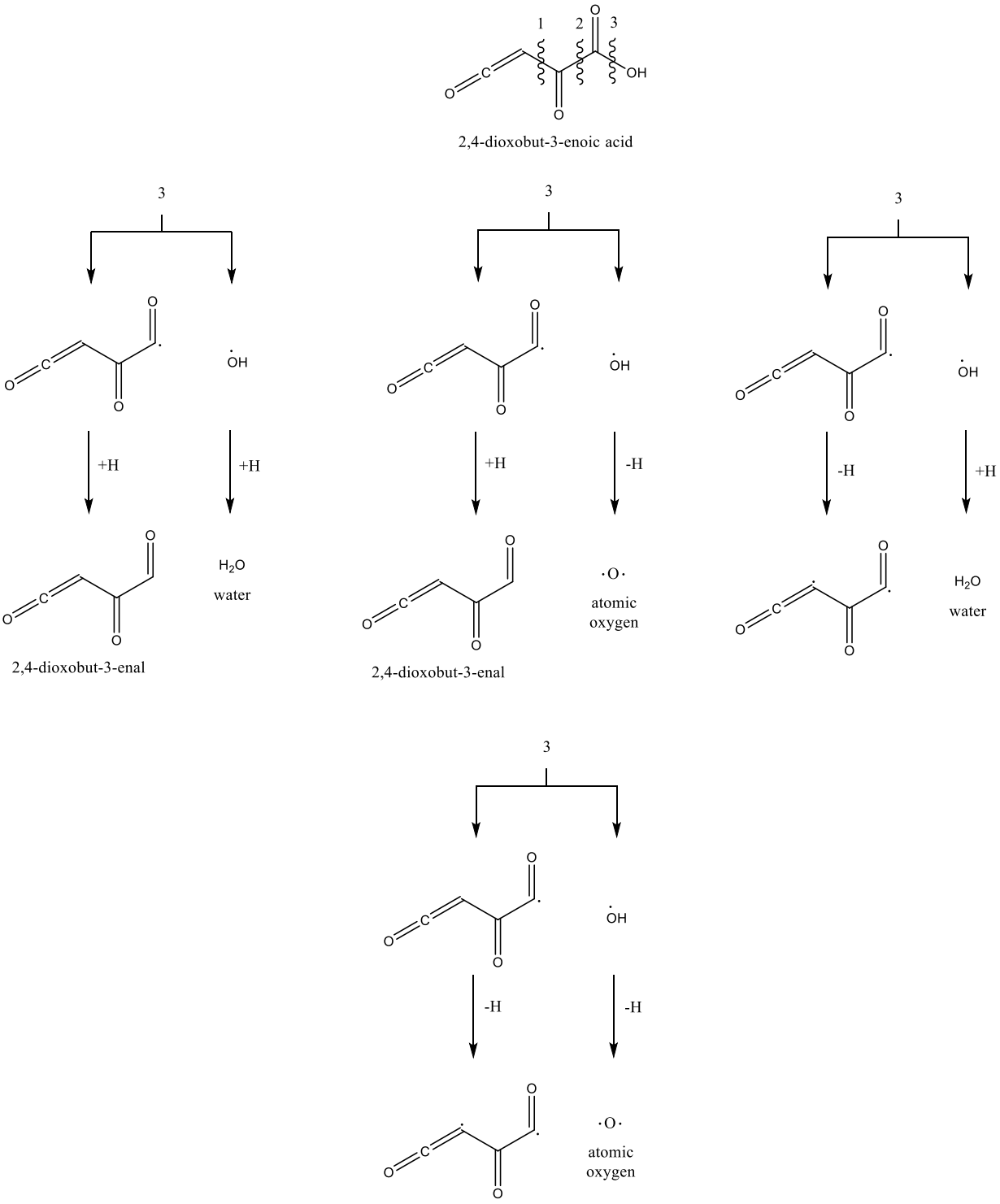

Figure S27C. Retrosynthesis of 2,4-dioxobut-3-enoic acid utilizing single-bond cleavage and subsequent hydrogen addition/elimination.

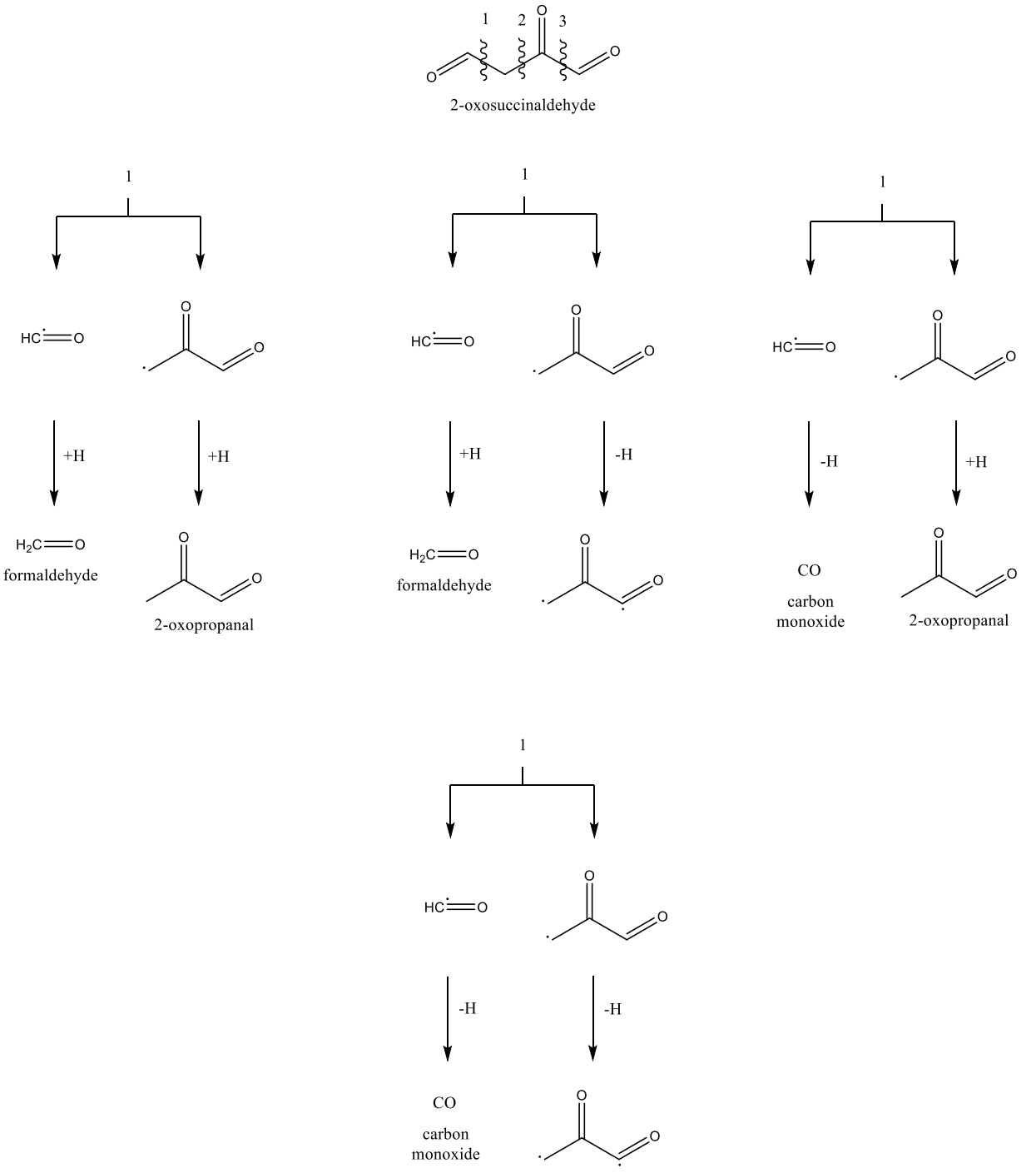

Figure S28A. Retrosynthesis of 2-oxosuccinaldehyde utilizing single-bond cleavage and subsequent hydrogen addition/elimination.

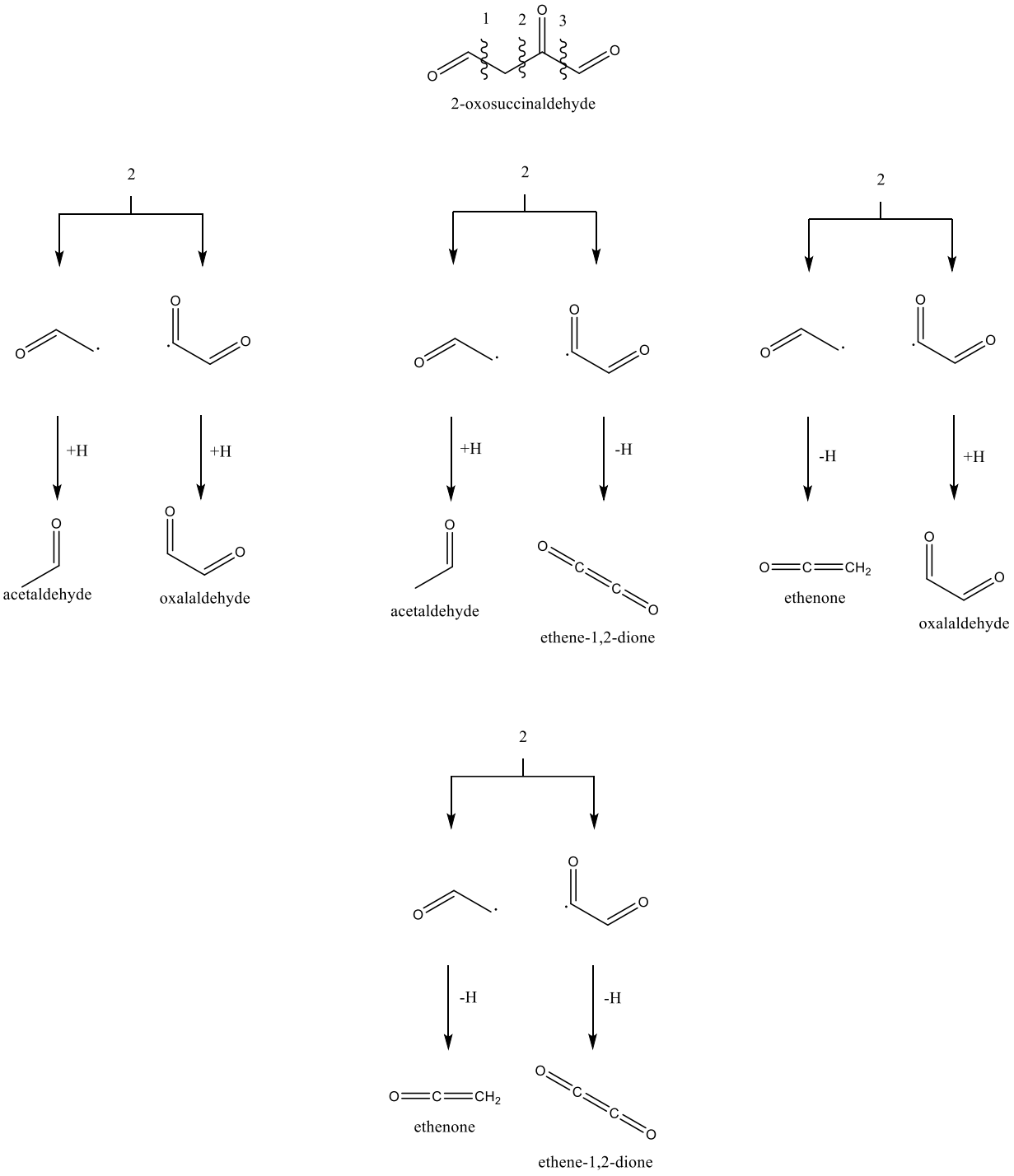

Figure S28B. Retrosynthesis of 2-oxosuccinaldehyde utilizing single-bond cleavage and subsequent hydrogen addition/elimination.

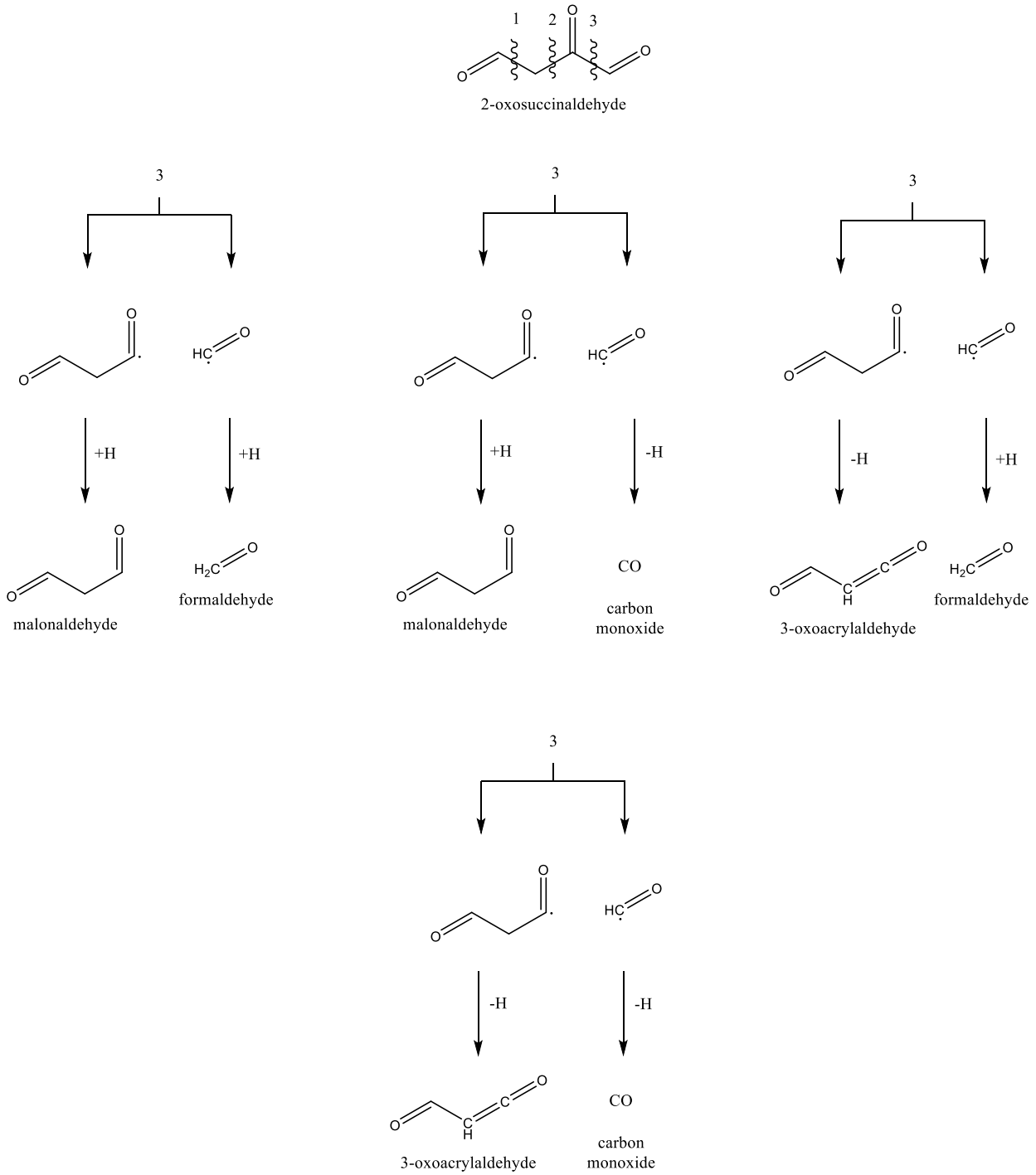

Figure S28C. Retrosynthesis of 2-oxosuccinaldehyde utilizing single-bond cleavage and subsequent hydrogen addition/elimination.

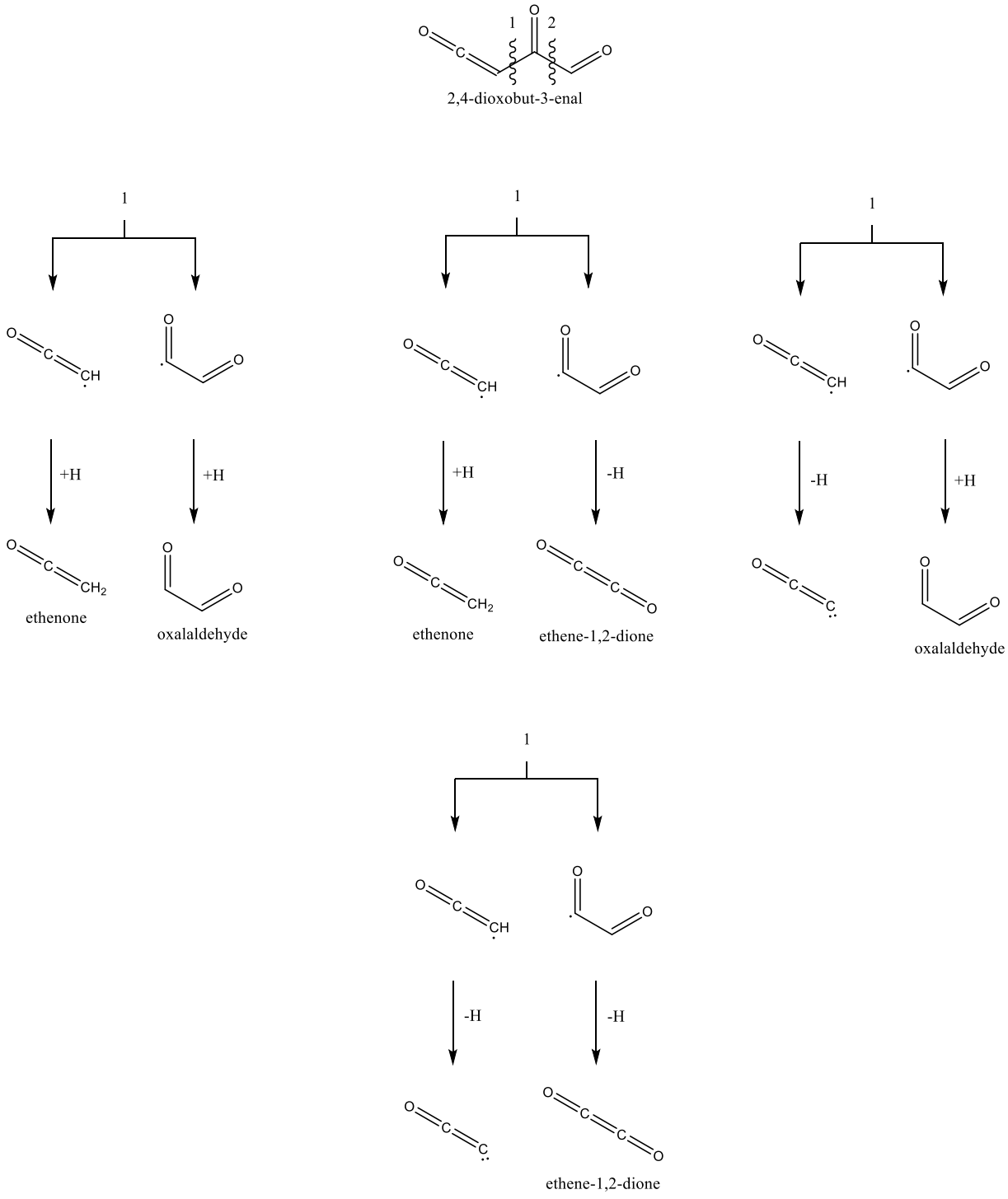

Figure S29A. Retrosynthesis of 2,4-dioxobut-3-enal utilizing single-bond cleavage and subsequent hydrogen addition/elimination.

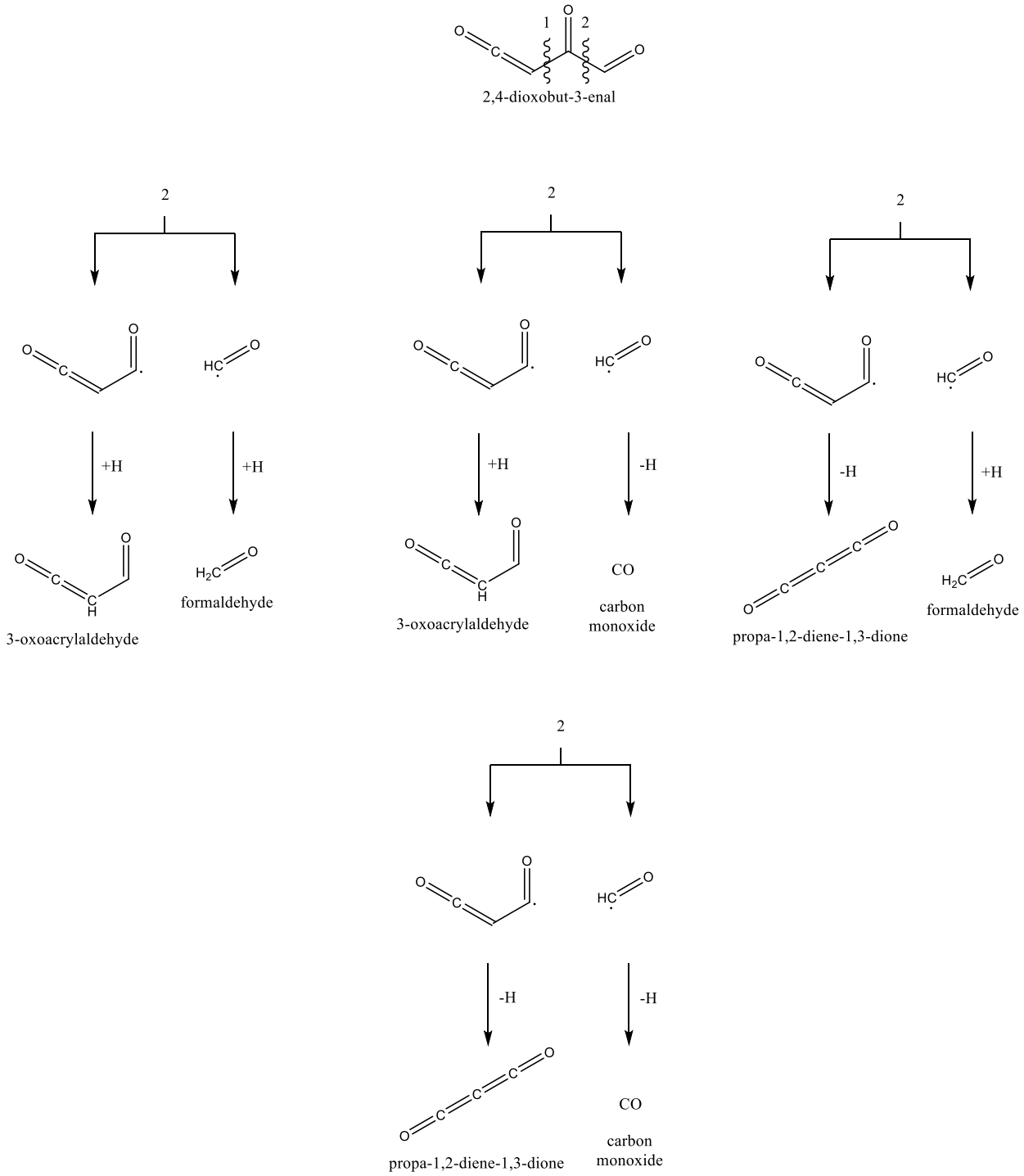

Figure S29A. Retrosynthesis of 2,4-dioxobut-3-enal utilizing single-bond cleavage and subsequent hydrogen addition/elimination.

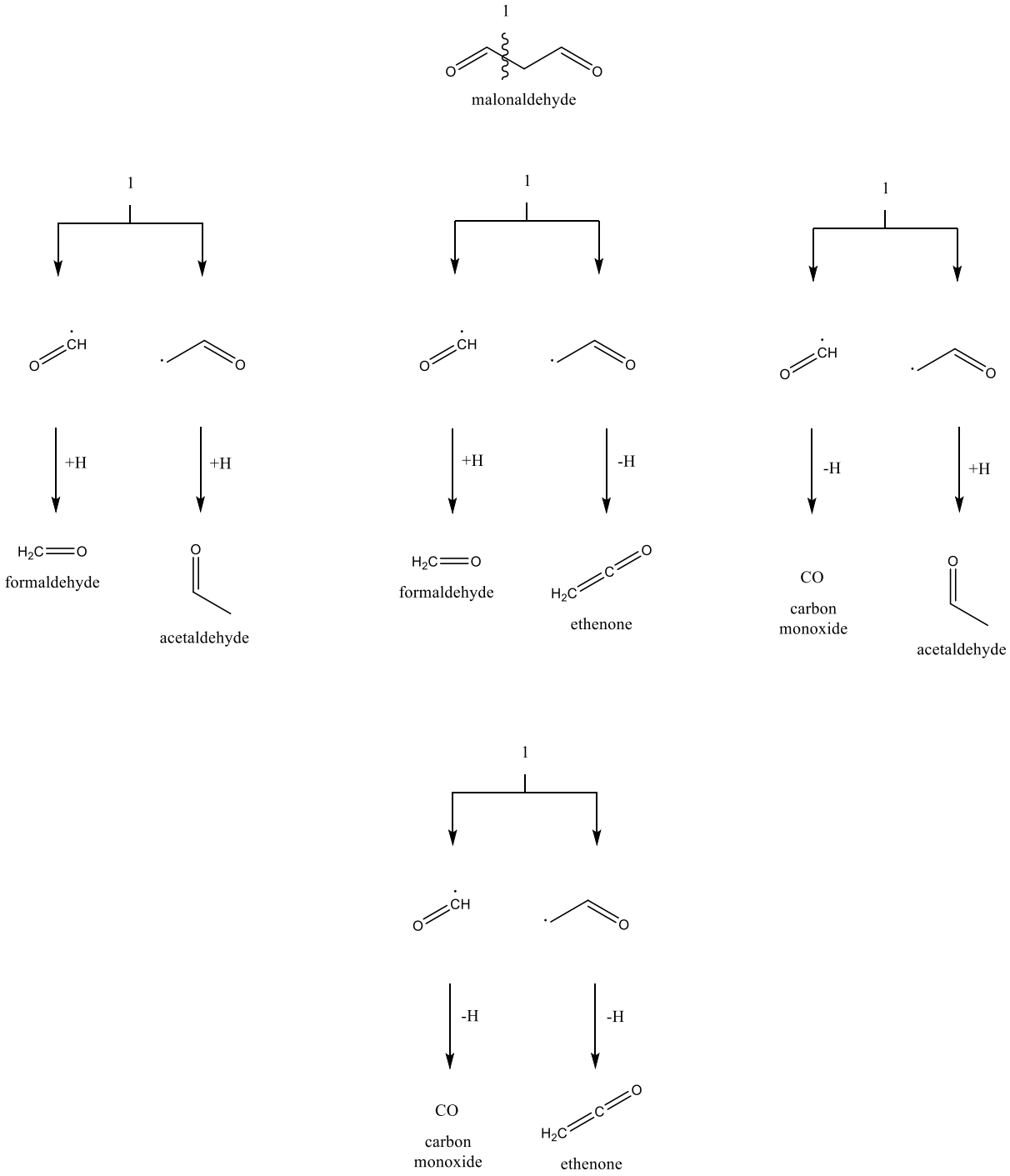

Figure S30. Retrosynthesis of malonaldehyde utilizing single-bond cleavage and subsequent hydrogen addition/elimination.

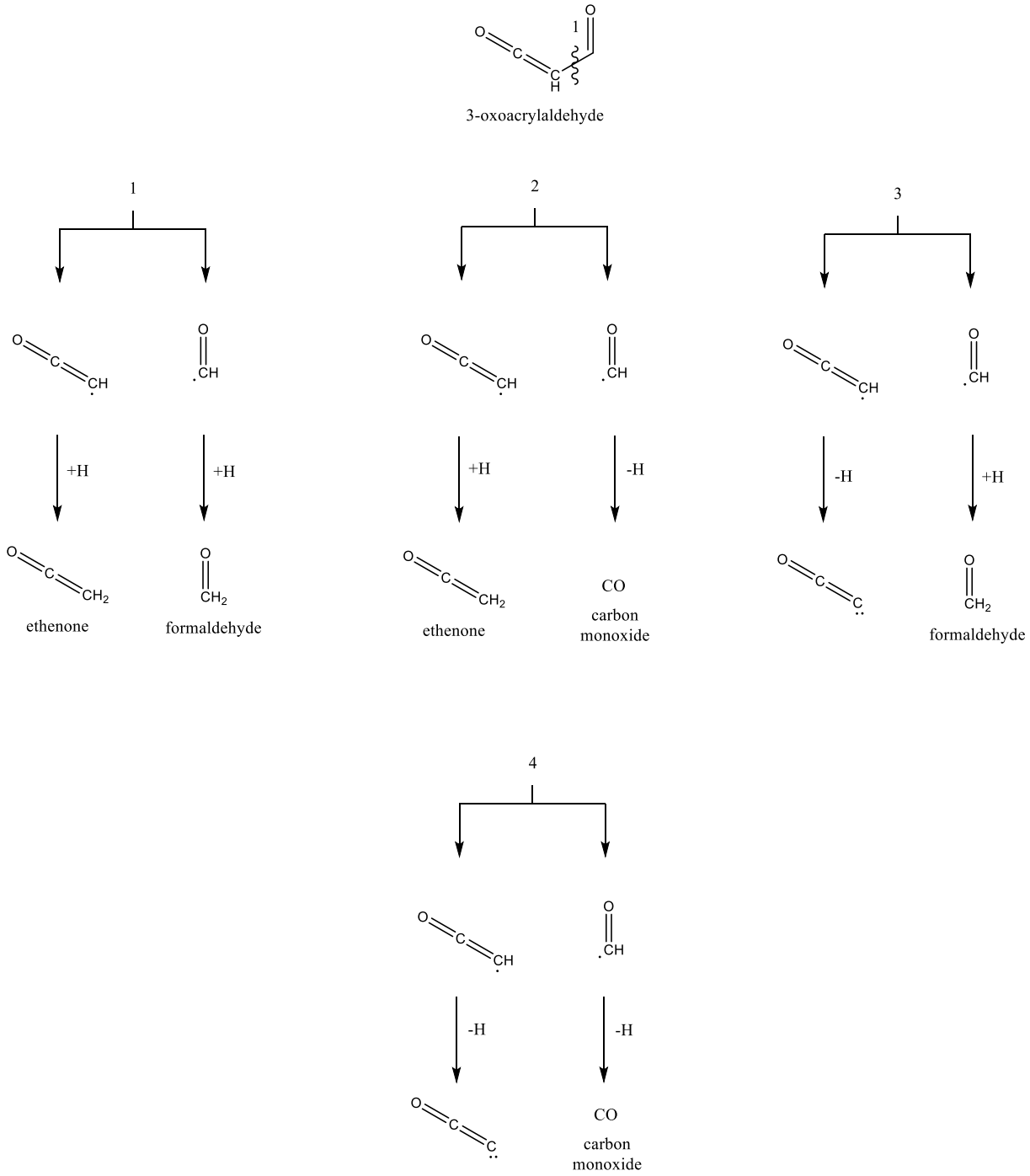

Figure S31. Retrosynthesis of 3-oxoacrylaldehyde utilizing single-bond cleavage and subsequent hydrogen addition/elimination.

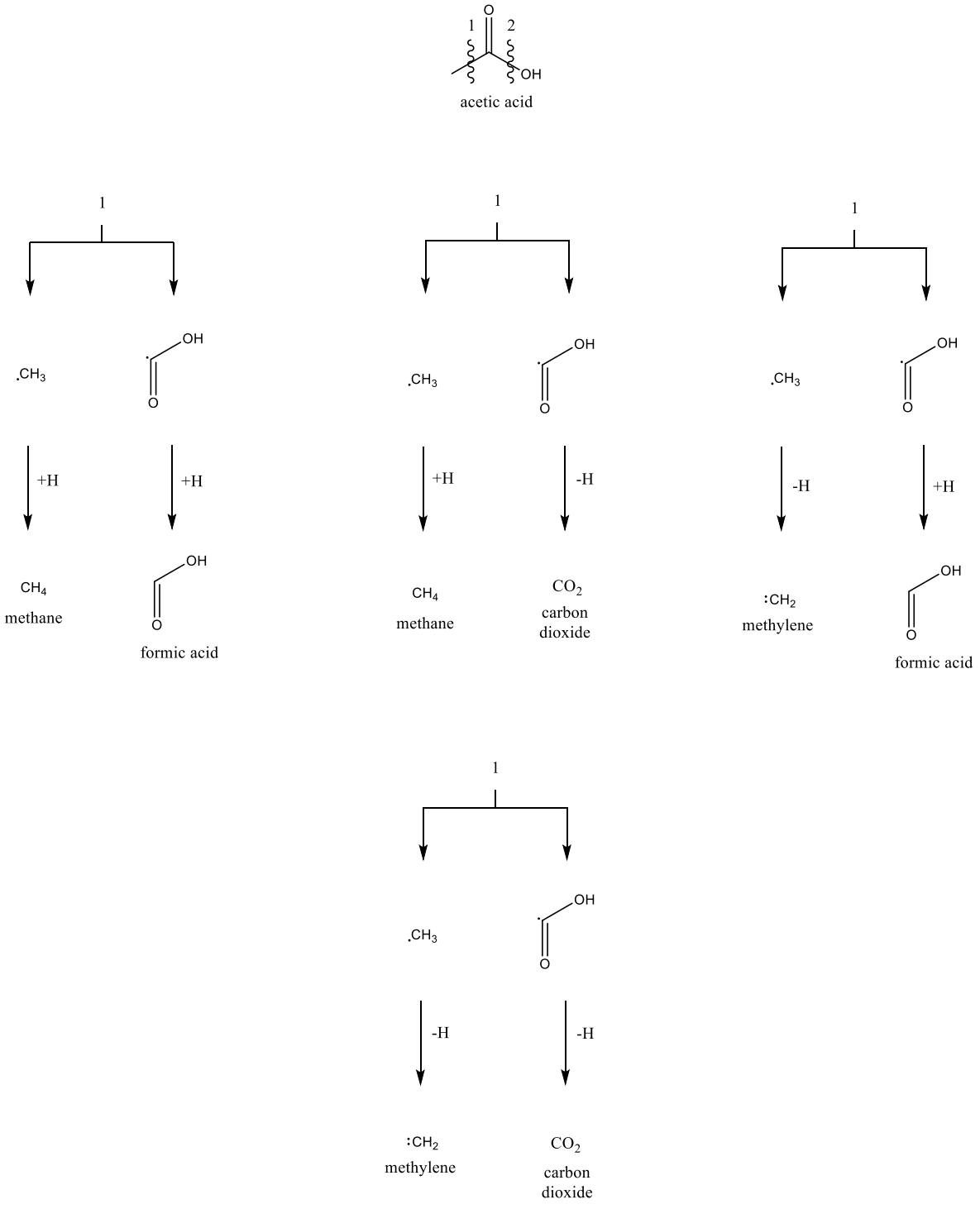

Figure S32A. Retrosynthesis of acetic acid utilizing single-bond cleavage and subsequent hydrogen addition/elimination.

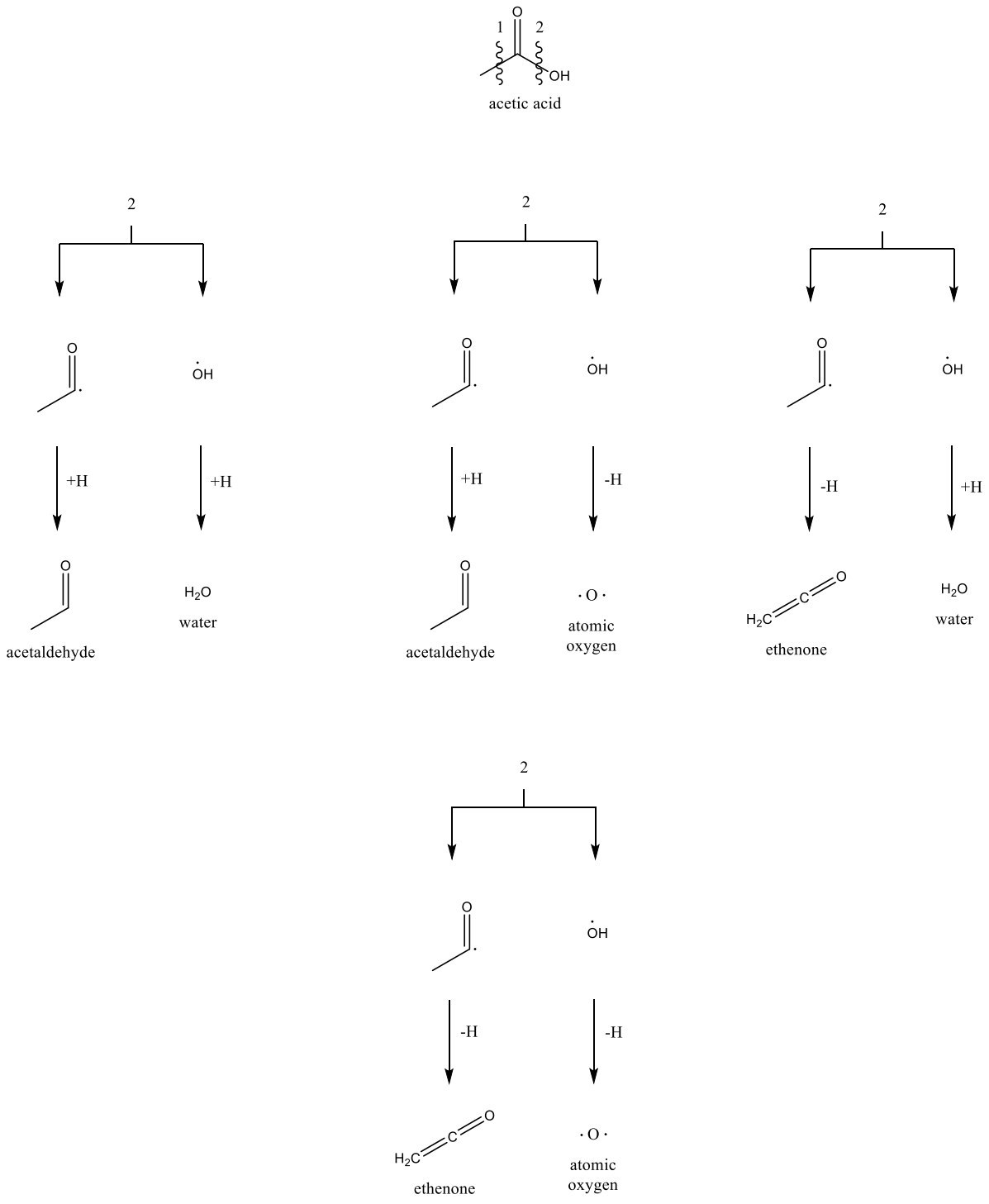

Figure S32B. Retrosynthesis of acetic acid utilizing single-bond cleavage and subsequent hydrogen addition/elimination.

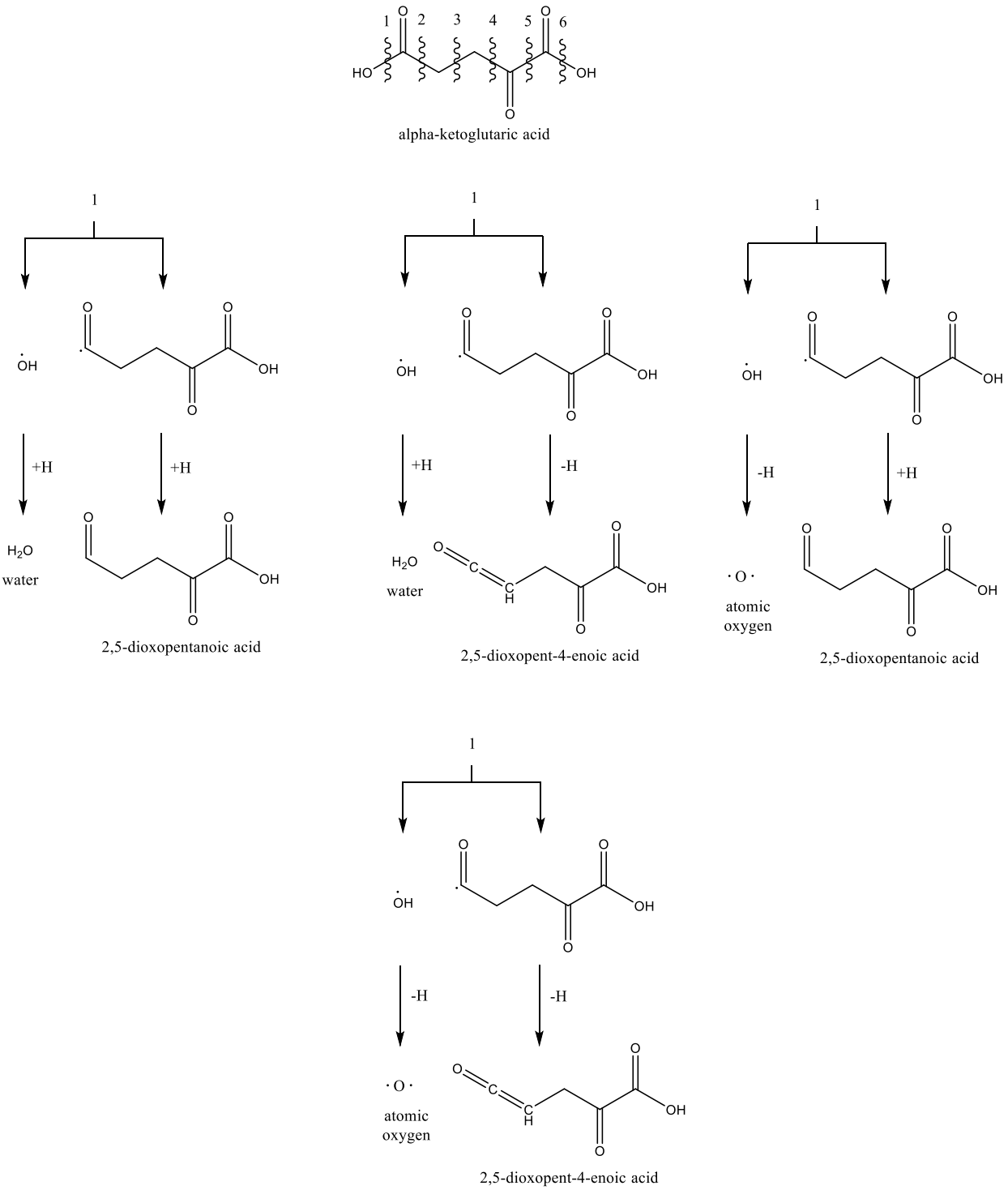

Figure S33A. Retrosynthesis of α-ketoglutaric acid utilizing single-bond cleavage and subsequent hydrogen addition/elimination.

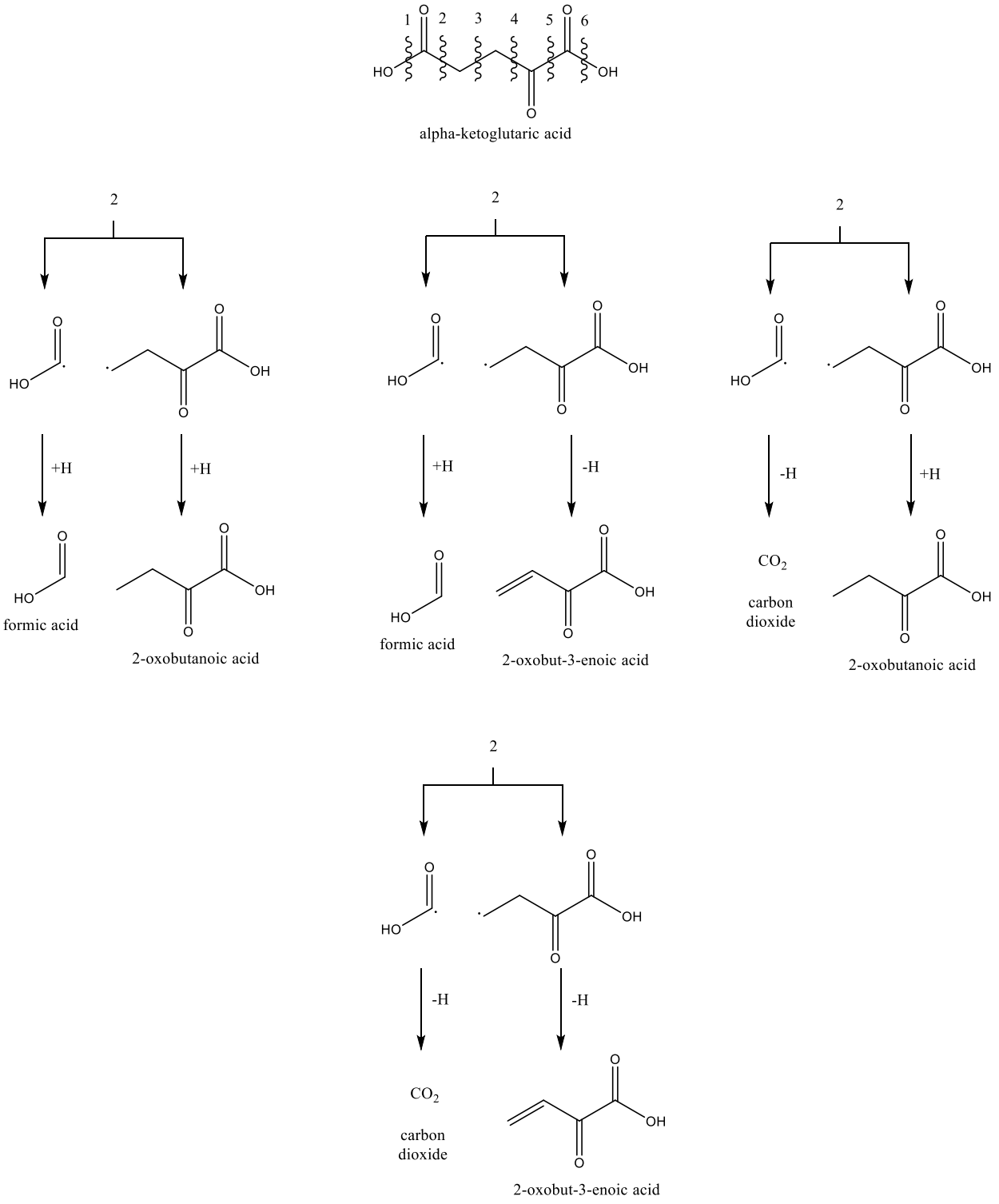

Figure S33B. Retrosynthesis of α-ketoglutaric acid utilizing single-bond cleavage and subsequent hydrogen addition/elimination.

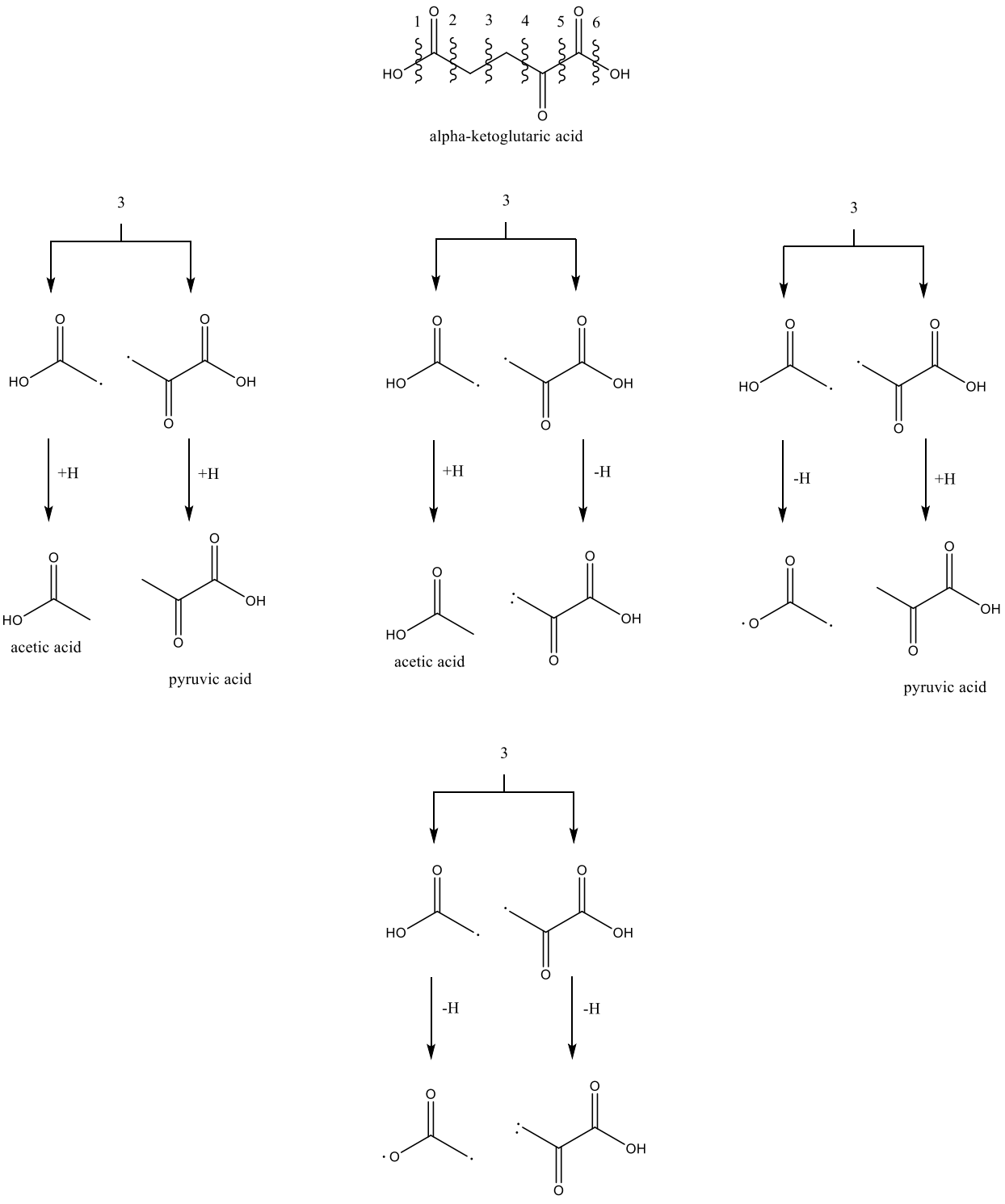

Figure S33C. Retrosynthesis of α-ketoglutaric acid utilizing single-bond cleavage and subsequent hydrogen addition/elimination.

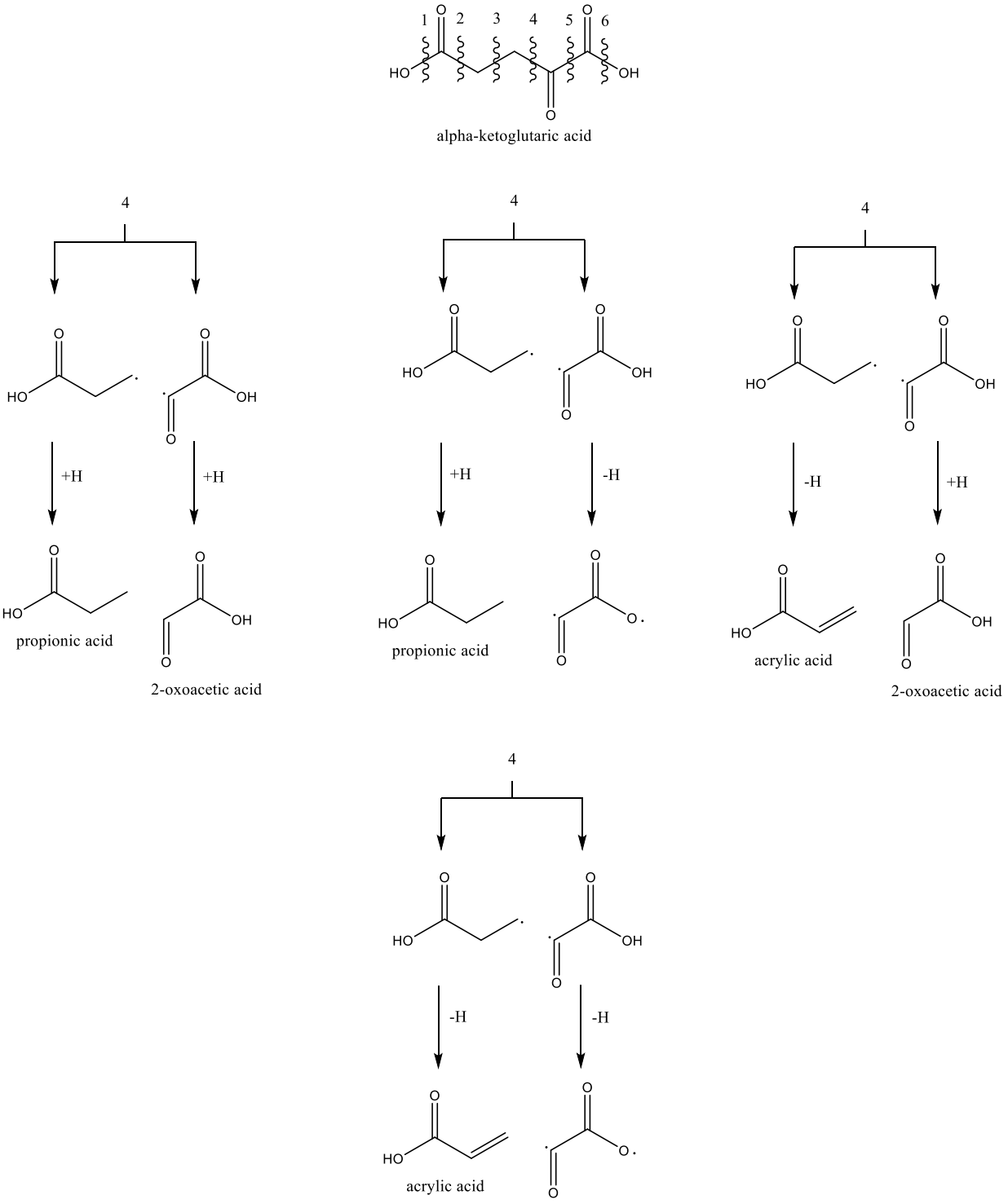

Figure S33D. Retrosynthesis of α-ketoglutaric acid utilizing single-bond cleavage and subsequent hydrogen addition/elimination.

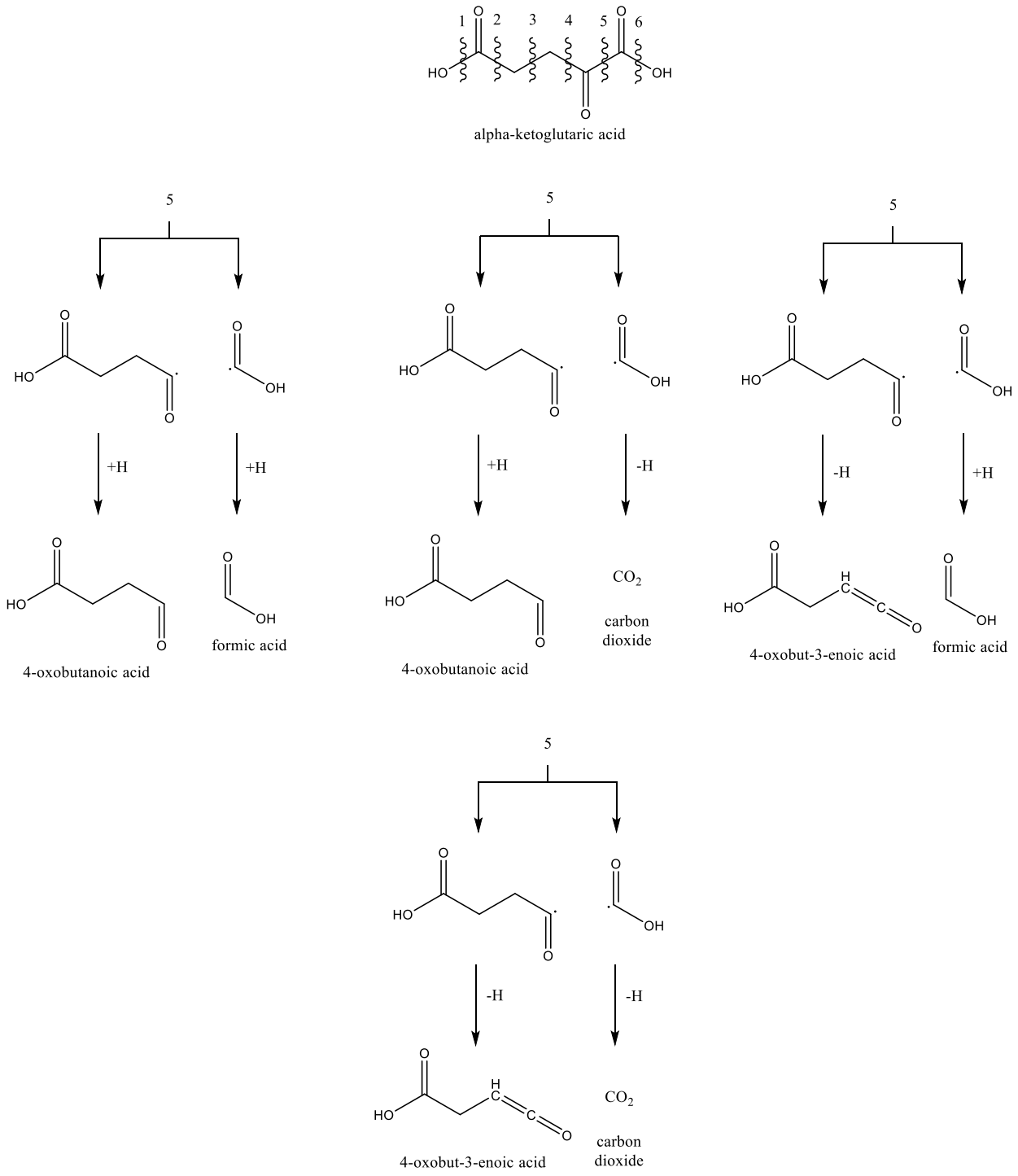

Figure S33E. Retrosynthesis of α-ketoglutaric acid utilizing single-bond cleavage and subsequent hydrogen addition/elimination.

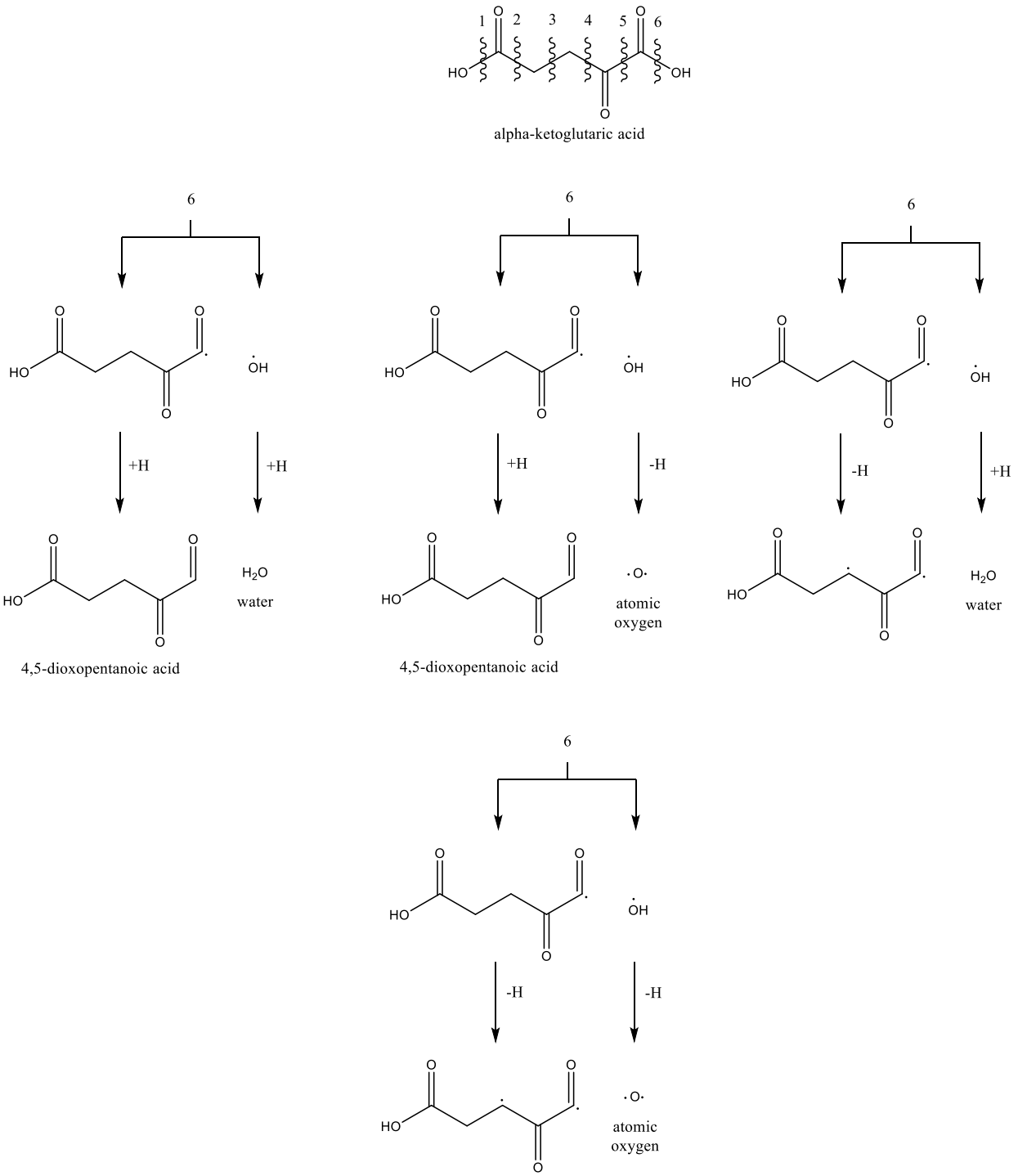

Figure S33F. Retrosynthesis of α-ketoglutaric acid utilizing single-bond cleavage and subsequent hydrogen addition/elimination.

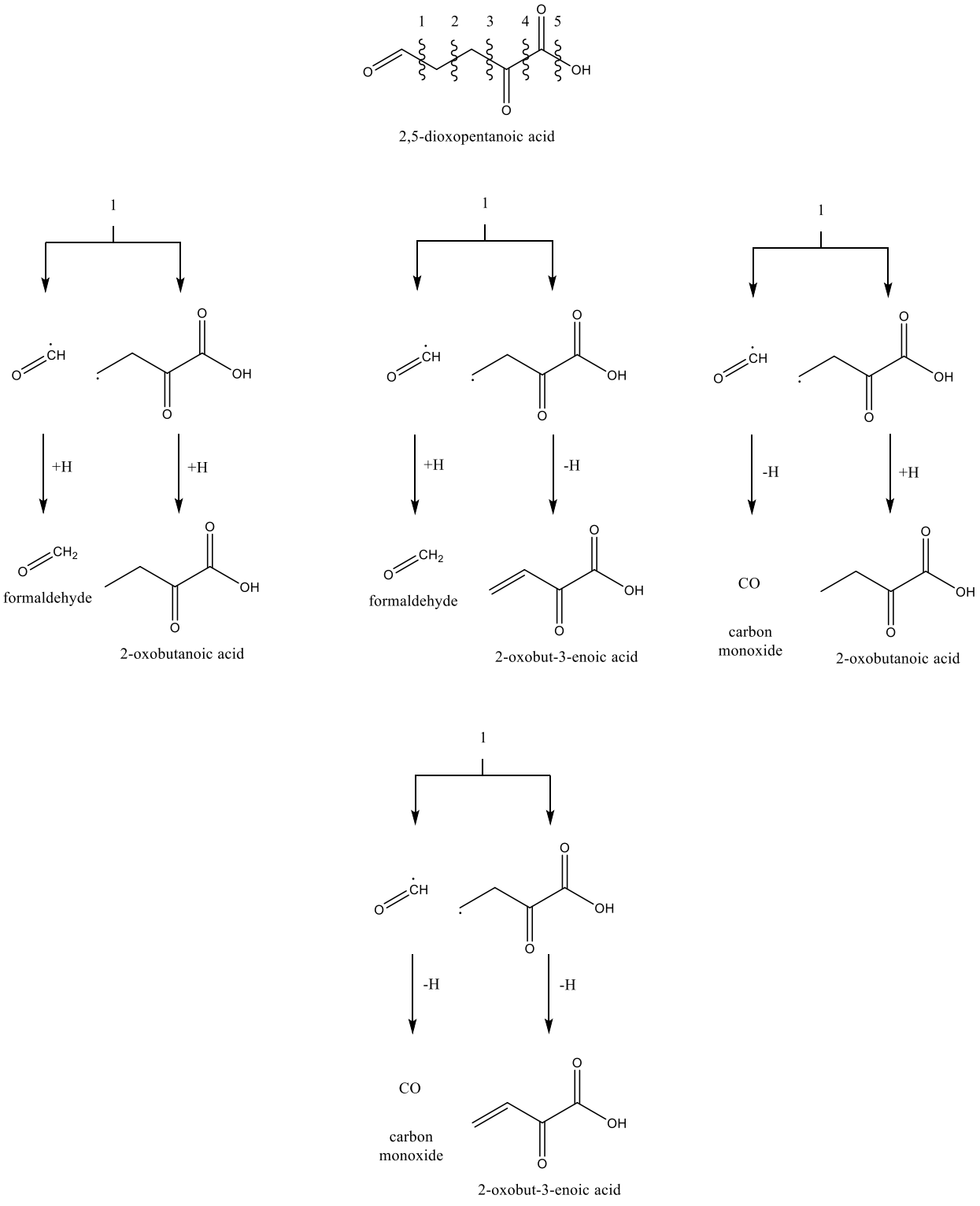

Figure S34A. Retrosynthesis of 2,5-dioxopentanoic acid utilizing single-bond cleavage and subsequent hydrogen addition/elimination.

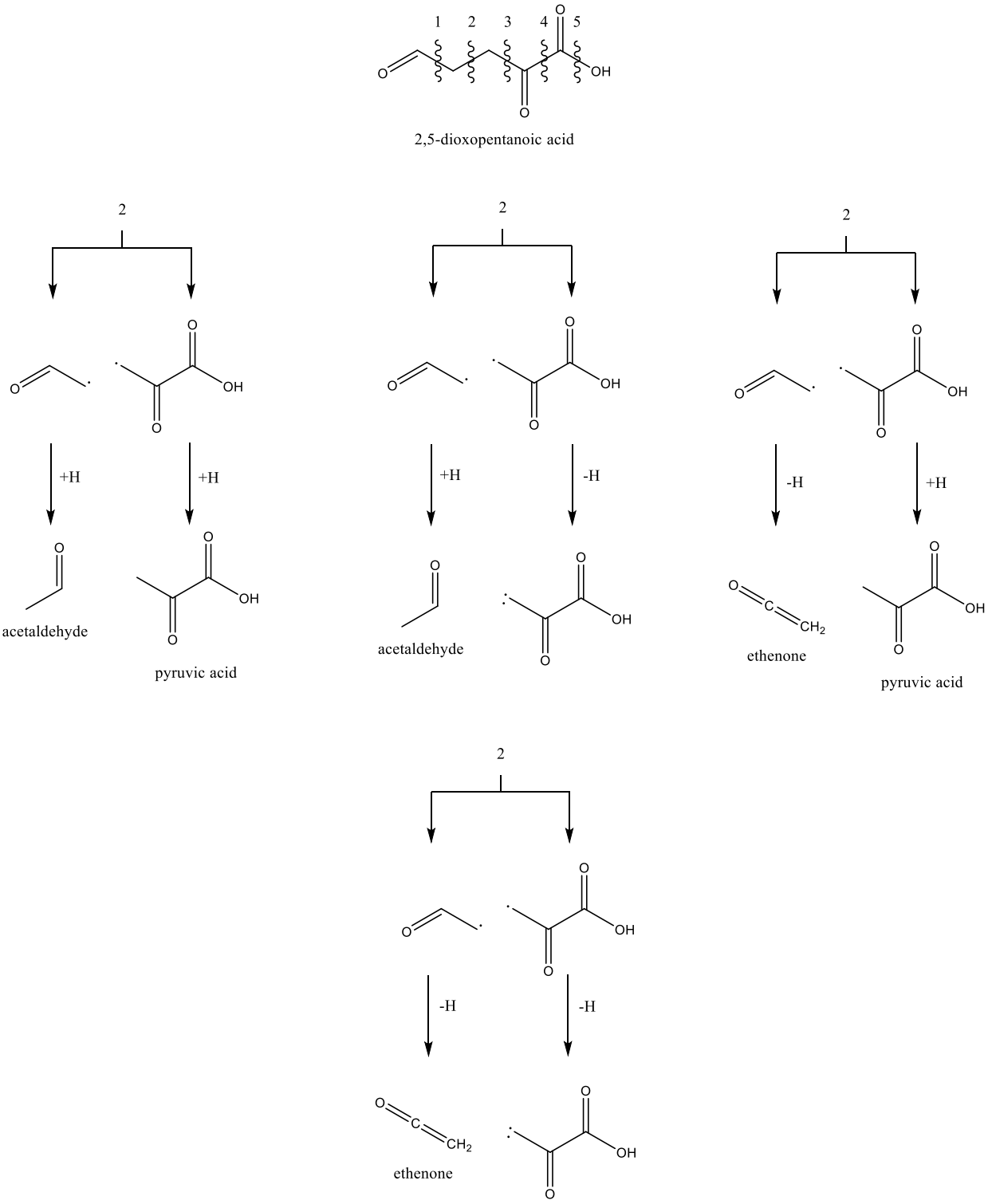

Figure S34B. Retrosynthesis of 2,5-dioxopentanoic acid utilizing single-bond cleavage and subsequent hydrogen addition/elimination.

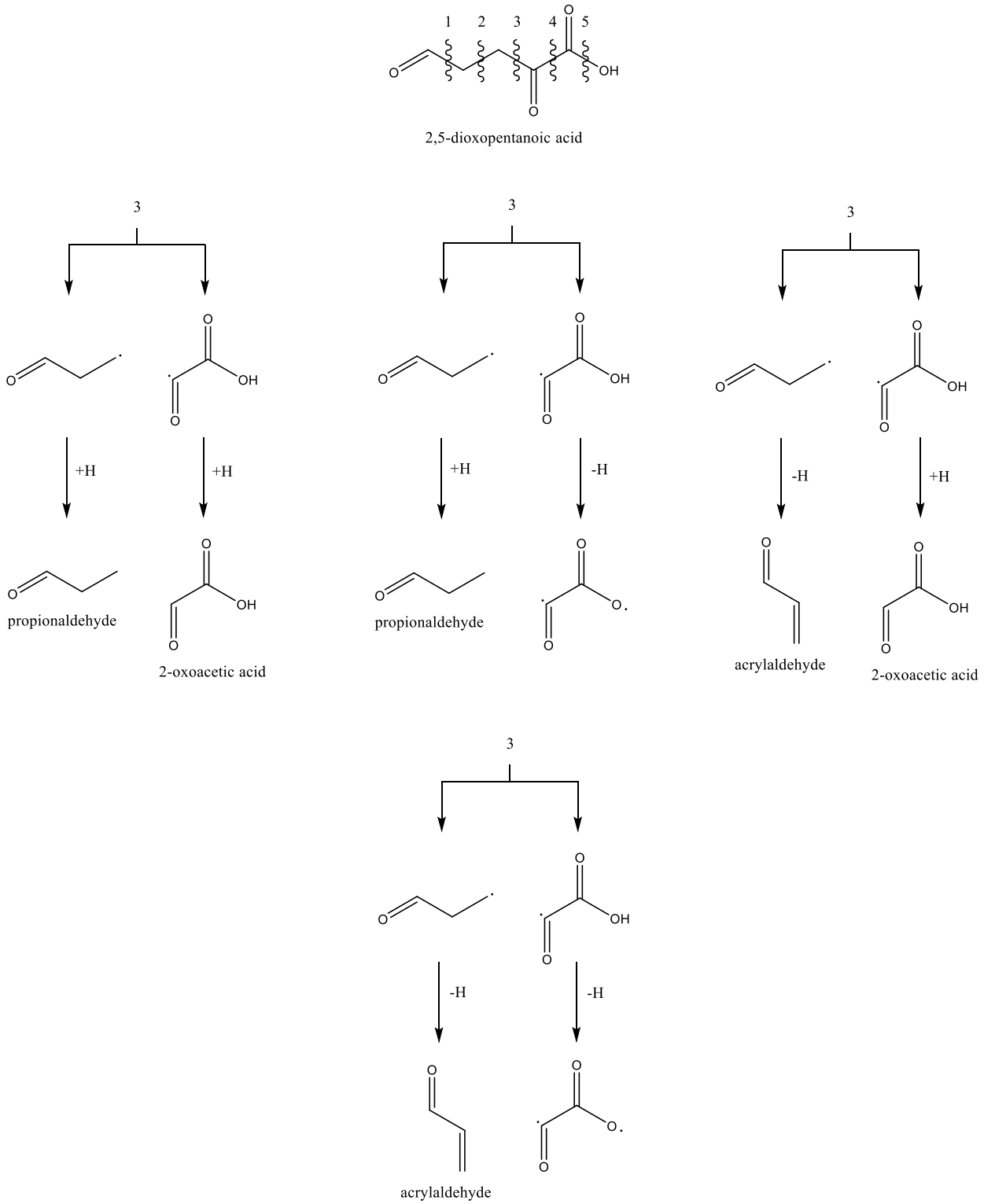

Figure S34C. Retrosynthesis of 2,5-dioxopentanoic acid utilizing single-bond cleavage and subsequent hydrogen addition/elimination.

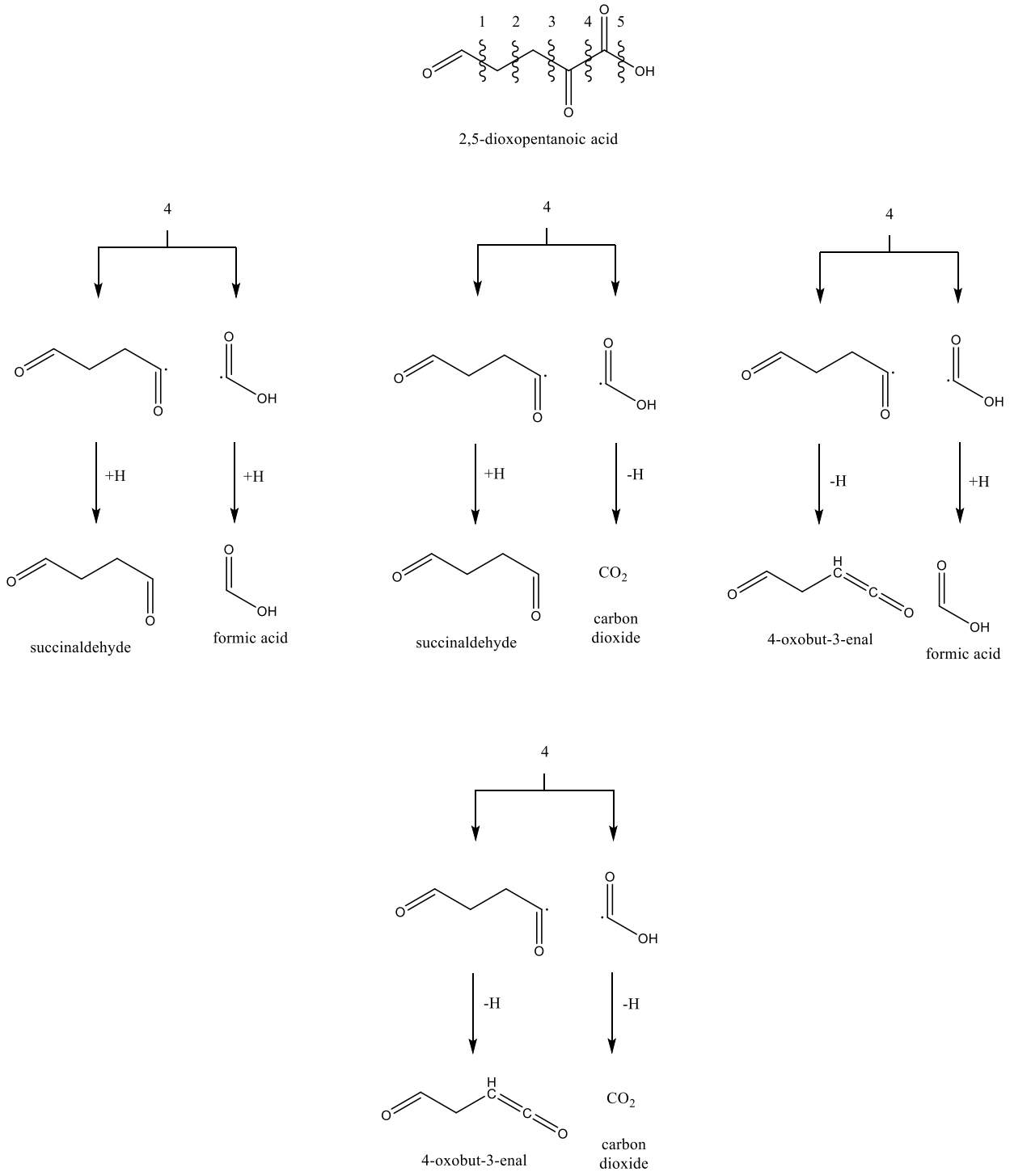

Figure S34D. Retrosynthesis of 2,5-dioxopentanoic acid utilizing single-bond cleavage and subsequent hydrogen addition/elimination.

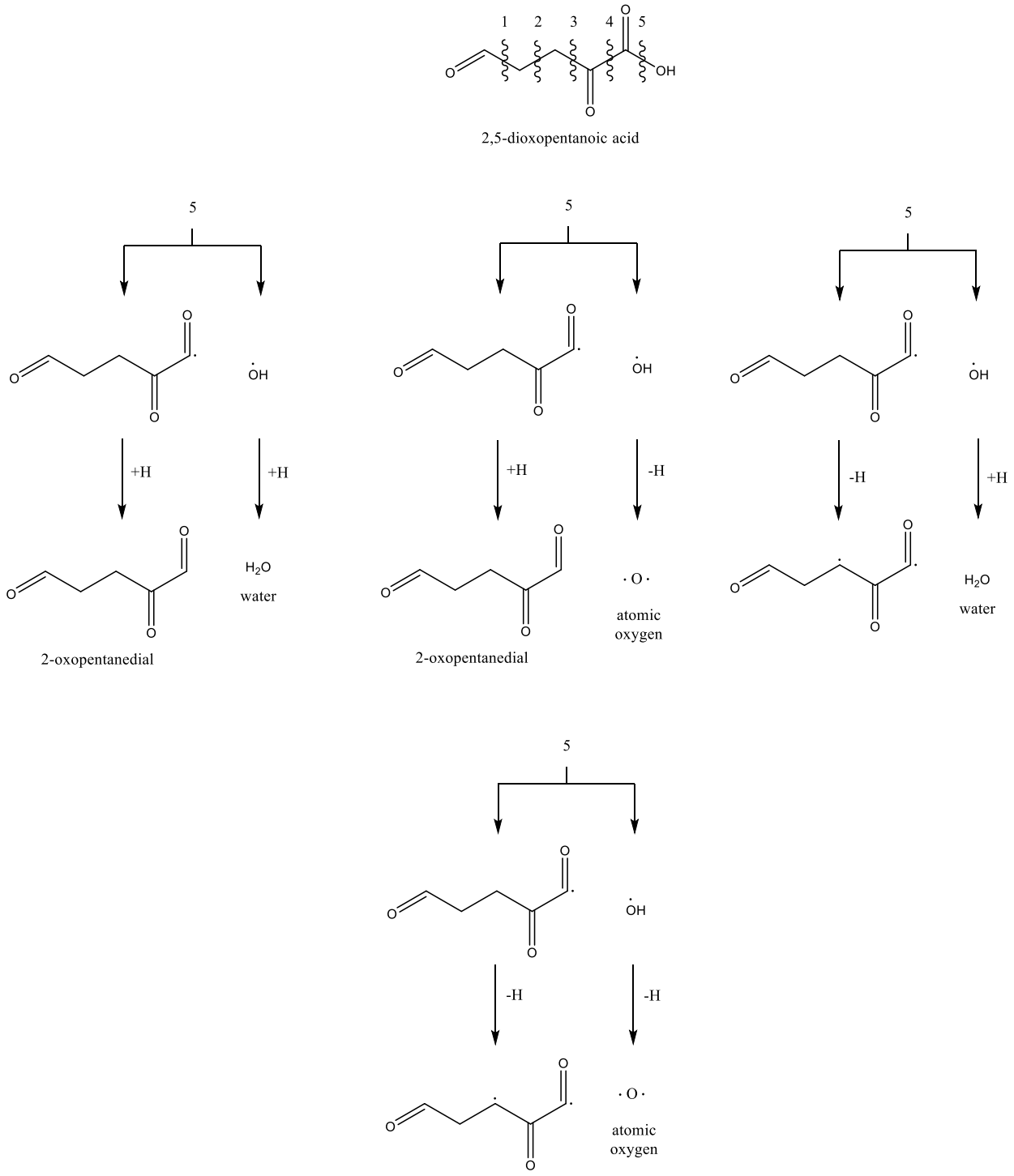

Figure S34E. Retrosynthesis of 2,5-dioxopentanoic acid utilizing single-bond cleavage and subsequent hydrogen addition/elimination.

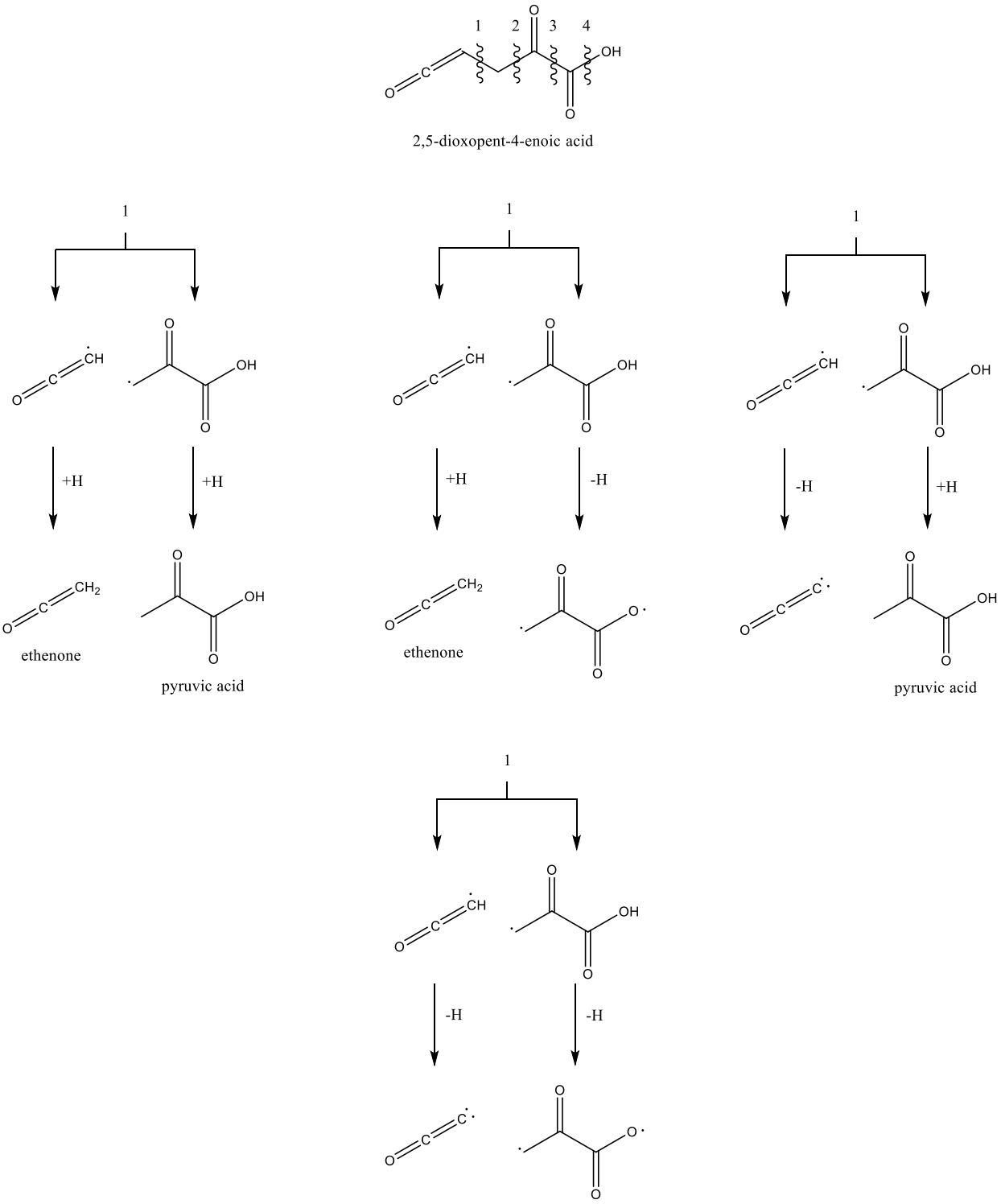

Figure S35A. Retrosynthesis of 2,5-dioxopent-4-enoic acid utilizing single-bond cleavage and subsequent hydrogen addition/elimination.

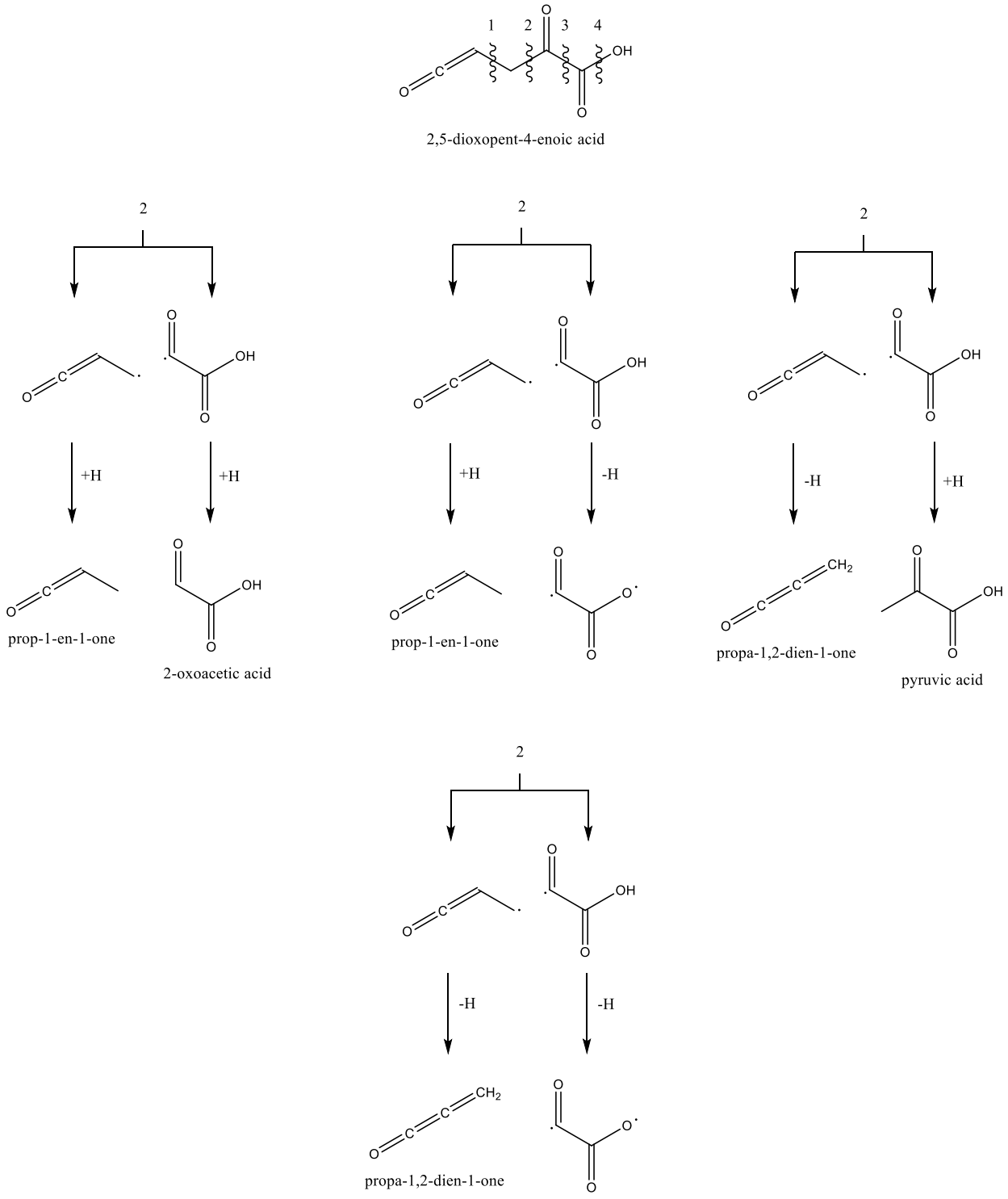

Figure S35B. Retrosynthesis of 2,5-dioxopent-4-enoic acid utilizing single-bond cleavage and subsequent hydrogen addition/elimination.

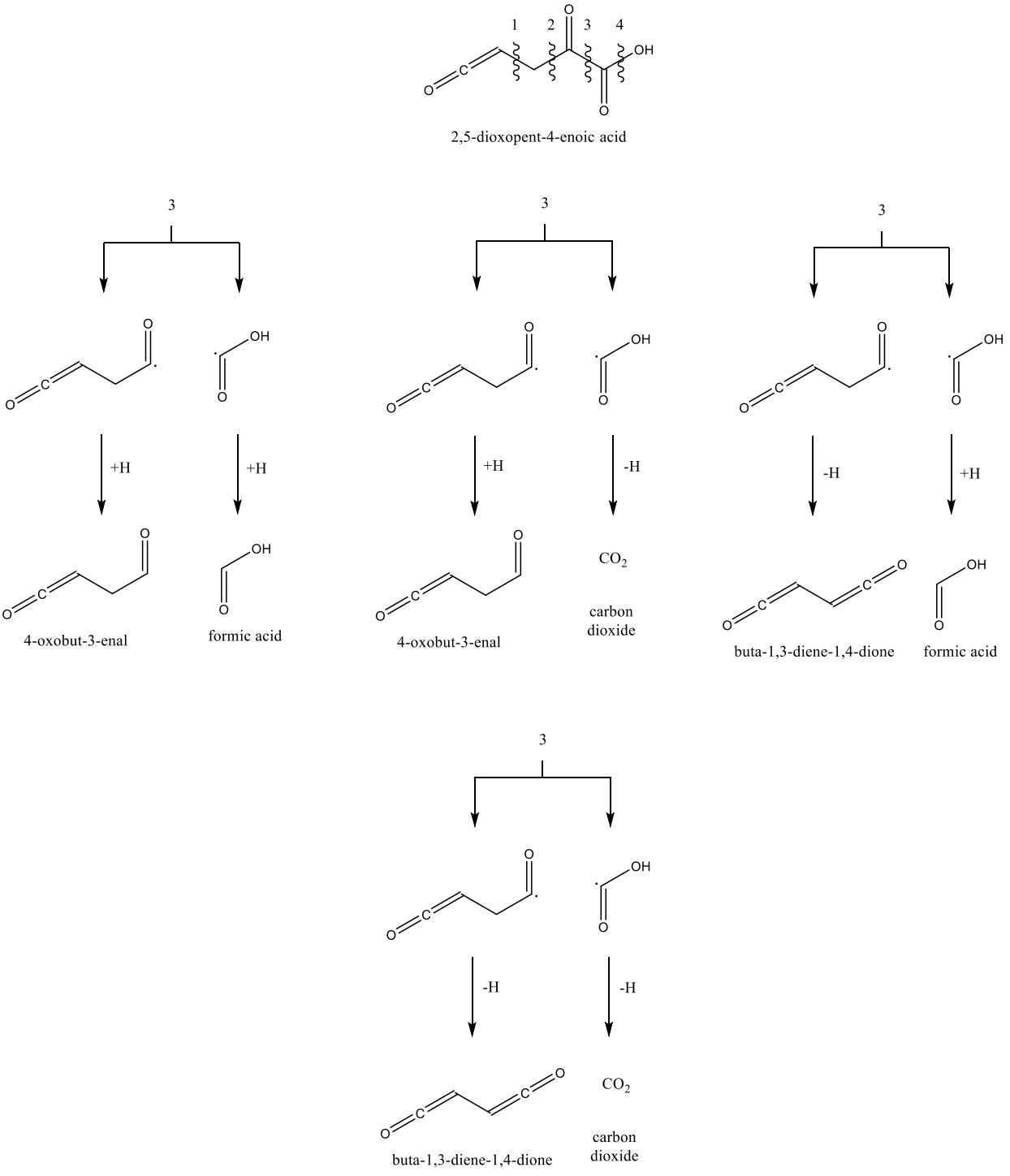

Figure S35C. Retrosynthesis of 2,5-dioxopent-4-enoic acid utilizing single-bond cleavage and subsequent hydrogen addition/elimination.

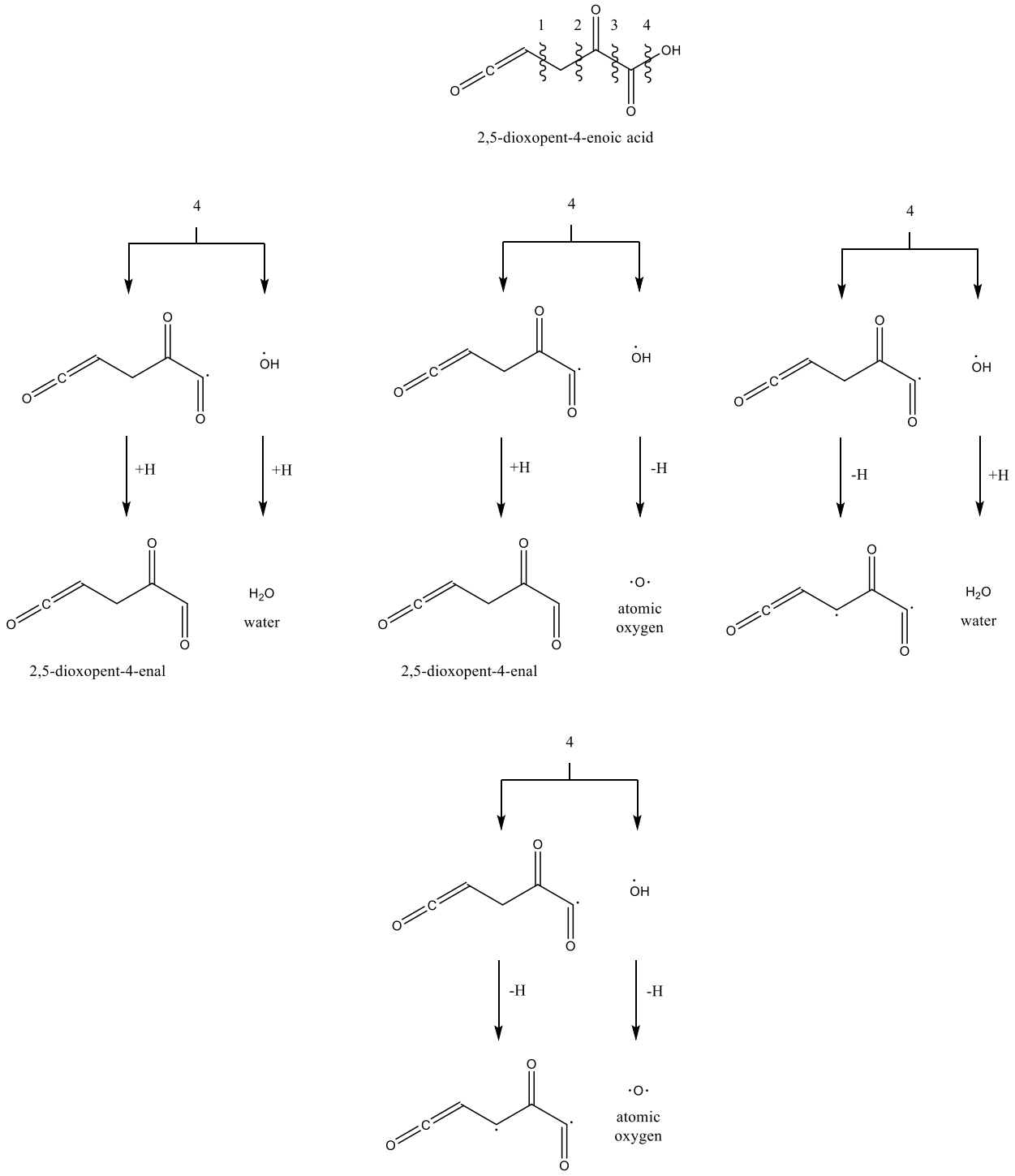

Figure S35D. Retrosynthesis of 2,5-dioxopent-4-enoic acid utilizing single-bond cleavage and subsequent hydrogen addition/elimination.

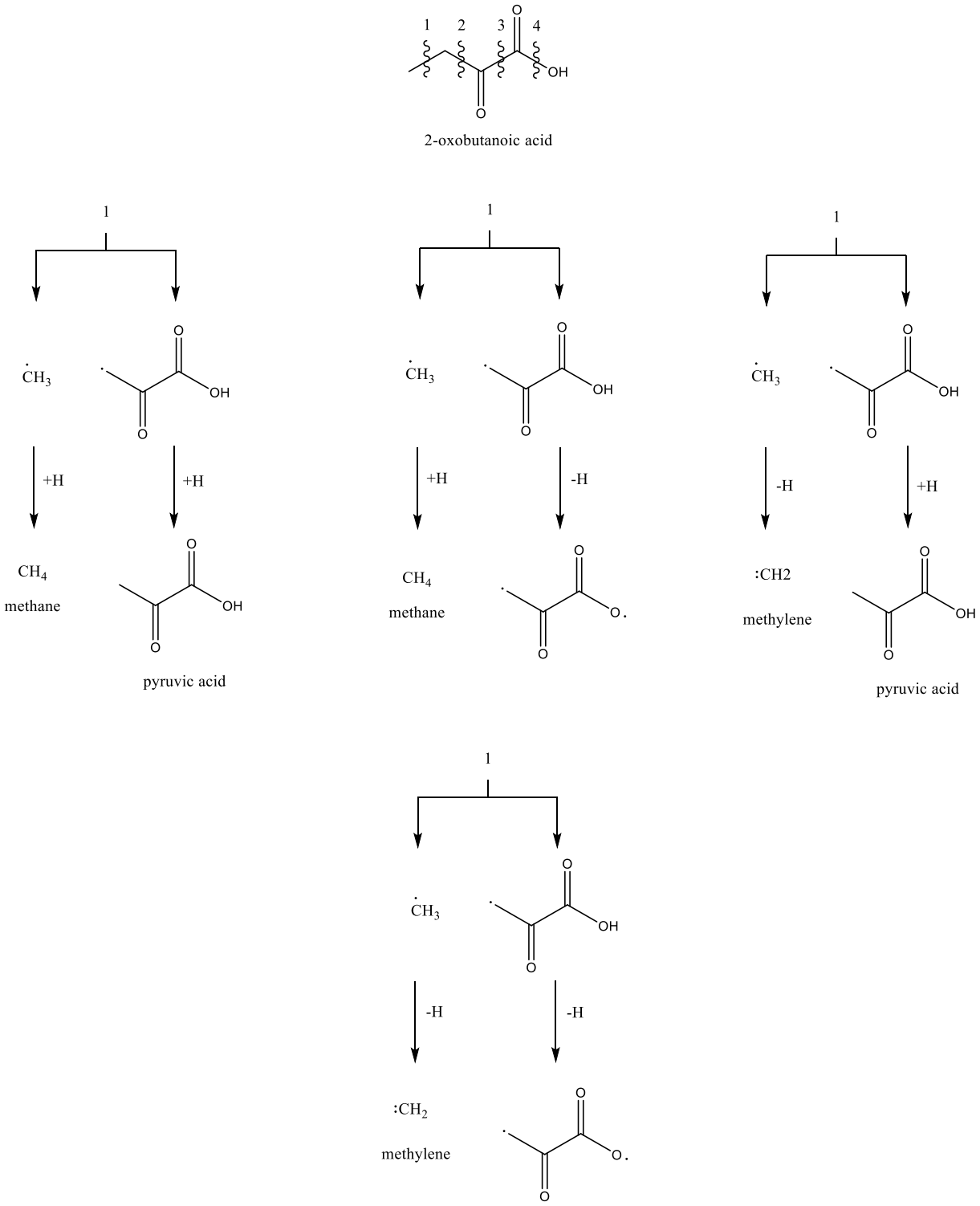

Figure S36A. Retrosynthesis of 2-oxobutanoic acid utilizing single-bond cleavage and subsequent hydrogen addition/elimination.

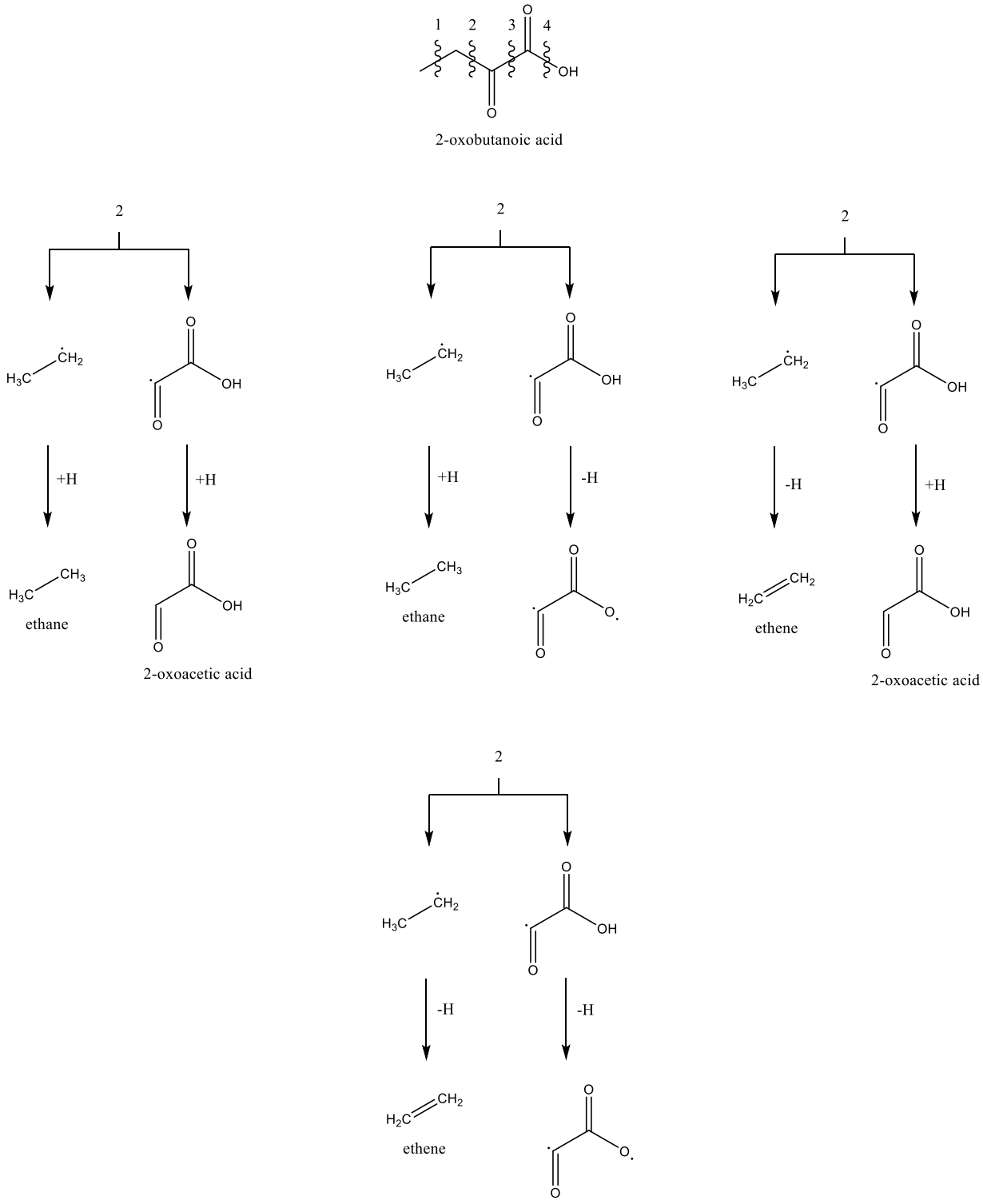

Figure S36B. Retrosynthesis of 2-oxobutanoic acid utilizing single-bond cleavage and subsequent hydrogen addition/elimination.

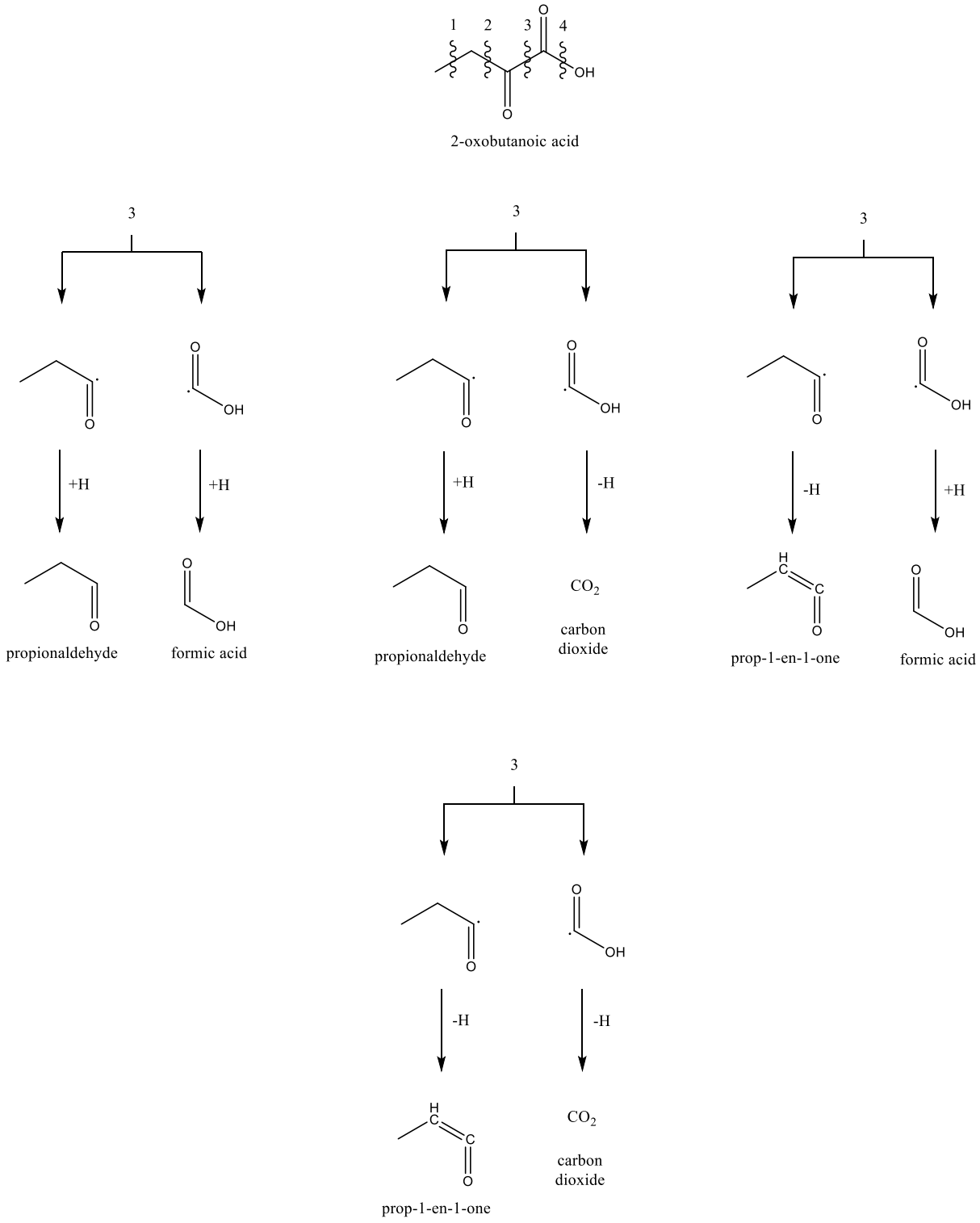

Figure S36C. Retrosynthesis of 2-oxobutanoic acid utilizing single-bond cleavage and subsequent hydrogen addition/elimination.

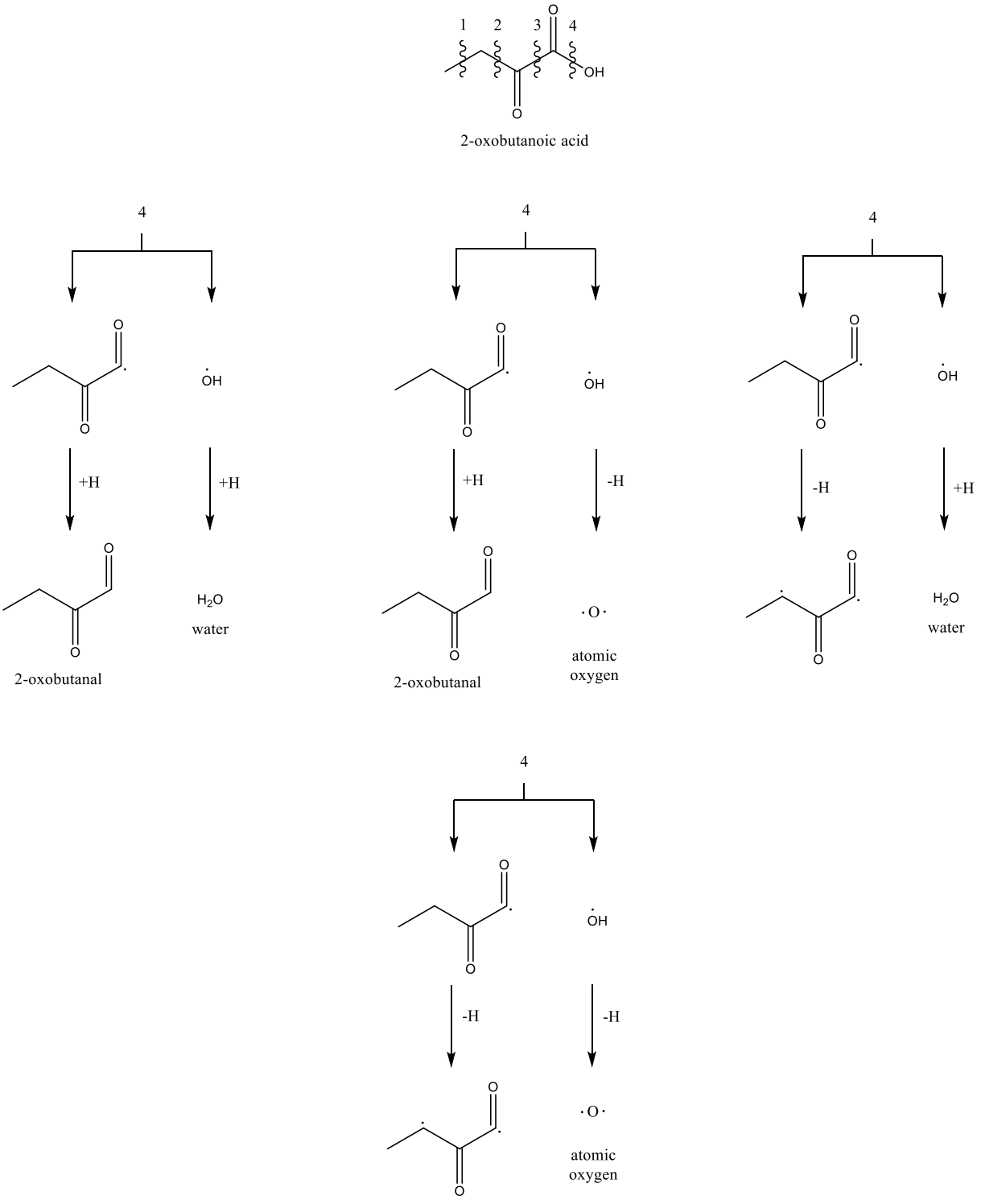

Figure S36D. Retrosynthesis of 2-oxobutanoic acid utilizing single-bond cleavage and subsequent hydrogen addition/elimination.

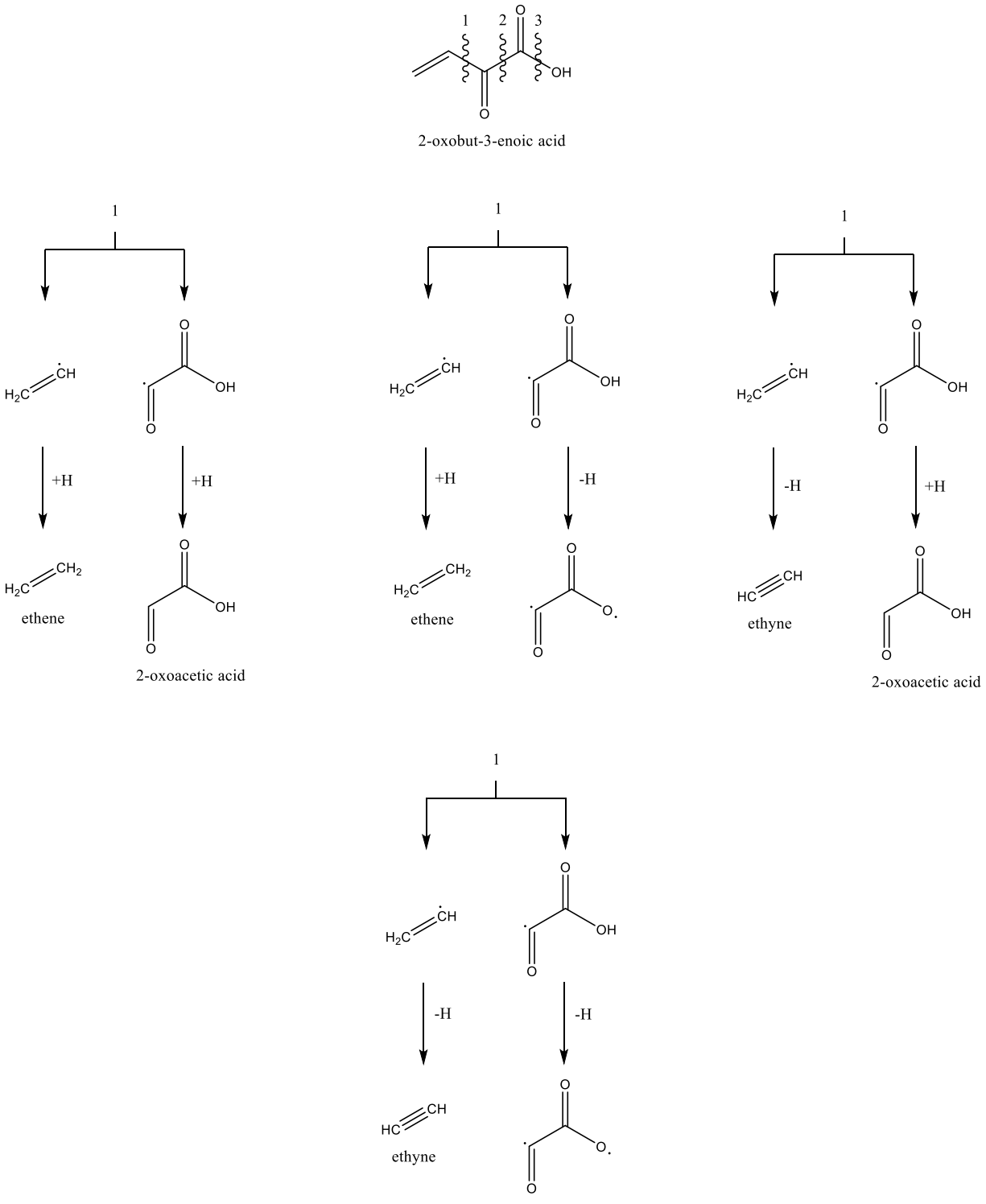

Figure S37A. Retrosynthesis of 2-oxobut-3-enoic acid utilizing single-bond cleavage and subsequent hydrogen addition/elimination.

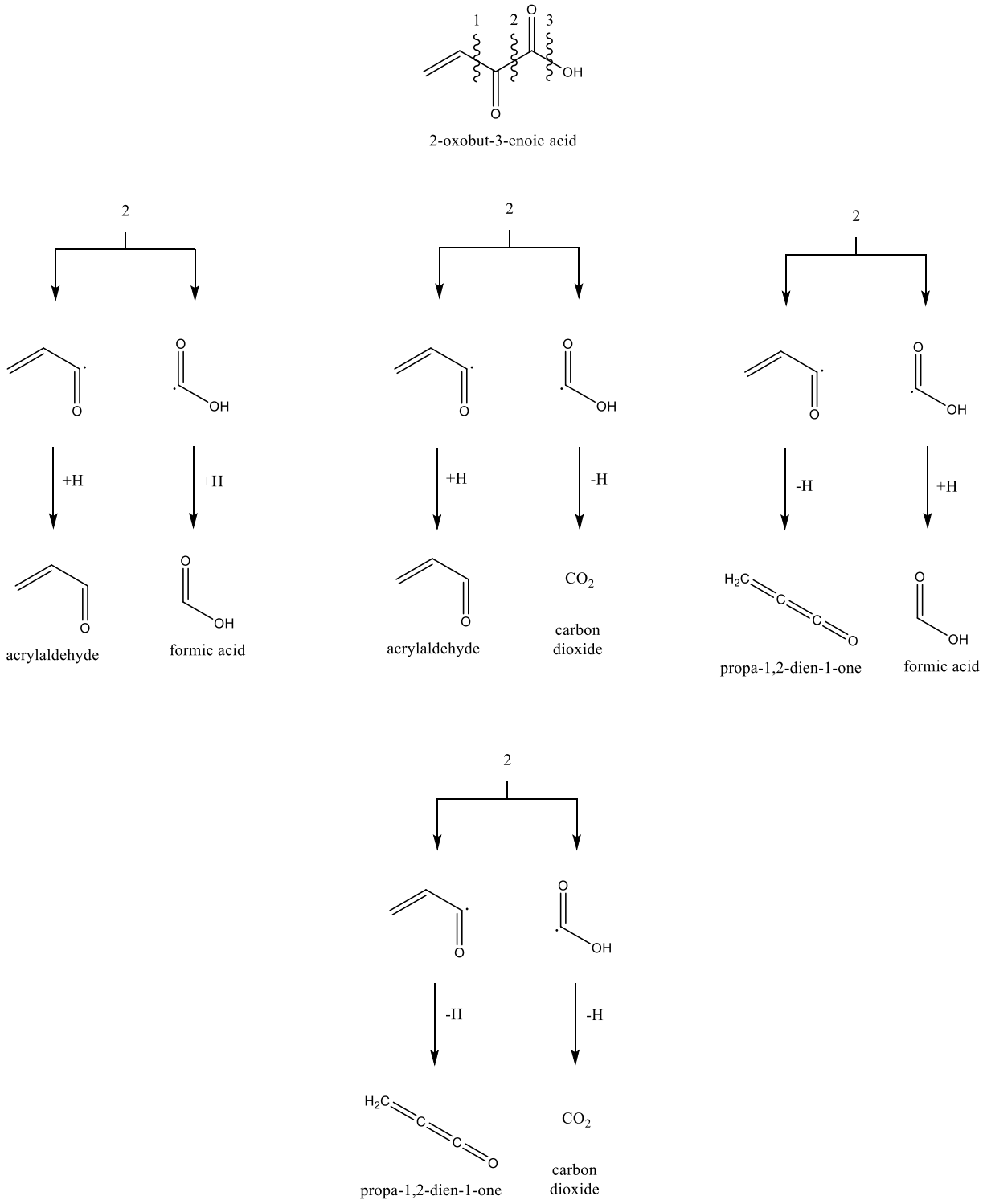

Figure S37B. Retrosynthesis of 2-oxobut-3-enoic acid utilizing single-bond cleavage and subsequent hydrogen addition/elimination.

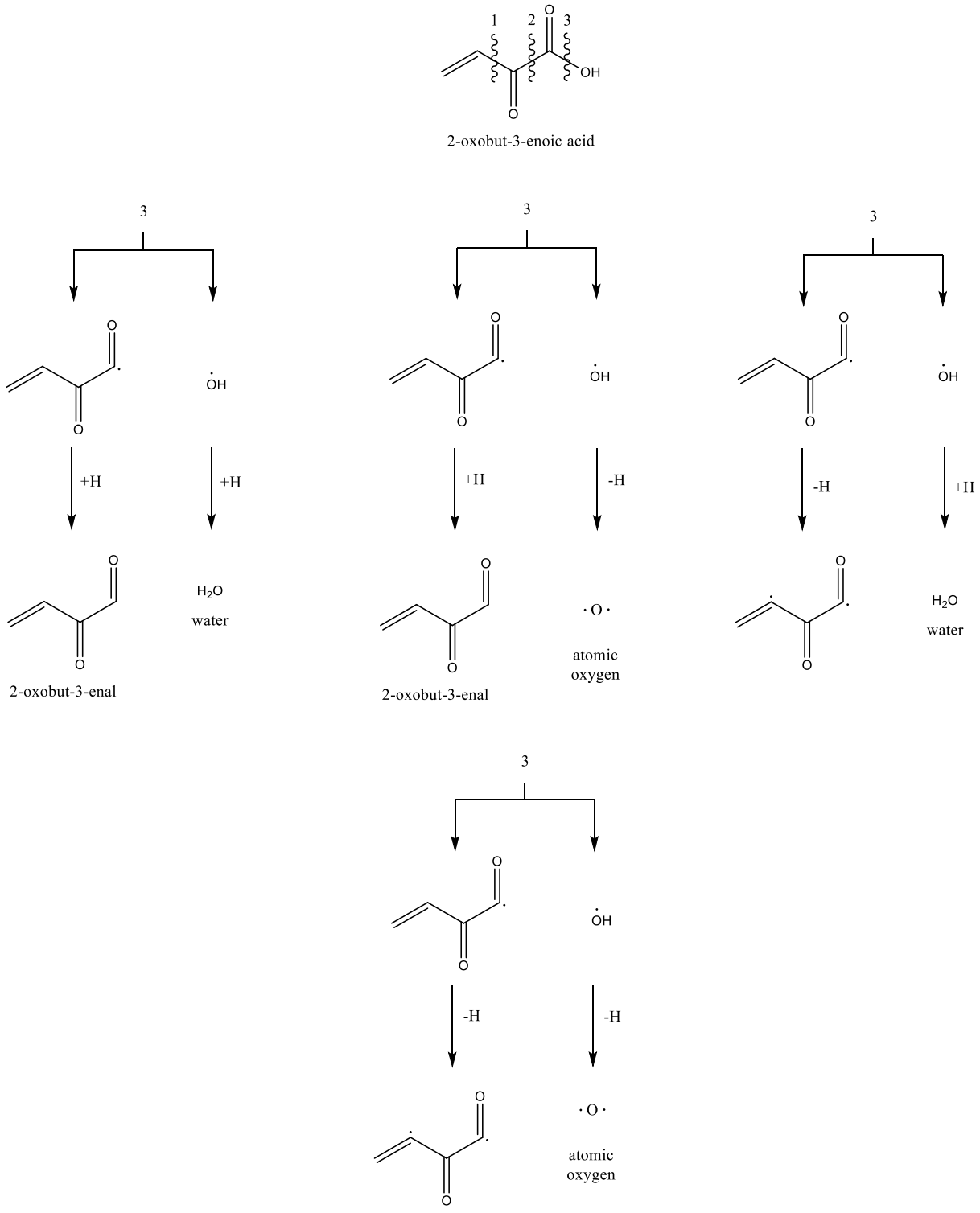

Figure S37C. Retrosynthesis of 2-oxobut-3-enoic acid utilizing single-bond cleavage and subsequent hydrogen addition/elimination.

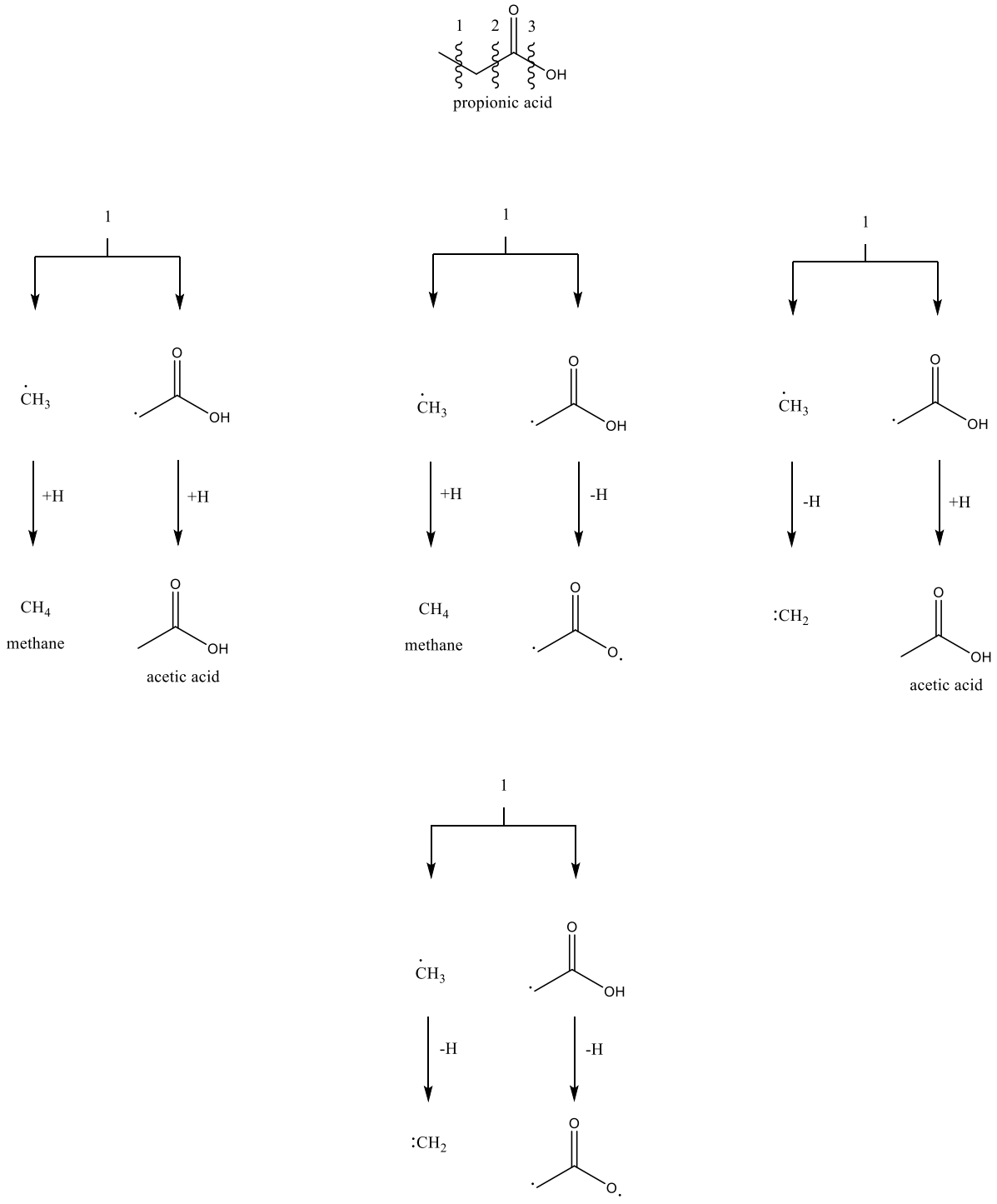

Figure S38A. Retrosynthesis of propionic acid utilizing single-bond cleavage and subsequent hydrogen addition/elimination.

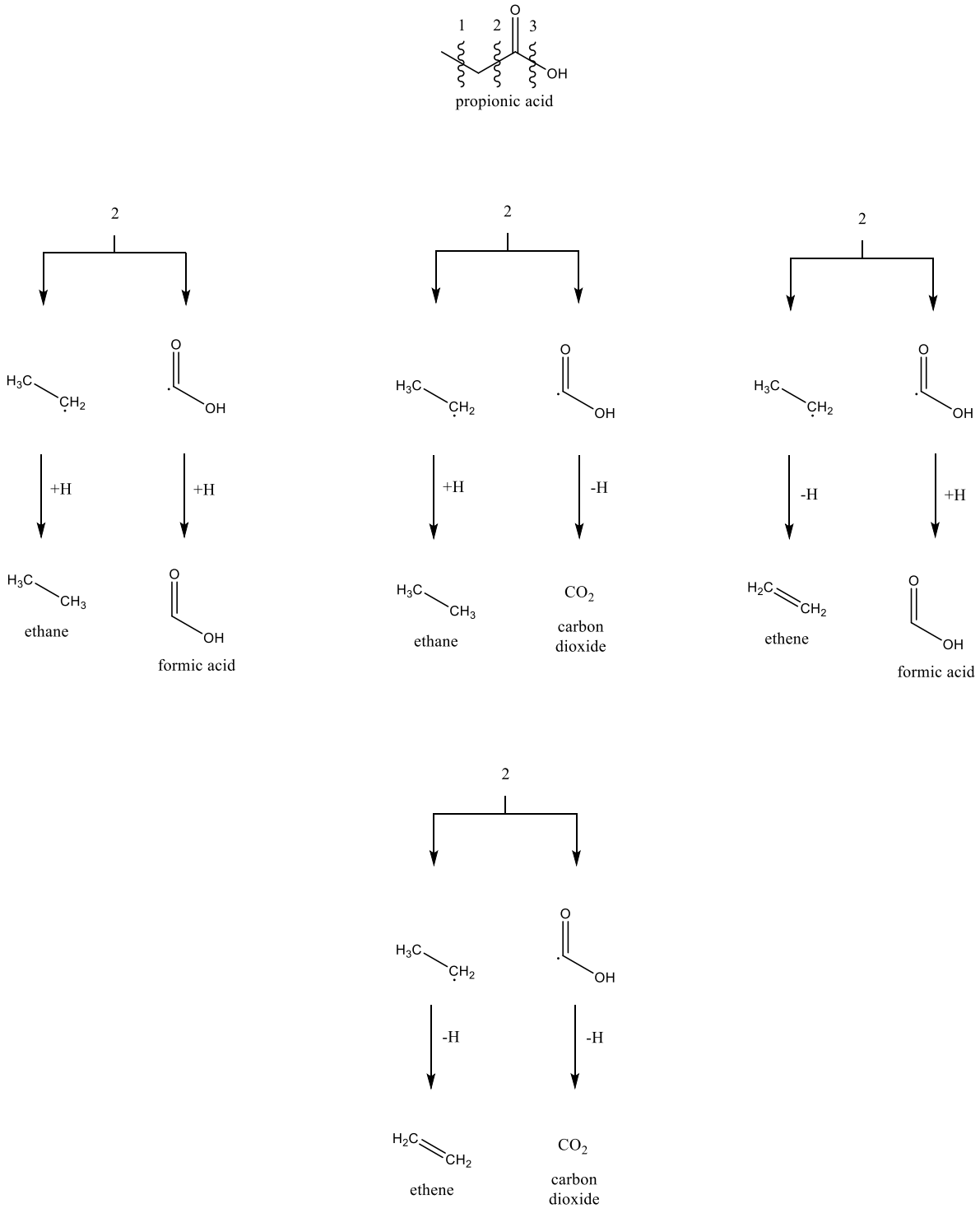

Figure S38B. Retrosynthesis of propionic acid utilizing single-bond cleavage and subsequent hydrogen addition/elimination.

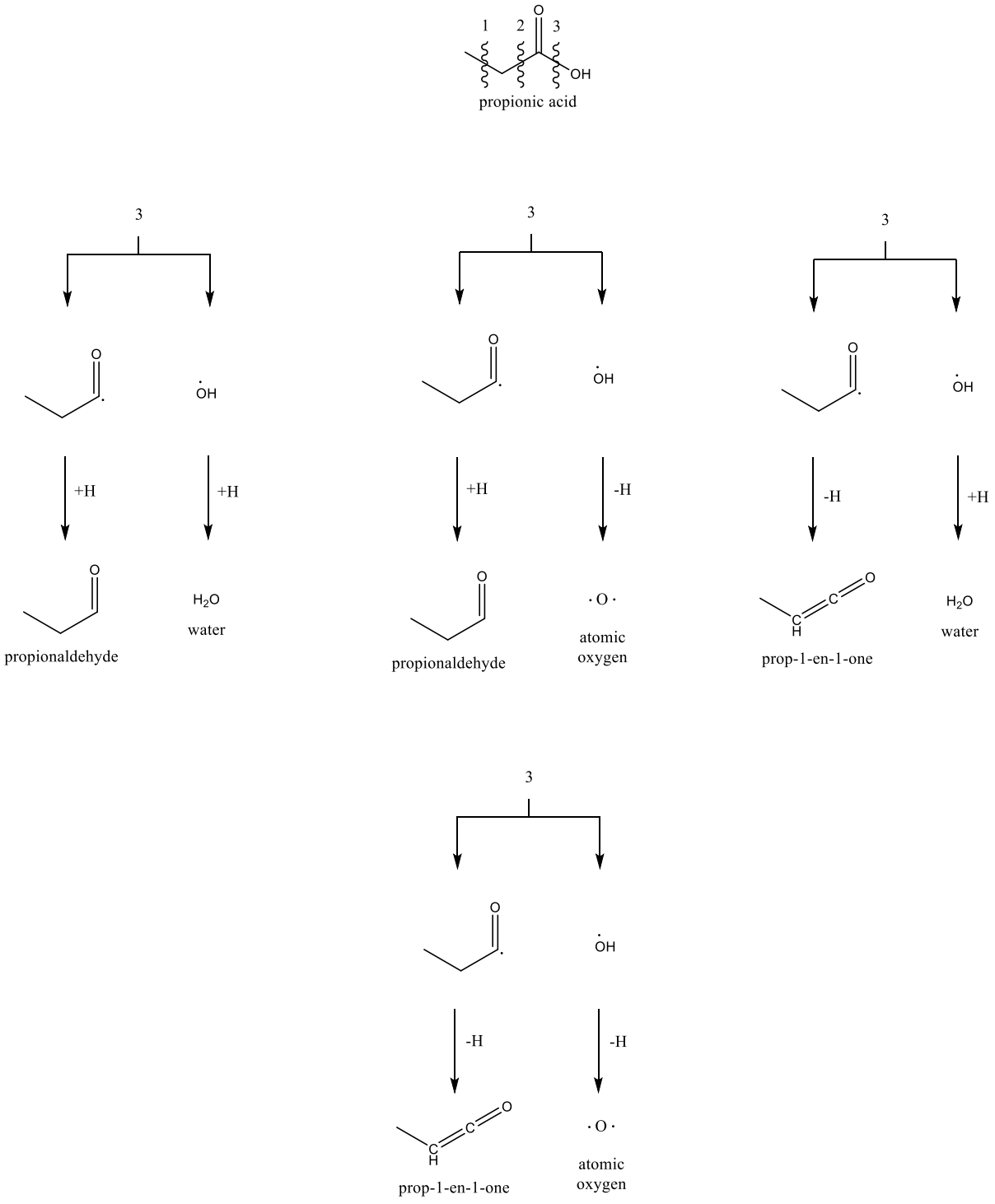

Figure S38C. Retrosynthesis of propionic acid utilizing single-bond cleavage and subsequent hydrogen addition/elimination.

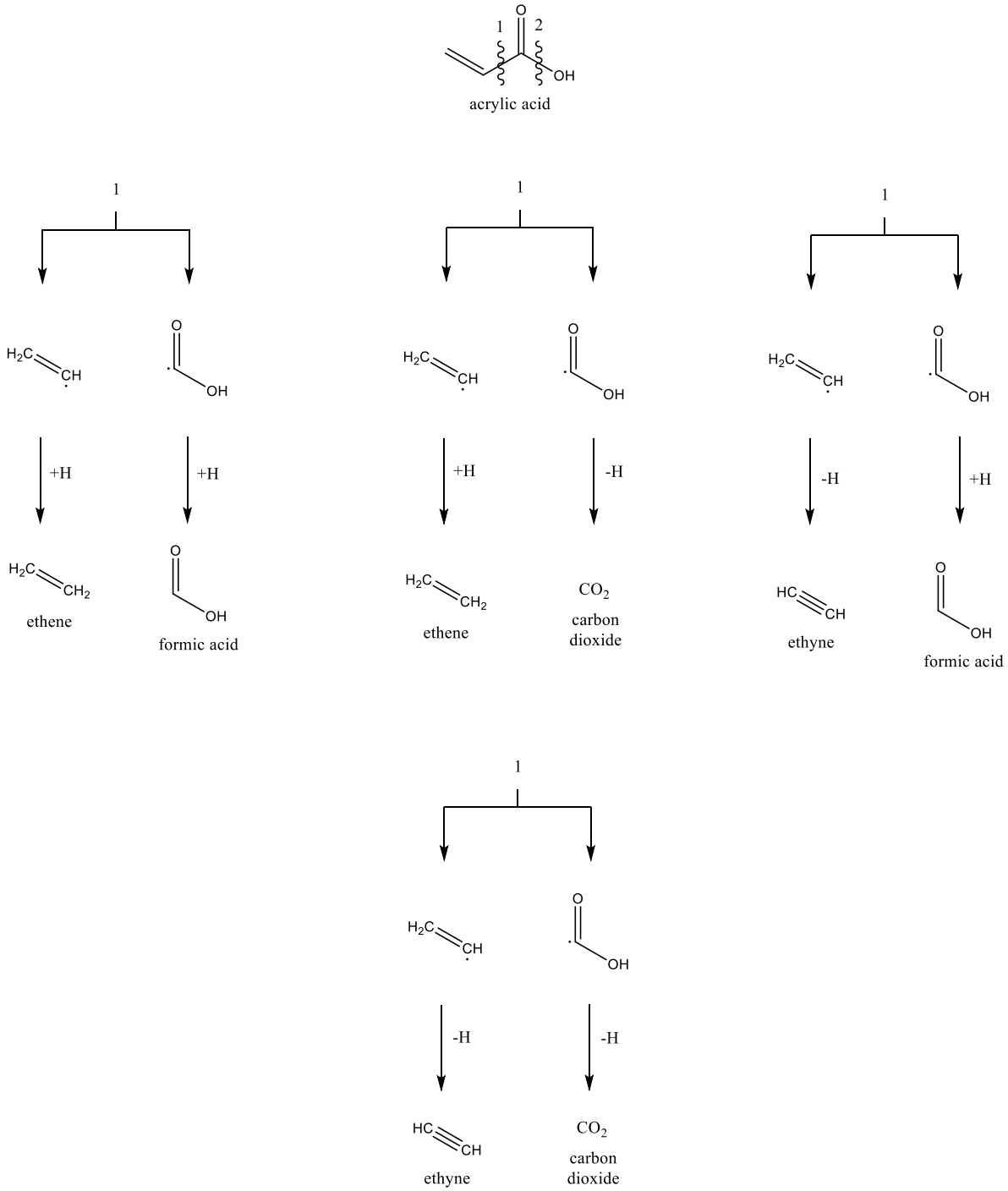

Figure S39A. Retrosynthesis of propionic acid utilizing single-bond cleavage and subsequent hydrogen addition/elimination.

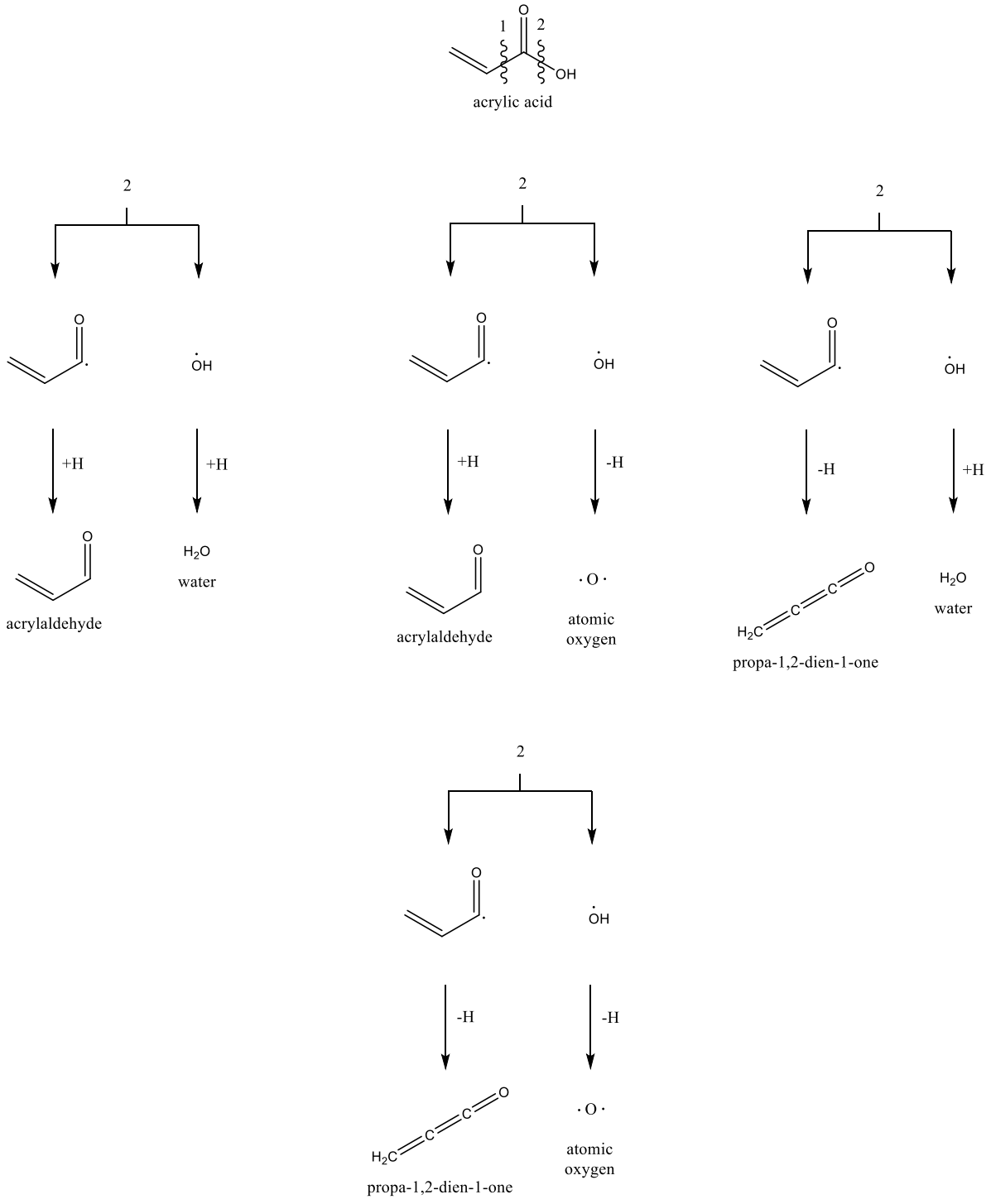

Figure S39B. Retrosynthesis of propionic acid utilizing single-bond cleavage and subsequent hydrogen addition/elimination.

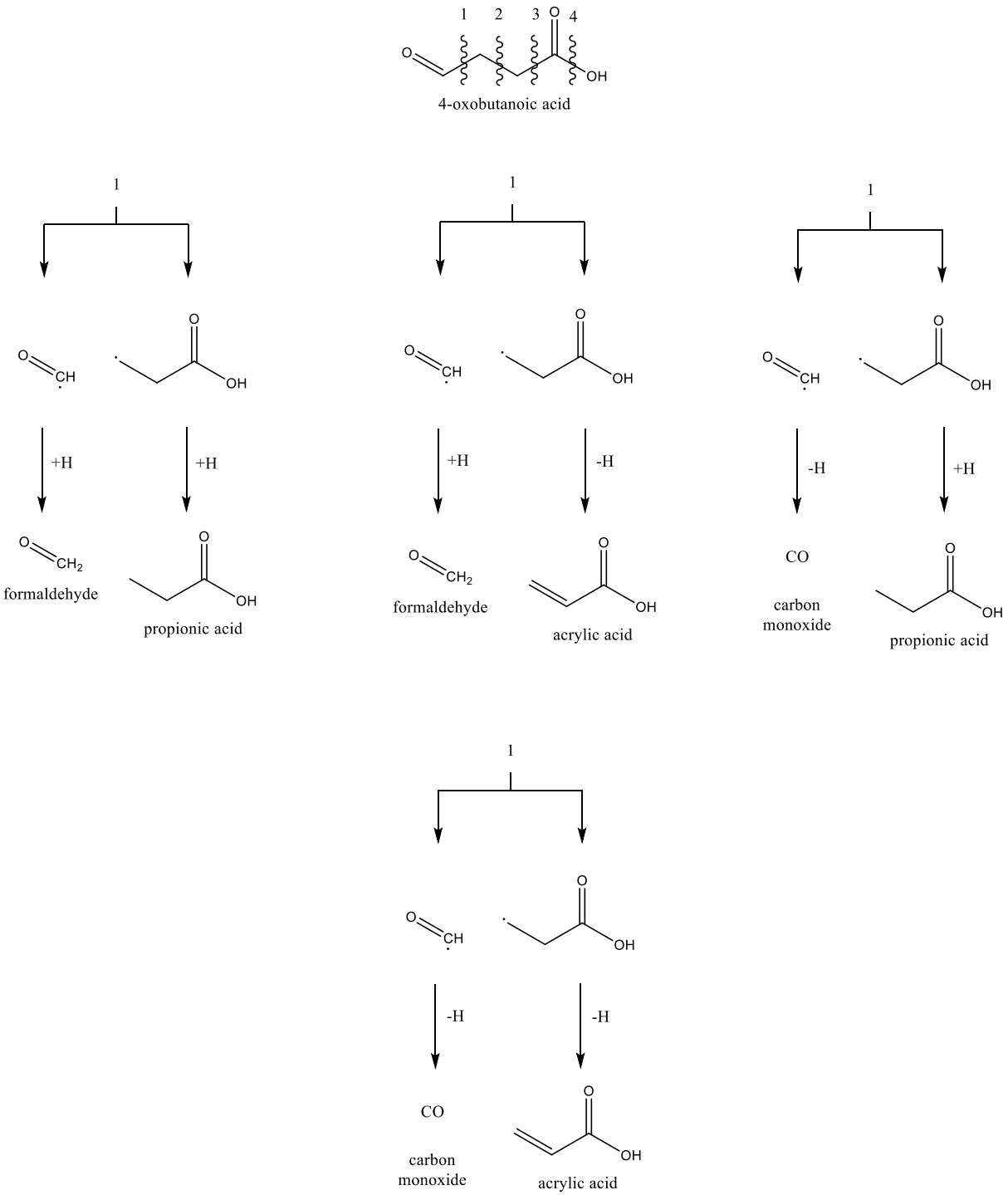

Figure S40A. Retrosynthesis of 4-oxobutanoic acid utilizing single-bond cleavage and subsequent hydrogen addition/elimination.

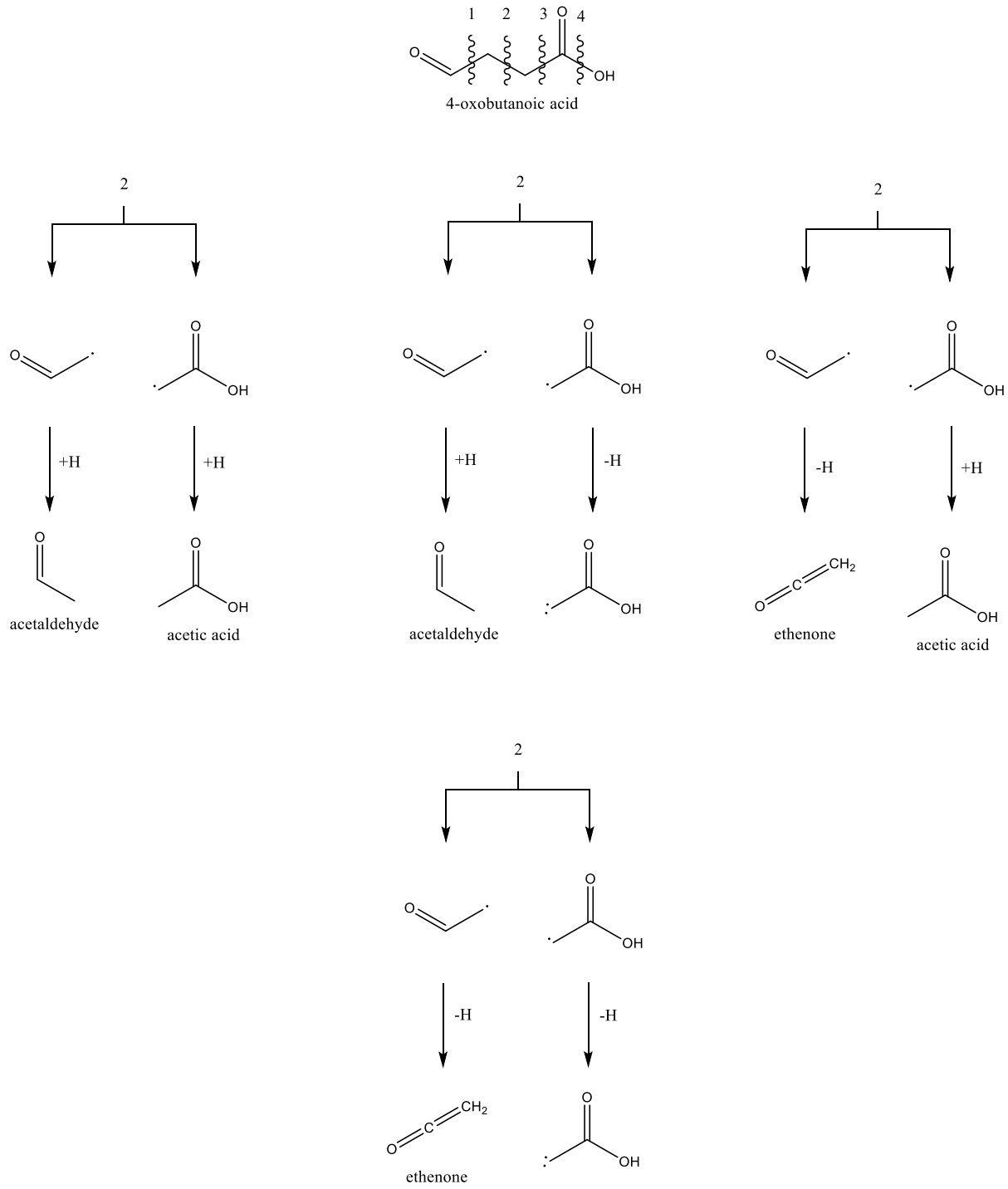

Figure S40B. Retrosynthesis of 4-oxobutanoic acid utilizing single-bond cleavage and subsequent hydrogen addition/elimination.

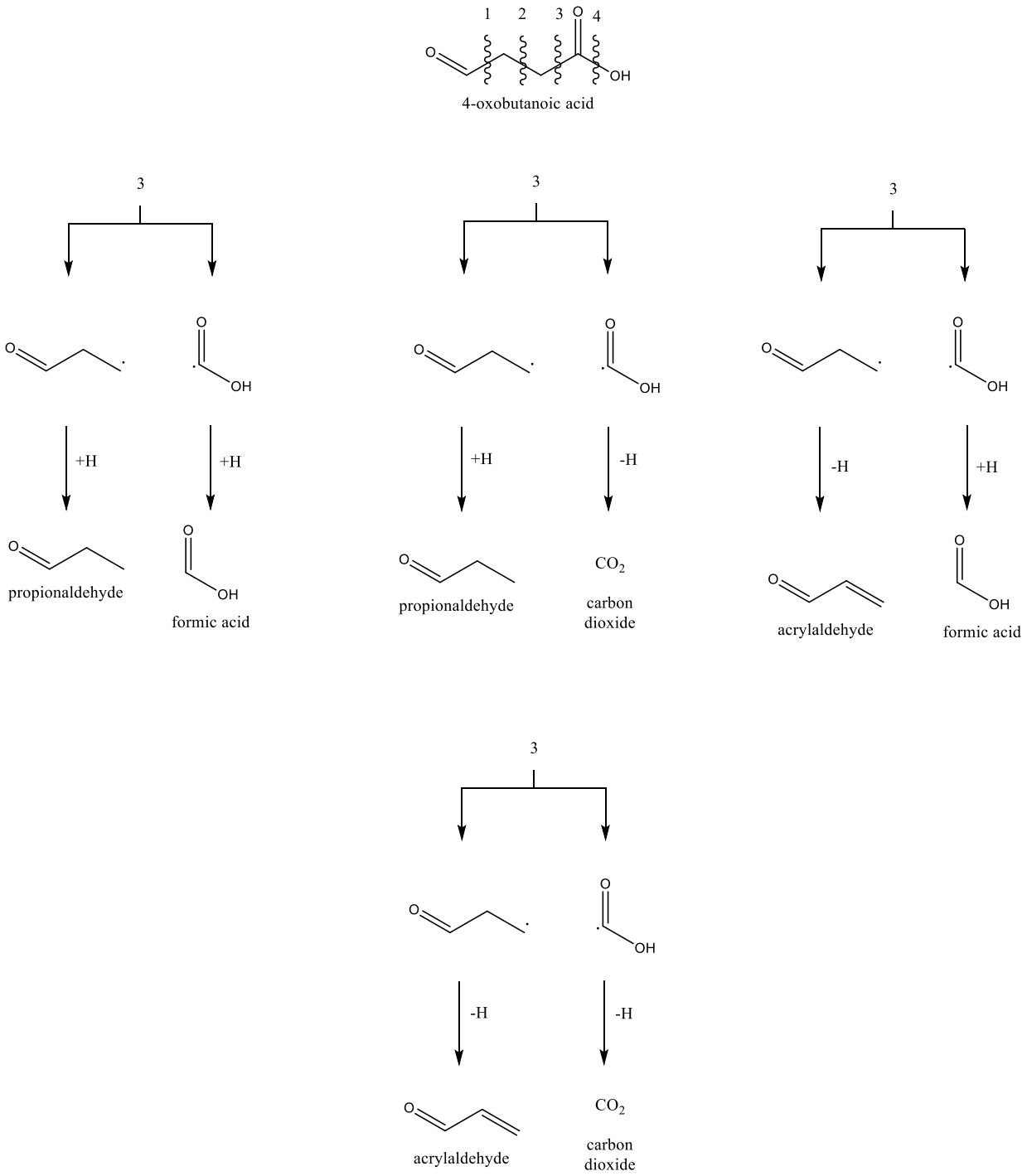

Figure S40C. Retrosynthesis of 4-oxobutanoic acid utilizing single-bond cleavage and subsequent hydrogen addition/elimination.

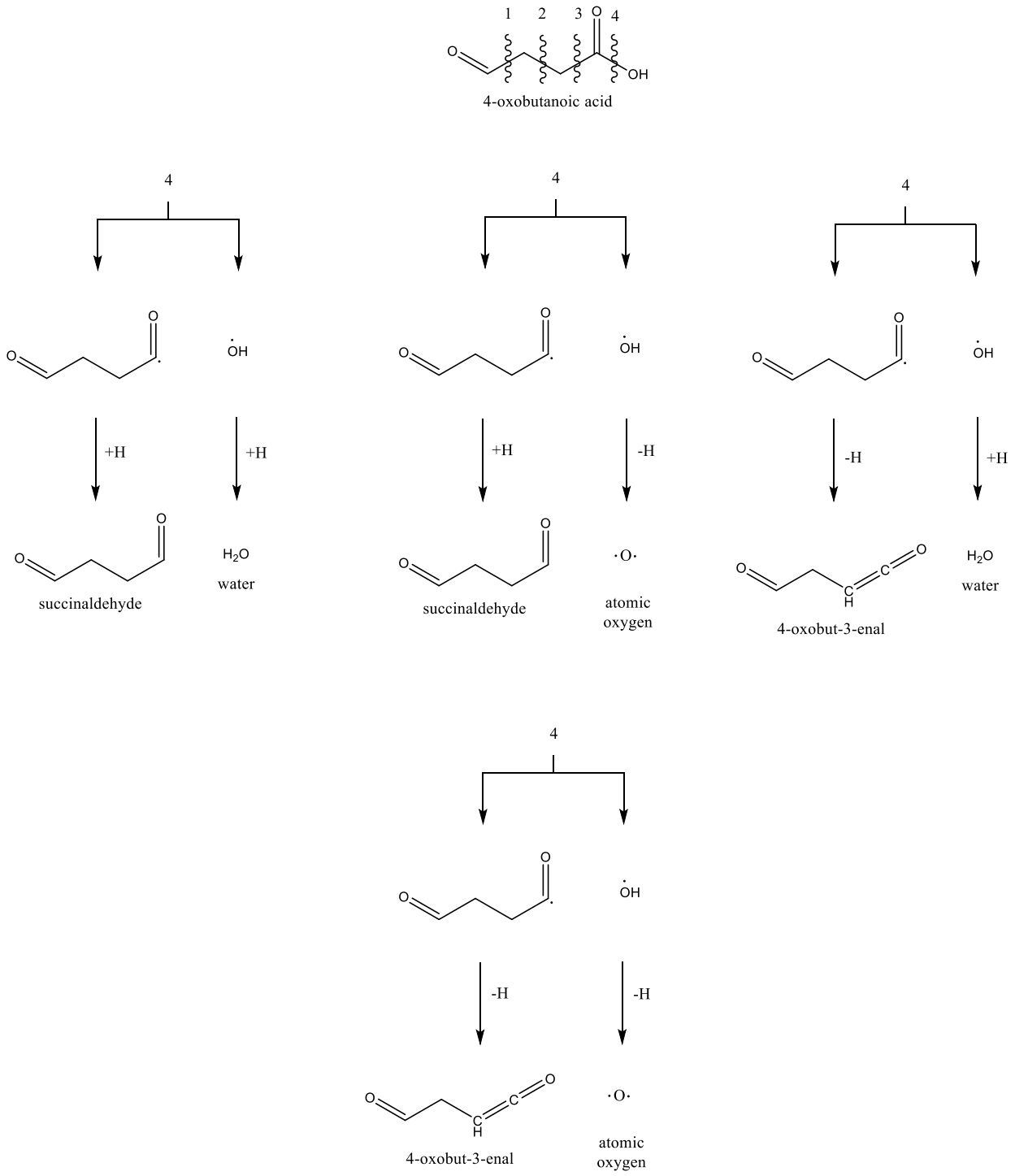

Figure S40D. Retrosynthesis of 4-oxobutanoic acid utilizing single-bond cleavage and subsequent hydrogen addition/elimination.

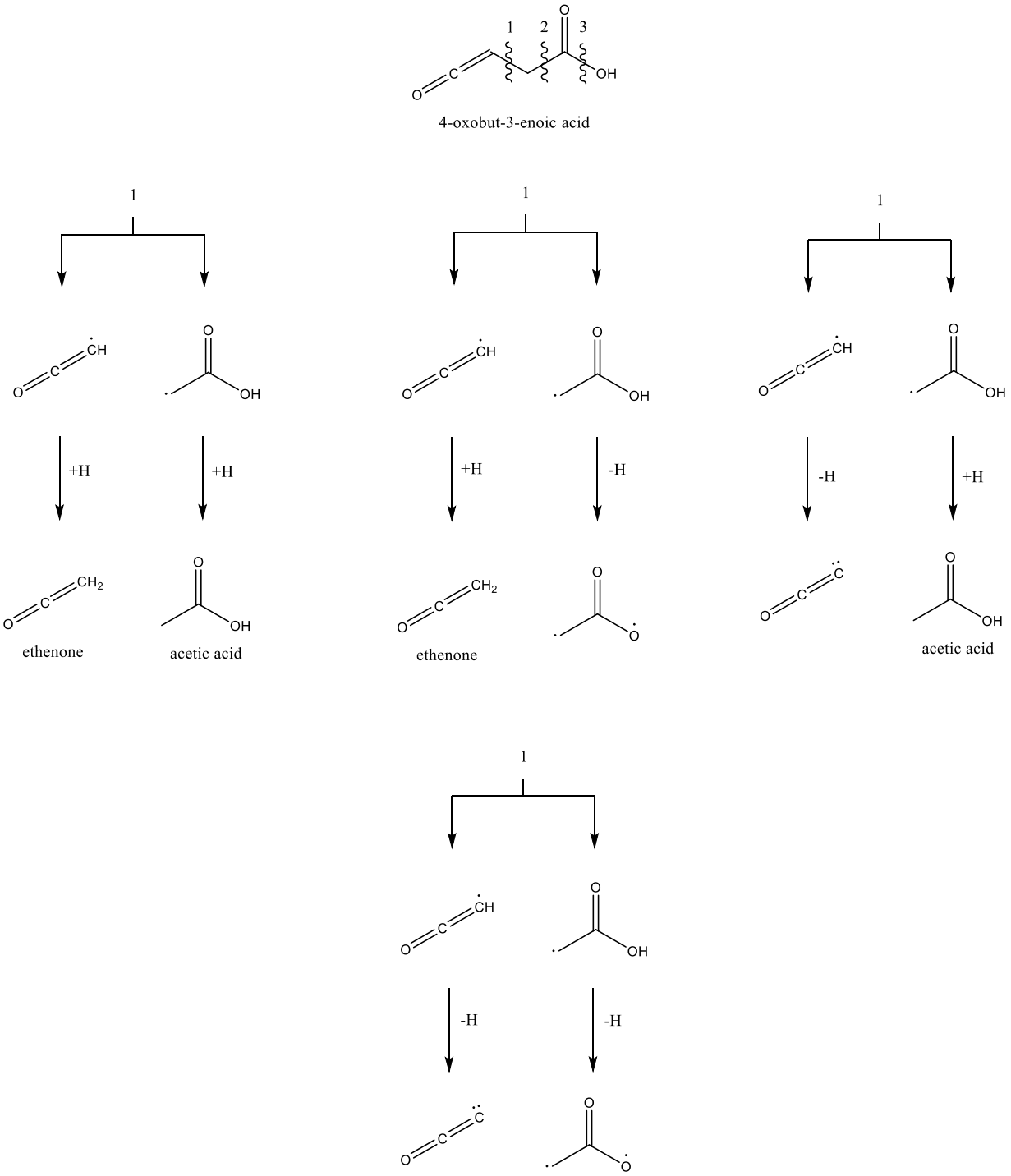

Figure S41A. Retrosynthesis of 4-oxobutanoic acid utilizing single-bond cleavage and subsequent hydrogen addition/elimination.

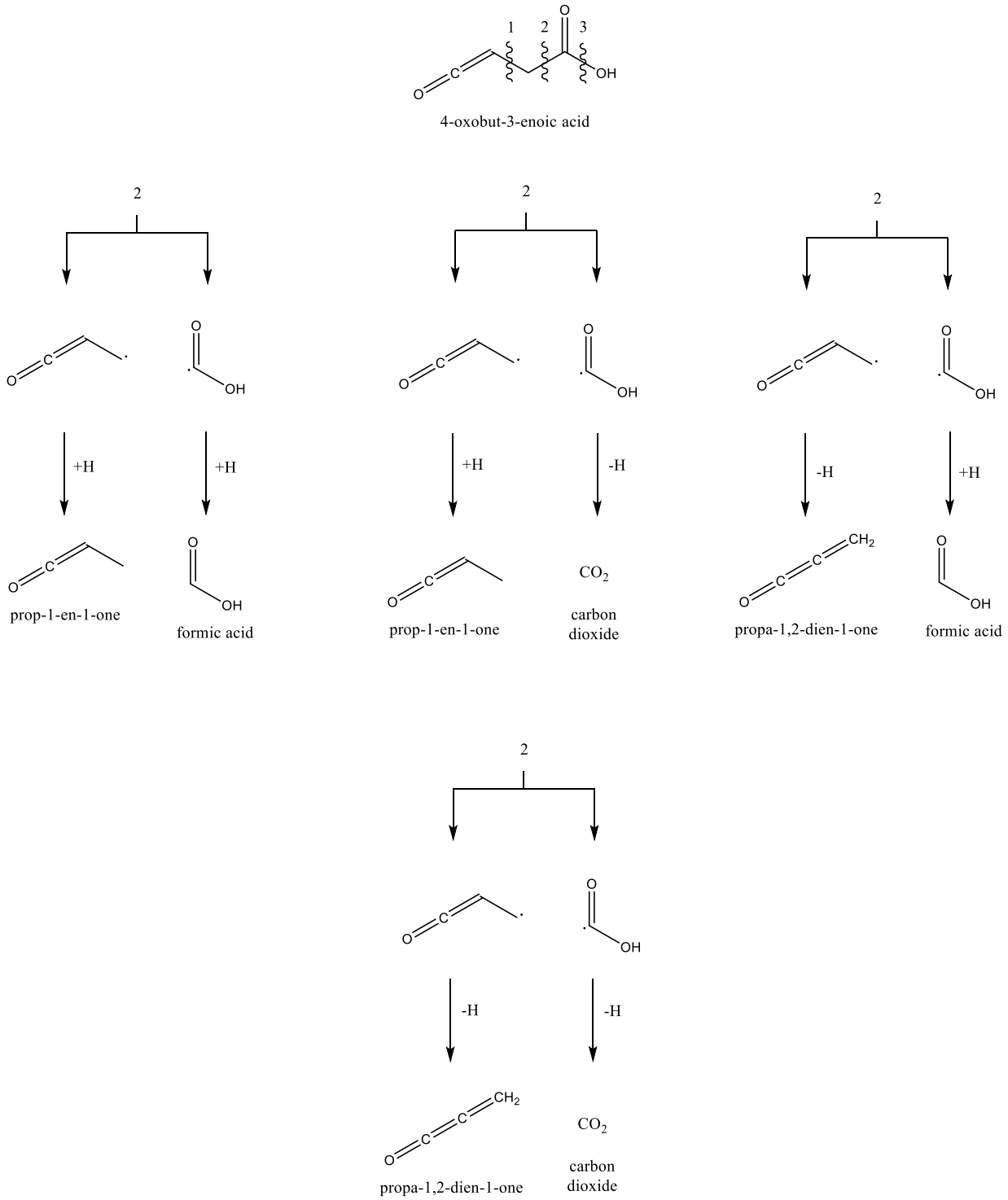

Figure S41B. Retrosynthesis of 4-oxobutanoic acid utilizing single-bond cleavage and subsequent hydrogen addition/elimination.

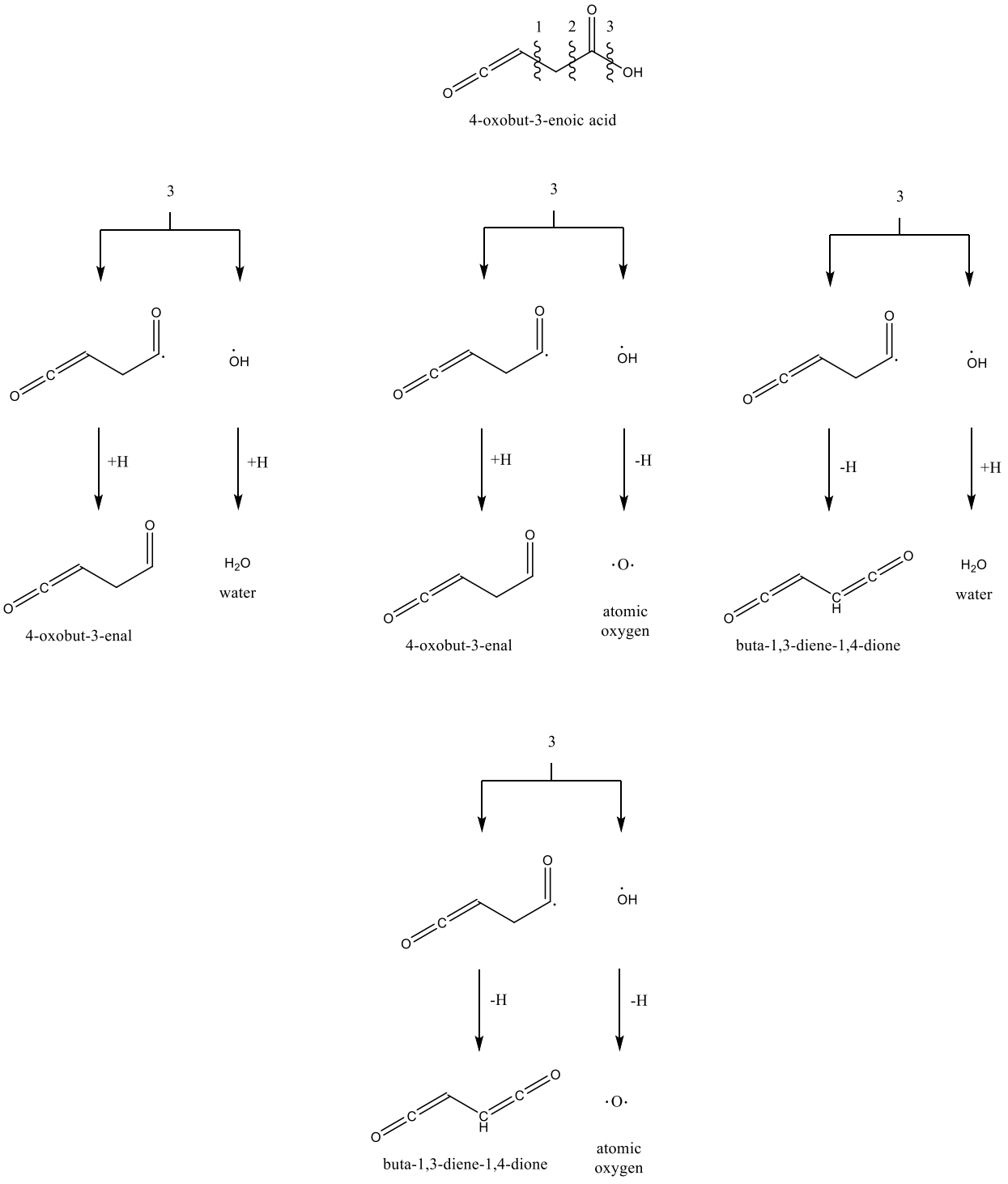

Figure S41C. Retrosynthesis of 4-oxobutanoic acid utilizing single-bond cleavage and subsequent hydrogen addition/elimination.

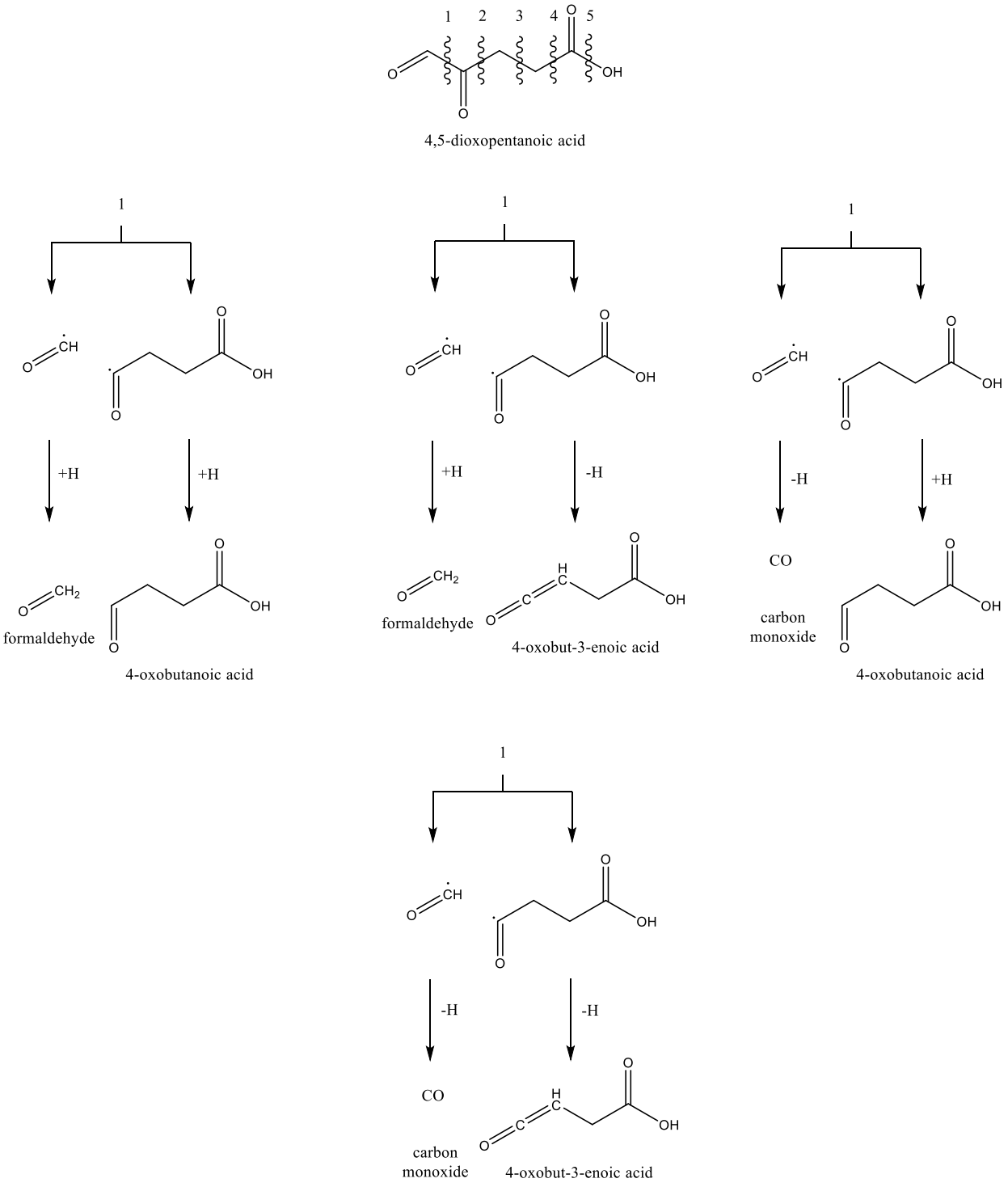

Figure S42A. Retrosynthesis of 4,5-dioxopentanoic acid utilizing single-bond cleavage and subsequent hydrogen addition/elimination.

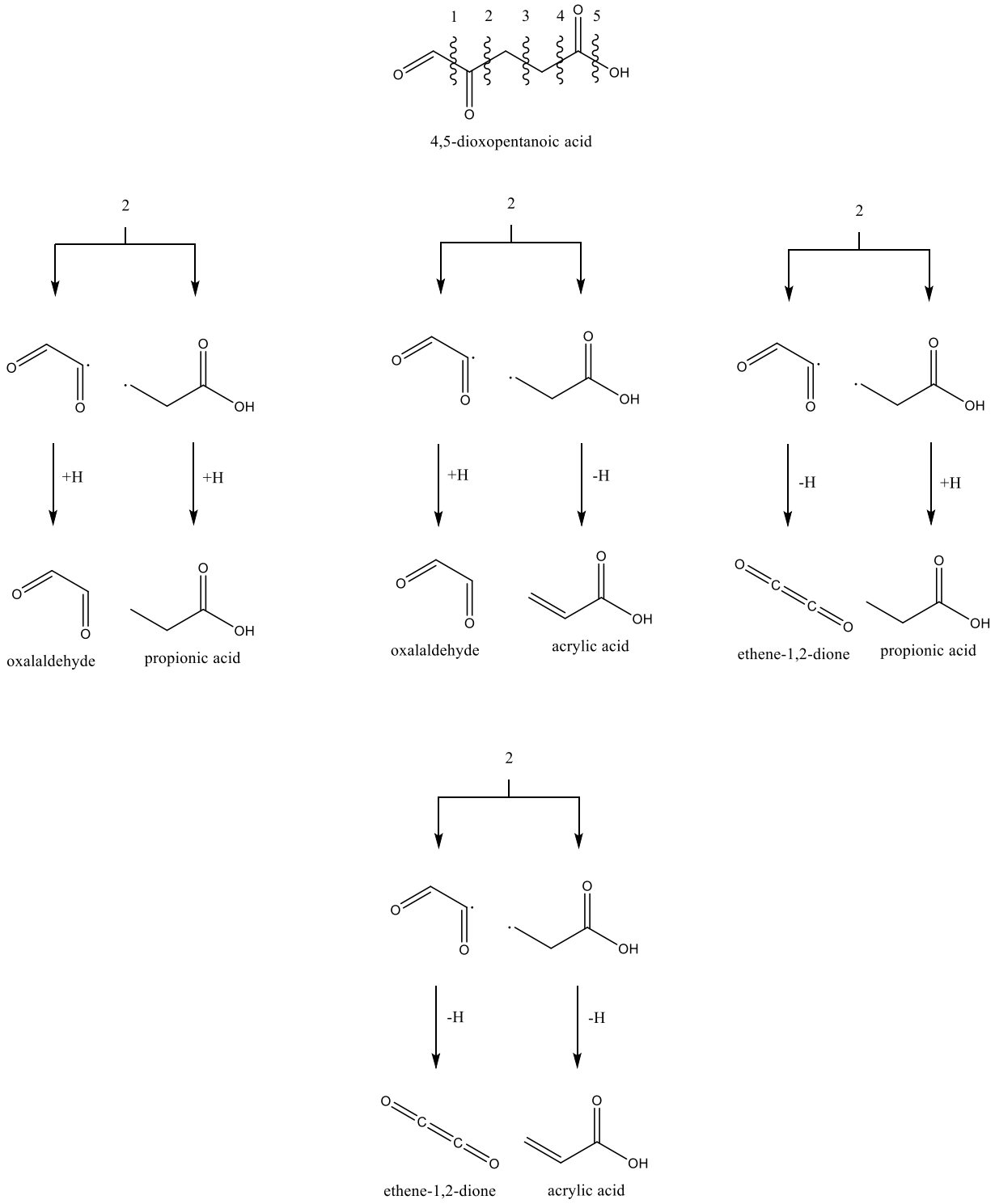

Figure S42B. Retrosynthesis of 4,5-dioxopentanoic acid utilizing single-bond cleavage and subsequent hydrogen addition/elimination.

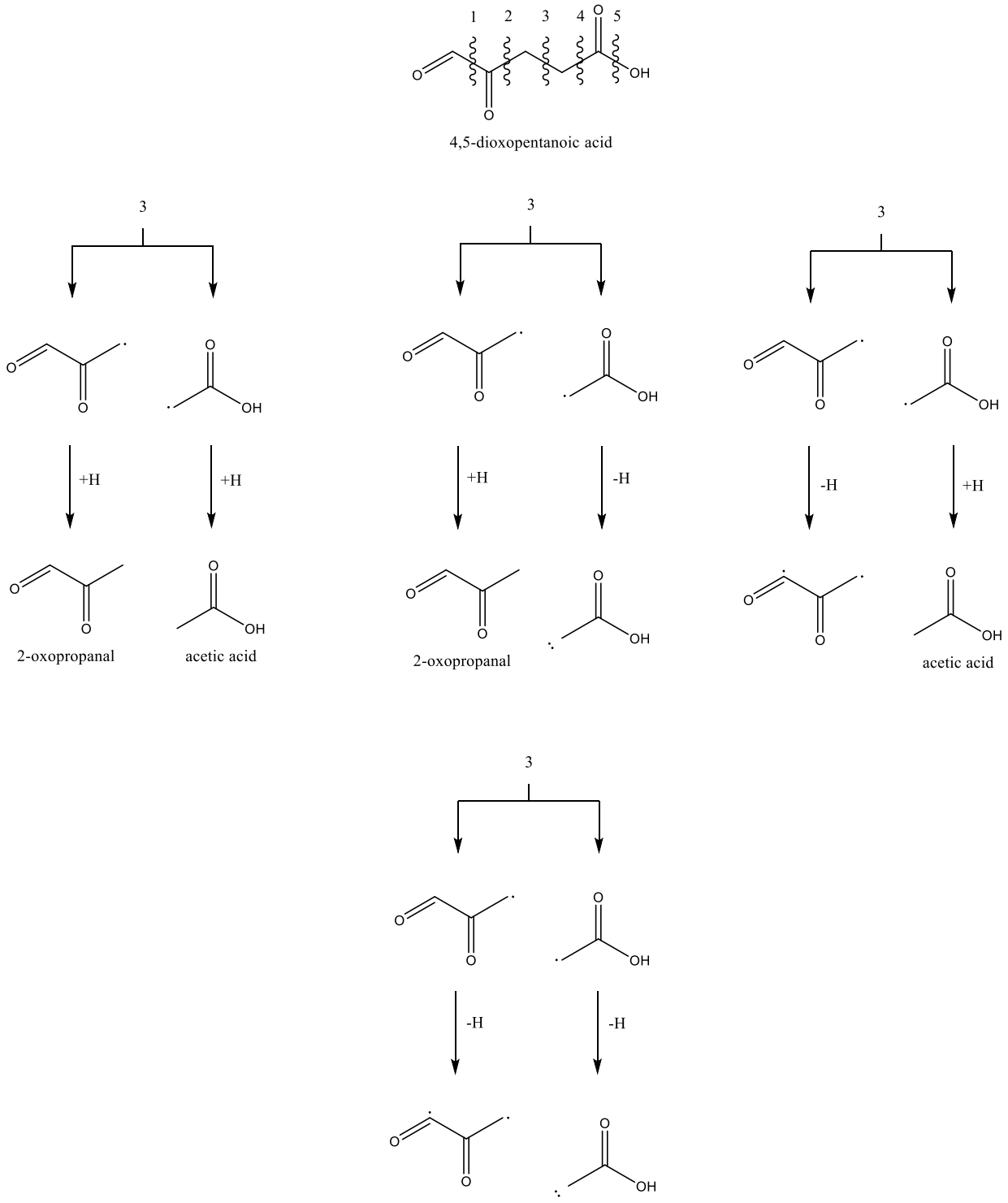

Figure S42C. Retrosynthesis of 4,5-dioxopentanoic acid utilizing single-bond cleavage and subsequent hydrogen addition/elimination.

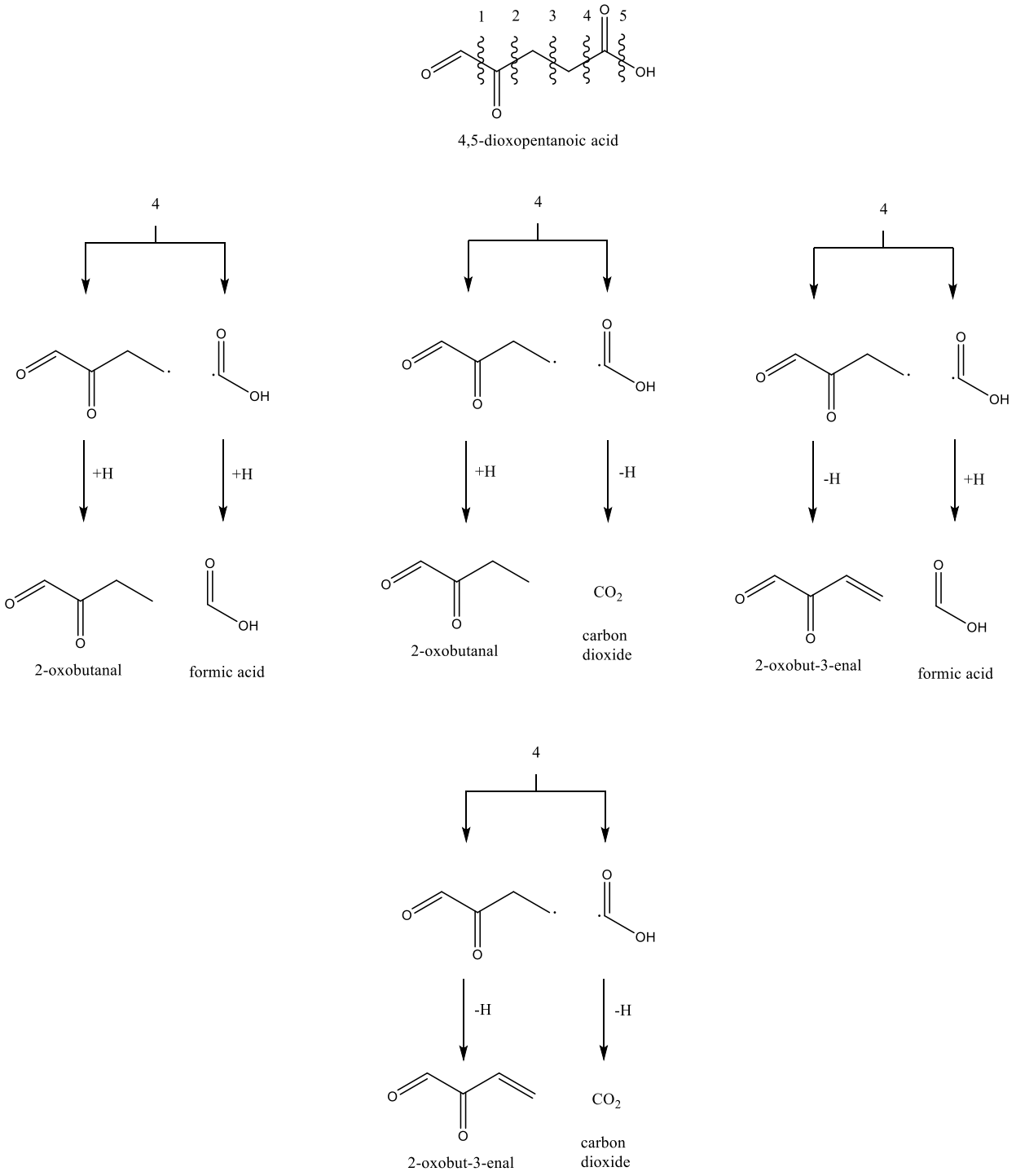

Figure S42D. Retrosynthesis of 4,5-dioxopentanoic acid utilizing single-bond cleavage and subsequent hydrogen addition/elimination.

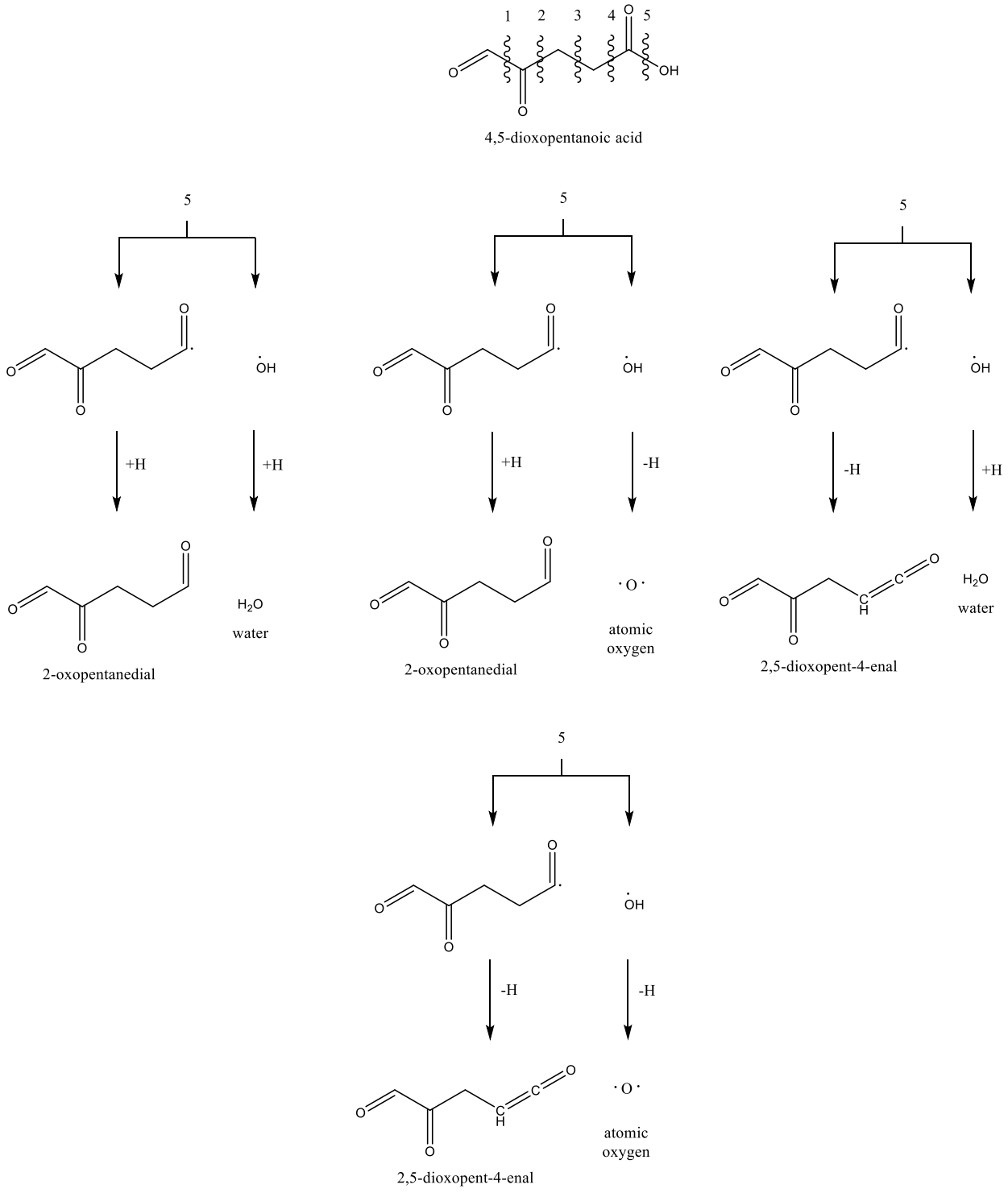

Figure S42E. Retrosynthesis of 4,5-dioxopentanoic acid utilizing single-bond cleavage and subsequent hydrogen addition/elimination.

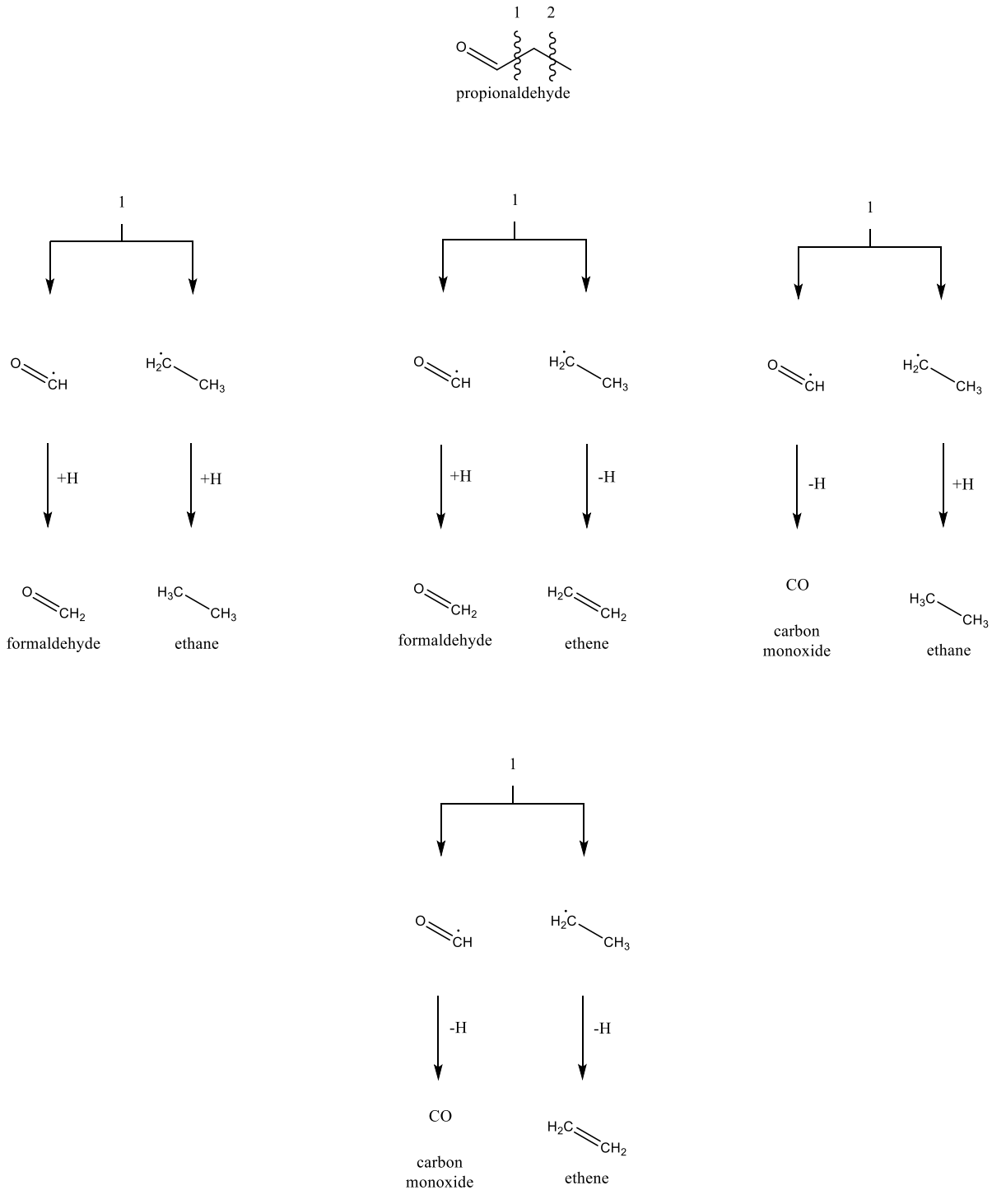

Figure S43A. Retrosynthesis of propionaldehyde utilizing single-bond cleavage and subsequent hydrogen addition/elimination.

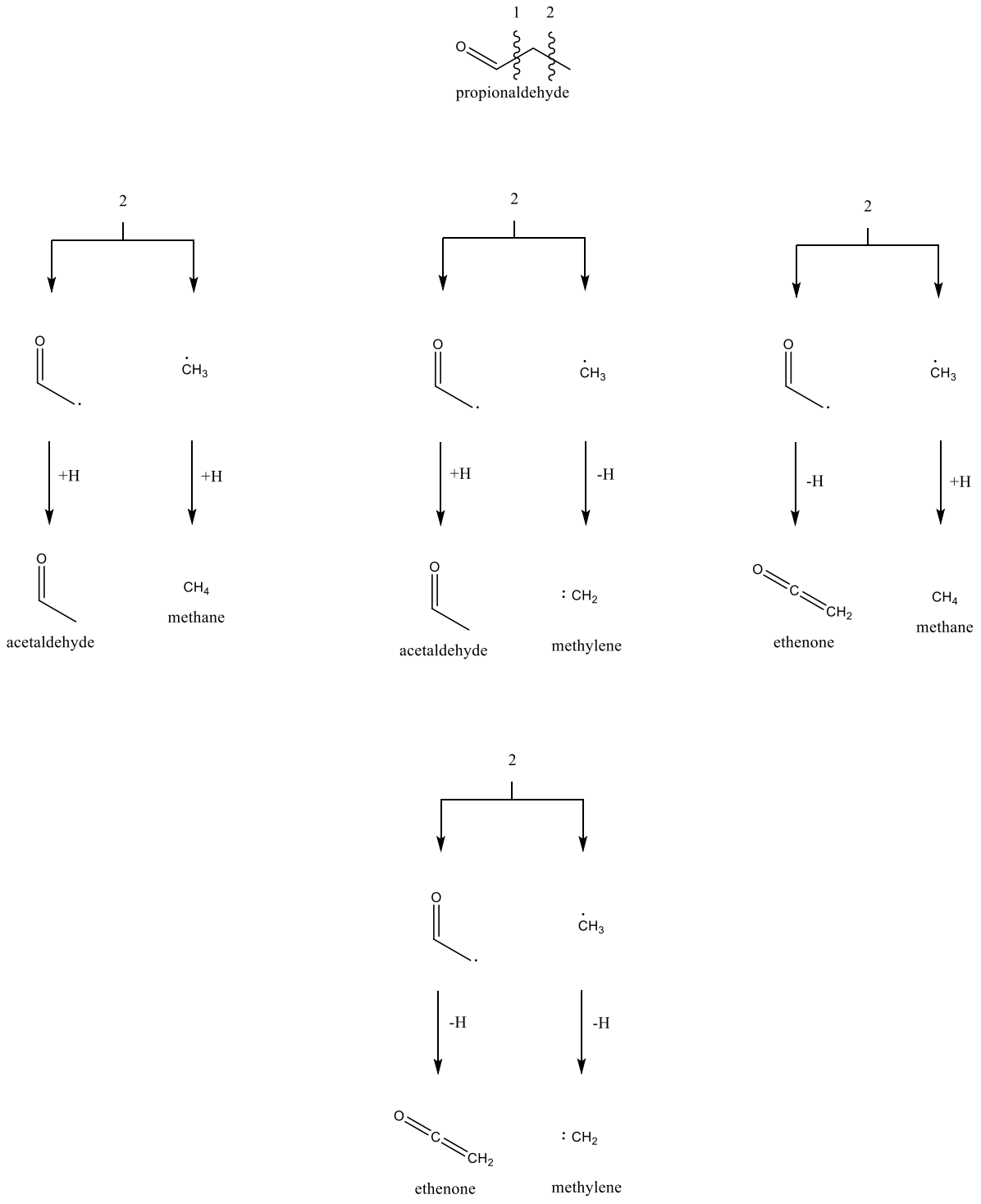

Figure S43B. Retrosynthesis of propionaldehyde utilizing single-bond cleavage and subsequent hydrogen addition/elimination.

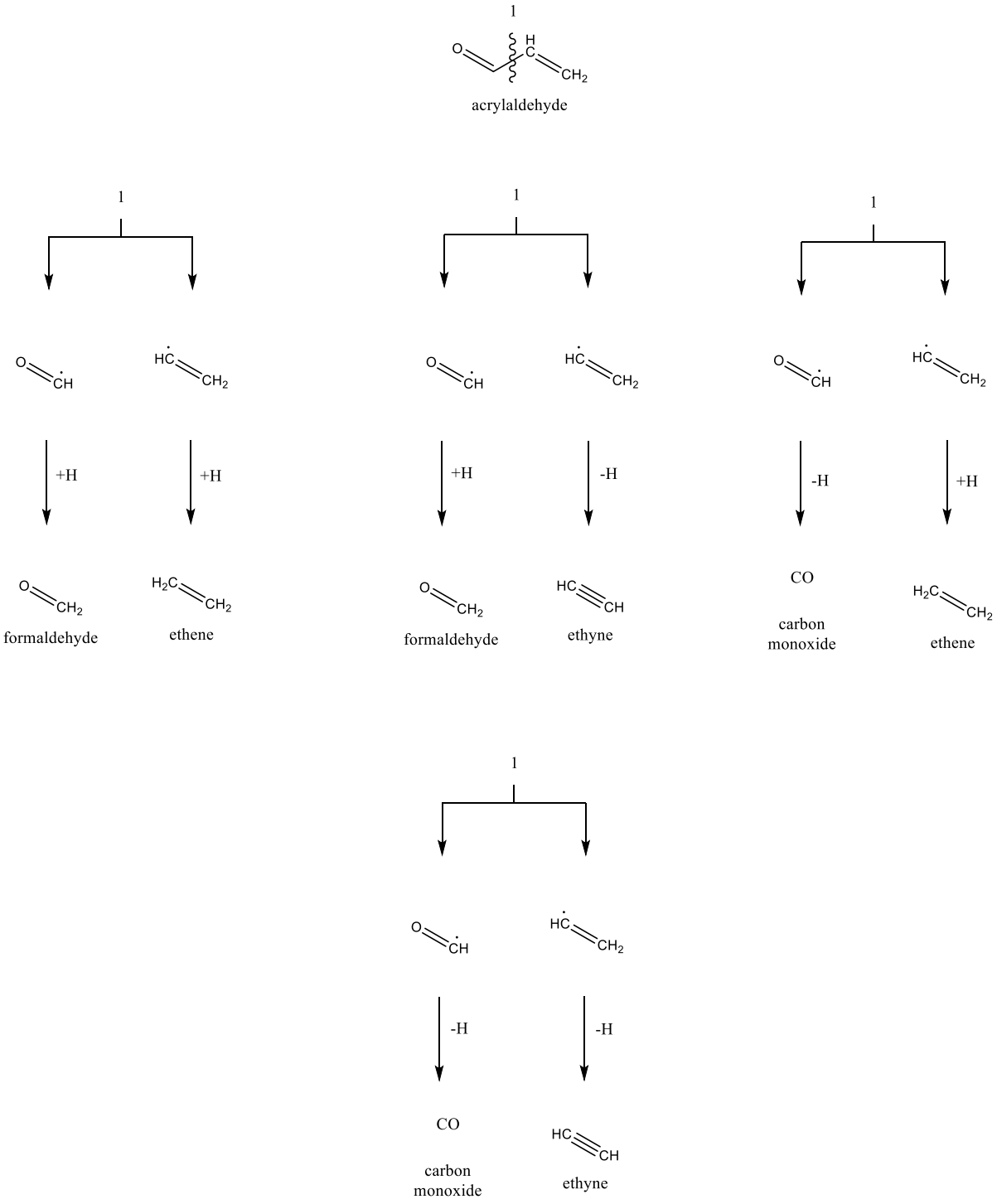

Figure S44. Retrosynthesis of acrylaldehyde utilizing single-bond cleavage and subsequent hydrogen addition/elimination.

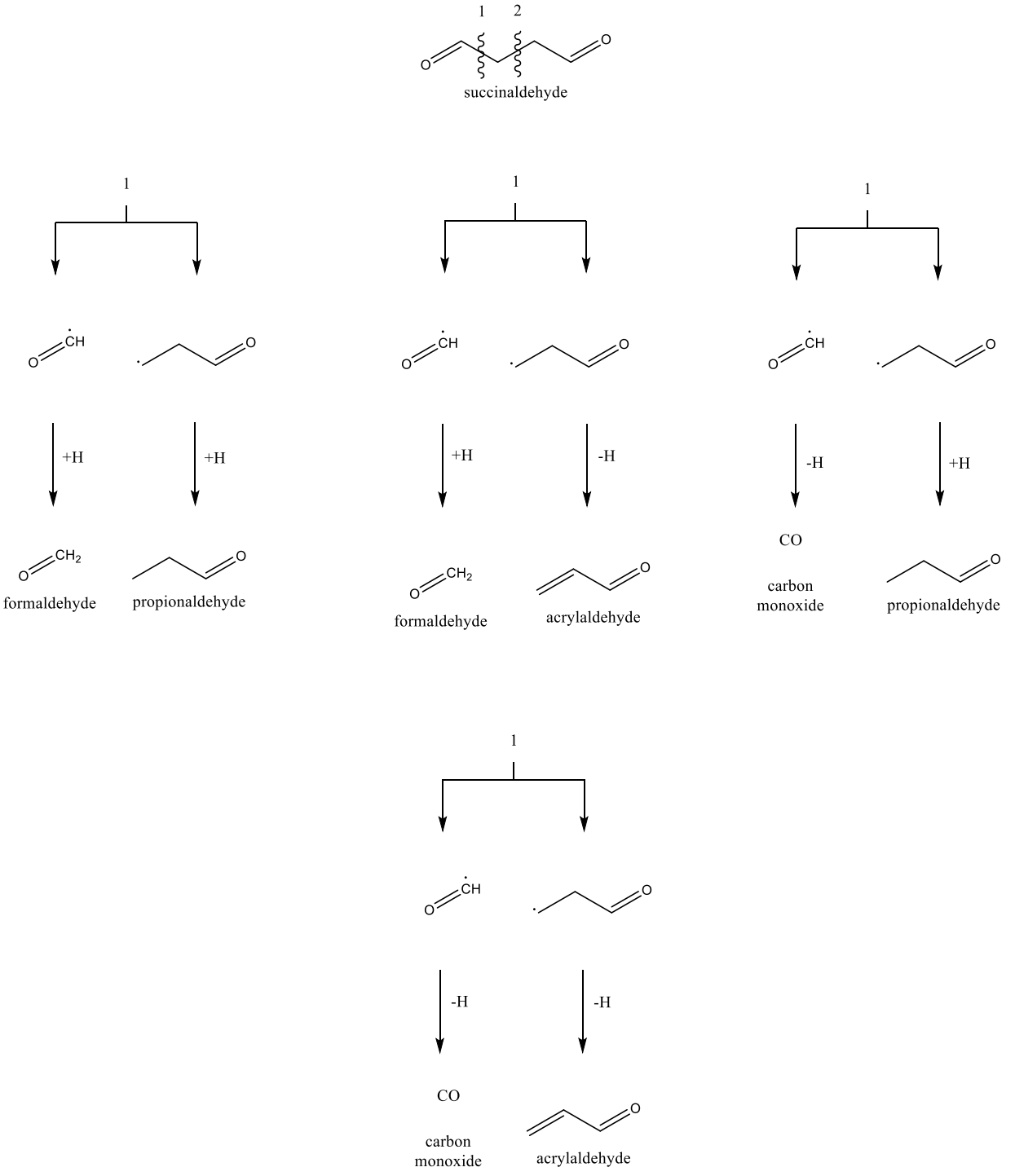

Figure S45A. Retrosynthesis of succinaldehyde utilizing single-bond cleavage and subsequent hydrogen addition/elimination.

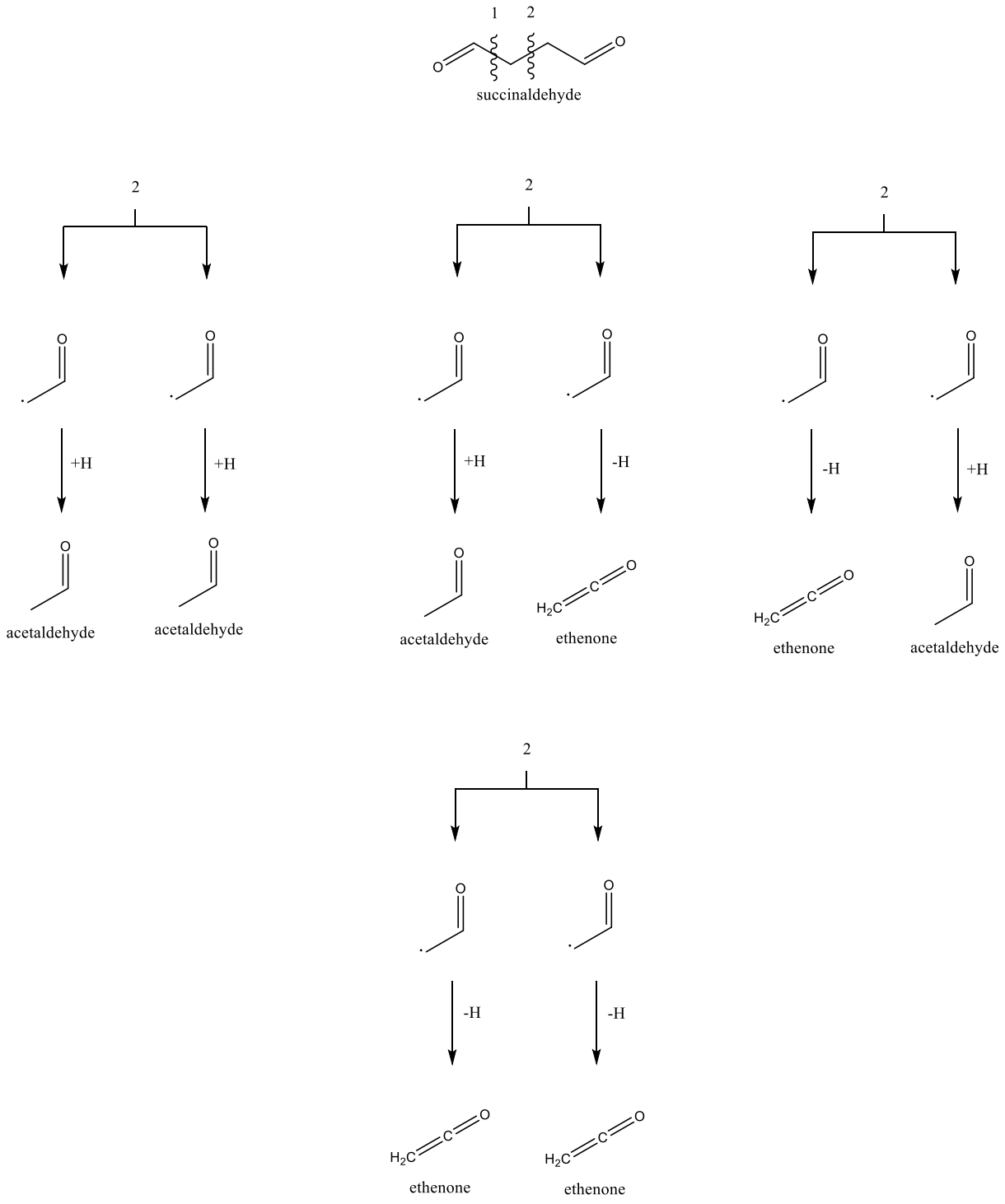

Figure S45B. Retrosynthesis of succinaldehyde utilizing single-bond cleavage and subsequent hydrogen addition/elimination.

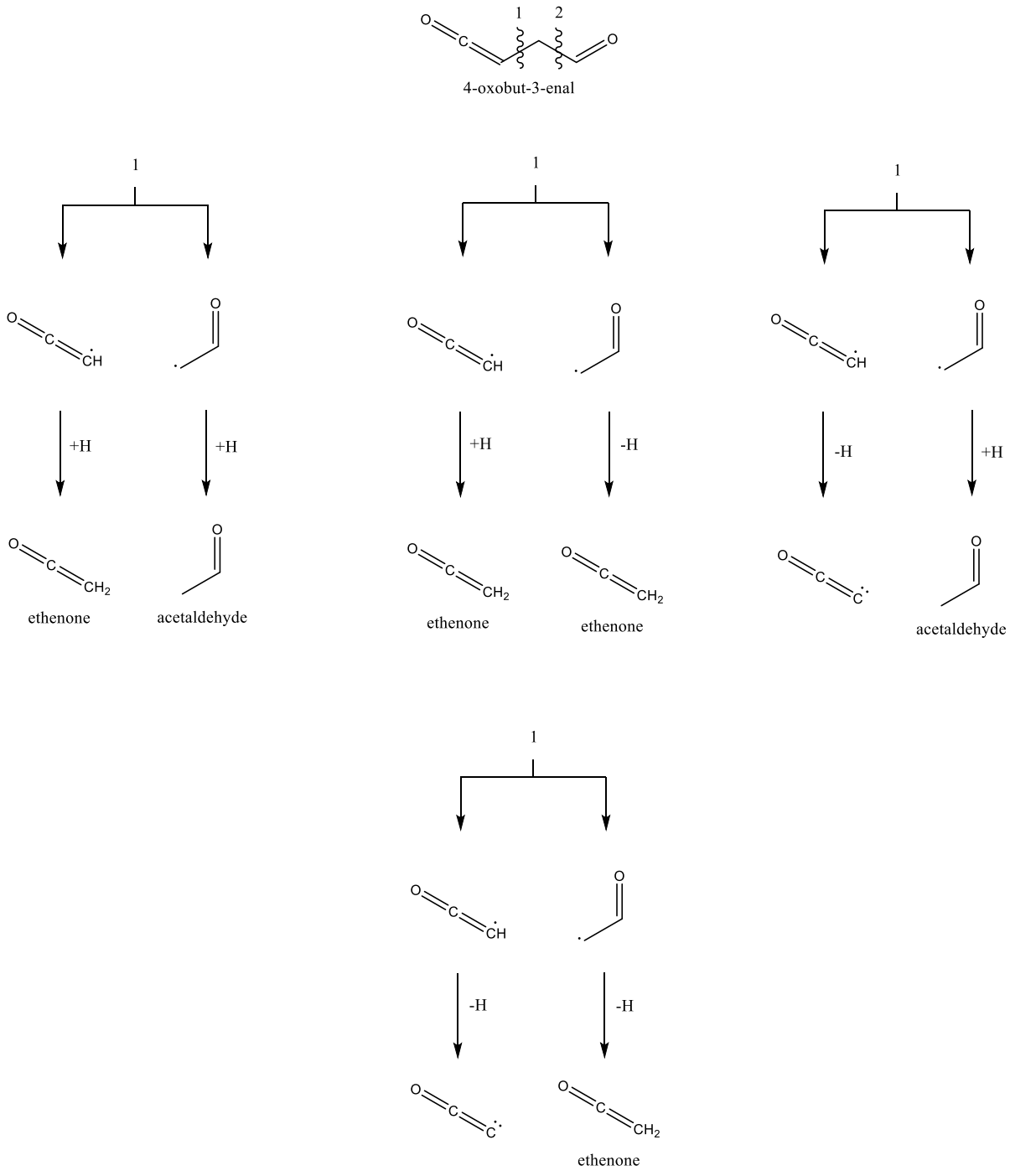

Figure S46A. Retrosynthesis of 4-oxobut-3-enal utilizing single-bond cleavage and subsequent hydrogen addition/elimination.

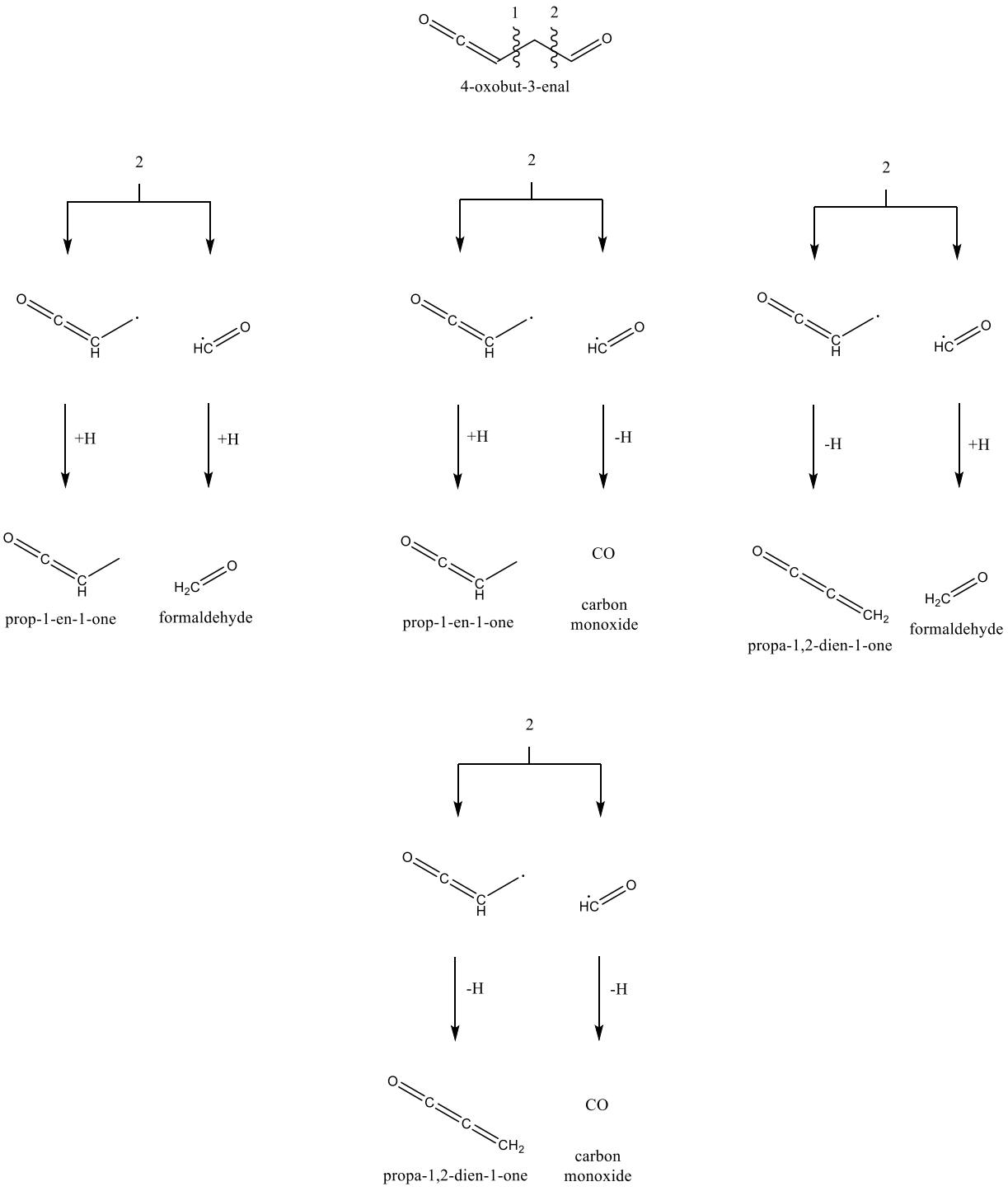

Figure S46B. Retrosynthesis of 4-oxobut-3-enal utilizing single-bond cleavage and subsequent hydrogen addition/elimination.

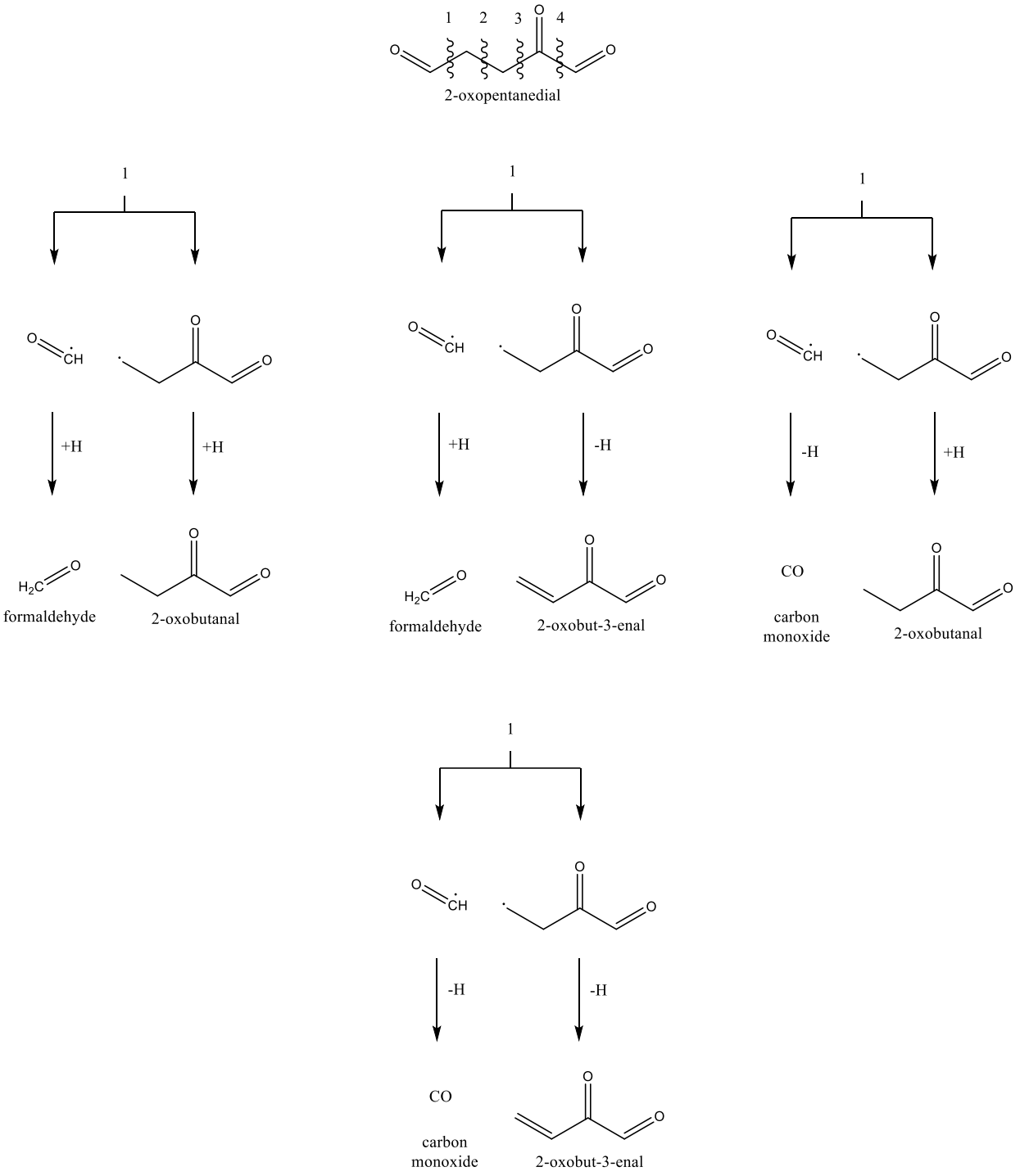

Figure S47A. Retrosynthesis of 2-oxopentanedial utilizing single-bond cleavage and subsequent hydrogen addition/elimination.

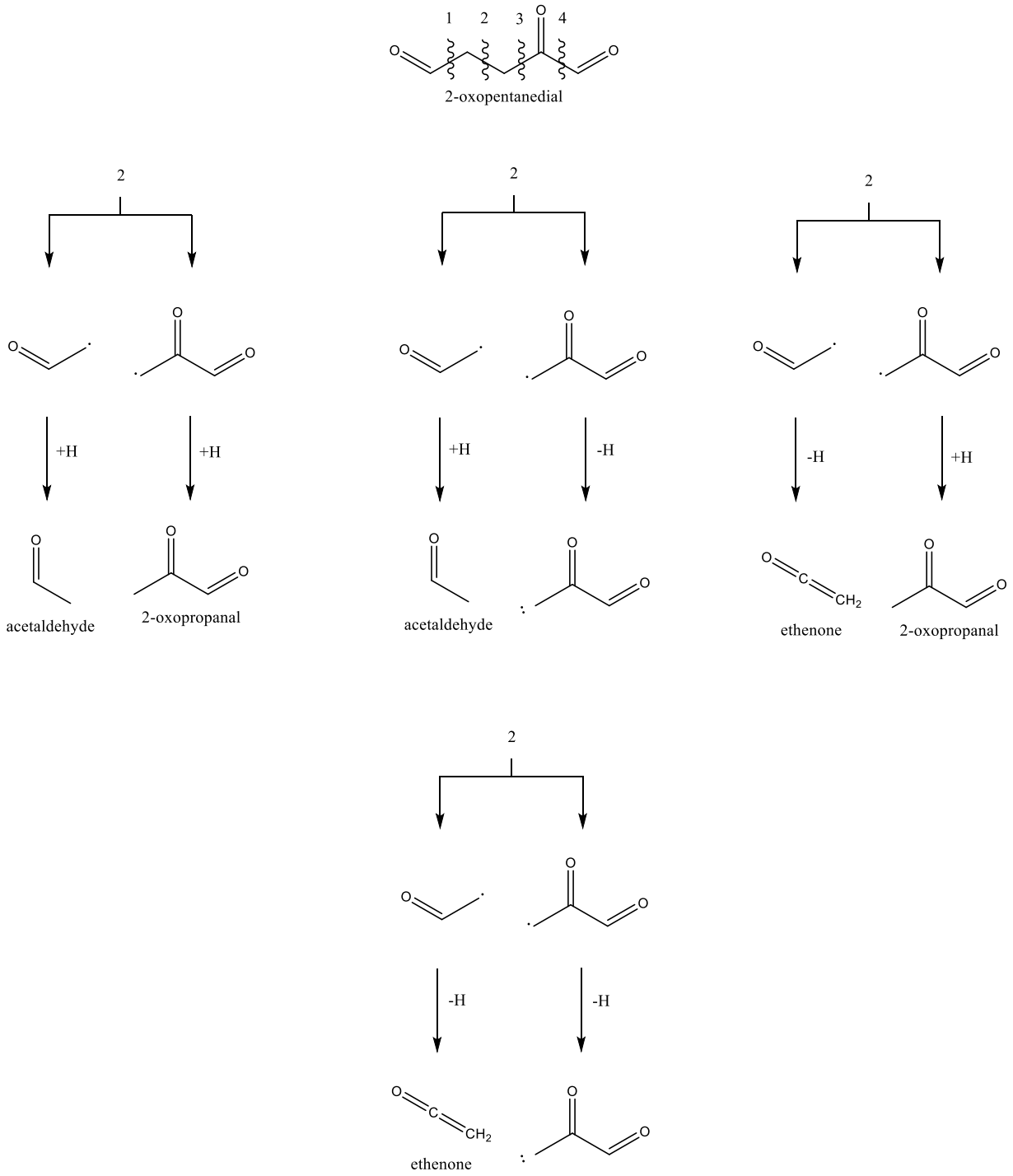

Figure S47B. Retrosynthesis of 2-oxopentanedial utilizing single-bond cleavage and subsequent hydrogen addition/elimination.

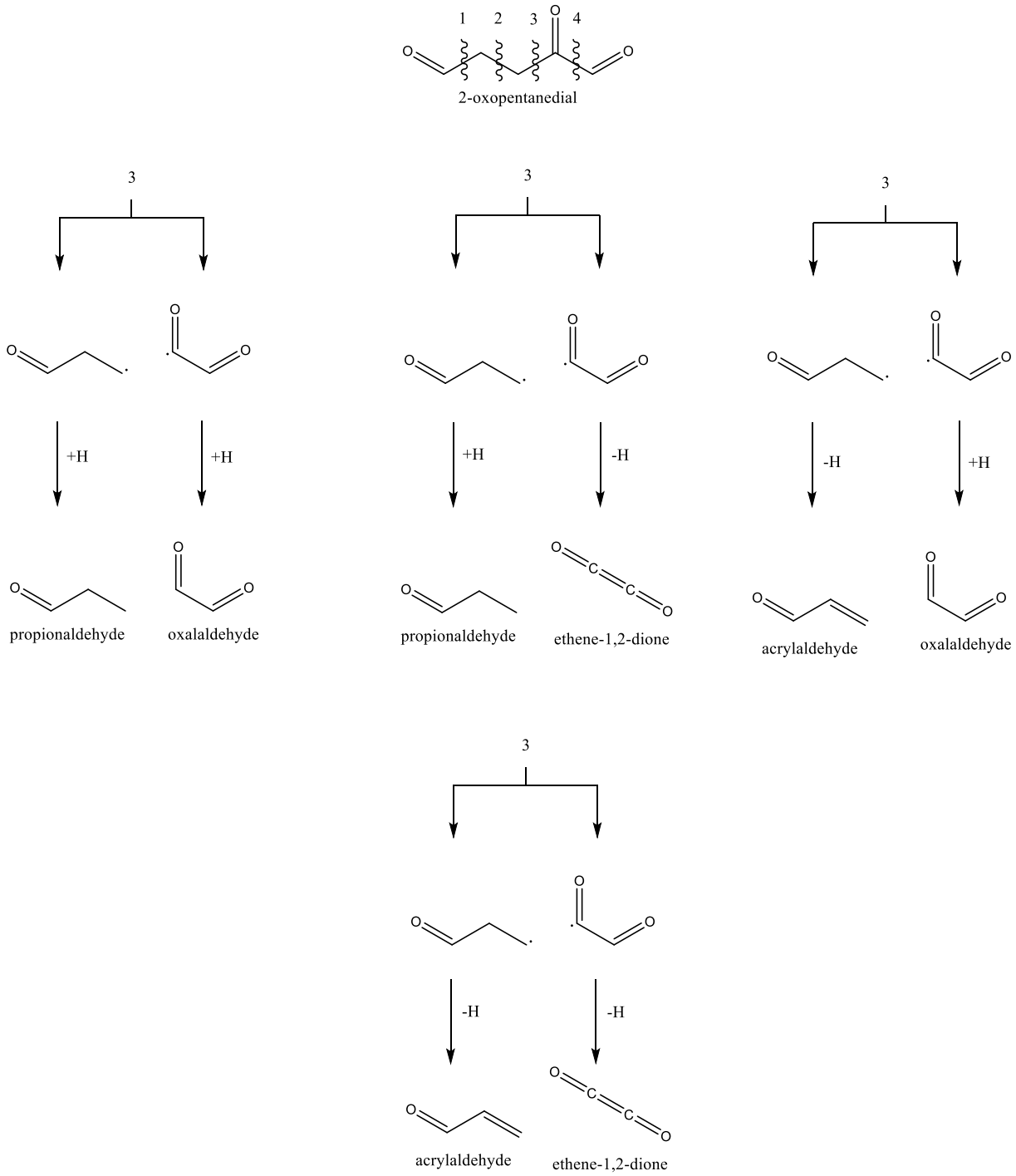

Figure S47C. Retrosynthesis of 2-oxopentanedial utilizing single-bond cleavage and subsequent hydrogen addition/elimination.

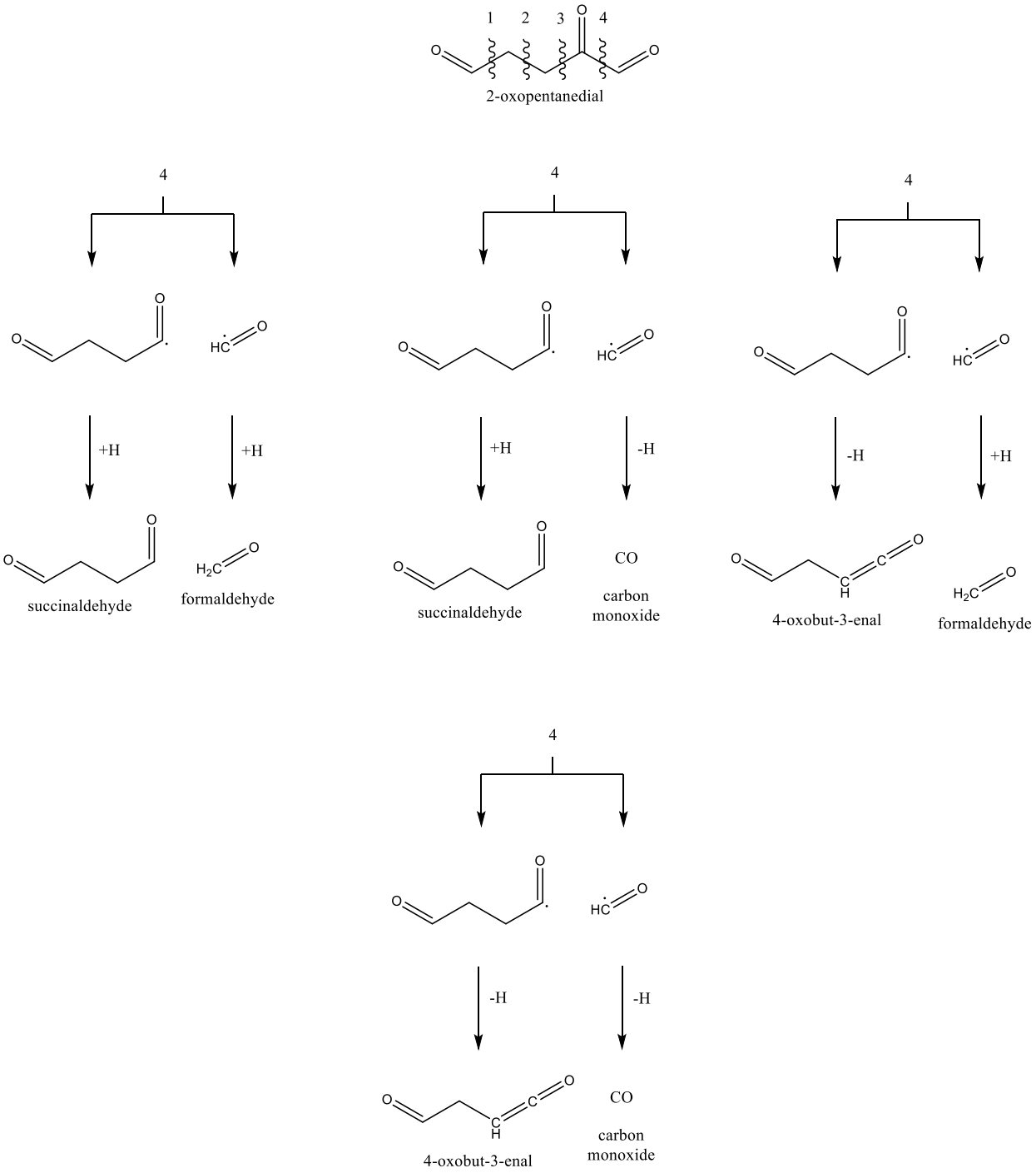

Figure S47D. Retrosynthesis of 2-oxopentanedial utilizing single-bond cleavage and subsequent hydrogen addition/elimination.

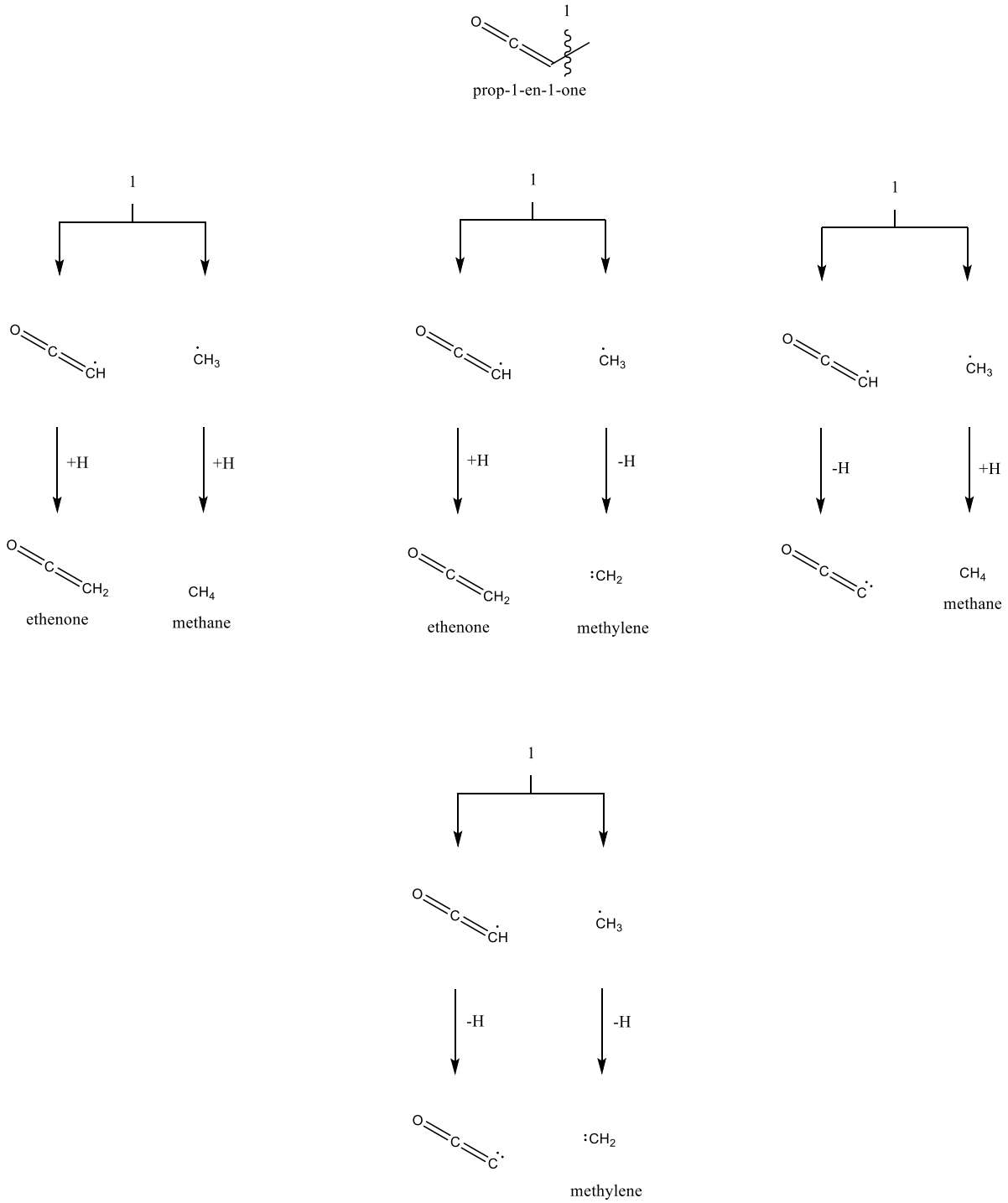

Figure S48. Retrosynthesis of prop-1-en-1-one utilizing single-bond cleavage and subsequent hydrogen addition/elimination.

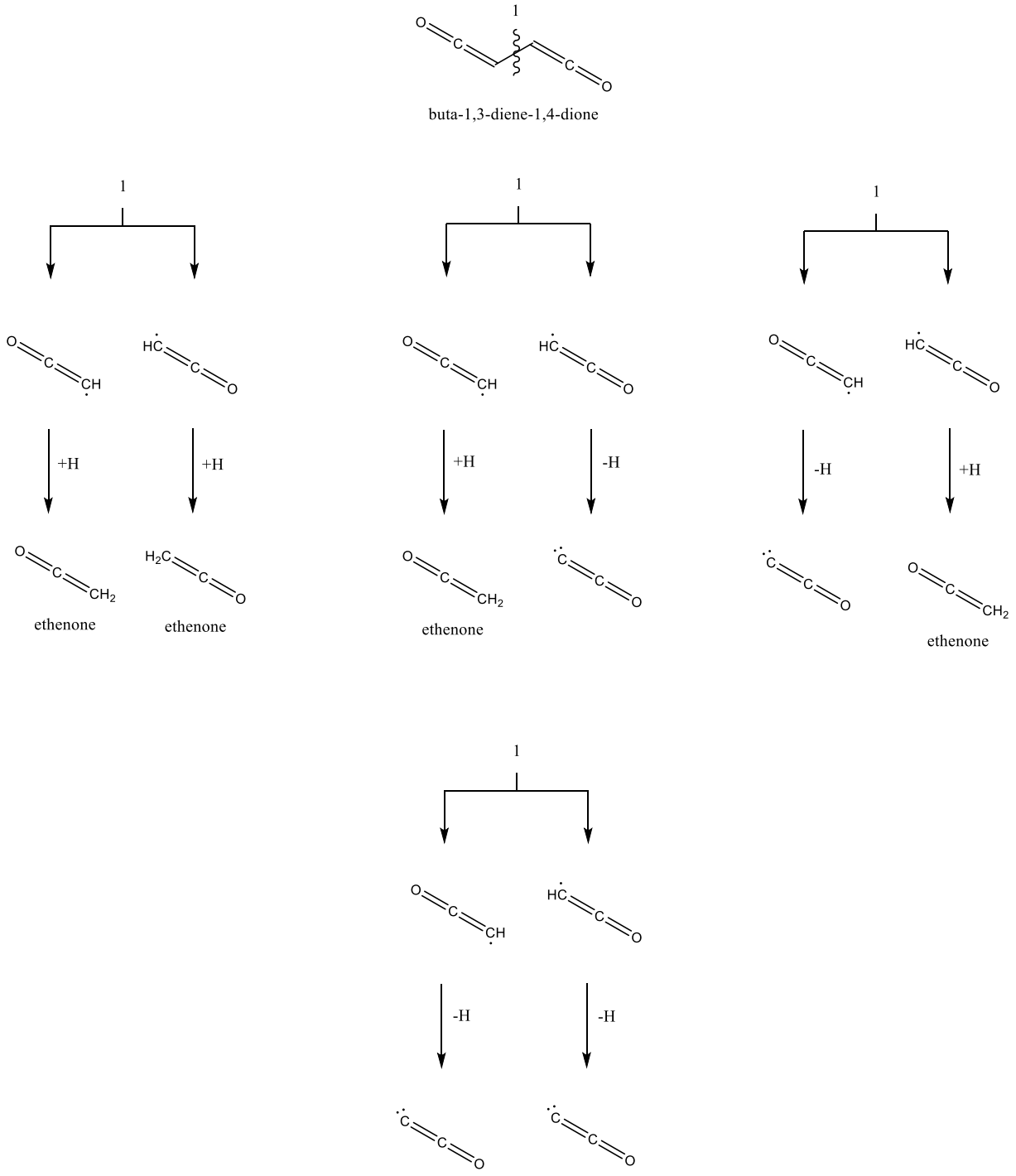

Figure S49. Retrosynthesis of buta-1,3-diene-1,4-dione utilizing single-bond cleavage and subsequent hydrogen addition/elimination.

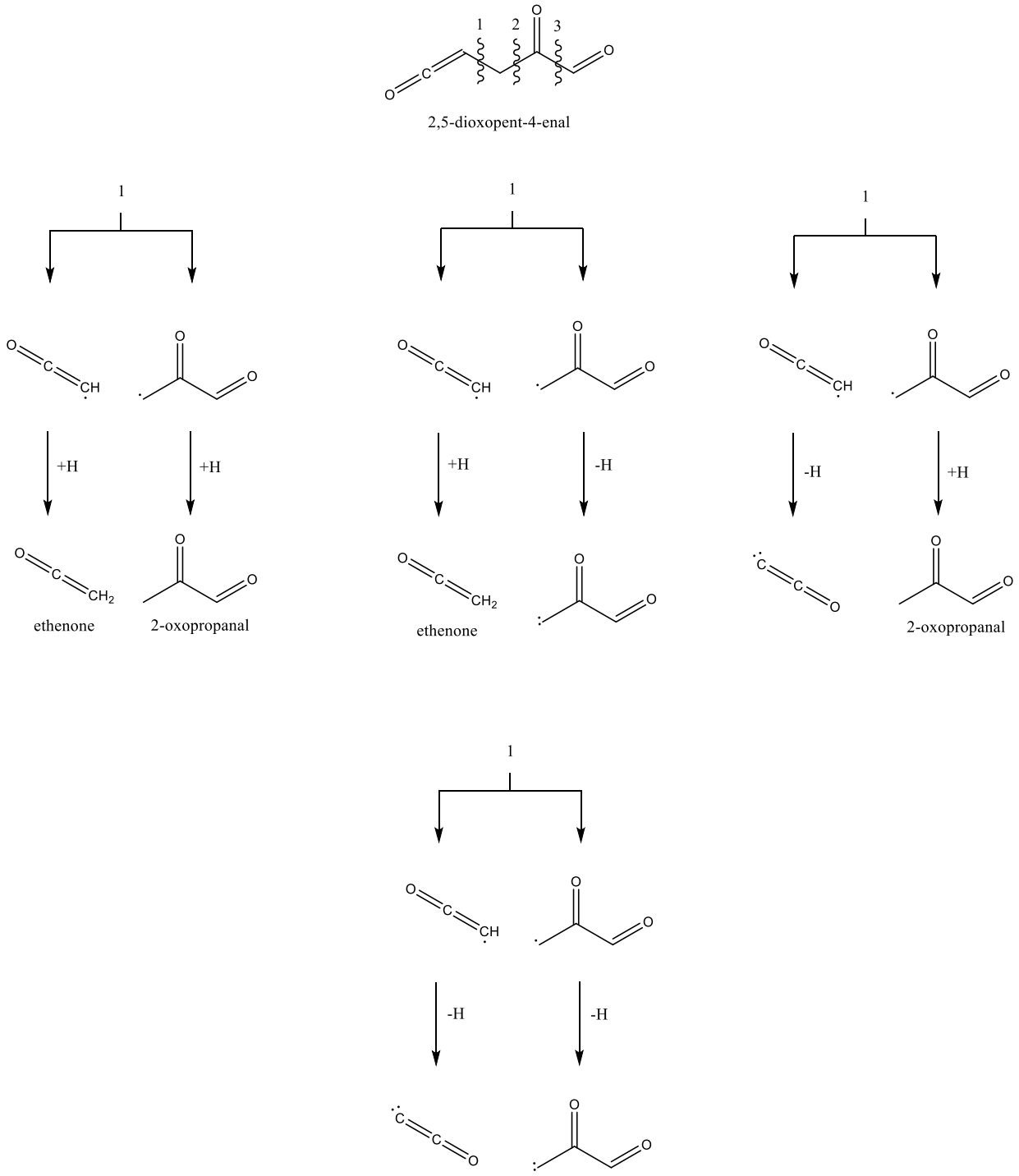

Figure S50A. Retrosynthesis of 2,5-dioxopent-4-enal utilizing single-bond cleavage and subsequent hydrogen addition/elimination.

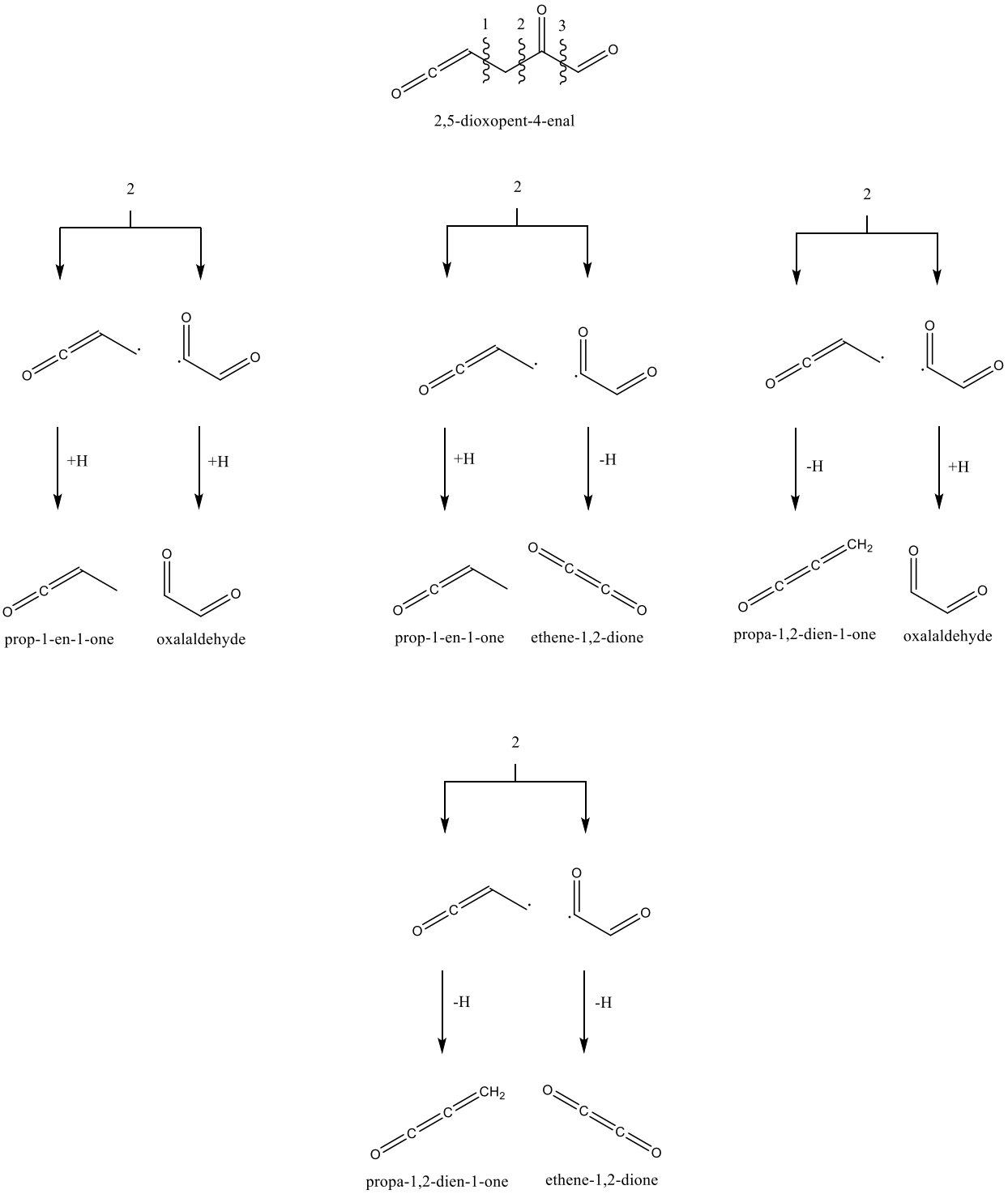

Figure S50B. Retrosynthesis of 2,5-dioxopent-4-enal utilizing single-bond cleavage and subsequent hydrogen addition/elimination.

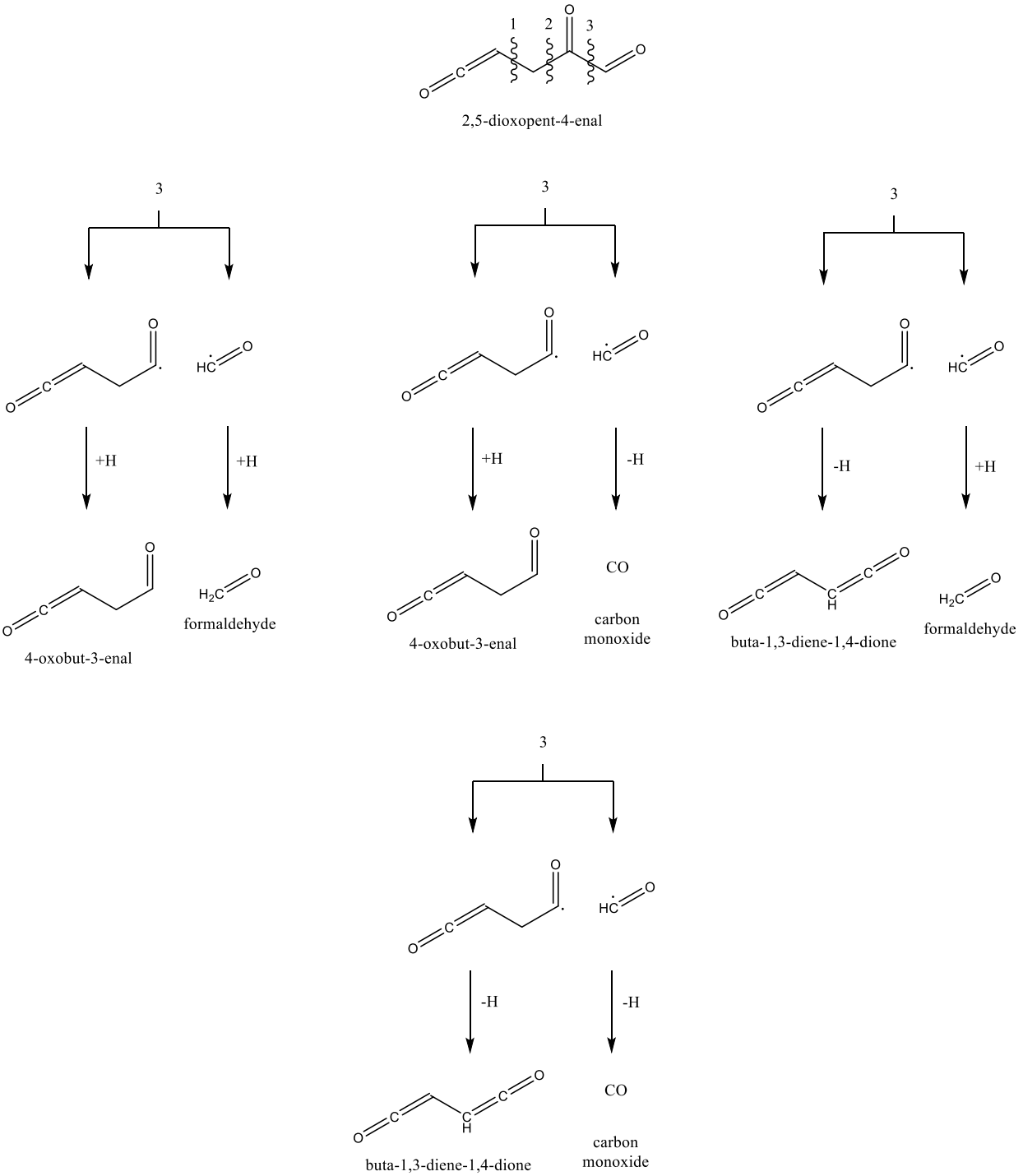

Figure S50C. Retrosynthesis of 2,5-dioxopent-4-enal utilizing single-bond cleavage and subsequent hydrogen addition/elimination.

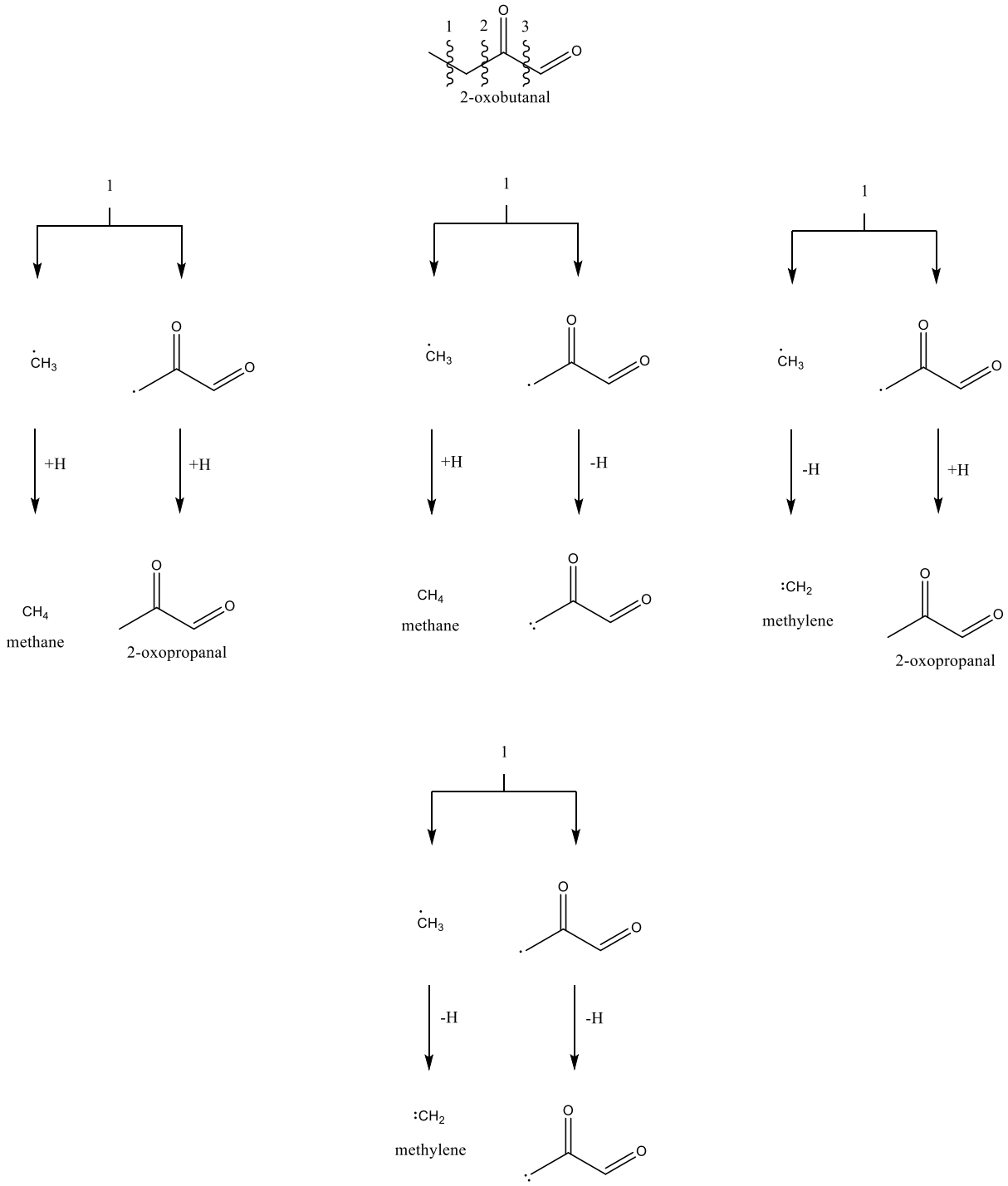

Figure S51A. Retrosynthesis of 2-oxobutanal utilizing single-bond cleavage and subsequent hydrogen addition/elimination.

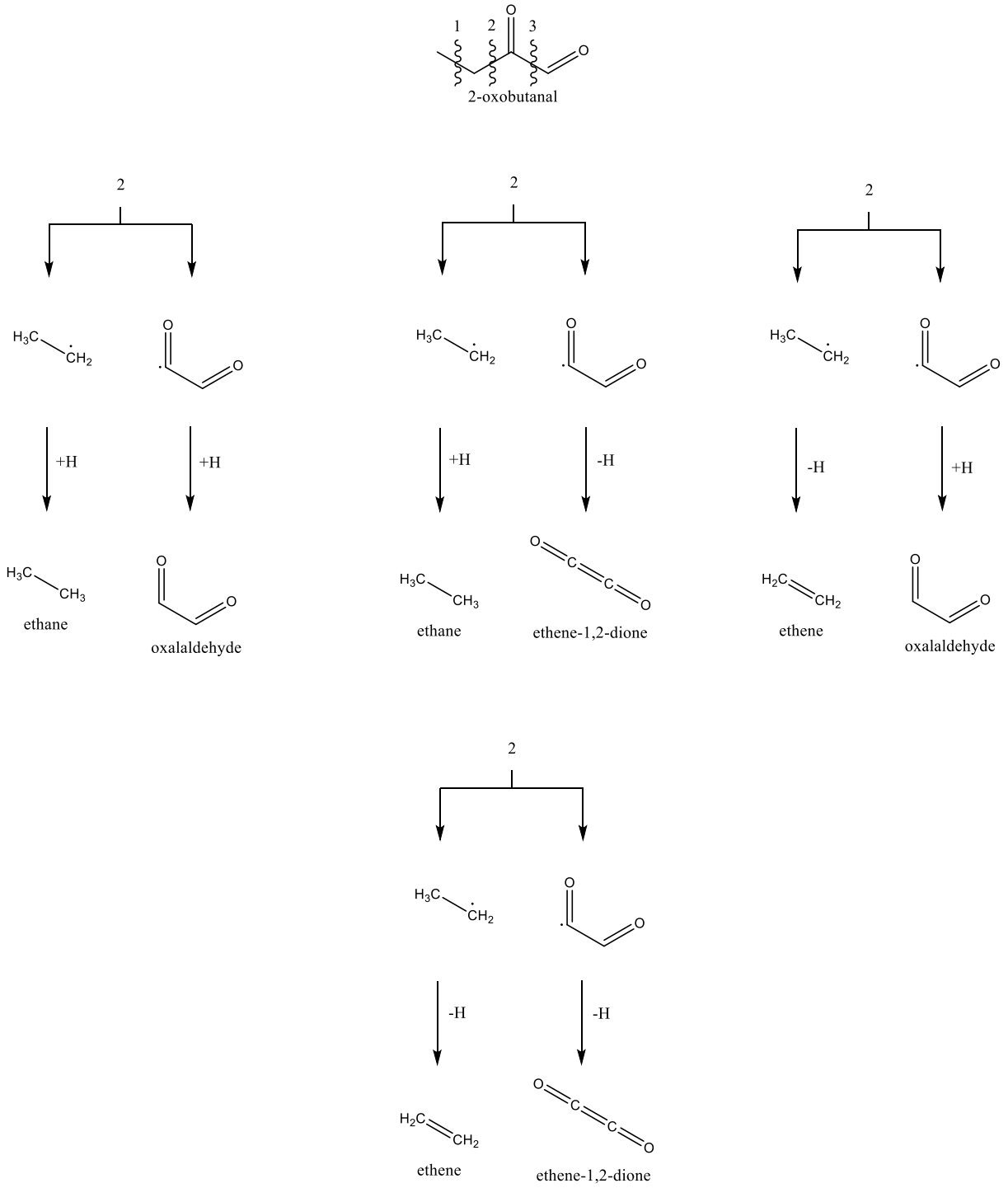

Figure S51B. Retrosynthesis of 2-oxobutanal utilizing single-bond cleavage and subsequent hydrogen addition/elimination.

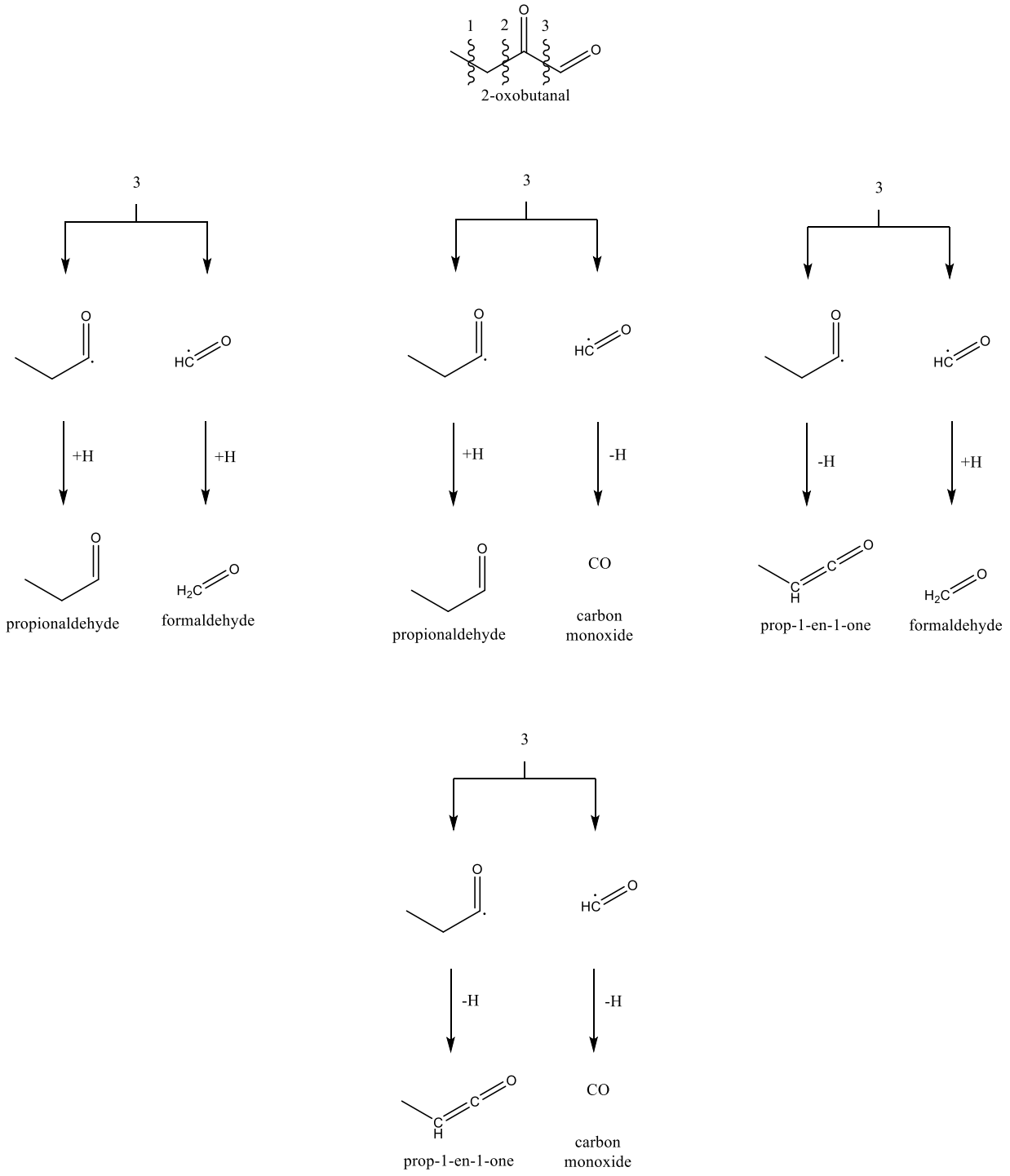

Figure S51C. Retrosynthesis of 2-oxobutanal utilizing single-bond cleavage and subsequent hydrogen addition/elimination.

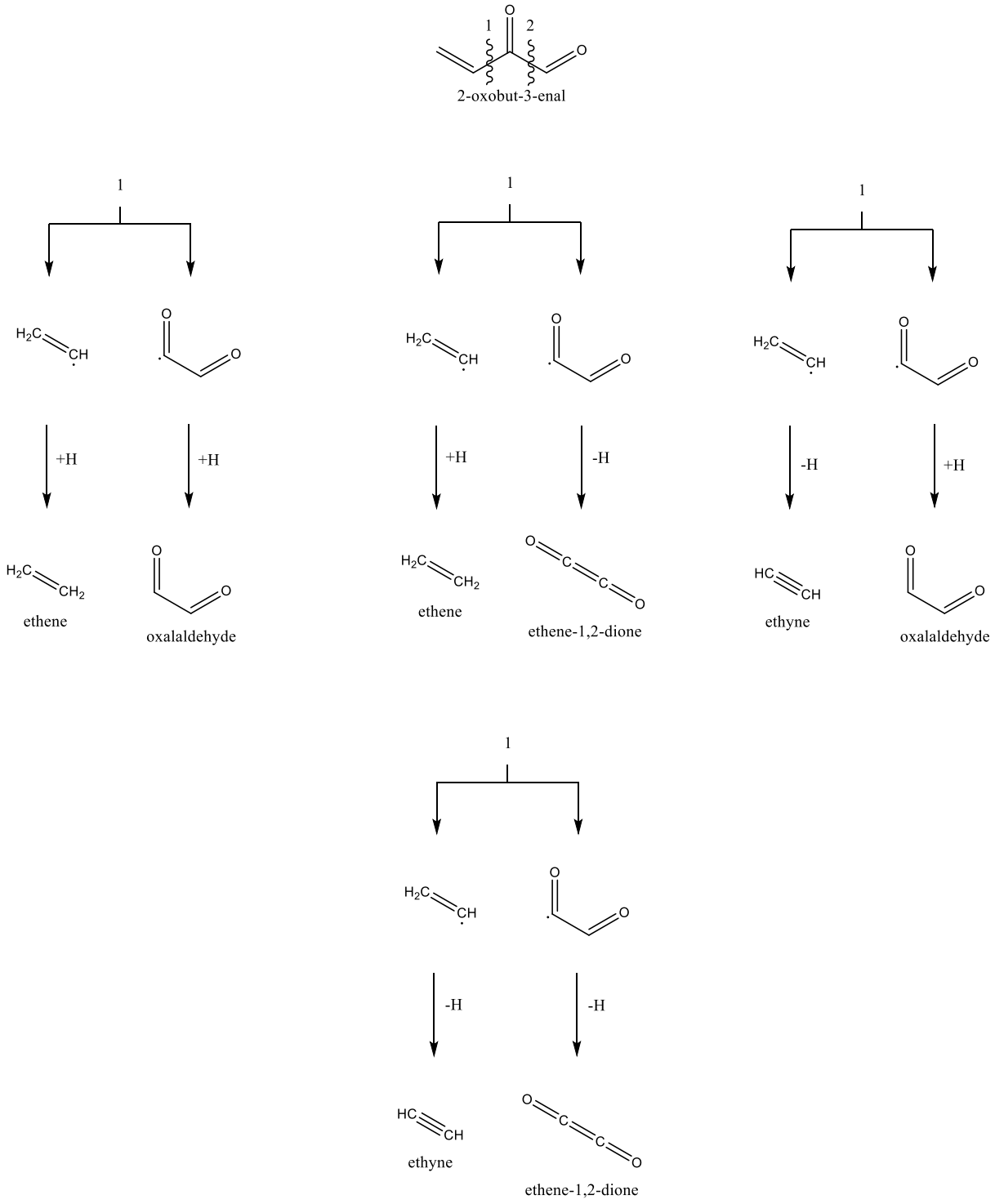

Figure S52A. Retrosynthesis of 2-oxobut-3-enal utilizing single-bond cleavage and subsequent hydrogen addition/elimination.

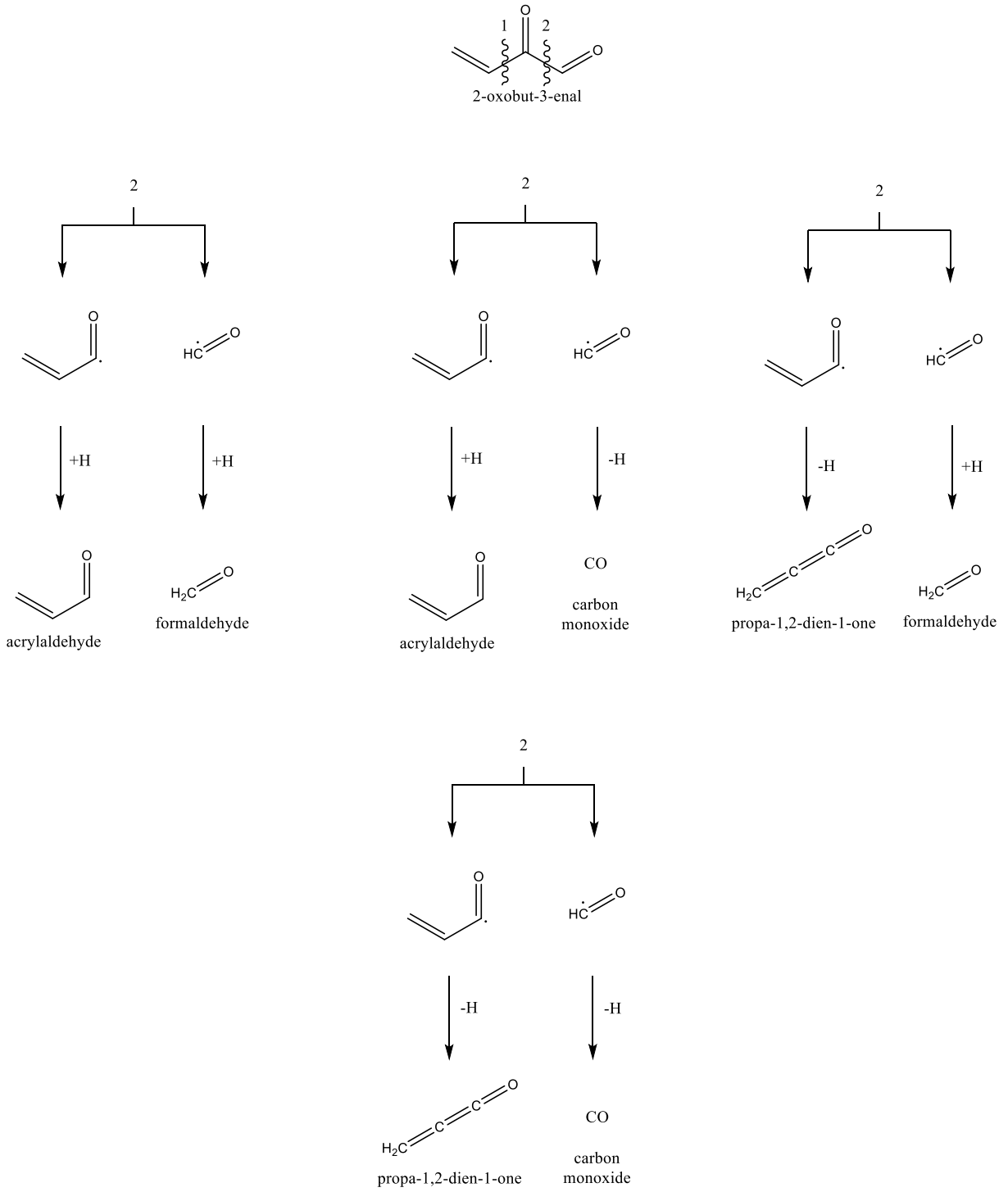

Figure S52B. Retrosynthesis of 2-oxobut-3-enal utilizing single-bond cleavage and subsequent hydrogen addition/elimination.

REFERENCES

1. M. Bajo-Fernández*, et al.* (2024) Structural elucidation of derivatives of polyfunctional metabolites after methyl chloroformate derivatization by high-resolution mass spectrometry gas chromatography. Application to microbiota metabolites. *J. Chromatogr. A* 1717:464656.

2. P. Hušek*, et al.* (2016) Profiling of urinary amino-carboxylic metabolites by in-situ heptafluorobutyl chloroformate mediated sample preparation and gas chromatography-mass spectrometry. *J. Chromatogr. A* 1443:211-232.

3. O. Mamer*, et al.* (2013) The complete targeted profile of the organic acid intermediates of the citric acid cycle using a single stable isotope dilution analysis, sodium borodeuteride reduction and selected ion monitoring GC/MS. *Metabolomics* 9(5):1019-1030.

4. R. J. Morton & R. I. Kaiser (2003) Kinetics of suprathermal hydrogen atom reactions with saturated hydrides in planetary and satellite atmospheres. *Planet. Space Sci.* 51(6):365-373.

5. R. I. Kaiser & K. Roessler (1998) Theoretical and Laboratory Studies on the Interaction of Cosmic-Ray Particles with Interstellar Ices. III. Suprathermal Chemistry-Induced Formation of Hydrocarbon Molecules in Solid Methane (CH_4), Ethylene (C_2H_4), and Acetylene (C_2H_2). *Astrophys. J.* 503:959-975.

6. M. Förstel, A. Bergantini, P. Maksyutenko, S. Góbi, & R. I. Kaiser (2017) Formation of Methylamine and Ethylamine in Extraterrestrial Ices and Their Role as Fundamental Building Blocks of Proteinogenic α-amino Acids. *Astrophys. J.* 845(1):83.

7. C. J. Bennett, C. S. Jamieson, Y. Osamura, & R. I. Kaiser (2006) Laboratory Studies on the Irradiation of Methane in Interstellar, Cometary, and Solar System Ices. *Astrophys. J.* 653(1):792.

8. A. Bergantini, S. Góbi, M. J. Abplanalp, & R. I. Kaiser (2018) A Mechanistical Study on the Formation of Dimethyl Ether (CH_3OCH_3) and Ethanol (CH_3CH_2OH) in Methanol-containing Ices and Implications for the Chemistry of Star-forming Regions. *Astrophys. J.* 852(2):70.

9. A. Potapov, H. Mutschke, P. Seeber, T. Henning, & C. Jäger (2018) Low-temperature Optical Properties of Interstellar and Circumstellar Icy Silicate Grain Analogs in the Mid-infrared Spectral Region. *Astrophys. J.* 861:84.

10. M. Bouilloud*, et al.* (2015) Bibliographic review and new measurements of the infrared band strengths of pure molecules at 25 K: H_2O, CO_2, CO, CH_4, NH_3, CH_3OH, HCOOH and H_2CO. *Mon. Not. R. Astron. Soc.* 451(2):2145-2160.

11. R. Luna, M. Á. Satorre, M. Domingo, C. Millán, & C. Santonja (2012) Density and refractive index of binary CH_4, N_2 and CO_2 ice mixtures. *Icarus* 221(1):186-191.

12. P. A. Gerakines & R. L. Hudson (2015) First infrared band strengths for amorphous CO_2, an overlooked component of interstellar ices. *Astrophys. J. Lett.* 808(2):L40.

13. R. Luna, C. Millán, M. Domingo, C. Santonja, & M. Á. Satorre (2022) Density and Refractive Index of Carbon Monoxide Ice at Different Temperatures. *Astrophys. J.* 935(2):134.

14. P. A. Gerakines & R. L. Hudson (2015) Infrared Spectra And Optical Constants Of Elusive Amorphous Methane. *Astrophys. J. Lett.* 805(2):L20.

15. R. L. Hudson, P. A. Gerakines, & Y. Y. Yarnall (2024) Infrared Spectroscopic and Physical Properties of Methanol Ices—Reconciling the Conflicting Published Band Strengths of an Important Interstellar Solid. *Astrophys. J.* 970(2):108.

16. P. A. Gerakines, W. A. Schutte, & P. Ehrenfreund (1996) Ultraviolet processing of interstellar ice analogs. I. Pure ices. *Astron. Astrophys.* 312:289-305.

17. R. L. Hudson (2017) An IR investigation of solid amorphous ethanol — Spectra, properties, and phase changes. *Spectrochim. Acta A* 187:82-86.

18. M. Á. Satorre*, et al.* (2017) Densities and refractive indices of ethane and ethylene at astrophysically relevant temperatures. *Icarus* 296:179-182.

19. R. L. Hudson, P. A. Gerakines, & M. H. Moore (2014) Infrared spectra and optical constants of astronomical ices: II. Ethane and ethylene. *Icarus* 243:148-157.

20. R. L. Hudson & F. M. Coleman (2019) Infrared intensities and molar refraction of amorphous dimethyl carbonate – comparisons to four interstellar molecules. *Phys. Chem. Chem. Phys.* 21(21):11284-11289.

21. R. L. Hudson & R. F. Ferrante (2019) Quantifying acetaldehyde in astronomical ices and laboratory analogues: IR spectra, intensities, ^{13}C shifts, and radiation chemistry. *Mon. Not. R. Astron. Soc.* 492(1):283-293.

22. W. Hagen, A. G. G. M. Tielens, & J. M. Greenberg (1981) The infrared spectra of amorphous solid water and ice Ic between 10 and 140 K. *J. Chem. Phys.* 56(3):367-379.

23. P. A. Gerakines, W. A. Schutte, J. M. Greenberg, & E. F. van Dishoeck (1995) The infrared band strengths of H_2O, CO and CO_2 in laboratory simulations of astrophysical ice mixtures. *Astron. Astrophys.* 296:810.

24. G. Socrates (2004) *Infrared and Raman Characteristic Group Frequencies* (Wiley) 3rd Ed.

25. Y. S. Kim, C. J. Bennett, L.-H. Chen, K. O'Brien, & R. I. Kaiser (2010) Laboratory studies on the irradiation of solid ethane analog ices and implications to Titan's chemistry. *Astrophys. J.* 711(2):744.

26. W. Hagen, A. Tielens, & J. Greenberg (1981) The infrared spectra of amorphous solid water and ice Ic between 10 and 140 K. *J. Chem. Phys.* 56(3):367-379.

27. C. J. Bennett, S.-H. Chen, B.-J. Sun, A. H. H. Chang, & R. I. Kaiser (2007) Mechanistical Studies on the Irradiation of Methanol in Extraterrestrial Ices. *Astrophys. J.* 660(2):1588.

28. J. H. Marks*, et al.* (2023) Complex Reactive Acids from Methanol and Carbon Dioxide Ice: Glycolic Acid ($HOCH_2COOH$) and Carbonic Acid Monomethyl Ester (CH_3OCOOH). *Astrophys. J.* 942(1):43.

29. A. J. Barnes & H. E. Hallam (1970) Infra-red cryogenic studies. Part 5.—Ethanol and ethanol-d argon matrices. *Trans. Faraday Soc.* 66(0):1932-1940.

30. M. J. Abplanalp & R. I. Kaiser (2016) Complex Hydrocarbon Chemistry in Interstellar and Solar System Ices Revealed: A Combined Infrared Spectroscopy and Reflectron Time-of-flight Mass Spectrometry Analysis of Ethane (C_2H_6) and D_6-Ethane (C_2D_6) Ices Exposed to Ionizing Radiation. *Astrophys. J.* 827:132.